

# Nanostructuring of Indium Tin Oxide with Sub-15 Femtosecond Laser Pulses for Technical and Biomedical Applications

DISSERTATION

zur Erlangung des Grades  
des Doktors der Ingenieurwissenschaften  
der Naturwissenschaftlich-Technischen Fakultät  
der Universität des Saarlandes

von

**Dipl.-Phys. Maziar Afshar**

Saarbrücken

2016

Tag des Kolloquiums:	14.12.2016
Dekan:	Univ.-Prof. Dr. Guido Kickelbick
Berichterstatter:	Prof. Dr. rer. nat. Helmut Seidel Prof. Dr.-Ing. Frank Mücklich
Vorsitz:	Prof. Dr.-Ing. Matthias Nienhaus
Akad. Mitarbeiter:	Dr. rer. nat. Tilman Sauerwald



I dedicate this work to you to Hanna, my sweet, little daughter and Somi, my lovely wife. Through both of you, I have found meaning in life and also a strength, eradicating all fears.

love you forever

# 1 Abstract

Modern laser technologies enable the production of nanostructures on a relatively large area for a variety of applications. Nonlinear effects occurring at high light intensities, such as multiphoton absorption, allow structuring in dimensions below the diffraction limit.

While existing applications for 2D confined nanostructures are essentially based on self-organizing structures without a well definable profile or in combination with complex processing steps, precisely flexible defined nanostructures were fabricated in this work. It is about the interaction of a tightly focused near infrared sub-15 femtosecond laser (repetition rate: 85 MHz) with sputtered polycrystalline ITO thin films exhibiting different electrical conductivities. Depending on the choice of parameters, total ablation, periodic nano-cuts or else crystal modifications can be generated, rendering the ITO layer resistant to a subsequent etching step. Using this innovative approach, nanowires attached to the substrate or even freestanding nanowires (in combination with a selectively etchable sacrificial layer) with a length-to-width ratio of more than one hundred were prepared. The applicability of such nanowires for self-heating resistive gas sensors for detection of oxidizing gases was demonstrated. As another demonstrator, ITO bioelectrodes were trimmed with respect to their impedance by coherent sub-20 nm wide and several microns long nano-cuts.

## 2 **Kurzfassung**

Moderne Lasertechnologien ermöglichen eine relativ großflächige Herstellung von Nanostrukturen für eine Vielzahl von Anwendungen. Bei hohen Lichtintensitäten auftretende nicht-lineare Effekte, wie z.B. Multiphotonenabsorption, erlauben das Unterschreiten der Beugungsgrenze.

Während existierende Anwendungen für räumlich 2D beschränkte Nanostrukturen wesentlich auf selbstorganisierenden, wenig steuerbaren Profile in Kombination mit aufwändigen Prozessen basieren, konnten in der vorliegenden Arbeit präzise definierbare Nanostrukturen hergestellt werden. Zentraler Punkt dieser Arbeit ist die Wechselwirkung eines eng fokussierten nahinfraroten Sub-15-Femtosekunden-Laserstrahls (Wiederholrate: 85 MHz) mit gesputterten ITO-Dünnschichten, die unterschiedliche elektrische Leitfähigkeiten aufweisen. Je nach Wahl der Parameter können totale Ablation, periodische Nanoschnitte aber auch Kristallmodifikationen erreicht werden, die die ITO-Schicht resistent gegenüber einem nachfolgenden Ätzschritt machen. Mit diesem innovativen Prozessansatz konnten substratgebundene bzw. freistehende (in Kombination mit einer selektiv ätzbaren Opferschicht) Nanodrähte mit einem Längen-zu-Breiten-Verhältnis von mehr als einhundert hergestellt werden. Die Verwendbarkeit solcher selbstheizbarer Drähte zur resistiven Detektion von oxidierenden Gasen konnte demonstriert werden. Als weiterer Demonstrator wurden ITO-Bioelektroden mit kohärenten sub-20 nm-breiten und mehrere Mikrometer langen Nanoschnitten bezüglich ihrer Impedanz modifiziert.

### 3 Eidestattliche Versicherung

Hiermit versichere ich an Eides statt, dass ich die vorliegende Arbeit selbstständig und ohne Benutzung anderer als der angegebenen Hilfsmittel angefertigt habe. Die aus anderen Quellen oder indirekt übernommenen Daten und Konzepte sind unter Angabe der Quelle gekennzeichnet. Die Arbeit wurde bisher weder im In- noch im Ausland in gleicher oder ähnlicher Form in einem Verfahren zur Erlangung eines akademischen Grades vorgelegt.

---

Datum, Ort

---

Unterschrift

# Contents

1	Abstract . . . . .	IV
2	Kurzfassung . . . . .	V
3	Eidstattliche Versicherung . . . . .	VI
<b>1</b>	<b>Introduction</b>	<b>1</b>
<b>2</b>	<b>Theory and Background</b>	<b>3</b>
2.1	Laser Technology . . . . .	3
2.1.1	Principles of Femtosecond Lasers . . . . .	6
2.1.2	Principles of Laser-Material Interaction . . . . .	8
2.1.3	Ablation and Modification through Single Laser Pulses . . . . .	10
2.1.4	Laser Induced Ablation Threshold . . . . .	17
2.1.5	Ablation and Modification through Laser Pulse Train . . . . .	19
2.1.6	Laser Beam Focusing and Scanning . . . . .	23
2.1.7	Laser Induced Periodic Self-Organized Structures . . . . .	24
2.1.8	Laser Structuring of Thin Films . . . . .	25
2.2	Material Properties . . . . .	27
2.2.1	Indium Tin Oxide (ITO) . . . . .	27
2.2.2	Glass Substrate . . . . .	35
2.2.3	Aluminum Nitride (AlN) . . . . .	36
2.2.4	Gold (Au) and Platinum (Pt) . . . . .	37
2.2.5	Photoresists . . . . .	38
<b>3</b>	<b>Experimental Methods</b>	<b>43</b>
3.1	Utilized Laser-Setup . . . . .	43
3.2	Material Characterization Methods . . . . .	45
3.2.1	Structural Analysis . . . . .	45
3.2.2	Optical Analysis . . . . .	49
3.2.3	Electrical Analysis . . . . .	54
3.2.4	Topographical Analysis . . . . .	57
3.2.5	Mechanical Analysis . . . . .	58
3.3	Device Characterization Methods . . . . .	62
3.3.1	Electrical Measurements . . . . .	62
3.3.2	Impedance Spectroscopy . . . . .	63

---

<b>4</b>	<b>From ITO Laser Nanostructuring to Applications</b>	<b>65</b>
4.1	Sub-100 nm Structuring of ITO Polycrystalline Thin Films . . . . .	67
4.1.1	Introduction . . . . .	67
4.1.2	Addendum I . . . . .	70
4.2	Simulation Based Application Design . . . . .	83
4.3	On-Chip Nanostructuring and Impedance Trimming of ITO electrodes . . . . .	85
4.3.1	Introduction . . . . .	85
4.3.2	Addendum II . . . . .	90
4.4	Single-Nanowire Polycrystalline ITO Gas Sensors . . . . .	99
4.4.1	Introduction . . . . .	99
4.4.2	Addendum III . . . . .	105
4.5	Freestanding ITO Nanowires; Fabrication and Simulation (Unpublished Data)	117
4.5.1	Introduction . . . . .	117
4.5.2	Addendum IV (Unpublished Data) . . . . .	121
<b>5</b>	<b>Summary and Outlook</b>	<b>133</b>
5.1	Summary . . . . .	133
5.2	Outlook . . . . .	134
	<b>List of Figures</b>	<b>137</b>
	<b>List of Tables</b>	<b>141</b>
	<b>Bibliography</b>	<b>143</b>
	<b>Acknowledgements</b>	<b>161</b>
	<b>Curriculum vitae</b>	<b>163</b>

# 1 Introduction

The invention of the laser in 1960 has had a huge impact on optical science and technology. It was the origin of many technical innovations and pushed the technology of optical instruments and tools consistently forward. More recently a combination of a laser and a microscope with integrated precise optics offers a way to focus and scan a laser beam precisely and quickly. The confinement of the beam is limited by Abbe's diffraction law of classical optics and it can be reduced down to a spot size of 200-300 nm in the visible range of light. Classical optics is ruled by linear physics. Such a strong confinement of the laser beams leads to a high intensity in the focal region which can induce local physical and chemical processes enabling the fabrication of sub-wavelength structures.

Using pulsed lasers increases the intensity in the focal region so much that it allows for nonlinear interaction with materials. Nonlinear effects, such as two-photon excitations, offer the possibility to confine the interaction within the focal volume. Making 3D structures in polymers (photo resists) using multi-photon polymerization is one of the advantages of this technique with high application potential in nano-science and nano-engineering. Using femtosecond laser pulses reduces the focal volume because of the threshold effect combined with the changed physical regime of the laser-material interaction. All these results provide a powerful tool to generate sub-wavelength structures far below the diffraction limit.

During the last decade a large scientific effort was focused on the optical generation of nanostructures in different materials and on their application. The 2014 Physics Nobel Laureate, Stefan Hell, broke the diffraction limited resolution barrier of about half the wavelength (200 nm) by using two overlapping lasers. With this technique it is now possible to generate polymerized 3D structures with feature sizes down to about 10 nm [1]. However, this is not yet a technology with industrial applicability and is still very complex and costly.

This project as a part of priority program 1327 funded by German Research Foundation (DFG) was focused on the optical generation of sub-100 nm structures for technical and biomedical applications. For this purpose a laser microscope is used with a near infrared Ti:sapphire femtosecond laser with high repetition rate of 85 MHz and a pulse length of about 9 fs. Utilizing chirped mirror and dispersive mediums the pulse length can be varied between 12 fs and 3 ps on the microscope. The laser beam can be driven in x and y direction and a piezo-actor can adjust the vertical distance between the sample and the objective. The precise positioning and scanning of the laser beam is also being used in another project in the same program for fluorescence imaging of cells [2].

In this thesis the results of the interaction of such laser pulses with indium tin oxide (ITO) films on glass are presented as well as demonstration of some applications for the processed

nanostructures. The ITO films in this work were prepared by DC magnetron sputtering method. Different film properties were deposited under various conditions. The main task by the deposition were two; achieving a good transparency by simultaneous change of the electrical properties to study the interaction between laser beam and ITO in dependency on the electrical properties. Laser lithography technique for applications has been one of the topics in this project, which is not addressed in this work [1]. The layout of the dissertation is arranged as follows:

The background theories about laser technology, utilized laser setup, laser-material processing and used materials are presented in Chapter 2. Material laser processing in case of thin films regarding our researches is discussed in this Chapter. A short description for the used materials is also provided. This is followed by Chapter 3 introducing the characterization methods. Describing the equipment used to characterize the fabricated layers and the realized demonstrators for the applications. Chapter 4, in form of a journey through ITO nanostructuring toward their applications, is attended to the publications with a short theoretical background to each idea as an introduction. The publications about the material processing results and applications are attached. The last application or better expressed the novel fabrication method of freestanding nanowires is still in format of a manuscript and will be submitted to a journal. The thesis ends up with a summary and outlook to push the ideas forward for further studies and for optimizing the results and performances.



## 2 Theory and Background

This Chapter is presenting a brief summary about the history of laser technology followed by an introduction to the physical principles of the interaction between laser and materials particularly in case of transparent thin films.

### 2.1 Laser Technology

Theoretical foundations for technical invention of the laser were laid in the 1950's. The first experimental development had been done in the microwave range by fabrication of a MASER (microwave amplification by stimulated emission of radiation), which was later transferred into the optical wavelength range. The first maser was built by C. H. Townes, J. P. Gordon, and H. J. Zeiger at Columbia University in 1953. When the physical principles behind this invention were transferred into the optical wave range, the new device was first called an "optical maser" and was later replaced by the word LASER (light amplification by stimulated emission of radiation). This was first implemented in a working device in 1960 by T. H. Maiman [3]. It was a ruby laser emitting at a wavelength of 694.3 nm. In the same year, the first HeNe gas laser (Javan *et al.*) and the first laser diode were fabricated.

This was the beginning of a new era providing a light source with intense coherent radiation enabling many interesting new applications. Laser light has a number of unique properties e.g. the very high degree of coherence of the radiation.

A laser oscillator usually comprises an optical resonator (laser resonator, laser cavity) in which light is trapped (e.g. between two mirrors) and a gain medium within this resonator e.g. a laser crystal which serves to amplify the light. Without gain medium the circulating light would become weaker and weaker in each resonator round trip, because it experiences some losses, e.g. upon reflection at the mirrors. However, the gain medium can amplify the circulating light, thus compensating the losses if the gain is high enough. The gain medium requires some external supply of energy. It needs to be "pumped", e.g. by injecting light (optical pumping) or by an electric current (electrical pumping in semiconductor lasers). The principle of laser amplification is the stimulated emission [4]. Stimulated emission is called the process by which an incoming photon of a specific frequency interacts with excited atomic electrons or other excited molecular states, causing them to drop simultaneously and coherently to a lower energy level. Hereby, the liberated energy generates new photons with identical phase, frequency, polarization, and flight direction as the photons of the incident wave.

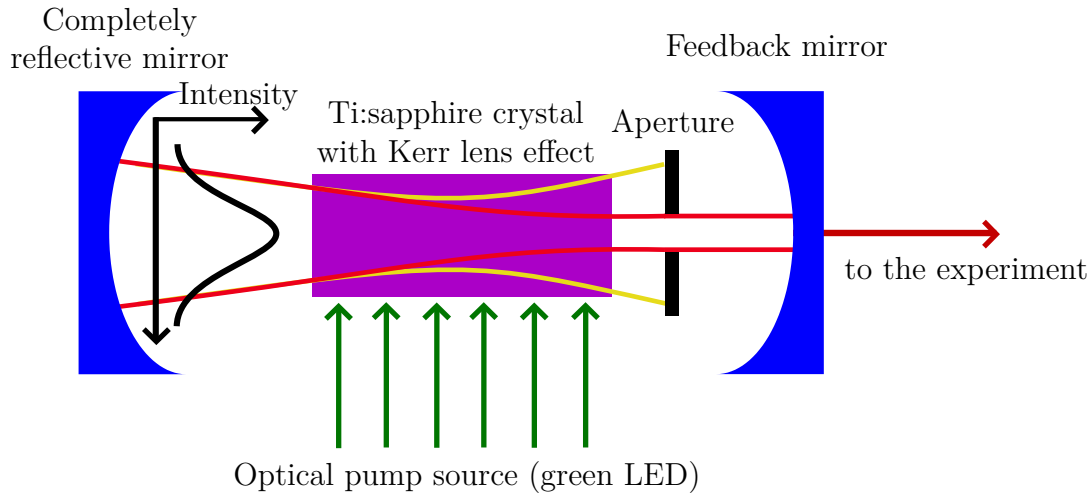


**Figure 2.1:** Schematic setup of a passive mode locked femtosecond laser.

The invention of the laser opened up a way to verify new theoretically predicted physical effects and made their experimental investigation and verification possible. This includes two-photon absorption (TPA), which was theoretically predicted by Maria Göppert in 1929 [5] as well as new effects which are discovered by using focused laser light such as second harmonic generation (SHG). Shortly after the invention of the laser, in 1961 the two-photon fluorescence excitation and second harmonic generation were both demonstrated as two nonlinear optical effects.

Exciting an electron to an energetic higher state, with the energy increase equal to the sum of the single photon energies can be understood as a simultaneous absorption of multiple photons with individual energies below the band gap energy of a material, so called multiphoton-absorption (MPA). This can result in subsequent phenomena, such as multiphoton ionization, optical breakdown and finally plasma formation, leading to the ablation of materials, which can be used for laser structuring. The SHG which is also interpreted as an effective combination of two photons with the same frequency, generating new photons with twice the energy and frequency of the initial photons, is a result of dipole oscillations of atomic charges. At high intensities of light is the amplitude of the oscillation big enough to be affected by the charge of neighboring atoms. This changes the first harmonic frequency of the oscillation to contain higher harmonics which are radiated in secondary electromagnetic wave (Maxwell law). It occurs by interaction of electromagnetic waves with a nonlinear material at high intensities.

Within a few years many new applications were invented and tested with lasers, including laser machining, laser welding, laser-induced breakdown spectroscopy and even medical applications [1].

Consequently, scientists started to study the interaction of different laser types with different materials. Already in 1965 "laser induced periodic surface structures" (LIPSS) were observed in semiconductors [6], with a periodicity close to the exposure wavelength. In a short period of time several types of lasers were being invented, including the previously mentioned semiconductor laser in 1961 and the HeNe laser in 1962 as well as the CO<sub>2</sub> laser,

the Nd:YAG laser and the dye laser in 1964. After the invention of the excimer laser in 1970 as a powerful and low priced UV-laser source with wavelengths below 351 nm, industrial micro- and nanoprocessing became popular.

More recent generations of lasers exhibit a pulsed emitting mode instead of a continuous mode in cw-lasers (continuous wave) of the earlier generations. This means that light is emitted at defined time intervals with a certain pulse length ( $\tau$ ) and can thus be particularly intense. There are various methods for pulse generation with commercial lasers, with pulse duration ranging from microseconds over nanoseconds and picoseconds down to a few femtoseconds. Concerning this parameter and regarding the typical times for physical relaxation processes in materials, pulsed lasers are divided into short- and ultra-short pulsed lasers (see Section 2.1.2). Ultra-short laser pulses have the advantage that high pulse intensities can be achieved at low average power. The shortest noncommercial laser pulse is 67 attoseconds [7]. One attosecond is the time it takes for light to travel the length of two hydrogen atoms.

Concerning pulse duration ( $\tau$ ), pulse energy ( $E_p$ ), pulse repetition rate (R) and the band width of the laser spectrum, different ways of pulse generation are used, resulting in very different pulsed laser setups. The most commonly used ones are mentioned in the following.

For nanosecond pulse duration, various types of Q-switched lasers (see explanation in Section 2.1.1) are available with pulse energies in the mJ range or more and a repetition rate between a few Hz and many kHz. Solid state bulk lasers give high pulse energies, whereas for small pulse energies fiber lasers are suitable. Nanosecond pulses in the UV spectral range are generated with excimer lasers either by Q-switching or by gain switching. Picosecond and femtosecond pulses are generated with mode-locking in active or passive form with a typical duration between 30 fs and 30 ps, having MHz or GHz pulse repetition rates and pulse energies of pJ to nJ. This method can be applied in solid state bulk lasers, fiber lasers, or semiconductor lasers. Gain-switched semiconductor lasers generate nanosecond or picosecond pulses, but with relatively small energy. This can be done by quickly switching the optical gain by the pump power electronically [4].

While cw-lasers may have a very small optical bandwidth (linewidth) for only a single resonator mode (single frequency operation), in some other lasers the band width can be very large, particularly for mode locked pulsed lasers. Some broadband gain media such as Ti:sapphire and Cr:ZnSe allow wavelength tuning over hundreds of nanometers.

This large variety of laser types provides the possibility to choose and trigger the physical effects of processing by selecting the laser parameter (e.g.  $\lambda$ ,  $\tau$ ,  $E_p$ , and R) within a wide range, making material processing with lasers to a standard industrial method for many applications. Laser processing is now more or less frequently used in cutting, drilling, welding, soldering, surface treatment, engraving, rapid prototyping, and polymerizing (lithography).

Since a femtosecond laser was the basis for the work presented in this thesis, the next Section briefly discusses the generation of femtosecond laser pulses in more detail.

### 2.1.1 Principles of Femtosecond Lasers

When cw-lasers are switched on, they often exhibit a transient behavior with strong irregularities in the pulse timing, caused by relaxation oscillations. The dynamic behavior of a laser is determined by the interaction of the intracavity light field with the gain medium. This manifests itself mainly through short intensity peaks (spikes) before the laser gradually goes over into continuous operation. The intracavity laser power can grow or decay exponentially according to the difference between gain and resonator losses. The rate of change in the gain is determined by stimulated and spontaneous emission and by other effects such as energy transfer [4]. This phenomenon can be used systematically to generate laser pulses. The perturbation in the system can be generated by different techniques.

Laser short pulses are being generated by modulating the pumping processes with the help of a Q-switch or by mode-locking. The Q-switching method is made possible with a time variant (modulated) resonator loss. An initially high population inversion pumped in the gain medium (saturated gain) within a low quality factor resonator (attenuated resonator) can suddenly be involved in an optical amplification (by opening the attenuator and reducing the resonator loss). Due to the large amount of energy already stored in the gain medium, the intensity of light in the laser resonator builds up very quickly. It causes the energy stored in the medium to be depleted almost as quickly. The net result is a pulse of light output from the laser releasing the laser energy in a short pulse with a high peak intensity. This only works, if the life time of the upper laser level is higher than the pumping time [8]. For the modulation of resonator losses switchable Pockels cells, acousto-optic modulators, rotating prisms or Kerr-cells can be used in form of active and passive Q-switching. Pulse lengths in the nanosecond range and pulse repetition frequencies of 10 Hz to 1 kHz are hereby realized [9].

In contrast, mode-locking is based on the principle of superposition of several laser modes. Each laser mode differs slightly in frequency. Superposing all laser modes in the same phase, gives a strong concentration of the laser energy into narrow peaks. In lasers with only a few oscillating modes, interference between the modes can cause beating effects in the laser output (fluctuations in intensity). For lasers with many thousands of modes, these interference effects merge to a near constant output intensity. If each mode, instead of oscillating independently, operates with a fixed phase with respect to other modes (mode-locked laser), the laser output will periodically produce an intense pulse of light. A large bandwidth leads to a large number of modes involved and, thus, to very short pulses. In a laser amplifier with high bandwidth, the mode coupling is achieved by a Q-factor modulation, for example with saturating absorbers or Kerr-lenses [8, 10]. This technique can produce pulses of light of extremely short duration, on the order of picoseconds ( $10^{-12}$  s) or femtoseconds ( $10^{-15}$  s).

The pulse duration  $\tau$  is generally limited by the uncertainty principle for time and energy, represented as pulse duration and bandwidth [8]:

$$\Delta\tau \cdot \Delta\nu \geq K, \quad (2.1)$$

where  $\Delta\nu$  is the laser spectral linewidth and  $K$  a pulse shape dependent constant, which is 0.441 for Gaussian pulses [10].

Due to the following relationship between the number of longitudinal modes  $N$  within the linewidth  $\Delta\nu$  for a cavity with a length of  $L$  and  $c$  as speed of light

$$N = \Delta\nu \frac{2L}{c}, \quad (2.2)$$

the following relation can be obtain for the pulse duration  $\tau$ :

$$\tau \geq \frac{K}{N} \frac{2L}{c}. \quad (2.3)$$

The more mode coupling, the shorter the pulse length. The equation follows from the Fourier transformation between time and frequency domains. In case of a Ti:sapphire laser the pulse duration is in the ps to fs range and the bandwidth is correspondingly large in the THz range with pulse energies in the nJ range. To achieve higher pulse energies, the pulse repetition frequency is generally reduced down to the kHz range.

The laser used in this project is a Ti:sapphire laser, with a doped titanium artificial sapphire crystal (monocrystalline  $\text{Al}_2\text{O}_3$ ) as active medium.  $\text{Ti}^{3+}$  ions in the aluminum oxide crystal are the laser medium, and they are excited by an optical pumping process. These ions have only a typical mass fraction of less than 0.1 % within the crystal. The wide bandwidth of this laser is due to the large number of subband levels involved in laser transitions [11]. These form wide bands through homogeneous vibrational broadening by interaction between excited states and phonons. A Ti:sapphire laser can be tuned over a very wide wavelength range of 660-1180 nm [11]. The life time in the upper laser level is relatively short with  $3 \mu\text{s}$  at  $20^\circ\text{C}$  [8]. For this reason, pumping with a flash lamp is difficult. Therefore, the laser is pumped by a green solid state laser, which in turn is pumped by a diode. Mode coupling is relatively easy to achieve in a Ti:sapphire laser, since the crystal serves as Kerr-lens at high intensities and thus the beam diameter is reduced. By using an aperture, it is achieved that the pulsed beam possesses lower losses than the continuous beam (see Fig. 2.1).

This results in a frequency spacing of the longitudinal modes of  $\delta\nu = c/2L = 150 \text{ MHz}$  with a resonator length of  $L = 1 \text{ m}$ . With a bandwidth of  $\Delta\nu = 75 \text{ THz}$  or  $150 \text{ nm}$  (central wavelength  $800 \text{ nm}$ ), a number of  $N = \frac{\Delta\nu}{\delta\nu} = 5 \times 10^5$  modes will arise. From this follows a possible shortest pulse duration of  $\tau = T/N = 2L/(c \times N) = 13 \text{ fs}$ , where  $T$  is a single cycle flight time in the cavity.

In case of  $N$  coupled modes the temporal energy distribution  $E$  is based on the following description [8]:

$$E(t) = \sum_{q=q_0}^{q_0+(N-1)} E_q \cos \left( 2\pi q \frac{t}{T} + \phi_q \right), \quad (2.4)$$

where  $N$  is the number of coupled modes,  $\phi_q$  the phase of each axial mode and the frequency of an axial mode  $q$  is given by  $f_q = qc/2L = q/T$ .  $L$  is the length of the resonator and  $q_0$  is the mode with the lowest frequency. This results in a pulse generation in form of a pulse train.

### 2.1.2 Principles of Laser-Material Interaction

Material processing is being done principally with both cw- and pulsed lasers. Pulsed lasers have some advantages which make them very interesting for several applications. They have high peak powers and therefore they achieve thresholds for material modification or removal at a lower average power. However, pulse length and repetition rate also have decisive influences on the interaction between laser and material. This will be explained in the following.

The interaction between laser beam and material, also called target, is determined by the energy transfer of the photons to the target. Thus, absorption processes in the target material and energy conversion from light to other forms determine the process of ablation or modification in the target.

The interaction between photons and material takes place in a volume element, where the light is being absorbed. For linear absorption the fluence  $F$  (energy per unit area) is the characteristic parameter, whereas for nonlinear absorption the intensity  $I$  (power per unit area) is deciding. Both parameters can be calculated indirectly from the laser pulse energy, from the laser beam profile and from the time-dependent intensity. For pulsed lasers, the relationship between  $E_p$ ,  $F$  and  $I$  is as follows:

$$E_p = \iint_{-\infty}^{\infty} F(x, y) dx dy, \quad (2.5)$$

$$F(x, y) = \int_{-\infty}^{\infty} I(x, y, t) dt, \quad (2.6)$$

with time  $t$  and  $x$  and  $y$  forming an orthogonal coordinate system perpendicular to the Poynting vector ( $\vec{S}$ ) in the  $z$  direction.

The standard beam profile is assumed to be Gaussian, so the fluence has the following distribution:

$$F(x, y) = F_0 e^{-\frac{2x^2}{x_0^2} - \frac{2y^2}{y_0^2}}, \quad (2.7)$$

where  $F_0$  is the maximum fluence and  $x_0$  and  $y_0$  are the lengths of the major and minor axes of an elliptical cross section around the optical axis of the Gaussian profile.  $E_p$  can be

calculated from Eq. 2.5 and yields the following relations in case of a radially symmetric profile ( $x_0 = y_0$ ):

$$F_0 = \frac{2E_p}{\pi\omega_0^2}, \quad F(r) = F_0 e^{-2\frac{r^2}{\omega_0^2}}, \quad (2.8)$$

where  $r$  is the distance to the optical axis,  $\omega$  is the Gaussian beam radius and is defined as the width of the Gaussian curve at  $F = \frac{F_0}{e^2}$ .

The time-dependent intensity of a Gaussian pulsed laser is:

$$I_t = I_0 e^{-4\ln(2)\frac{t^2}{\tau^2}}, \quad (2.9)$$

with  $I_0$  for maximum intensity and  $\tau$  for the pulse length at full width half maximum power (FWHM). Using Eq. 2.6 for a radially symmetric beam the following relations are obtained:

$$I_0 = \frac{2F_0}{\tau} \sqrt{\frac{\ln(2)}{\pi}} = \frac{4E_p}{\tau\omega^2} \sqrt{\frac{\ln(2)}{\pi^3}}. \quad (2.10)$$

### Absorption of Laser Radiation

The penetration of the radiation into the target will be considered as the dissipation of the energy in a homogeneously absorbing medium. Depending on the intensity, a single photon absorption or multiphoton absorption process can be induced [5]. The general equation for simultaneous absorption of photons depending on the intensity is as follows:

$$\frac{dI}{dz} = \sum_m \alpha_m I^m, \quad (2.11)$$

where  $m$  is the count of simultaneously absorbed photons, known as order of multiphoton absorption and  $\alpha_m$  is the absorption coefficient for each order of absorption. The linear absorption law for low energy densities (single photon,  $m=1$ ) according to Lambert-Beer formulates the intensity loss  $dI/dz$  over depth as follows:

$$\frac{dI}{dz} = \alpha I, \quad (2.12)$$

with  $\alpha$  as the attenuation (absorption) coefficient of each material which is wavelength dependent. This differential equation can be solved to obtain an exponential intensity distribution inside the absorbing medium

$$I(z) = I_0 e^{-\alpha z}. \quad (2.13)$$

At a constant pulse length, the same relationship can be obtained for the fluence  $F$  by simple replacement with  $I$  [12]:

$$F(z) = F_0 e^{-\alpha z}. \quad (2.14)$$

The first crucial effect of the laser radiation on the material is the interaction with the outer electrons of molecules or atoms. These electrons exchange energy with the crystal lattice. Outer electrons of atoms in solid states can absorb the electromagnetic wave in the visible (VIS), near infrared (NIR), or ultraviolet (UV) range of the spectrum.

Equation 2.11 can be solved for multiphoton absorption. Assuming that just one order of absorption is involved, the intensity distribution over the depth of the absorber is given by [13]:

$$I(z) = ((m-1)\alpha_m z + I_0^{1-m})^{\frac{1}{1-m}}, \quad (2.15)$$

and the fluence distribution is:

$$F(z) = \left\{ \left( \frac{\tau}{2} \sqrt{\frac{\pi}{\ln(2)}} \right)^{1-m} (m-1)\alpha_m z + F_0^{1-m} \right\}^{\frac{1}{1-m}}. \quad (2.16)$$

In order to have a correct understanding of the process, the absorbed energy distribution needs to be taken into account in two dimensions; across the focal spot and inside the target beneath the surface.

### 2.1.3 Ablation and Modification through Single Laser Pulses

Besides intensity, the main issue to control the physical processes by the interaction between single laser pulses and each specific material is the pulse length. Whereas the ablation of solids under action of short laser pulses occurs with a conventional evaporation in a thermodynamic equilibrium between electrons and ions, it is in drastically different conditions under the action of ultra-short pulses.

The heating of a solid by a short laser pulse induces an expansion of its lattice, resulting in a change of binding energy between atoms as an increase of attractive forces to bring the atoms back to their equilibrium position. The energy of evaporation per atom equals to its binding energy. So only atoms with the energy in excess of binding energy leave a solid [14].

The interaction between a material and ultra-short laser pulses can excite the electrons, so that they leave the lattice "cold" without interacting with it. Any phase transformation in such a laser affected solid occurs under non-equilibrium conditions which is drastically



different from transitions in equilibrium. The time-dependent statistical distribution of energies and time for reaching the equilibrium state strongly depend on the laser and material parameters. The minimum time for reaching equilibrium is about one hundred femtoseconds or less [14]. The light pulses of ultra-short lasers fall below this limit.

The major difference between ultra-fast laser ablation and equilibrium evaporation is that energy densities in excess of energy of vaporization can be delivered into the electronic part of any solid during the period shorter than major relaxation times in solids. The electrons are reaching their maximum energy (temperature) at the end of a pulse, while the lattice remains cold [14]. It can start other ablation processes which are presented in the following.

High peak intensities in the TW range and high surface energy densities up to tens of J/cm<sup>2</sup> allow phase transitions such as crystal-to-crystal, solid-to-liquid, conversion to plasma, ablation and creation of extreme pressure-temperature conditions in the confined interaction zone.

### Thermal Effects

The energy of excited electrons can in turn excite the lattice in an electron-phonon interaction (coupling). This happens in crystals in a picosecond time interval. The induced heating and thermal stress can result in a thermal ablation or modification of the material. If this coupling breaks by inducing faster processes, a non-thermal ablation of the material will be implemented. This makes fs-lasers to a powerful tool with respect to non-thermal processes.

For laser pulse lengths in the ps, ns or  $\mu$ s range and for cw-lasers, electron-lattice-coupling is responsible for the conversion of electromagnetic energy into heat, which propagates into the material. This can be described in a thermodynamic energy consideration by assuming that the total electromagnetic energy from  $N$  pulses with  $E_p$  as pulse energy is converted into thermal energy ( $Q$ ). In a first approximation, this was considered without any thermal diffusion. For a volume element  $dV$  with a defined density ( $\rho$ ) and a specific heat capacity ( $c_p$ ) the following equation is obtained:

$$\frac{dQ}{dV} = -N \frac{dE_p}{dV} = \rho c_p \Delta T, \quad (2.17)$$

describing a temperature increase  $\Delta T$ . By adding the fluence in Eq. 2.17 the change of temperature in a material caused by an absorption of the  $m$ -th order can be computed as:

$$\Delta T = \frac{1}{\rho c_p} \sum_m \alpha_m \left( \frac{2}{\tau} \sqrt{\frac{\ln(2)}{\pi}} \right)^{m-1} F(z)^m. \quad (2.18)$$

For a fixed absorption order  $m$ , by excluding all other orders of absorption and by adding equations 2.6, 2.16 and the fluence distribution of a Gaussian beam profile, the increased

temperature for single- and multiphoton absorption respectively are given by the following equations:

$$\Delta T = \frac{\alpha_1}{\rho c_p} F_{0\max} e^{-2\frac{r^2}{\omega_0^2}} e^{-\alpha_1 z}, \quad (2.19)$$

$$\Delta T = \frac{\alpha_m}{\rho c_p} \left( \frac{2}{\tau} \sqrt{\frac{\ln(2)}{\pi}} \right)^{m-1} \left\{ \left( \frac{\tau}{2} \sqrt{\frac{\pi}{\ln(2)}} \right)^{1-m} (m-1)\alpha_m z + F_{0\max}^{1-m} e^{-2(1-m)\frac{r^2}{\omega_0^2}} \right\}^{\frac{m}{1-m}}. \quad (2.20)$$

Such a thermal process heats up the material to the melting point and beyond, leading to thermal evaporation, which is described as thermal ablation. Based on classical nucleation theory, the thermal melting processes can be categorized in heterogeneous and homogeneous melting [15]. Usually melting starts at the surface, where the energy barrier for heterogeneous nucleation of a liquid layer at the solid-vapor interface is zero. In this case the melting front propagates into the material with a speed ultimately limited by the speed of sound. Typical times for melting by this mechanism are in the range of 100 ps. In contrast, homogeneous nucleation is considered as a mechanism for rapid thermal melting of solids irradiated with ultra-short laser pulses. For sufficient superheating of the solid phase the dynamics of melting is mainly determined by the electron-lattice equilibration rather than by nucleation kinetics. Therefore, complete melting of the excited material volume should occur within a few picoseconds. This time scale lies between the longer time scale for heterogeneous, surface-nucleated melting and the shorter time scale for a possible nonthermal melting mechanisms [15, 16].

The heat transfer in solid states has two parts; one comes from the electrons and another part comes from lattice vibrations (phonons) [17]. By corresponding the energy of electrons and ions (lattice) to a thermal energy, respectively, two temperatures  $T_e$  and  $T_l$  for electrons and for the crystal lattice can be imagined.

This gives a macroscopic time dependent model for the thermal ablation, the so called two-temperature model (TTM). For a description of laser-material interaction, particularly when using short laser pulses, the two-temperature-model works well. It is assumed that the temperatures of the electrons  $T_e$  and of the lattice  $T_l$  can be considered separately [15, 18, 19]:

$$c_e \frac{\partial T_e}{\partial t} = -\frac{\partial Q(z)}{\partial z} - \gamma(T_e - T_l) + P(t), \quad (2.21)$$

$$c_l \frac{\partial T_l}{\partial t} = \gamma(T_e - T_l), \quad (2.22)$$

with  $Q = -\kappa_e \partial Q / \partial z$  as heat flux. The  $\kappa_e$  depends on the thermal conductivity of electrons and  $P$  represents the transferred pulse-power. Two characteristic thermodynamic times can be defined:

$$\tau_e = \frac{c_e}{\gamma}, \quad \tau_l = \frac{c_l}{\gamma}, \quad (2.23)$$

where  $\tau_e$  is the cooling time of electrons (typically a few ps) and  $\tau_l$  is the heating time of the lattice (typically a few ns),  $\gamma$  is the electron-lattice coupling constant and  $c_e$  and  $c_l$  are the respective heat capacities.

For fs-lasers it can be assumed that the thermal conductivity of the electrons is negligible and there is no electron-lattice coupling. For this case a logarithmic relationship for the ablation temperature can be obtained [18].

This model becomes more realistic when thermal diffusion processes are included, resulting in a heat affected zone, which is defined as a zone around the crater, whose properties and structure have been altered by the laser processing [20]. The thermal diffusion length  $L_{th}$  induces a heat-affected zone which depends on the pulse duration of each individual pulse as follows [21]:

$$L_{th} \propto \sqrt{2\kappa\tau}, \quad (2.24)$$

$\kappa$  is the thermal conductivity and  $\tau$  the pulse duration. By use of pulsed lasers in material processing, results depend differently on the pulse lengths. The relation between the time constants in case of a nanosecond laser pulse is:  $\tau \gg \tau_l \gg \tau_e$ . Thus, during exposure to the laser pulse, both electron-electron interaction and electron-phonon interaction take place. The spreading of the heat during the laser pulse can make a change in the vicinity of the irradiation point which is defined by the thermal diffusion length. In particular, this region can be melted and subsequently resolidified through the heat or thermal shock waves. This prohibits a very precise structuring [12, 15, 19].

In contrast, by a ps laser pulse with  $\tau_l \gg \tau \gg \tau_e$ , which is a longer pulse length than the electron-electron interaction time, the thermal conduction by the electrons becomes dominant. Thus, the vicinity of the processed area has a clear limitation but is only moderately influenced by the laser [12, 15, 19].

For a fs laser pulse with  $\tau_l \gg \tau_e \gg \tau$ , the thermal conduction occurs only after the end of the laser pulse and absorption process. The characteristic time for the electron-lattice interaction lies in the ps-range [12, 15, 19], which is much longer than the transfer of energy by the laser pulse. In this case, the heat affected zone is negligibly small and the so called cold ablation is possible. The ablation is induced through other processes which are discussed in the following.

The threshold for ablation depends on the fluence of the laser pulse, therefore it is called threshold fluence. There are single and multi-pulse thresholds for ablation. Generally, a first

laser pulse reduces the threshold for the next incident pulse. It means that the ablation threshold with several pulses is lower than a single pulse threshold. This can be explained by material fatigue, which has a huge influence on processing with high repetition rates and low scan speeds (Section 2.1.5).

Considerations on the temperature in thin films under the influence of several fs pulses with high pulse repetition rate can be found in [20]. It was shown there that the ablation threshold decreases with increasing pulse repetition frequency, but becomes saturated at very high levels.

### Multiphoton- and Avalanche Ionization

At zero temperature ( $T = 0\text{ K}$ ) all electrons of a solid crystal are in their lowest energy level within the valance band ( $V_B$ ). The conduction band is empty and the band gap is without any occupied defect states. The electrons from the valance band can be excited through electromagnetic waves (laser beam) or thermally or even through interaction with other electrons if the energy is enough to overcome the band gap energy in an interband transition. For an interband transition a single photon with energies in the visible (VIS) or ultraviolet (UV) range can be sufficient. This single photon can be replaced by 2 or 3 photons which together have the same energy as the required single photon to overcome the band gap. This process is called multiphoton absorption [5].

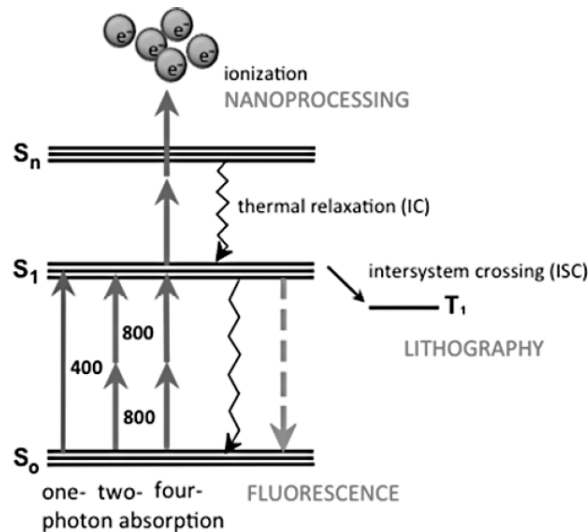


**Figure 2.2:** Schematic energy levels and excitation in a two-photon process, e.g. between  $S_0$  and  $S_1$  states [1].

In laser processing with large peak intensities, such as in case of fs-lasers, multiphoton absorption can be observed. Instead of a single photon with shorter wavelength, two or more photons, each with a longer wavelength corresponding to a smaller energy than the bandgap

$h\nu = E < E_g$ , are absorbed simultaneously ( $h$  is Planck's constant and  $\nu$  is the frequency). For the simultaneous absorption of two photons the following equation must be valid:

$$E_g < \Delta E = E_1 + E_2, \quad (2.25)$$

where  $E_1$  and  $E_2$  are the energies of the two photons and their sum is larger than the band gap. If this process leads to ionization, it is called multiphoton ionization (MPI). Multiphoton absorption is a nonlinear optical process. Decisive for the linear absorption is the fluence, for nonlinear processes, however, it is the intensity (power per unit area) [12]. It results in multiphoton absorption analog to Eq. 2.12 for the  $m$ -photon absorption with the absorption coefficient  $\alpha_m$ , e.g.  $\alpha_2$  for two-photon absorption.

The electrons within the conduction band can absorb even smaller energies and accumulate them. Through interaction with lattice vibrations (phonons) this energy can excite new electrons from the valance band to overcome the band gap. The density of electrons in the conducting band can be increased continuously. If this ratio exceeds the ratio of electron recombination and diffusion, an avalanche process regarding increasing electron density becomes possible. This avalanche ionization can finally lead to an electrical breakdown of the binding states and destroy the lattice and crystal structure, thus causing material removal [22, 23, 24].

In dielectrics there is an average electron density of about  $10^8 / \text{cm}^3$  in the conduction band [25]. Due to an atom density of  $10^{23} / \text{cm}^3$ , the probability for an avalanche ionization without multiphoton excitation is negligibly low, e.g. for a laser spot volume with a cross-sectional area of  $100 \mu\text{m}^2$  and a thickness of a few hundred nanometers, where only a few electrons are present. Only by multiphoton absorption the density of electrons in the conduction band can be increased to reach the threshold density for an electron avalanche. The first group of electrons excited in a multiphoton process are the so called *seed* electrons for the avalanche ionization.

These generated electrons are responsible for the removal of material and their generation process depends on the intensity as well as on the pulse duration. For pulse duration beyond the sub-10 ps range the electrons are generated thermally and below that they are mainly generated by multiphoton absorption.

The time-dependent behavior of electrons in the conduction band can be described by the Fokker-Planck equation, which describes the time evolution of the probability density function of the velocity of a particle in statistical mechanics under the influence of drag and random forces like drift and diffusion [26, 27]:

$$\frac{\partial f(\mathbf{u}, t)}{\partial t} + \frac{\partial J(\mathbf{u}, t)}{\partial \mathbf{u}} = S(\mathbf{u}, t), \quad (2.26)$$

where  $f$  is the density function of electrons in the conduction band,  $\mathbf{u}$  is the energy level of electron states and  $J$  is the energy flow, containing the charge losses through recombination

processes into the valance band and diffusion as well as thermal diffusion and thermal conductivity.  $S$  is the generation function of electrons in the conduction band by multiphoton (MPI) or avalanche ionization (AI).

By integrating the Eq. 2.26 over all energy levels in the conduction band ( $u$ ) the rate equation for the electrons in the conduction band is achieved as follows [25, 28]:

$$\frac{dn(t)}{dt} + J(t) = \left( \frac{dn(t)}{dt} \right)_{\text{MPI}} + \left( \frac{dn(t)}{dt} \right)_{\text{AI}} = S(u, t), \quad (2.27)$$

with an electron density of:

$$n(t) = \int_0^\infty f(u, t) du. \quad (2.28)$$

The generation of conducting electrons by multiphoton absorption ( $m$ -th order) is possible if the excitation overcomes the band gap:  $nE_{\text{ph}} > E_g$ . Combined with Eq. 2.2 the generation rate by multiphoton absorption is as follows:

$$\left( \frac{n(t)}{dt} \right)_{\text{MPI}} = \frac{\alpha_m}{mE_{\text{ph}}} I(t)^m, \quad (2.29)$$

where  $\alpha_m$  is the  $m$ -photon absorption coefficient and  $E_{\text{ph}}$  is the energy of photons. For the avalanche ionization an exponential increase of the electron density in the conduction band is assumed, which is in agreement with numerical computations [27]. It is also assumed that the whole laser energy is applied for electron generation. It requires immediate ionization without any time delays. This results in an avalanche ionization ratio proportional to the intensity with the avalanche coefficient ( $a$ ) as a characteristic material parameter [29]. This gives the ratio for the electron generation in the conduction band through avalanche effect as follows:

$$\left( \frac{n(t)}{dt} \right)_{\text{AI}} = aI(t)n(t). \quad (2.30)$$

## Coulomb-Explosion

The simple definition of Coulomb explosion is an energy coupling from electronic excitation into the atomic binding force, breaking the bindings. The electronic excitation is caused by an intense electromagnetic field like ultra-short laser pulses. It is based on a huge repulsive Coulomb force between particles with the same electric charge, e.g. cations which can break the bonds that hold the solid together resulting in a plasma of ionized atoms.

The ablation threshold fluences for this phenomenon are in the range of 10 TW to 400 TW and can be achieved by picosecond or femtosecond lasers. This kind of ablation is a "cold" alternative ablation compared to thermal ablation.

This effect has been proven by investigating solids at near ablation threshold fluences. The solid emits high energy ions which cannot be produced by thermal dissociation of the molecules [30]. This was observed by irradiating dielectrics with ultra-short NIR-laser pulses in two different ablated phases [29]. One phase contains very high energetic ions at low concentrations generated from a flat laser ablation crater whereas the other phase contains very high concentration of lower energetic ions [31]. The first phase is achieved at low repetition rates and at low fluences whereas the second phase is achieved when higher repetition rates and fluences occur. Laser pulses in the lower picosecond range which generate thermal ablation do also generate the second phase. Long pulses maintain the charge diffusion in the solid state which prevent a Coulomb explosion.

### 2.1.4 Laser Induced Ablation Threshold

The laser induced ablation threshold is the threshold fluence ( $F_{th}$  [ $J/cm^2$ ]) or a minimum amount of energy at which a material removal in solids is generated. This fluence depends on the physical ablation process which in turn depends on the laser parameters such as wavelength, intensity, and pulse length. Thus, the threshold fluence varies even for the same material when changing these parameters.

The simplest way to calculate it is the imaginary removal of a first atomic mono-layer. The ablation threshold for metals with ultra-short laser pulses can be defined as a condition for electrons in a mono-atomic surface layer with a minimum energy equal to the sum of the atomic binding energy and the work function of electrons. Hence, the threshold fluence is proportional to the laser wavelength. For dielectrics it is analogous to metals with an additional part necessary for the excitation of electrons over the band gap. In this case, the density of free electrons depends on the laser intensity and pulse length [14].

E.g. in a thermal ablation through a linear absorption up to the melting temperature ( $T_M$ ), this threshold fluence can be calculated from Eq. 2.19 and 2.20 on the surface:

$$F_{th} = \frac{\rho c_p}{\alpha_1} \Delta T_M. \quad (2.31)$$

It is characteristic for each material. However, multiphoton absorption is intensity dependent and therefore  $F_{th}$  additionally depends on the pulse length  $\tau$ . In this case the melting fluence for a m-photon absorption is given as follows:

$$F_{th} = \sqrt[m]{\frac{\rho c_p \Delta T_M}{\alpha_m} \left( \frac{\tau}{2} \sqrt{\frac{\pi}{\ln 2}} \right)^{m-1}}. \quad (2.32)$$

In case of silicate glass it is observed that for ultra-short pulses at the lower fs range the MPI process dominates to reach the ablation threshold over the melting process. So the calculated values agree with the measured values [12]. Over 50 fs, additional processes like

avalanche ionization get involved leading to deviations in the measured values with respect to the calculated values from Eq. 2.32.

The processes are based on electronic dynamics in solids. The threshold fluence is determined by the intensity which yields a critical electron density during the laser pulse. A method to describe the ablation thresholds in dielectrics is developed with the help of the critical plasma electron density. Since the plasma frequency of the generated charges in solids equals the laser frequency, the transparent solid changes to a highly absorbing medium. For a mode locked Ti:sapphire laser with a central wavelength at 800 nm this critical density would be fulfilled at  $10^{21} / \text{cm}^3$  [23, 32].

Starting from a Gaussian laser pulse with a pulse length of  $\tau$ , this critical density of electrons can be calculated from Eq. 2.30 for an avalanche ionization process. The threshold is supposed to be pulse length independent if it is just triggered from avalanche processes.

The electron density  $n$  for an  $m$ -photon absorption process leading to a multiphoton ionization can be calculated from Eq. 2.29 as follows:

$$n = \frac{2^m}{\sqrt{4m}} \left( \frac{\ln 2}{\pi} \right)^{\frac{m-1}{2}} \frac{\alpha_m F_0^m}{m E_{ph} \tau^{m-1}}. \quad (2.33)$$

It can be seen that a pulse length dependency exists in this case. For a critical electron density of  $n_{cr} = 10^{21} / \text{cm}^3$  the ablation threshold can be calculated from:

$$F_{th} = \frac{1}{2} \sqrt[m]{\sqrt{4m} \left( \frac{\pi}{\ln 2} \right)^{\frac{m-1}{2}} \frac{m E_{ph} n_{cr} \tau^{m-1}}{\alpha_m}}. \quad (2.34)$$

It shows that the shorter pulse lengths support lower ablation threshold fluences. For higher pulse lengths the electron density generated from MPI will be smaller. Even if this density from MPI is not enough to reach the critical value ( $n_{cr}$ ), the generated electrons in the conduction band can serve as seed electrons to start an avalanche process and trigger a dielectric breakdown. It means that for higher pulse lengths the avalanche ionization is more depending on the existing electrons in the conduction band which can be distributed inhomogeneously within the crystal and bring fluctuations in ablation threshold fluences at different positions in the material [12].

Summarizing many experimental and theoretical studies shows that for ultra-short pulses the ablation threshold is independent of pulse duration. For pulses longer than several tens of picoseconds, which are long enough to ensure a heat- and charge-carrier-diffusion, the loss for generated electrons has to be taken into account and will change the values. The following dependencies are observed in previous studies [33]:

$$F_{th} \sim \sqrt{\tau} \quad \text{for} \quad 10 \text{ ps} \leq \tau \leq 10 \text{ } \mu\text{s} \quad (2.35)$$



and

$$F_{\text{th}} \sim \tau \quad \text{for } \tau \geq 10 \mu\text{s}. \quad (2.36)$$

Further points to be mentioned concerning the differences in ablation mechanisms for the long pulse regime and short pulse mode are firstly the effect of intensity on the absorption properties of materials with band gap. As the long pulse lasers with intensities in range of  $10^8 \text{ W/cm}^2$  to  $10^9 \text{ W/cm}^2$  induce just a negligible ionization in dielectrics up to UV-range, the femtosecond laser pulses with intensities in range of  $10^{12} \text{ W/cm}^2$  to  $10^{13} \text{ W/cm}^2$  can fully ionize the dielectrics because of a different energy absorption mechanism. Secondly, the electron to lattice energy exchange time by a long pulse ablation mode is several order of magnitude shorter than the pulse length. As a result, electrons and ions get into a thermal energy equilibrium and the ablation has a thermal evaporation character.

### 2.1.5 Ablation and Modification through Laser Pulse Train

Section 2.1.3 is based on constant material properties over time during the interaction with a single laser pulse. However, in case of high repetition rated lasers with very small time intervals between incident pulses, the properties of the illuminated spot are as defined just for the first pulse and each following pulse interacts with a changed medium. This is often observed as a reduction of the threshold fluences as compared to single pulse ablation. This phenomenon is called *incubation* and can be explained by different processes like thermal stress, laser induced defects, and heat accumulation, which are all discussed in the following. In transparent media, such effects can change the band structure in form of band gap narrowing or by the generation of band gap states and make interband excitation easier [34, 35].

The dependency of the ablation threshold fluence on the pulse number can be described by a simple potential law:

$$F_{\text{th}}(N) = F_{\text{th}}(1) \cdot N^{\xi-1}, \quad (2.37)$$

with  $F_{\text{th}}(1)$  as single pulse ablation threshold fluence and  $\xi$  the incubation coefficient. For  $\xi = 1$ , the ablation threshold is not depending on the pulse number. For  $\xi < 1$ , the incubation (pulse number) dependency is present and the smaller this value the more impact does the pulse number have. For  $\xi > 1$ , a conditioning effect in the material even increases the threshold fluence by crystallographical or morphologic recoveries.

Also for ultra-short pulsed lasers this model can explain the behavior of incubation in semiconductors and other materials [36, 37, 38].

## Mechanical Ablation

There is an analogy between Eq. 2.37 and the fatigue tests in metals by repeated loading (strain) tests. This pulse number dependency of the laser induced damage threshold can be correlated to an accumulative thermally induced mechanical strain caused by the thermal expansion in the irradiated volume or photomechanical fragmentation, which disintegrates the target into clusters as a result of the mechanical stress imposed by the very rapid thermal expansion of the surface [39, 40].

## Laser Induced Defects

Defects in materials reduce the ablation threshold because of the excess charges from resulting band gap states. These states support the interband excitation of valance electrons even with lower energies than  $E_g$ . That is the reason for utilizing pure and low defect materials for high power optics. Such points are the seed for the ignition of the ablation processes for surrounding regions in the material. But the size and density of these defects decide about their effects [41]. Even particles on the surface can have the same effect because of the electrical field enhancement [42].

High energy ionizing radiation produces structural changes and generates defect states in transparent dielectrics. The most prominent point defects are vacancies and interstitials with formation energies of a few eV. Other defects like Frenkel pairs need energies above 10 eV [43]. These enable additional transitions over the band gap (F-centers). This effect is also observed in glass using fs-laser pulses in a multiphoton absorption process [44]. It can be generated with fs-lasers within the first radiation phase and stays mostly constant. It changes the optical properties of the medium and increases the absorption (reduces the transmission) of light at characteristic wavelengths [45]. This absorption changes can even be generated at fluences below the threshold limit and make permanent changes in the crystal. It was observed in different glasses by using a 60 fs laser that the generation of such defects at fluences below the single pulse threshold grow proportional to  $I^m$ , where  $m$  is the expected order of multiphoton absorption processes [46].

The density of such defects in a material has a crucial impact on the ablation process. Beyond a critical volume density the electrical tension will be so large that the solid gets destroyed. The threshold fluence for this kind of ablation can be calculated in form of a threshold pulse number which generates the threshold density [12]:

$$N_{th} = \frac{C_1}{F_0^m} e^{-C_2 F_0^m}, \quad (2.38)$$

where  $C_1$  and  $C_2$  are material parameters which characterize the thermomechanical and electrical stress and the F-center generation rate in each material.  $F_0$  is the initial laser fluence in  $m$ -photon absorption.

## Heat Accumulation

Heat accumulation refers to a phenomenon which occurs especially in poor thermal conductors such as glass during laser machining with high pulse repetition rates of ultra short pulses. The material passes through non-cyclic warm-up phases by the action of the laser pulse and cooling phases between pulses, but reaches an elevated temperature and cannot return to its original temperature between these pulses.

At MHz repetition rate, up to several thousand pulses hit the same spot on the target surface. The coupling between consecutive pulses occurs in three stages. First, the temperature accumulation takes place, until the thermal evaporation threshold is achieved. Second, after ablation occurs, the density of vapors begins to build-up near the ablating surface. Finally, due to both thermal effect and density increase the vapor becomes ionized and laser-matter interaction changes to laser-plasma interaction. The temperature rises slightly above the material binding energy, resulting in an efficient material removal by non-thermal and thermal mechanisms [14].

The first model for this ablation mechanism was given by Kim *et al.* [47]:

$$\Delta T = \frac{F_{\text{abs}}\omega_0^2 R}{2c_p \rho d K} \ln\left(\frac{4NK}{R\omega_0^2}\right), \quad (2.39)$$

where  $d$  is the thickness of the sample,  $F_{\text{abs}}$  is the absorbed fluence as a part of  $F_0$ ,  $\omega_0$  is the beam radius of the sample, and  $N$  is the laser pulse number of the incident beam with the repetition rate of  $R$ . The rest are characteristic parameters of the target material; thermal capacity ( $c_p$ ), density ( $\rho$ ), and thermal diffusivity ( $K$ ).

What remains of generated heat from each pulse in the spot volume adds to the heat of the next incoming pulses till a melting or sublimation point is reached. Beyond a critical temperature  $T_c$ , the material will be destroyed. This model is developed for dental material and is not valid for other materials such as glasses. It means that the model should be modified for new materials and especially for thin films.

At constant parameters like pulse number ( $N$ ) and repetition rate ( $R$ ) the threshold fluence can be calculated as follows:

$$F_{\text{th}} = \frac{4c_p \rho d K T_c}{a R \omega_0^2 \ln\left(\frac{8NK}{R\omega_0^2}\right)}. \quad (2.40)$$

Close to and below the ablation threshold, it is possible to make morphological and crystallographic changes in the material which have an effect on properties such as refractive index, E-modulus and chemical etch rates in etching media.

In case of line scanning, one of the main parameters for heat accumulation is the pulse number  $N_{\text{eff}}$  which interacts at a point (spot volume) and is given by Dalili *et al.* [20] as follows:

$$N_{\text{eff}} = \sqrt{\frac{\pi}{2}} \cdot \frac{d \cdot R}{v}, \quad (2.41)$$

where the beam diameter  $d$ , the pulse repetition rate  $R$  and the scanning speed  $v$  are applied. Based on the thermal diffusivity ( $K = \lambda/(c_p \cdot \rho)$ ) and using the thermal conductivity ( $\lambda$ ), its heat capacity ( $c_p$ ) and its density ( $\rho$ ), the cooling time of the spot down to room temperature can be calculated. The so called effective cooling time  $t_{\text{eff}}$  [48] is given by:

$$t_{\text{eff}} = \frac{d^2}{\lambda/(c_p \cdot \rho)}. \quad (2.42)$$

A mean temperature  $T_a$  is determined as a function of the maximum surface temperature  $T_M$  during the laser influence [20]:

$$T_a \cong 2T_M \left( \frac{\tau}{\tau_{\text{pf}}} \right)^{1/2}, \quad (2.43)$$

where  $T_M$  is the maximum surface temperature during laser processing,  $\tau$  is the pulse duration and  $\tau_{\text{pf}}$  is the time between two pulses (reciprocal of the pulse repetition frequency).

## A Case Study

The laser used in this work has a repetition rate of 85 MHz. This corresponds to a time between two incident pulses of just about 10 ns. With a scan speed of 1000  $\mu\text{m/s}$  the laser spot with a diameter of 375 nm (cf. 2.1.6) moves only 10 pm between two pulses. With this high repetition rate the overlap between incident pulses is huge. The overlap ratio can be calculated as follows:

$$\text{Overlapping [\%]} = 100 \left( 1 - \frac{v}{R \cdot D} \right), \quad (2.44)$$

where  $v$  is the scan speed,  $R$  the repetition rate and  $D$  the spot diameter. It gives a 99.99968 % overlap for a scan speed of 100  $\mu\text{m/s}$  compared to 99.99698 % for 1000  $\mu\text{m/s}$ . When scanning continuously, a "pixel" is defined as a region along the scan line with dimension of the spot-diameter. A new pixel-fluence ( $F_{\text{Pixel}}$ ) can be calculated for each pixel regarding the scan speed. Different values are calculated for different speeds as depicted in Tab. 2.1.

ITO films are structured in three different ways which are discussed in Section 4.1. For different ITO films it was observed that the intensity has significantly more impact on the

**Table 2.1:** Fluence per Pixel versus scan speed for an average power of 15 mW;  $v$  presents the scan speed and  $N_{\text{eff}}$  the pulse number.

$v$ [ $\mu\text{m/s}$ ]	$N_{\text{eff}}$ a.u.	$F_{\text{Pulse}}$ [ $\text{J/cm}^2$ ]	$F_{\text{Pixel}}$ [ $\text{J/cm}^2$ ]
100	399494	0.16	63831
200	199747	0.16	31915
300	133166	0.16	21277
400	99873	0.16	15958
500	79899	0.16	12766
600	66582	0.16	10638
700	57071	0.16	9119
800	49937	0.16	7979
900	44388	0.16	7092
1000	39949	0.16	6383

nature and dimension of the structures than the velocity which correlates with the pixel-fluence. Hereby, it should be mentioned that higher power or intensity is a higher pulse energy and causes different physical processes, whereas a lower scan speed brings a higher pixel-fluence. These two quantities induce different processes and consequently lead to different results [49, 50].

Using the material parameters of ITO with a heat capacity of 382 J/kgK an effective cooling time of 0.725  $\mu\text{s}$  can be calculated from Eq. 2.42. In comparison to the intervals between the pulses (0.012  $\mu\text{s}$ ) this is an extremely long time span, leading to heat accumulation in the film. However, a linear dependence between the width of the modified regions and  $1/\sqrt{v}$  was not observed. Based on the discussion in [48] this can not be regarded as a heat diffusion controlled process.

### 2.1.6 Laser Beam Focusing and Scanning

The optical setup for focusing needs to be adapted to the laser beam properties depending on the application. A broad industrial portfolio of optical systems is available for welding, cutting, drilling or ablation, with focal lengths ranging from half a centimeter up to 70 cm, depending on the beam quality of the laser unit. Focus diameters down to 10  $\mu\text{m}$  and even below can be achieved by modern modular systems which are based on the mirror-principle, the lens-principle or a combination of both in a hybrid system. Hereby, processing speeds close to 100 m/s and positioning times of a few ms are possible.

For lenses, the working distance is generally smaller, the bigger is the enlargement. However, some special lenses provide a working distance of above 10 mm at 50x magnification and with a numerical aperture of 0.4 – 0.5.

Focusing the laser beam down to the sub-wavelength range is difficult because of the Abbe's diffraction limit. In 1873 Ernst Abbe found that light with wavelength  $\lambda$ , propagating in a medium with refractive index  $n$  and converging to a spot with angle  $\theta$  will make a spot with a diameter  $d$  [51]:

$$d = \frac{\lambda}{2n \sin \theta}, \quad (2.45)$$

$n \sin \theta$  is called the numerical aperture (NA) and can reach about 1.4 to 1.6 in modern optics. Some objectives with oil-immersion or water-immersion lenses can have a magnification of larger than 100 with numerical apertures larger than 1. The immersion oil or water must fill the gap between the front element and the object as an refractive index-matching material. When two substances with the same index are next to each other, light passes from one to the other without reflection nor refraction. These lenses give higher resolution at high magnification. Numerical apertures as high as 1.6 can be achieved with oil immersion objectives. This makes laser spots with sub-wavelength dimensions possible.

New applications in biology, medicine and nanotechnology have appeared by coupling the laser beam into a microscope. A combination of immersion oil objectives with high NA and mirrors on programmable galvo scanners can be used as an alternative in research for industrial modular systems (c.f. Section 3.1).

### 2.1.7 Laser Induced Periodic Self-Organized Structures

Under certain conditions so called "laser induced periodic surface structures" (LIPSS) or *ripples* can be observed on various materials like dielectrics, semiconductors or metals [52, 53, 54]. So called nanogratings, in contrast, have only been observed in the volume of transparent bulk materials like fused silica, tellurium dioxide, single crystal sapphire or borosilicate glasses [55].

The first ripples were observed on silicon and germanium with a millisecond-pulsed ruby laser [6]. Many experiments demonstrated that intense laser light can stimulate physical processes which result in surface structures at a periodicity close to the laser wavelength, also called low-spatial frequency LIPSS (LSFL). Besides LSFL, surface ripples of subwavelength periodicity (high-spatial frequency LIPSS (HSFL)) were observed when exposing dielectrics to ultra-short-pulsed laser light [56, 57, 58, 59, 60, 61]. Thereby, different periodicities were observed from a few hundred down to a few ten nanometers [62]. LSFL are mostly in parallel arrangements and appear especially at sub-threshold fluences close to the total ablation fluence. The ripples appear on the target surface parallel or perpendicular to the projection of the electric field vector of laser radiation. These phenomena are different for metals, semiconductors and dielectrics [63].

Similar effects occur by irradiating glasses with ultra-short laser pulses in form of birefringent domains [52, 64]. This birefringence is caused by periodic nanogratings, which are oriented perpendicular to the laser polarization. All reports so far demonstrated that

nanogratings in fused silica consist of small cavities with a size of several ten nanometers surrounded by a nanoporous structure [55]. They form a grating structure with a period around  $\frac{\lambda}{2n}$ , with  $n$  being the refractive index of the material and  $\lambda$  the wavelength of the incident laser pulses [55, 65].

A variety of theories for explaining the physical origin of LIPSS formation has been proposed, but no complete understanding has been reached yet. One concept is based on an interference of the electrical field of the laser beam with induced surface waves, which can describe the periodicity of ripples in the range of the lasers wavelength [66]. The results in this case are defined by the wavelength of the laser beam and the refractive index of the material.

Another theory is based on the assumption of some fabrication induced stress in the material which can be relaxed through laser radiation. It can also exhibit a preferred direction in the material but has a periodicity which is independent from the laser wavelength. This is particularly observed in glasses and polymers [67, 68].

The most convincing concepts are based on the assumption of interference effects between two different waves which set up a periodically varying pattern of dissipation, resulting in ablation. Proposals for the origin of the two interfering waves are:

- the incident laser light and a scattered surface wave
- the incident beam and a second harmonic surface wave
- second harmonic light and a scattered second harmonic surface wave

Alternatively, the interference patterns may also be generated by oppositely traveling plasma waves in a laser induced surface plasma, which are excited simultaneously by laser light striking from opposite directions [62].

In all cases, there is a conditioning effect after the first laser pulse, because the first structures have an impact on the next generating structures and can amplify the process in a certain direction [69, 70]. This is a point which can be exploited to make useful applications from originally undesired structures, generated mainly on the edge of ablation trenches [70, 71, 72].

### 2.1.8 Laser Structuring of Thin Films

There are many studies about ultrafast laser material micromachining [20, 73, 74]. In the fields of micro-/nanotechnology and device fabrication, thin films are of high interest to be structured by lasermachining for various applications. Solid state thin films can be categorized into metals, dielectrics and semiconductors and laser machining is being applied to all three groups.

Thin film micromachining has been utilized for preparing e.g. semiconductor masks and devices, solar cells and also for the fabrication of MEMS devices. There are many studies on

laser structuring of relevant metal layers like Ni, Cr, Au, Cu, Ag and even steel [75, 76, 77, 78, 79, 80, 81]. Semiconductor thin films are also studied extensively [57, 82, 83, 84, 85, 86, 87]. The last group belongs to dielectrics and transparent materials which have their major application field in optics [22, 23, 24, 56, 88, 89, 90, 91, 92].

From the last Section it can be seen that the amount of energy per volume of each material plays a crucial role for the ablation process. This volume depends in turn on the penetration depth of the laser radiation into the bulk material. In case of transparent or semitransparent materials and in case of MPA this depth can be beneath the surface of the bulk volume and the absorption is confined to a focus volume with a very high intensity. This volume is also known as *voxel* coming from "volume pixel" (see Fig. 2.3). In this volume the intensity is above the threshold for multiphoton excitation and it can be used for polymerization processes in polymers and therefore is regarded as a pixel for 3D multiphoton polymerization.

In case of thin films the interaction volume or depth is defined through the thickness of the material itself, being typically in the range of a few hundred nanometers, whereas the focus volume for nonlinear effects at certain intensities is close to the  $\mu\text{m}$  range in axial length. It means that the whole film thickness would be in the voxel volume for multiphoton absorption as well as in the beam focus volume for single photon absorption (Fig. 2.3).

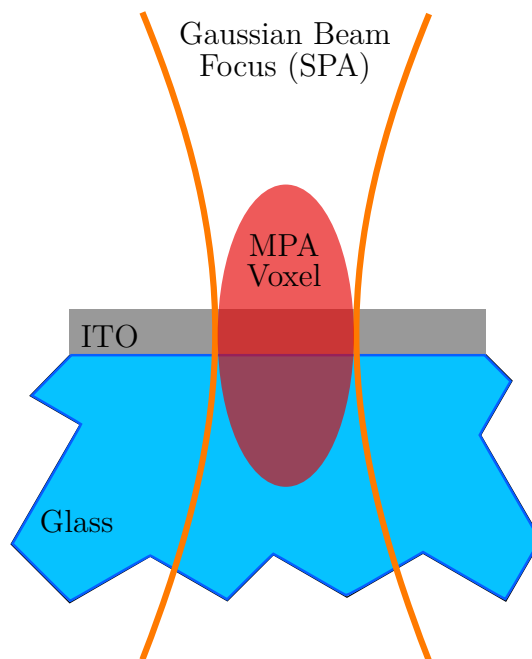


**Figure 2.3:** Schematic shape of a focused laser beam profile for thin film ITO processing. A Gaussian focused beam for SPA and a voxel of high intensity for MPA are shown.

This scale relation can be experimentally examined in this work by moving the objective toward the ITO layer precisely in vertical direction. Thereby a fluorescent light from ITO can be observed at intensities below the ablation threshold limit. This intensity is much stronger as compared to the same from glass and can be seen over a range of  $1\ \mu\text{m}$  to  $2\ \mu\text{m}$  of vertical objective displacement. The intensity starts in a weak amplitude, reaches a maximum and again gets weaker and finally disappears. This behavior shows a multiphoton excitation



in ITO, occurring besides single absorption by free electrons. However, how the ablation or modification processes in ITO correlate with this effect is still not understood. The underlying substrate plays an important role for the thermal and electrical diffusion from the thin film outward and affects the ablation or modification results.

## 2.2 Material Properties

In this Section the applied materials are being introduced. Indium tin oxide (ITO) as the main target of laser processing is explained in detail. Other materials, like aluminum nitride (AlN), gold (Au), platinum (Pt), and glass substrates are presented briefly and from the point of view which is interesting and useful for the application.

### 2.2.1 Indium Tin Oxide (ITO)

ITO is an n-type semiconductor metal oxide (MOX). It is based on indiumoxide  $\text{In}_2\text{O}_3$  doped with 5 – 10 %  $\text{SnO}_2$ . The crystal structure is like indiumoxide a cubic bixbyite [93].  $\text{Sn}_4^+$  ions are usually located at substitutional lattice sites built on  $\text{In}_3^+$  positions and due to their fourfold valence electrons release an excess conduction electron into the crystal. In case of a strong tin doping, ITO becomes a degenerate n-type semiconductor, i.e. the Fermi level lies practically in the conduction band. The charge carrier density of ITO is normally in the range of  $10^{20} / \text{cm}^3$  to  $10^{21} / \text{cm}^3$  [94, 95], the resistivity in the range of  $1 \times 10^{-4} \Omega \text{cm}$  [94]. Even the non-doped metal oxides usually possess semiconductor properties (e.g.  $\text{In}_2\text{O}_3$ ,  $\text{ZnO}$ ,  $\text{SnO}_2$ ). This is due to intrinsic defects like built-in oxygen vacancies, which act as donors as they give two electrons to the conduction band. In case of a high doping, oxygen vacancies in ITO practically play no role in the conductivity of the layers [96]. However, the ITO properties strongly depend on the parameters of the fabrication process, e.g. on the pressure and oxygen content in a reactive sputtering process. This can be attributed to tin-oxygen complexes [95] and interstitial oxygen atoms [96] in the layer. An increasing number of built-in oxygen ions leads to a growing number of scattering centers which impair the electrical conduction.

ITO as the most well known transparent conducting oxide (TCO) is being already used in the production of solar cells, semiconductor lasers, as well as displays and OLEDs. It is currently the most common oxide for transparent electrodes. Indium is a so-called post-transition metal and it is rather rare in the earth's crust; consequently the cost of ITO as a material has risen sharply in recent years as a consequence of the rapidly rising demand on the market.

### Fabrication of ITO Thin Films

In industrial production processes, sputtering is most commonly used deposition method for ITO thin films. Possible alternative manufacturing processes are thermal evaporation,

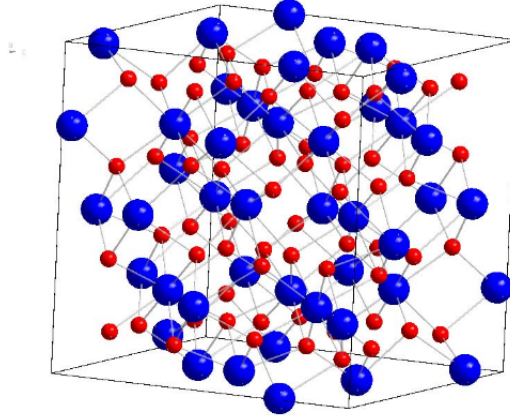


**Figure 2.4:** Crystal structure (primitive cell) of indium tin oxide (ITO) [97].

pulsed laser deposition and wet chemical processes like sol-gel [97]. The sputtering process can be done directly with ITO-targets or reactively with metallic In/Sn-targets. In both deposition processes an argon-oxygen plasma is normally used. With a ceramic ITO target a pure argon plasma can also be used. The properties of ITO thin films are strongly dependent on the sputter parameters, such as oxygen partial pressure and the temperature [98]. Higher temperatures result in a better crystallinity of the layer. However, this often leads to higher intrinsic stress which changes the band structure and the optoelectrical properties. That is why ITO layers are usually annealed after deposition. The annealing at 400 °C to 700 °C [95] can be done in air, in vacuum or in a reducing atmosphere and improves optical as well as electrical properties.

## Optoelectrical Properties of ITO

The direct band gap of ITO can be tuned in a wide range of 3.5 eV to 4.2 eV [93]. Thus, in the visible spectrum photons have insufficient energy for exciting electrons to overcome the band gap which makes ITO layers optically transparent. A secondary band gap exists above the conduction band, which is also responsible for the optical transparency of ITO [94, 99]. The large number of electrons in the conduction band can therefore also not be excited by optical photons.

ITO doping results in an increasing of the effective band gap due to the Burstein-Moss effect [100]. The effective band gap ( $E_F - E_V$ ) increases by shifting the Fermi level towards the conduction band [94]. This can be described by the following formula [101]:

$$\Delta_{\text{BM}} = \left( 1 + \frac{m_e^*}{m_p^*} \right) E_F, \quad (2.46)$$

where  $m_e^*$  is the effective mass of electrons and  $m_p^*$  is the effective mass of holes. This results in the following relationship between the broadening of the band gap and the carrier density  $n_e$  with the position of the Fermi level  $E_F = \frac{\hbar^2}{2m_e^*}(3\pi^2n_e)^{2/3}$  [102]:

$$\Delta_{\text{BM}} = \frac{\hbar^2}{2m_e^*}(3\pi^2n_e)^{2/3}, \quad (2.47)$$

where  $n_e$  is the carrier density and  $(m^*)^{-1} = (m_e^*)^{-1} + (m_p^*)^{-1}$ .

This effect is based on the location of the lower free states within the conduction band, which are occupied through heavy doping. The next free states are only available at higher energies, leading to a practical increase of the band gap. However, in case of ITO the Burstein-Moss effect is not fully present, because of a change in the band structure by the heavy doping, having a counteracting effect [93]. There are many-body effects, such as electron-electron scattering and electron-impurity scattering, which are referred to the band gap normalization  $\Delta_{\text{RN}}$  [102]. In summary, both effects are shown in Fig. 2.5.

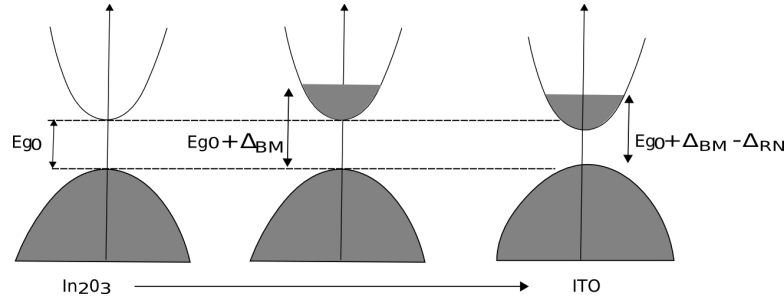


**Figure 2.5:** Change of band gap for tin doped  $\text{In}_2\text{O}_3$  caused by Burstein-Moss-shift  $\Delta_{\text{BM}}$  and by band-gap-normalization  $\Delta_{\text{RN}}$ , as discussed in [102, 103].

In addition to the grain size of ITO, also the band gap reduces with increasing deposition rate [104]. This is because the grain boundaries, which include space charge zones, represent potential barriers. They are poorly conductive and have a high proportion of tin and oxygen [105]. When the grain size decreases, the number of barriers increases, leading to a lower carrier concentration and, hence, to lower conductivity. Due to the Burstein-Moss shift, a lower carrier concentration leads to a smaller band gap.

Based on the metallic character of ITO with respect to the electrical conductivity, the Drude approach is applicable. This is allowed for TCOs by assuming that the charge carriers behave like quasifree electrons within the conduction band. The mass of electrons ( $m_e$ ) is replaced by an effective mass ( $m_e^*$ ) which is related to the crystal properties and the band structure. This effective mass is inversely proportional to band bending so that for flat band structures it is heavier and electrons are more localized with a lower mobility [17]. In ITO,  $m_e^*$  is 0.28-0.43 times of the electron rest mass  $m_e$  [106, 107, 108].

By simplification, the ITO crystal can be regarded as an ionic compound with free electrons behaving like an electron gas. These electrons are responsible for the conductivity in the material, which can be calculated by applying the kinetic gas theory. Inside of the gas there

is no electrical field. An external electrical field accelerates the electrons during their free flight phases between bouncing off heavier, relatively immobile positive ions. The equation of motion for such an electron is given by [17]:

$$\frac{d\vec{v}_d}{dt} + \frac{m_e}{\tau_s} \vec{v}_d = -e\vec{E}, \quad (2.48)$$

where ( $\vec{v}_d$ ) is the drift velocity and  $\tau_s$  is defined as the average scattering time between subsequent collisions of free electrons with ions, defects or impurity atoms.

Under stationary conditions the velocity of electrons is invariant and the acceleration vanishes ( $\frac{d\vec{v}_d}{dt} = 0$ ). In this case the mobility of electrons is defined as follows:

$$\mu = \frac{\vec{v}_d}{\vec{E}} = \frac{e\tau_s}{m_e}, \quad (2.49)$$

where  $m_e$  is the electron rest mass ( $9.109 \times 10^{-31}$  Kg) and  $e$  the electron electrical charge ( $1.602 \times 10^{-19}$  C). An electric field generates a current density ( $\vec{j}$ ), which is given with a charge carrier density of  $n$  as follows:

$$\vec{j} = ne\mu\vec{E}, \quad (2.50)$$

and the conductivity can be calculated from  $\sigma = \vec{j}/\vec{E}$ :

$$\sigma = \frac{n\tau e^2}{m_e} = \frac{1}{\rho}, \quad (2.51)$$

where  $\rho$  is the resistivity. By combining Eq. 2.49 and Eq. 2.51 the conductivity can be calculated from  $\mu$  and  $n$ :  $\sigma = en\mu$ . For thin film layers with a thickness  $t$  it is very common and convenient to use the sheet resistance  $R_{\square} = \frac{\rho}{t}$ , given in  $\Omega/\text{square}$ .

Interestingly, this approximation coincides very well with the Hall- and four-probe measurements. From measured values for  $\mu$  and  $n$  (Tab. 1 in Section 4.3.2) a resistivity of  $2.661 \times 10^{-4}$   $\Omega\text{cm}$  can be calculated for sputtered films and  $3.942 \times 10^{-4}$   $\Omega\text{cm}$  for annealed films which is in very good agreement with experimental values of  $2.66 \times 10^{-4}$   $\Omega\text{cm}$  and  $3.95 \times 10^{-4}$   $\Omega\text{cm}$ , respectively. This exact agreement is a mere coincidence, although it can partly be explained by a high density of quasifree electrons ( $10^{21}/\text{cm}^3 \lesssim$ ) at room temperature. This makes the scattering of electrons at grain boundaries irrelevant and the only resistance for charge carrier transportation comes from ionized defects in crystals [109].

Incident light on a surface boundary is partially reflected, transmitted and absorbed, so that the initial intensity of light splits up into a reflected intensity ( $I_R$ ), a transmitted intensity

( $I_T$ ) and an absorbed intensity ( $I_A$ ). Normalized for the initial intensity  $I_0$  the conservation of energy gives:

$$1 = R + T + A. \quad (2.52)$$

where  $R$ ,  $T$ ,  $A$  are the coefficients of reflection, transmission, and absorption.

This can be measured in a transmission/reflection measurement. The results for one charge of deposited ITO films are presented in Fig. 2.6.

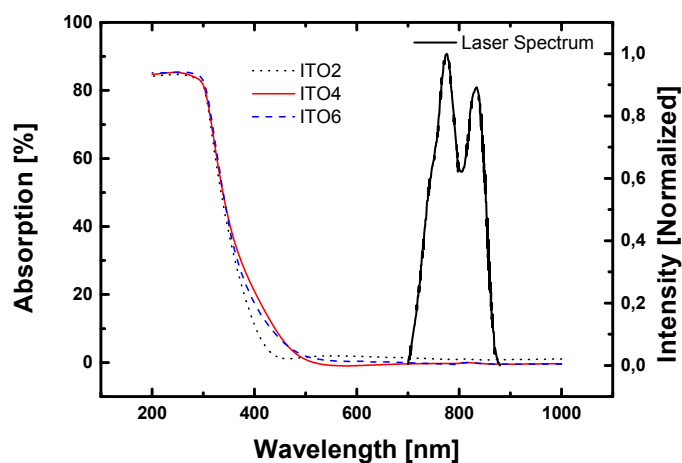


**Figure 2.6:** Calculated absorption curves from transmission-reflection measurement on sputtered ITO on glass substrate compared with the laser spectrum.

The interaction of electromagnetic waves with solids can be described by the dielectrical function ( $\epsilon$ ) of the material. It illustrates the relation between the electric field ( $\vec{E}$ ) and the electric displacement field ( $\vec{D}$ ):

$$\vec{D} = \epsilon_0 \vec{E} + \vec{P} = \epsilon_0 \epsilon \vec{E}, \quad (2.53)$$

where  $\epsilon_0$  is the vacuum permittivity and  $\vec{P}$  is the macroscopic density of the permanent and induced electric dipole moments in the material (polarization density). In conducting and semiconducting materials it can be explained by the Drude-Lorentz-modell [17]. In semiconductors, the electron mass should be replaced by the effective electron mass. Using an oscillating electric field in Eq. 2.48 yields:

$$m_e^* \frac{d^2 \vec{x}}{dt^2} + \frac{m_e^*}{\tau_s} \frac{d \vec{x}}{dt} = -e \vec{E}_0 e^{-i\omega t}, \quad (2.54)$$

with  $\omega = 2\pi f$  and  $f$  the frequency of the electromagnetic wave (light). Assuming a forced oscillating movement by the electrons with the same frequency the differential equation can be solved as follows:

$$\vec{x} = \frac{e\vec{E}(t)}{m_e^* \left( \omega^2 + i\frac{\omega}{\tau_s} \right)}. \quad (2.55)$$

The polarization in a free electron gas is defined as  $ne \cdot \vec{x}$  and gives the following dielectric function:

$$\epsilon(\omega) = \epsilon_{\text{opt}} - \frac{ne^2}{\epsilon_0 m_e^* \left( \omega^2 + i\frac{\omega}{\tau_s} \right)} = \epsilon_{\text{opt}} \left( 1 - \frac{\omega_p^2}{\left( \omega^2 + i\frac{\omega}{\tau_s} \right)} \right), \quad (2.56)$$

where  $\epsilon_{\text{opt}}$  is called high frequency permittivity and contains the background polarity of the undoped material and the plasma frequency  $\omega_p$ :

$$\omega_p = \sqrt{\frac{ne^2}{\epsilon_{\text{opt}} \epsilon_0 m_e^*}}. \quad (2.57)$$

This is the frequency of longitudinal oscillations of free electrons with respect to the fixed positive ions in a solid (plasmon). The plasma wavelength ( $\lambda_p = 2\pi c/\omega_p$ ) can be shifted due to the charge carrier density ( $\lambda_p \propto n^{-1/2}$ ). In ITO it can be varied within a wide range by changing the charge carrier density to tune the optical properties.

The optical properties are determined by the band edge and the plasma edge in the transmission/absorption curve. Energies higher than the band edge energy are being absorbed in the material and the energies below the plasma edge are not. In other words, the plasma edge gives the lowest absorbing energy which can interact with free electrons in the conduction band.

## Thermal Properties

The thermal properties of ITO depend strongly on the fabrication process. However, Ashida *et al.* found an interesting phenomenon in reactively sputtered polycrystalline ITO films applying the nanosecond thermoreflectance method. The thermal diffusivity of 200 nm thick films with widely varying electrical conductivities were investigated. The thermal diffusivity of the ITO films ranged from  $2.3 \times 10^{-6} \text{ m}^2/\text{s}$  to  $1.5 \times 10^{-6} \text{ m}^2/\text{s}$  which was associated with the electrical conductivity of the films [110, 111]. The contribution of free electrons to the thermal conductivity reached 40 % for highly degenerate ITO films with a constant contribution of phonons (see Fig. 2.7). The phonon contribution to the heat transfer in ITO films with various resistivities was found to be almost constant  $\lambda_{\text{ph}} = 3.95 \text{ W/mK}$ . The mean

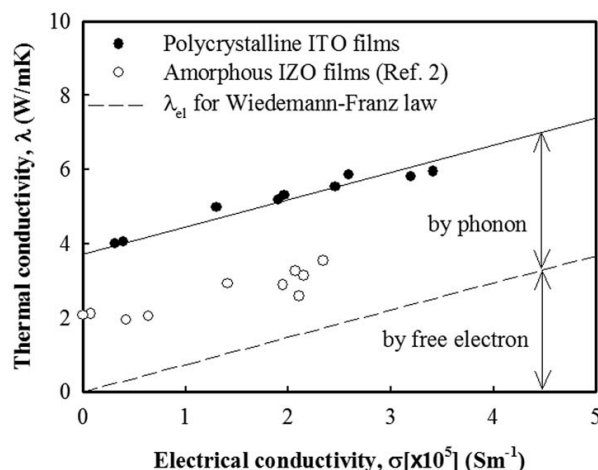


**Figure 2.7:** Thermal conductivity versus electrical conductivity for polycrystalline sputtered ITO films deposited at various  $\text{O}_2$  flow rates [111].

free path of phonons in the ITO films was estimated to be 0.99 nm, which coincides with the lattice constant of bixbyite  $\text{In}_2\text{O}_3$  [111].

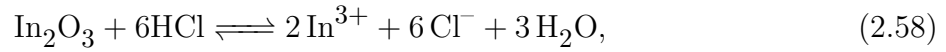
The thermal conductivity of ITO was taken from this study and used for simulations. Polycrystalline ITO has a heat capacity of  $2.58 \times 10^6 \text{ J/mK}$  and a thermal conductivity ranging from 4 W/mK to 5.95 W/mK [111]. The latter increases with increasing oxygen content in the sputtering chamber with ceramic targets [111]. The layers were sputtered with a partial oxygen content of 0 – 5 %.

The melting temperature of ITO is about 2000 °C [105]. The thermal expansion coefficient is  $7.2 \times 10^{-6} /\text{K}$  [112], which is the same as for glass. This means that virtually no thermal stress should be present for ITO layers on glass [113]. Investigations by Kaune *et al.* on sputtered ITO thin films on glass substrates showed a film stress in the range of 100 MPa [113]. This is mainly due to intrinsic stress caused by the layer growth. However, ITO films on polymer films are much more under thermal stress than those on glass [112].

## Chemical Structuring of ITO

ITO can be patterned by wet chemical etching, by dry etching or by laser-based techniques. Commonly used in the industry is etching in halogenic acids, particularly in hydrochloric acid (HCl). However, it can also be etched with high etch rate in HF, HI, and in aqua regia, a mixture of hydrochloric acid and nitric acid. The addition of catalysts, such as oxidizing agents, can accelerate the etching process [98, 114, 115, 116]. It is also the addition of catalysts such as oxidizing agents, accelerate the etching process [117]. The etching in non-halogenic acids is also possible, but with a lower etch rate.

The etching process of ITO in hydrochloric acid can be described by the reaction equation for  $\text{In}_2\text{O}_3$  [114]:



which gives water, chlorine ions, and indium ions. The etch rate depends crucially on the concentration of the etching solution, its temperature and on layer properties [116]. In particular, grain size, crystallinity, oxygen and tin content play an important role [118]. Thus, the etch rate is strongly dependent on the manufacturing process and on a possible annealing step, which reduces the etch rate substantially. Amorphous ITO can be etched with a high etch rate [98]. However, a direct relationship between the etch rate and electrical conductivity which, in turn, depends on grain size is not found [118].

## Mechanical Properties

Mechanical properties of ITO thin films, such as Young's modulus and Poisson's ratio, are process dependent just like other non-mechanical parameters. The literature values from Neerincx *et al.* for Young's modulus and Poisson's ratio of sputtered ITO layers are 116 GPa and 0.35, respectively [119].

Mechanical properties of thin films can be characterized by nanoindentation experiments. A brief introduction to this method is given in Section 3.2.5.

Parameters like grain size, film thickness and internal stress can have an influence on the nanoindentation results, causing statistical scatter. Because of these variations it is more convenient to get a statistical distribution of the measured elastic moduli. Additionally, the size of nanoindents may also have an impact on the dislocation assisted mechanical properties known as indentation size effect and possibly also on elastic properties, due to the material pile-up or sink-in during indentation [120]. Furthermore, to limit the influence of the substrate on the measured properties, nanoindents were performed with a constant maximum depth of 40 nm in 200 nm thick films with 27 indents at two different areas of the sample. The results are obtained from the data acquisition system (nanoDM) for each point with a resolution of 0.1 nm. A statistical distribution of data for elastic moduli for all 27 points is shown in Fig. 2.8.

A guideline for nanoindentation measurements on thin films is that the indentation depth should only be about 10% of the total film thickness to avoid an influence of the substrate. In the presented case this value was 20%, due to some technical problems with the calibration of the indentation tip. However, because of a relatively high hardness of the used *SCHOTT* thin glass substrates of about 700 GPa this increased depth is not expected to have a negative effect on the results.



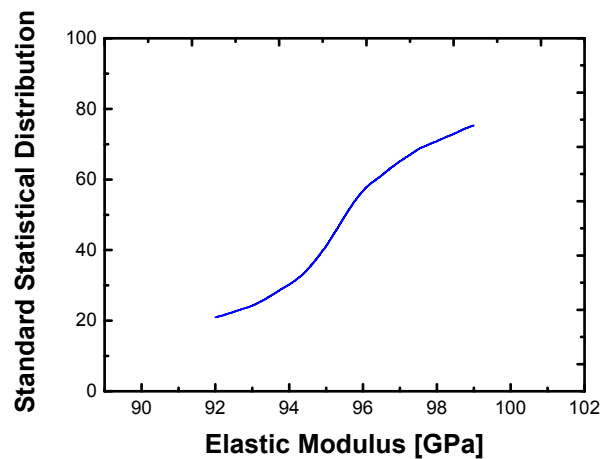


**Figure 2.8:** Standard statistical distribution of the measured elastic modulus from nanoindentation experiments on sputtered polycrystalline ITO thin films on glass substrates.

The measurements yielded an average value of 95 GPa for Young’s modulus. The average value for the hardness is about 10 GPa. The data scattering on Fig. 2.8 is not easy to interpret. Although it is a relatively high deviation, it is not abnormal. It shows among other things that the film quality of ITO varies on the sample. A more exact interpretation needs a systematic study which was not possible in this project.

## 2.2.2 Glass Substrate

In the applied structuring method in this work a high-numerical aperture (N.A.) oil immersion objective (EC Plan Neofluar 40x from *Zeiss*, N.A. 1.3) with a working distance of 210  $\mu\text{m}$  was used to focus the light tightly into the sample. To guarantee the pulse length and prohibit any contamination of the samples by immersion oil, the illumination of the ITO layers was done from the back through the glass substrates.

The choice of glass as a standard substrate for all applications is also supported by other properties, such as good electrical and thermal isolation, a high transparency in the optical range of the spectrum, chemical stability and bio-compatibility. The first point makes an isolation of electrical parts toward the substrate unnecessary and makes the processing easier. A refractive index of 1.51 matches very well with the optical setup including an intermediate immersion oil.

The applied substrates are AF 32<sup>®</sup> eco thin glass 4 inch wafers from *SCHOTT*. It is an alkali-free flat glass fabricated in a special down-draw technique with a thickness of 145  $\mu\text{m}$ . A fire-polishing of the surface results in a low RMS roughness value of below 1 nm. Furthermore, the coefficient of thermal expansion of AF 32<sup>®</sup> eco is the same as that of silicon by  $3.2 \times 10^{-6} / \text{K}$ . For this reason, it is perfectly suited for use as an optical packaging material in the semiconductor industry. Due to its high transformation temperature, it can be used in high-temperature applications of up to approximately 600  $^{\circ}\text{C}$  [121].

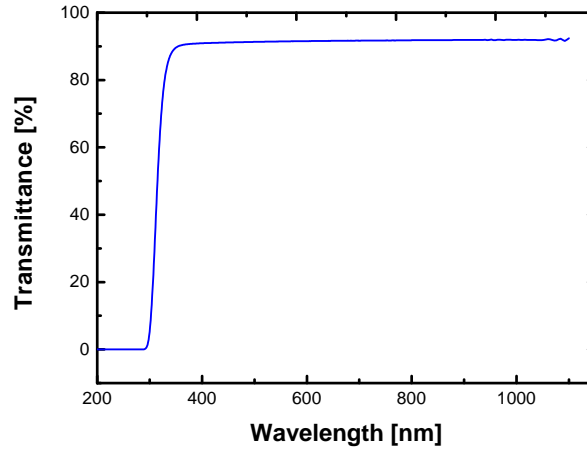


**Figure 2.9:** Transmittance of the used glass wafers.

The transmittance of such substrates was measured and is illustrated in Fig. 2.9 for different wavelengths.

### 2.2.3 Aluminum Nitride (AlN)

Aluminum nitride (AlN) is a solid with a crystal structure predominantly in wurtzite form with a melting point of  $T_m > 2400^\circ\text{C}$ . The atomic binding between Al and N is partly ionic and partly covalent in nature. The band gap of wurtzite polycrystalline AlN is about  $E_g = 6.2\text{ eV}$ . Impurities, such as e.g. oxygen atoms, can change the band gap and optoelectrical properties [122].

AlN became attractive in the middle of the 1980s for applications in microelectronics, optoelectronics and for optical coatings, due to its relatively high thermal conductivity, its excellent electrical insulation, its piezoelectric properties, its high hardness and its low dielectric constant. In addition, it is not toxic and easy to recycle. Thermal conductivities in the range of  $110\text{ W/mK}$  to  $260\text{ W/mK}$  for polycrystalline AlN were measured [123]. It is stable at high temperatures. In addition, the thermal expansion coefficient of AlN has a value of  $4.3 \times 10^{-6}/\text{K}$  [124], which is close to that of the used glass substrates of  $3.2 \times 10^{-6}/\text{K}$  [121].

The standard fabrication method for AlN is by reactive sputtering from pure Al targets. The purity of the target from oxide contamination is very important to get good results. After fabrication an oxide layer with a thickness of  $50\text{ \AA}$  to  $100\text{ \AA}$  grows in air, which passivates the surface and stops the further decomposition of AlN [125]. This layer protects the material up to  $1370^\circ\text{C}$ . At higher temperatures bulk oxidation occurs.

In this work AlN is utilized as a sacrificial layer to release freestanding laser induced nanostructures from ITO. It was chosen for this purpose because it satisfies all requirements. Such a sacrificial layer must be transparent for the laser beam, should have a higher ablation threshold than ITO, and should possess a refractive index close to that of glass and ITO.

Furthermore, a very low surface roughness is required to serve as substrate for ITO sputtering and it should be etchable selectively versus ITO.

AlN films are synthesized according to a standardized process by Ababneh by DC reactive sputtering in an  $N_2$  atmosphere [126]. The optical properties are measured in a transmission-reflection measurement as shown in Fig. 2.10. It shows a high transparency for the laser beam spectrum. According to the literature, the refractive index of AlN has values in the range of 1.8 to 2.5, which fits very well to the desired range for good index-matching [127].

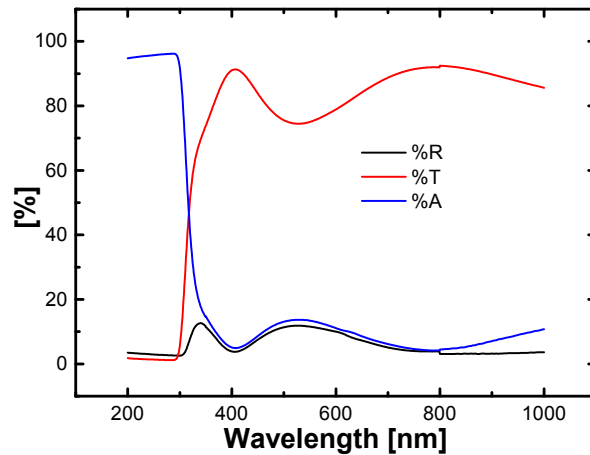


**Figure 2.10:** Transmission-reflection measurement on sputtered AlN on glass substrate.

The surface roughness of the sputtered films on the glass substrates was analyzed by atomic force microscopy (AFM). With a value of 1.5 nm it is low enough for sputtering of high quality ITO films on top (see Section 4.15). The roughness of the glass substrate was in the range of 1 nm, according to specifications.

AlN can be etched in phosphoric acid ( $H_3PO_4$ ). The etch rate depends on the crystal structure and morphology of AlN. At a temperature of 80 °C an etch rate of 75 nm/min was obtained. The etch rate of ITO in phosphoric acid is much lower, thus enabling a selective etch process for a sacrificial layer surface micromachining technology.

## 2.2.4 Gold (Au) and Platinum (Pt)

Gold (Au) is mainly used as conducting inert material for metallization to make the conductive pads and paths. In addition to a relatively low resistivity ( $\rho_{Au} = 2.2 \times 10^{-6} \Omega\text{cm}$  [128]), gold has a good biocompatibility and is being used for biomedical applications.

Gold layers are deposited in a DC magnetron sputtering machine from a 99.9% pure gold target. It can be etched in aqua regia (nitrohydrochloric acid) as a mixture of 37% HCl and 70%  $HNO_3$ . The etch rate is changing over time because of the reaction between HCl and  $HNO_3$  and the generation of gold-salts in the medium. The average etch rate is around 10  $\mu\text{m}/\text{min}$  at room temperature and can be increased by heating. In the presented applications, a lift-off process is applied to structure the deposited gold layer, which yielded very good edges by using an image reversal photoresist (Section 2.2.5).

For the fabrication of freestanding structures (Section 4.15), the first chips were fabricated with a metallization of sputtered gold. However, better results were achieved by replacing it with platinum (Pt), having a low resistivity of  $\rho_{\text{Pt}} = 1 \times 10^{-5} \Omega\text{cm}$  [128]. The platinum layer is DC sputtered in an argon plasma with a 99.9% pure target. For structuring the platinum layer a lift-off process was used with an image reversal photo resist. A typical thickness in the presented applications is on the order of a few hundred nm.

## 2.2.5 Photoresists

Photoresists are photochemically modifiable polymers which are used for the production of structures in the micrometer and nanometer range in a lithography process. The main ingredients are polymers or epoxy resins, solvents, as well as a photosensitive component.

Resist have the property to change their solubility in certain solvents (developers) after selective exposure to a certain wavelength by a mask defined lithography process or by a scanning laser beam. Depending on the photochemical effects they are divided into different types which are briefly discussed in this Section.

### Positive Photoresist

In positive photoresists after exposure and development only the unilluminated areas remain (positive pattern of the mask). The main component of most positive resists is a synthetic resin, which is also referred to as *novolac* (Fig. 2.11). Novolacs are phenol-formaldehyde resins (synthetic polymers obtained by the reaction of phenol or substituted phenol ( $\text{C}_6\text{H}_5\text{OH}$ ) with formaldehyde ( $\text{CH}_2\text{O}$ ) with a formaldehyde to phenol molar ratio of less than one. The chain length of these macromolecules is variable; it affects especially the temperature stability of the resist. It is included as a binder in a proportion of about 20 % in a synthetic resin and is soluble in water. They all contain the same photoactive compound (PAC) which responds to the whole UV-spectrum from 310 nm to 440 nm covering the three main mercury lines, i, h and g. They may be used with broadband as well as with monochromatic exposure. Different novolak resists or fractions thereof were chosen to adapt them to different demands [129]. The processing consists of the following steps: dispense, prebake, exposure, post exposure bake, development and an optional hard bake.

The resin is usually a diazo compound, for example. Diazonaphthoquinone (DNQ) admixed as photosensitive component. DNQ inhibits the dissolution of the novolac resin, but upon exposure to light, the dissolution rate increases even beyond that of pure novolac. Diazonaphthoquinone reacts under the action of UV light and in the presence of water to carboxylic acid, and thus brings about a solubility in turn, the solubility in aqueous alkali solutions (e.g. NaOH). All AZ1500-series resists are compatible with all common developers used for positive photoresists, like AZ351B (diluted 1:4).

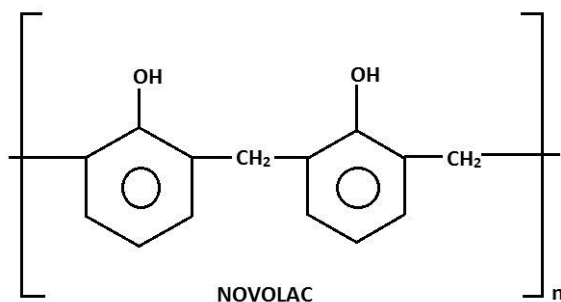


**Figure 2.11:** Novolac molecular structure.

In this work AZ1518 from *MicroChemicals GmbH* was used as a standard photoresist. The processing was done following the data sheets for standard spin-coating and exposure with a mask-aligner with i-line from a mercury-vapor lamp [130, 131].

### Negative Photoresist

In negative photoresists after development only those areas remain, which were not protected by the mask during exposure (negative pattern of the mask). Exposed areas lose their solubility in the developer liquid through photoinduced polymerization while the unexposed areas remain soluble. SU-8 is the most common product originally invented by IBM designed for micromachining and other microelectronic applications, where a thick, chemically and thermally stable polymer image is desired. Because of the biocompatibility it was used as a passivation layer to passivate the paths and prevent electrical short circuits and depress the parasitic effects on biochips [130] in this project (Section 4.3). Other reasons for the utilization of SU-8 are more convenient lithographically fabricated passivation layers and its optical transparency which was useful for transparency of the whole chip. This product is being sold by *Microchem*.

The basic substance of this epoxy based photoresist is bisphenol A-novolac epoxy dissolved in an organic solvent with up to 10 wt% of mixed triarylsulfonium/hexafluoroantimonate salt as the photoacid generator. The light irradiated on the resist interacts with the salt in the solution creating hexafluoroantimonic acid that then protonates the epoxide groups in the resin monomers. The monomers are thus activated but the polymerization will not proceed significantly until the temperature is raised as part of the post expose bake. It is at this stage that the epoxy groups in the resin cross-link to form the cured structure. When fully cured, the high cross-linking degree is responsible for the excellent mechanical properties of the resist [132, 133].

SU-8 exhibits adhesion to various substrates such as Si and glass, as well as metals including gold. However, the substrate must be well prepared and should be clean and dry. The processing consists of the following steps: dispense, softbake, exposure, post exposure bake, development and an optional hard bake.

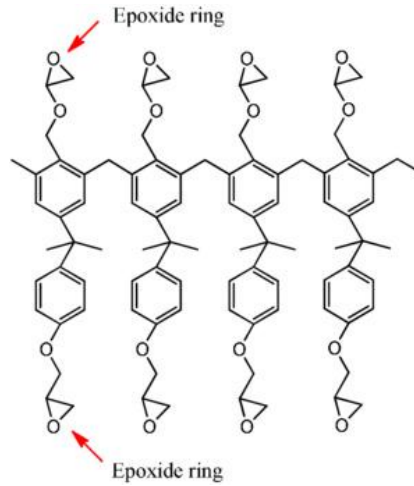


**Figure 2.12:** SU-8 molecular structure [134].

The soft bake is the most important of the bake steps for stress formation. It is performed after spinning. Its function is to remove the solvent from the resist and make the layer solid. Typically at least 5% of the solvent remains in the layer after the soft bake. However, the thicker the coating, the harder it becomes to remove the solvent, as evaporating solvent through thick layers becomes increasingly difficult with coating thickness. The bake is performed on a programmable hot plate to reduce the skinning effect of solvent depletion at the surface, creating a dense layer which makes the remainder of the solvent more difficult to remove. In order to reduce stress, the bake procedure is generally a two step process made up of holding at 65 °C before ramping to 95 °C and holding again for a time dependent on the layer thickness. The temperature is then lowered slowly to room temperature.

The exposure is thickness dependent and to reach the proper exposure energy a correction factor due to the used substrate should be added which is 1.5 for glass substrate. SU-8 is most commonly exposed with conventional near UV (350 nm to 400 nm) radiation, although i-line (365 nm) is recommended. It is also recommended to use a long pass filter to eliminate UV radiation below 350 nm.

The passivation is achieved through a relatively thick SU-8 layer and a optimized fabrication process to realize stress free and crack free layers. The electrical properties of SU-8 can be summarized with its high resistivity of  $\rho = 7.8 \times 10^{14} \Omega\text{cm}$  and a permittivity of  $\epsilon_r = 3.28$  at 1 GHz [133]. The main developer for SU-8 is 1-methoxy-2-propanol acetate. Development time is primarily a function of SU-8 thickness [133].

### Image Reversal Photoresist

Reversal resists are special positive resists which are intended for lift-off-techniques which call for a negative wall profile. They behave in the usual process sequence as a positive resist and may even be used in this way. Although they comprise a novolak resin and naphthoquinone diazide as photoactive compound (PAC) they are capable of image reversal (IR) resulting in a negative pattern of the mask. In the presented fabrications here AZ5214E

from *MicroChemicals GmbH* was used for lift-off processes with a light sensitivity for i- and h-line (310 nm to 420 nm). It may be used with broadband as well as monochromatic exposure. In fact, AZ5214E is almost exclusively used in the IR-mode. The processing consists of these steps: dispense, prebake, exposure, reversal bake, flood exposure, development and an optional postbake.

The image reversal capability is obtained by a special cross-linking agent in the resist formulation which becomes active at temperatures above 110 °C and only in exposed areas of the resist. The cross-linking agent together with exposed PAC leads to an almost insoluble (in developer) and no longer light sensitive substance, while the unexposed areas still behave like a normal unexposed positive photoresist. After a flood exposure (no mask required) these areas are dissolved in standard developer for positive photoresist, the cross-linked areas remain. The overall result is a negative image of the mask pattern [135].

A positive photoresist profile has a positive slope of 75 ° to 85 ° depending on the process conditions and the performance of the exposure equipment (only submicron-resists get close to 90 °C). This is mainly due to the absorption of the PAC which attenuates the light by penetrating through the resist layer. The result is a higher dissolution rate at the top and a lower rate at the bottom of the resist.

The most critical parameter of the IR-process is reversal-bake temperature, once optimized it must be kept constant within  $\pm 1$  °C to maintain a consistent process. Thus, it may for example result in bubbles or foaming by thermally mobilized nitrogen which inevitably arises during the exposure. This temperature also has to be optimized individually for each process. In any case it will fall within the range from 115 °C to 125 °C. If the image reversal activation temperature is chosen too high ( $>130$  °C) the resist will thermally cross-link also in the unexposed areas, giving no pattern. The flood exposure is absolutely uncritical as long as sufficient energy is applied to make the unexposed areas soluble. 200 mJ/cm<sup>2</sup> is a good choice, but 150 mJ/cm<sup>2</sup> to 500 mJ/cm<sup>2</sup> will have no major influence on the performance [135].

The developing step is by immersing the layer for about 1 minute into a standard developer prepared with AZ351B 1:4 diluted.





# 3 Experimental Methods

This Chapter describes the experimental methods used in this project. It begins with an introduction to the utilized laser setup. Then the material characterization methods are introduced, including those for material analyzing before and after laser processing as well as those for characterization of completely fabricated chips.

## 3.1 Utilized Laser-Setup

Nanoprocessing with femtosecond laser pulses is becoming more efficient with shorter pulses (see Section 2.1.2). The efficiency can be enhanced by multiphoton effects while  $m$ -photon excitation follows a  $P^m/\tau^{m-1}$  dependency. With ultra-short pulses, e.g. below 20 fs, the ablation threshold can be overcome even with low-power systems. With high repetition rate laser oscillators, material processing can be done already with an average power in the lower mW range [1].

Near infrared (NIR) laser microscopy, as one of the new approaches in biomedical research to make diffraction limited manipulations, can overcome the diffraction limit by using NIR laser pulses in femtosecond range. In this project, an integrated femtosecond laser in an inverse microscope is applied to achieve laser nanostructuring on a large variety of materials (Fig. 3.1). Tightly focused laser light of sub-15 femtosecond pulses with a repetition rate of 85 MHz at a central wavelength of 800 nm (spectral width of 120 nm) enables nanoscale processing of a variety of materials, including ITO layers. The focusing of the beam is carried out with an objective mounted on a piezo actuator, allowing precise adjustments with steps in the nanometer scale. The beam can be scanned in  $x$ - and  $y$ -direction by using galvo-scanners with adjustable scan speeds. Reflective optical elements in form of mirrors are not dispersive, but the lenses and filters are, so that the pulse length will be changed (pulse broadening) after propagation through the setup due to group velocity dispersion effects. To compensate for that and to be able to change the pulse length of a package of different wavelengths toward longer pulses, chirped mirrors<sup>1</sup> and other dispersive media made of silica glass are additionally installed in the beam path. With the help of this setup, the pulse length on the microscope can be varied between 3 ps and 12 fs but at the cost of intensity. The laser has an output power of 415 mW. To achieve the minimum pulse length of 12 fs on the sample, a

---

<sup>1</sup>A dielectric dispersive mirror which is usually used for dispersion compensation in mode-locked lasers. The basic idea is that the Bragg wavelength is not constant but varies within the structure, so that light at different wavelengths penetrates to a different extent into the mirror structure and thus experiences a different group delay [4].

huge part of its power gets lost through optical parts resulting in an average power of about 25 mW.

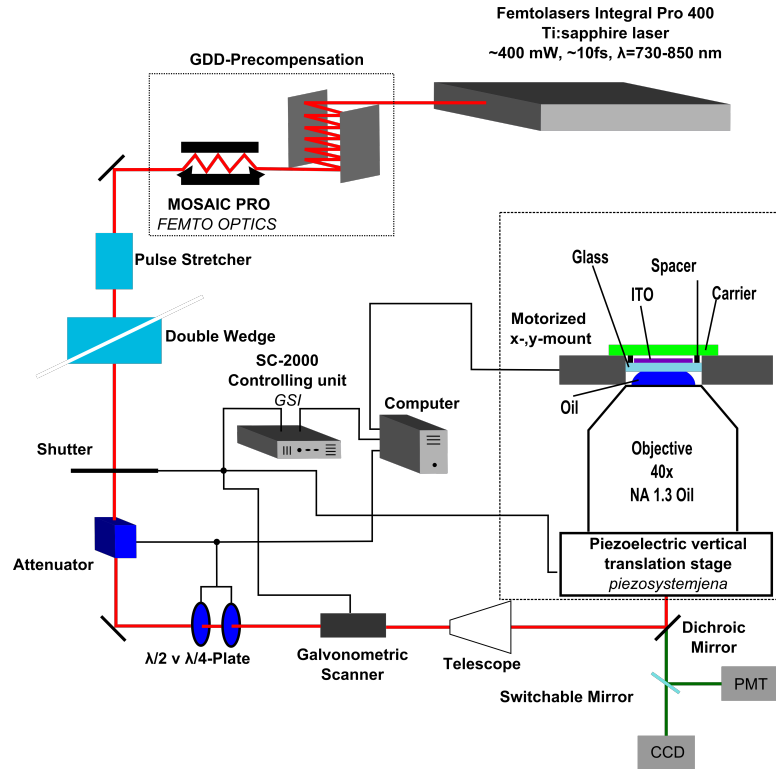


**Figure 3.1:** Scheme of the high resolution laser-microscope setup.

By applying a  $TEM_{00}$  mode with a Gaussian profile and with the optimum widening for a homogeneous coverage of the rear lens in the objective, a diffraction limited spot size can be achieved with a diameter of  $d = \frac{0.61\lambda}{NA} = 375 \text{ nm}$  and with an exposure area of  $0.11 \mu\text{m}^2$ . The central laser wavelength  $\lambda$  is at 800 nm and the numerical aperture (NA) of the objective is with 1.3 close to those of glass and immersion oil. Mean and transient values for laser parameters are summarized in Tab. 3.1 for the maximum reachable power on the sample.

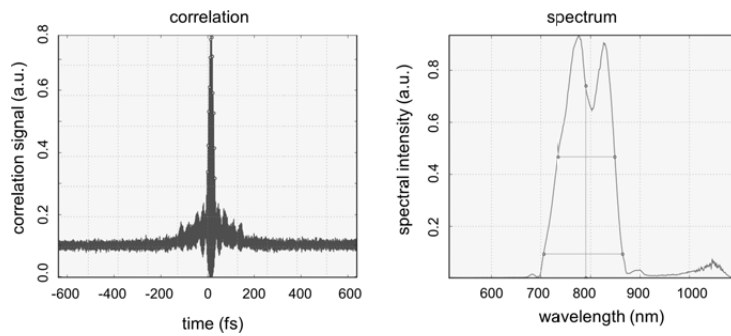


**Figure 3.2:** The pulse length of 12 fs is measured with a second-order interferometric scanning autocorrelator on the objective. The laser pulse features an M-shaped broadband spectrum [1].

Using an oil immersion objective (EC Plan Neofluar 40× from *Zeiss*, NA = 1.3) with high numerical aperture enables sub-wavelength spot sizes. The working distance of this objective is 210  $\mu\text{m}$ . In combination with thin glasses as substrate, it is possible to focus the laser beam tightly from the back through the substrate onto the thin film on top. In contrast to front side illumination, this setup prevents any contamination with immersion oil and additionally avoids any shielding effects of the plasma on the surface which could disturb the processing.

**Table 3.1:** A summary of laser parameters using an oil immersion objective from *Zeiss* (NA = 1.3).

$S_{\text{spot}}$ [ $\mu\text{m}^2$ ]	$R$ [a.u.]	$\tau$ [fs]	$P_{\text{avg}}$ [mW]	$I_{\text{avg}}$ [MW/cm $^2$ ]	$E_{\text{pulse}}$ [nJ]	$P_{\text{peak}}$ [KW]	$I_{\text{peak}}$ [TW]	$F$ [J/cm $^2$ ]
0.11	85	$\sim 12$	25	22.7	0.294	24.5	22.3	0.267

A CCD camera enables monitoring of the process over a side connection of the microscope. Galvo-scanners and the piezo driver are controlled by interfaces which were programmed in LabVIEW. Also, a software was developed to generate the x, y, and z coordinate points for the scan line to write a desired structure at a chosen scan speed. This software is able to generate the data set for different applications, including 3D structures.

## 3.2 Material Characterization Methods

Different techniques are applied to characterize the used materials, according to their desired applications and including the result of laser processing. This Section gives a brief summary about these methods and the setups which were used for each technique. The results achieved are presented in the relevant Sections or in the included publications.

### 3.2.1 Structural Analysis

In this part, analysis methods using an electron beam are shortly presented. For an electron beam as for any particle beam a de Broglie wavelength can be attributed, which is inversely proportional to their kinetic energy. Thus, a resolution much higher than with a light microscope can be achieved.

#### Scanning Electron Microscope

In a scanning electron microscope (SEM), an electron beam is being scanned in a preset pattern over an object to get an enlarged image of the surface and the structures on it by detecting the electrons after their interaction with the object. The beam is generated in an electron source (gun) and gets accelerated in an electric field with a voltage of typically 1 kV to 10 kV. In this case of observing ITO, the electrons have been accelerated mostly with 5 kV.

When the electron beam interacts with the material, it loses energy by different mechanisms. This includes conversion into heat, emission of low-energy secondary electrons and of high-energy backscattered electrons as well as light emission (cathodoluminescence) or X-ray emission. These electrons of different sources or energies propagate in the chamber, which is under high vacuum. They are received by detectors and give information about different properties of the material, such as surface topography. From this an image of the surface can be generated. A secondary electron detector was the favorite imaging mode used in this project. The interaction volume for the various scattering types and imaging modes is illustrated in Fig. 3.3 as a depth ranged issue. The imaging resolution is dependent on the volume generated by the emission type.

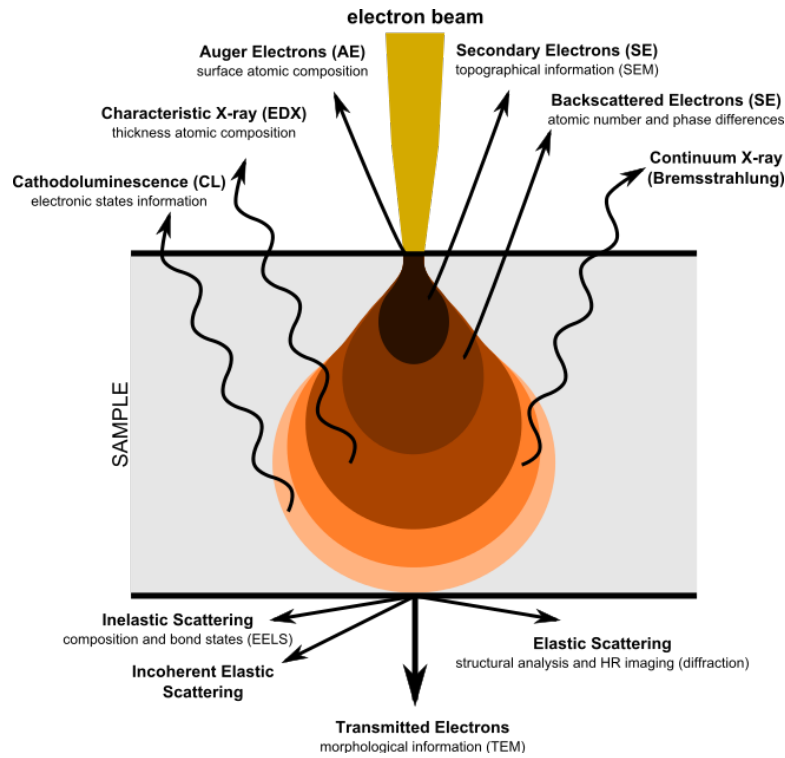


**Figure 3.3:** Scheme of the interaction volumes by the various types of scattered electrons and X-rays [136].

With this method, the surface structure of the films including sub-20 nm structures were imaged and measured. When imaging cross sections, the thickness of deposited layers could be measured. For this purpose, the sample was tilted 52 degrees. It should be noted that the true thickness is calculated from the following relation:

$$d = \frac{d_{\text{measured}}}{\sin 52^\circ}. \quad (3.1)$$

The electrons from the beam should flow off from the sample to prevent surface charging effects. The surface must be conductive and be short circuited to the holder. For this purpose, on almost all samples a gold layer of about 10 nm was sputtered on which was connected to the holder with a conductive tape. Only the freestanding nanowires (Section 4.15) were measured

without coating in a so called environmental scanning electron microscope (ESEM). This method can produce images of sufficient quality and resolution with the samples contained in a low pressure gas ambient. The gas atmosphere serves as a short circuit and conducts the electrons (see Section 4.15).

For the measurements with the desired resolution a FEI STRATA DB235 system and a dual-beam FIB System of Type Helios Nanolab 600 from *FEI* were utilized.

### Transmission Electron Microscopy

Transmission electron microscopy (TEM) is a microscopy technique in which a beam of electrons is transmitted through an ultra-thin sample, interacting with the material as it passes through it. An image is formed from the interaction of the electrons transmitted through the specimen; the image is magnified and focused onto an imaging device, such as a fluorescent screen, on a layer of photographic film, or to be detected by a sensor such as a CCD camera. The preparation of samples for the test was done by using ion beam slicing and polishing using a micromanipulator in SEM. The desired area must be thin enough so that the thickness of the sample is smaller than the penetration depth of the electrons in the material. Thus, sufficiently accelerated electrons are used.

In TEM the electrons are typically accelerated in the range from 100 kV to 400 kV. The contrast is not dependent on the absorption, but on scattering and diffraction of the electrons within the sample. If the transmitted electrons are used to get the image, this mode is called bright field. Thicker regions of the sample, or regions with a higher atomic number will appear dark. The image is in effect assumed to be a simple two dimensional projection of the sample down the optic axis. The other mode is dark field imaging which is based on diffracted electrons.

By TEM analysis on two different materials with different atomic numbers ( $Z$ ), this difference appears in the image. Electrons are scattered stronger by the atoms with larger  $Z$  than those with smaller  $Z$ . Highly scattered electrons are substantially less transmitted and reach the screen in a significantly smaller number. Therefore, heavier elements have a darker contrast on the picture than the lighter ones. This effect can be used in so called  $Z$ -contrast image for identifying clusters and material transitions in the medium.

For TEM measurements a JEM 2011 system from *JOEL* was utilized.

### Energy Dispersive X-Ray Spectroscopy

Energy dispersive X-ray spectroscopy (EDX) is a widespread analysis method that often operates together with scanning electron microscopes because of a common vacuum chamber and an electron gun. The composition of an unknown material is determined in this method by irradiating the sample with high-energy electrons ( $> 5$  keV). The electrons are decelerated inside a volume of interaction by various mechanisms (see Fig. 3.3), including collisions with orbital electrons in the lower atomic orbitals (e.g. K-Shell). High energetic electrons ionize

the atoms. Now electrons from outer shells (e.g. L-Shell) move to the free energetically more favorable conditions by releasing characteristic X-rays (e.g.  $\gamma = K_{\alpha 1}$ ). This X-ray energy is characteristic for each element. From the intensities of the individual emission lines the elementary composition can be calculated.

The radiated X-ray is measured by a solid state detector, its signal being proportional to the energy. By using a focused electron beam as excitation source a high spatial resolution is achieved. The excitation volume depends on the energy of the electrons. Since the film layers (e.g. ITO) are thin, the incoming electron energy is reduced by 5 keV to ionize the L-electrons, thus minimizing the substrate-signal and reduce the error of measurement. This method is a more qualitatively measurement for comparing the samples from different processes and with varying compositions.

### X-ray Diffractometry

X-ray diffractometry is a nondestructive analysis method for identifying the crystal structure, crystal defects, and mechanical stress in materials. Therefore, X-rays interact with material in different forms. The superposition of elastically scattered electromagnetic waves at atoms of crystal planes, results in diffraction patterns which can be analyzed to extract the material properties. The X-ray source is the characteristic Cu  $K_{\alpha}$ -line with a wavelength of 1.5406 Å which is in the same order of magnitude as the lattice constant.

Two beams with identical wavelength and phase approach a crystalline solid and are scattered off two different atomic layers. They traverse different ways, with a length of  $2d\sin\theta$ . If this length is equal to an integer multiple of the wavelength of the radiation a constructive interference occurs. The diffraction pattern exhibits, if Bragg's Law is satisfied:

$$n \cdot \lambda = 2 \cdot d \cdot \sin\theta, \quad (3.2)$$

where  $n$  is the order of interference,  $\lambda$  the X-ray wavelength,  $d$  the lattice constant, and  $\theta$  the angle of incidence as shown in Fig. 3.4.

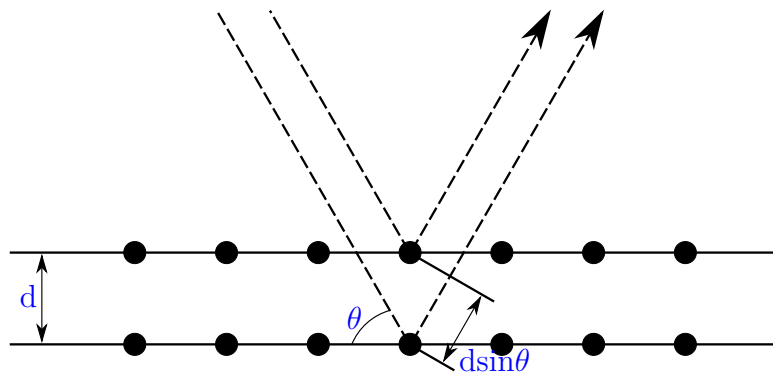


**Figure 3.4:** Schematic view of the Bragg condition by scattering of two beams from two different atoms (atom layers).

By using a data bank of all phases of different materials it is possible to make a phase analysis to obtain the crystal orientations in polycrystalline materials.

Grazing incidence X-ray, typically from a crystalline structure uses small incident angles for the incoming X-ray, so that diffraction can be made surface sensitive. It is used to study surfaces or thin films such as ITO because of limited wave penetration in material in the order of nanometres. Below the critical angle an evanescent wave is generated which exponentially damps in a very short distance, so that Bragg reflections are only coming from the surface structure.

These measurements were done by a material research diffraction X'pert PRO MPD system from *PANalytical*.

### 3.2.2 Optical Analysis

For an optical way of material structuring the optical properties of involved materials are of course decisive parameters for achieving the desired results. In this project, two strong standard methods were applied for measuring the needed properties of each layer. A short introduction to each method is given in this Section.

The only directly measurable optical quantity of a thin film material in interaction with light is the intensity of the reflected and the transmitted component. Thus the optical properties of a layer, such as the complex refractive index, can be measured only indirectly. This can be used in so called transmission and reflection measurements as well as in a model based method like ellipsometry.

#### Ellipsometry

Ellipsometry is an optical method for an indirect determination of the thickness and the complex refractive index of a thin layer on a known substrate. Here, the measuring principle is based on the change in the polarization between incident and reflected wave. The incident wave has a defined direction of linear polarization and the polarization properties of the reflected wave give information on the sample (Fig. 3.5).

The measurement can be carried out at one or more angles and wavelengths. Directly measured values are  $\Psi$  and  $\Delta$ , which represent the amplitude ratio and phase difference between two orthogonal light polarization components, respectively; p as parallel and v as vertical component to the surface of the sample. These two components possess different reflection coefficients and dipole radiations which cause an amplitude and phase change related to each other resulting in an elliptical polarization [138]:

$$\rho = \frac{r_p}{r_v} = \tan\psi e^{i\Delta} \quad \text{with} \quad \tan\Psi = \frac{|r_p|}{|r_v|}, \quad \Delta = \delta_{rp} - \delta_{rv}, \quad (3.3)$$

$r$  is the intensity and  $\delta$  is the phase of the respective components.

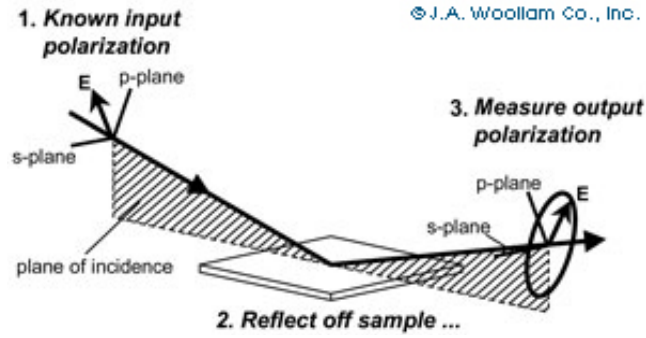


**Figure 3.5:** Typical ellipsometry configuration, where linearly polarized light is reflected from the sample surface and the polarization change is measured to determine film thickness and refractive index [137].

Spectroscopic ellipsometry gives the incident light energy as a function of wavelength. Spectroscopic ellipsometry thereby gives more information about the sample, such as the dispersion of the refractive index, which cannot be determined with a single wavelength. In contrast, a single-wavelength ellipsometer has a simpler structure and operation; it can use a single laser as radiation source. A spectroscopic ellipsometer applies Xe-, quartz-, tungsten-, halogen or SiC-globar lamps or a combination thereof to cover a wide spectral range with enough intensity. The source light is linearly polarized prior to reaching the sample. The polarization state is determined by a rotating analyzer and by a photodetector, after reflection from the surface. The measured signal in case of an elliptical polarization is a sinusoidal signal with a constant offset DC as follows:

$$V(t) = DC + a \cos(2\omega t) + b \sin(2\omega t), \quad (3.4)$$

where  $a$  and  $b$  are variables defined by  $\Psi$  and  $\Delta$  as follows:

$$\alpha = \frac{a}{DC} = \frac{\tan^2 \Psi - \tan^2 P}{\tan^2 \Psi + \tan^2 P}, \quad (3.5)$$

$$\beta = \frac{b}{DC} = \frac{2 \tan \Psi \cos \Delta \tan P}{\tan^2 \Psi + \tan^2 P}, \quad (3.6)$$

with  $P$  as azimuth angle of the input polarizer with respect to the plane of incidence. The inverted equations for the determination of  $\Psi$  and  $\Delta$  are as follows:

$$\tan \Psi = \sqrt{\frac{1 + \alpha}{1 - \alpha}} |\tan P|, \quad (3.7)$$

$$\cos \Delta = \frac{\beta}{\sqrt{1 - \alpha^2}} \frac{\tan P}{|\tan P|}. \quad (3.8)$$



In case of a multilayer structure, the unknown optical constants for each layer can be calculated by using fitting parameters in an optical model with an optimal match between measured and calculated values (Fig. 3.6). A precise optical model of the layer arrangement is essential, containing the optical constants of each layer and their thicknesses; even the roughness of the surface and also transition layers at interfaces are important for reliable results [138].

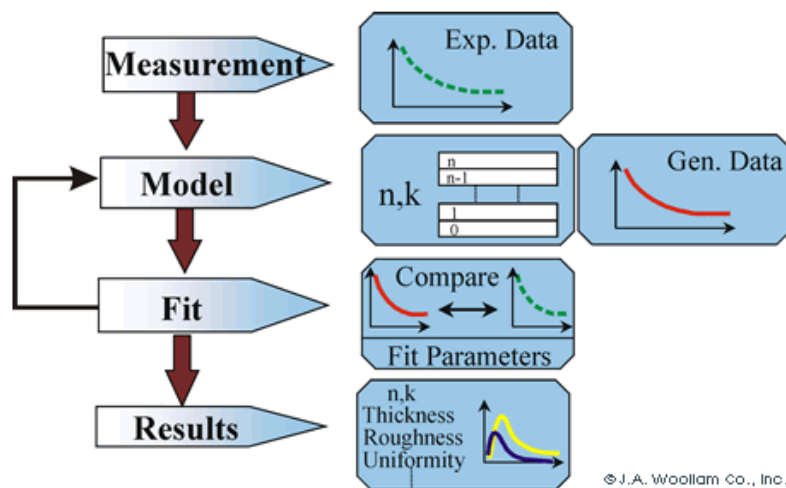


**Figure 3.6:** Flowchart for ellipsometry data analysis [137].

The model uses Snell's law and Fresnel's equations for thin films including multireflection of light in thin films to get the total reflecting light. The complex refractive index ( $N = n - ik$ ) of each layer contains the real part in form of the refractive index ( $n$ ) and the extinction coefficient ( $k$ ), with  $n$  being related to the phase velocity while  $k$  indicates the amount of attenuation when the electromagnetic wave propagates through the material. Alternatively, the optical properties can be represented as a complex dielectric function, which is defined as  $\epsilon = N^2$  and the absorption coefficient  $\alpha = \frac{4\pi k}{\lambda}$ . The dielectric function of a material describes the electrical and optical properties versus frequency, wavelength, or energy. It describes the polarization (electric polarizability) and absorption properties of the material [137].

When modelling for the unknown constants, a preliminary estimate is given for the purpose of starting the calculation. The calculated values are compared to experimental data. Any unknown material properties can then be varied to improve the match between experiment and calculation. The number of unknown properties should not exceed the amount of information contained in the experimental data. A mean squared error (MSE) of an estimator is used to quantify the difference between calculated and measured curves. The unknown parameters are varied until a minimum MSE value is reached.

The optical constants for a material will vary for different wavelengths and must be described at all wavelengths probed with the ellipsometer. For the optical modeling, a dispersion relationship for the optical constant versus wavelength is being used. The adjustable parameters of the dispersion relationship allow the overall optical constant shape to match the experimental results. This greatly reduces the number of unknown parameters.

For this dispersion relation different models exist, depending on the optoelectrical properties of each material. For transparent materials with  $k=0$  the Cauchy-model is the best description of the dispersion of the refractive index. Electrically conducting absorbing layers often exhibit a transparent wavelength region where the Cauchy model can also be applied. However, within the absorbing region both the real and the imaginary part of the optical constants are required. This can be done by the Lorentz-Oscillator-Model based on Lorentz harmonic oscillators [137, 138].

The utilized system for the measurements in this work was a spectroscopic ellipsometer M-2000/A-SE from *J.A. Woollam Co. Inc.*

### Transmission and Reflection Measurements

For making transmission and reflection measurements, light of a specific wavelength is irradiated on the sample and detectors measure the intensity of the transmitted and reflected light under each proper angle in order to maximize the effect. In general, the measurement is carried out for many wavelengths to determine the transmission and reflection in a specific range of the light spectrum. The standard reflection angle is above the critical angle for total reflection. For transmission the light is radiated vertically onto the sample, and the transmission is measured on the other side.

The relation of Eq. 2.52 between reflected, transmitted and absorbed light intensities is valid, so that from the transmission  $\mathbf{T}$  and reflection  $\mathbf{R}$  of the sample the absorption  $\mathbf{A}$  can be determined. Optical properties of thin films are generally determined from measurements of the film-substrate arrangement. The optical properties of the substrate must be known in order to be able to extract the layer properties from the measurements. Using reflection and transmission measurements does not make it easier, since the reflection at the interface between film and substrate must also be considered. A mathematical relationship for this is derived in the following.

When an electromagnetic (EM) wave  $\vec{E}_I e^{i(\vec{k} \cdot \vec{r} - \omega t)}$  strikes an optical boundary layer, it can be split up into its vertical  $E_I^S$  and parallel  $E_I^P$  components relative to the plane of incidence. At the interface between two media a transmitted electromagnetic wave  $\vec{E}_T e^{i(\vec{k}_T \cdot \vec{r} - \omega t)}$  and a reflected electromagnetic wave ( $\vec{E}_R e^{i(\vec{k}_R \cdot \vec{r} - \omega t)}$ ) occur, whose amplitudes can also be described in two polarization planes ( $E_T^S, E_T^P$  and  $E_R^S, E_R^P$ ).

Due to a coordination system with  $xz$ -plane on incident wave, the components in the  $x$  and  $y$  directions for electric field vectors  $\vec{E}$  and the magnetic field vector  $\vec{H}$  can be obtained by adding the amplitudes with parallel and perpendicular polarization [139].

Additionally, the  $x$  and  $y$  components (tangential components) of  $\vec{E}$  and  $\vec{H} = \vec{B}/\mu$  must be continuous at the interface, assuming no charge on the boundary surface and with tangential alignment to the interface derived from the Maxwell-equations. The reflection and transmission of light can be summarized in Fresnel relations with  $n_0$  the refractive index of

air,  $n_1$  of the layer and  $n_2$  of the substrate and  $\mu_1$  and  $\mu_2$  the magnetic permeability of the media.

For the general case of a bilayer system and media with complex refractive indices  $N = n + ik$  with incident or reflecting angle  $\alpha$  and transmitting angle  $\beta$  all components of the electric field can be calculated as follow:

$$\frac{E_{\text{R}}^{\text{P}}}{E_{\text{I}}^{\text{P}}} = \frac{\frac{n_2}{\mu_2} \cos \alpha - \frac{n_1}{\mu_1} \cos \beta}{\frac{n_1}{\mu_1} \cos \alpha + \frac{n_2}{\mu_2} \cos \beta} = r_{\text{p}}, \quad (3.9\text{a})$$

$$\frac{E_{\text{T}}^{\text{P}}}{E_{\text{I}}^{\text{P}}} = \frac{2 \frac{n_1}{\mu_1} \cos \alpha}{\frac{n_1}{\mu_1} \cos \beta + \frac{n_2}{\mu_2} \cos \alpha} = t_{\text{p}}, \quad (3.9\text{b})$$

$$\frac{E_{\text{R}}^{\text{S}}}{E_{\text{I}}^{\text{S}}} = \frac{\frac{n_1}{\mu_1} \cos \alpha - \frac{n_2}{\mu_2} \cos \beta}{\frac{n_1}{\mu_1} \cos \alpha + \frac{n_2}{\mu_2} \cos \beta} = r_{\text{s}}, \quad (3.9\text{c})$$

$$\frac{E_{\text{T}}^{\text{S}}}{E_{\text{I}}^{\text{S}}} = \frac{2 \frac{n_1}{\mu_1} \cos \alpha}{\frac{n_1}{\mu_1} \cos \alpha + \frac{n_2}{\mu_2} \cos \beta} = t_{\text{s}}, \quad (3.9\text{d})$$

where  $r_{\text{p}}$  and  $r_{\text{s}}$  are the so-called Fresnel reflection coefficients,  $t_{\text{s}}$  and  $t_{\text{p}}$  are the Fresnel transmission coefficient. For nonmagnetic materials all  $\mu = \mu_0$  and can be ignored. The derivation does not depend on whether the refractive indices are real or complex.

For dielectrics the absorption factor disappears and  $N_{\text{j}} = n_{\text{j}}$ . For vertical irradiation in media with the same magnetic permeability equal to vacuum ( $\mu = 1$ ), parallel and perpendicular components are indistinguishable ( $\alpha = \beta = 0$ ). Thus it follows [140]:

$$r_1 = \frac{n_0 - n_1}{n_0 + n_1}, \quad (3.10)$$

$$t_1 = \frac{2n_0}{n_0 + n_1}. \quad (3.11)$$

For the following calculation  $\mu = 1$  is assumed. These relationships are for amplitudes, but as mentioned before just the intensity is a measurable parameter as square of the amplitude. The following relations are obtained:

$$\mathbf{R}_1 = |r_1|^2 = \frac{(n_0 - n_1)^2}{(n_0 + n_1)^2}, \quad (3.12)$$

$$\mathbf{T}_1 = \frac{n_1}{n_0} |t_1|^2 = \frac{n_1}{n_0} \frac{4n_0^2}{(n_0 + n_1)^2}. \quad (3.13)$$

In case of a thin layer, multiple reflections occur and the following relation for reflection and transmission of a layer-substrate arrangement is calculated [140]:

$$\mathbf{R} = \frac{(n_0^2 + n_1^2)(n_1^2 + n_2^2) - 4n_0n_1^2n_2 + (n_0^2 - n_1^2)(n_1^2 - n_2^2) \cos 2\delta_1}{(n_0^2 + n_1^2)(n_1^2 + n_2^2) + 4n_0n_1^2n_2 + (n_0^2 - n_1^2)(n_1^2 - n_2^2) \cos 2\delta_1}, \quad (3.14)$$

$$\mathbf{T} = \frac{8n_0n_1^2n_2}{(n_0^2 + n_1^2)(n_1^2 + n_2^2) + 4n_0n_1^2n_2 + (n_0^2 - n_1^2)(n_1^2 - n_2^2) \cos 2\delta_1}, \quad (3.15)$$

with  $n_0$  the refractive index of the ambient,  $n_1$  of the layer and  $n_2$  of the substrate.  $\delta_1$  is the phase shift as it passes through the layer. For an absorbing film, for  $n_1$  a complex refractive index  $N_1 = n_1 - ik_1$  must be used. The result for transmission is as follows [139]:

$$\mathbf{T}_1 = \frac{n_2}{n_0} \frac{[(1 + g_1)^2 + h_1^2][(1 + g_2)^2 + h_2^2]}{e^{2\alpha_1} + (g_1^2 + h_1^2)(g_2^2 + h_2^2)e^{-2\alpha_1} + C \cos 2\gamma_1 + D \sin 2\gamma_1}, \quad (3.16)$$

with

$$g_1 = \frac{n_0^2 - n_1^2 - k_1^2}{(n_0 + n_1)^2 + k_1^2} \quad h_1 = \frac{2n_0k_1}{(n_0 + n_1)^2 + k_1^2}, \quad (3.17)$$

$$g_2 = \frac{n_1^2 - n_2^2 + k_1^2}{(n_1 + n_2)^2 + k_1^2} \quad h_2 = \frac{-2n_2k_1}{(n_1 + n_2)^2 + k_1^2}, \quad (3.18)$$

$$\alpha_1 = \frac{2\pi k_1 d_1}{\lambda} \quad \gamma_1 = \frac{2\pi n_1 d_1}{\lambda}, \quad (3.19)$$

$$C = 2(g_1g_2 - h_1h_2) \quad D = 2(g_1h_2 + g_2h_1). \quad (3.20)$$

The utilized system for these measurements was a Cary 5000 UV-Vis-NIR from *Agilent*.

### 3.2.3 Electrical Analysis

Electrical properties of sputtered ITO films as well as ITO nanowires were in focus of these studies. These are essential parameters for different applications based on electrical effects. Here three main methods are presented.

#### Four-Point Probe Measurement

The four-point probe method or four-terminal sensing is an electrical impedance measuring technique that uses separate pairs of current-forcing and voltage-sensing electrodes to make more accurate measurements than the simpler and more usual two-terminal sensing. Four-terminal sensing is used in some ohmmeters and impedance analyzers, and in wiring for strain gauges and resistance thermometers. Here, four-point probes are used to measure

sheet resistance of thin ITO films. In combination with a controlled variation of temperature the temperature coefficient of resistance was also studied.

The separation of current and voltage electrodes eliminates the effect of inner probe resistance and contact resistance from the measurement. This is an advantage for precise measurement of low resistance values. An array of linearly placed gold tips with equal spacing is used with the voltage reading sense wires as the inside pair, while the constant current feeding wires are the outside pair.

For inline arrangement of tips the resistivity is defined as :

$$\rho = \frac{1}{\sigma} = G \frac{V}{I}, \quad (3.21)$$

where the correction factor  $G$  is a function of sample geometry, the position of the probes on the sample, and the spacing between probes. These all affect the electrical field lines in the sample. Depending on the electrical field line distribution in the sample, various  $G$  values for a variety of shapes, dimensions, and aspect ratios have been calculated.  $G$ -value For extended thin films with a thickness  $d$  much smaller than the spacing between the tips on homogeneous substrates a  $G$ -value of  $\frac{\pi}{\ln 2}$  was determined [141]. In this case the sheet resistance can be the calculated as follows:

$$R_{\square} = \frac{\pi}{\ln 2} \frac{V}{I}. \quad (3.22)$$

The combination of the four-point probe with a heatable chuck with controlled temperature gives the opportunity to measure the temperature coefficient of resistance (TCR) in the material under investigation [50]. Here the temperature could be adjusted in the range from 10 °C to 90 °C and used this setup to measure the TCR of ITO films which show a metal-like behavior. The following equation was used to fit the measured curves for calculating the temperature coefficient of resistance:

$$\rho = \rho_0(1 + \alpha\Delta T), \quad (3.23)$$

with  $\Delta T = T_2 - T_1$ ,  $\rho_0 = \rho(T_0)$ , and  $\alpha$  the TCR-coefficient.

## I/V Measurement

Standard measurements of the detected currents versus applied voltages were performed in two case studies. It was applied to ITO micro test structures on glass substrates for extracting the maximum current density in air. The test structures had different dimensions so that the wires had a length of 400 and 2000  $\mu\text{m}$  and a width range of 10  $\mu\text{m}$  to 80  $\mu\text{m}$ . Such structures were fabricated by lithography and a lift-off process with gold being used for contact pads and gold tipped contact probes. With this setup the behavior of ITO microstructures and their electrical breakdown was studied [50].

Such I/V measurements were also applied to fabricated nanowires for studying the maximum current density they can carry after laser processing but also to study the self-heating effect. For this purpose the measurements in air were repeated in a heatable chamber under defined atmosphere and a constant cooling power, to find out the temperature coefficient of resistance for the fabricated nanowires.

A long term reliability measurement of nanowires including their drift behavior was done with this method.

## Hall Measurement

A Hall measurement was performed in order to determine the charge carrier density and mobility in deposited ITO layers. Samples were prepared for Hall measurements with contacts made in a Van der Pauw arrangement.

The Hall effect is based on a deflection of the current of charge carriers in a magnetic field as a result of the Lorentz-force:

$$\vec{F} = q[\vec{E} + (\vec{v} \times \vec{B})], \quad (3.24)$$

a particle of charge  $q$  moves with velocity  $\vec{v}$  in presence of an electric field  $\vec{E}$  and a magnetic field  $\vec{B}$  and experiences a force  $\vec{F}$ . The charge carriers in semiconductors can be electrons (n type) or holes (p type) and for each of them the same calculations are valid with n or p indices.

When a current is flowing in a conductive sample and is then exposed to a vertical magnetic field, the charge carriers experience a deflection. This leads to an accumulation of the charge carriers at one side of the sample which causes a measurable electrical voltage increase, the so called Hall voltage ( $U_H$ ). The sign of the resulting Hall voltage depends on the sort of carriers (i.e. holes or electrons or a combination thereof). Since ITO is a degenerate n-type semiconductor, the charge carriers are electrons. This case is schematically shown in Fig. 3.7.

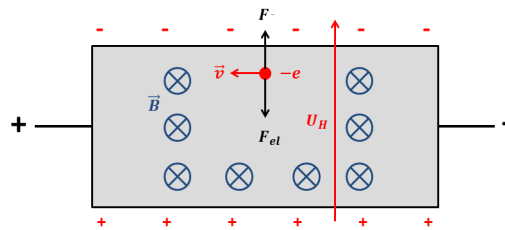


**Figure 3.7:** ITO thin film in a magnetic field  $\vec{B}$ , with  $\vec{v}$  the drift velocity of electrons,  $\vec{F}$  the Lorentz force, and  $\vec{F}_{el}$  the electric field force [130].

The induced force of the electric field ( $q\vec{E}$ ) counteracts the Lorentz force. Looking at this field as the inside of a parallel plate capacitor constellation, the following relation for the charge carrier density  $N$  is obtained [142]:

$$N = \frac{IB}{qdU_H}, \quad (3.25)$$

with  $I$  being the current flowing through the sample,  $B$  the magnetic field,  $q$  the charge of an electron,  $d$  the film thickness and  $U_H$  the Hall voltage. With electrons being the major charge carriers in n-type ITO and from the Hall coefficient  $R_H = \frac{U_{Hn}t}{IB} = \frac{-1}{Ne}$ , the electron mobility can be calculated as follows:

$$\mu_n = -\frac{\sigma U_{Hn}t}{IB}, \quad (3.26)$$

where the value of  $U_{Hn}$  (Hall voltage of electrons),  $t$  (sample thickness),  $I$  (current) and  $B$  (magnetic field) can be measured directly, whereas the conductivity  $\sigma$  can be obtained from measuring the resistivity. The index  $n$  stands for parameters of electrons.

### 3.2.4 Topographical Analysis

Two different profilometry methods were used for two different purposes: thickness measurements and roughness measurements. To make quick thickness analyses on the sputtered films or spin-coated layers, an electromechanical profiler was used. For more precise measurements on the surface of films particularly in the case of sputtered materials, an atomic force microscope (AFM) was applied.

#### Atomic Force Microscopy

Atomic-force microscopy (AFM) is a very-high-resolution method for surface analysis with demonstrated resolution on the order of fractions of a nanometer.

The AFM consists of a cantilever with a sharp tip (probe) at its end to scan the surface. The cantilever is typically silicon or silicon nitride with a tip radius on the order of nanometers. When the tip is brought into proximity of a sample surface, forces between the tip and the sample lead to a deflection of the cantilever according to Hooke's law. Depending on the situation, forces that are measured in AFM include mechanical contact force, van der Waals forces, capillary forces, chemical bonding, electrostatic forces, magnetic forces, Casimir forces, solvation forces, etc.. Typically, the deflection is measured using a laser spot reflected from the top surface of the cantilever into an array of photodiodes.

The AFM can be operated in different modes, depending on the application. In general, possible imaging modes are divided into static (contact) modes and a variety of dynamic

(tapping) modes where the cantilever is vibrated or oscillated at a given frequency in a certain distance to the surface.

The roughness of different films was characterized by atomic force microscopy (AFM) measurements using an Image 3100 system from *Veeco* in form of amplitude and phase of a silicon cantilever in tapping mode. The evaluation of data was done with WSxM 4.0 software (*Nanotec*) [143].

## Profilometry

The Dektak 150 is a stylus (contact) profilometer that is used to measure height differences (steps) on samples. This system operates by the stylus physically making contact with the sample surface and moving the stage from front to back (e.g. the stylus is held statically in place) to measure changes in surface height.

The thicknesses of different layers were measured with a Dektak 150 surface profiler from *Veeco*. It delivers surface profiles along a line scan and even over long distances up to 200 mm. This system drives a stylus electromechanically in contact mode with different contact forces between 0.03 mg to 15 mg. The vertical deflection of the stylus converts to an electrical signal with a linear variable differential transformer (LVDT). This gives a vertical resolution of 0.1 nm in the smallest scan range of 6.5  $\mu\text{m}$ .

### 3.2.5 Mechanical Analysis

Indentation is the act of bringing two bodies into hard contact; one being a probe, extremely stiff and minimally altered by the interaction, the second is the specimen whose properties are aimed to be quantified. It is the response to the applied load that provides an indication of the mechanical properties.

Stress measurements are one of the most common ways to test the mechanical properties of materials. These tests are quick and easy, repeatable and inexpensive. In macroscopic testing a load is applied and the residual imprint left by that load is optically measured to determine the contact area. The ratio of the applied load  $P_{\text{applied}}$  to the residual contact area  $A_{\text{residual}}$  gives the hardness ( $H_{\text{macro}} = \frac{P_{\text{applied}}}{A_{\text{residual}}}$ ) [144]. This hardness value is the plastic response of the material to an applied load. The measurement of the residual contact area is only as good as the resolution of the imaging technique.

It is well known that thin films do not necessarily have the properties of the same bulk materials. Therefore there is a necessity for measuring their mechanical properties independently from the bulk. The classically available microindentation machines do not allow for loads low enough to isolate the properties of thin films from those of the substrate. Therefore, specific machines for nanoindentation experiments had to be developed to reach precisely controlled indentation depths in the nanometer range. The guideline is to have an indentation depth of only about 10% of the total film thickness to exclude the influence of the substrate.



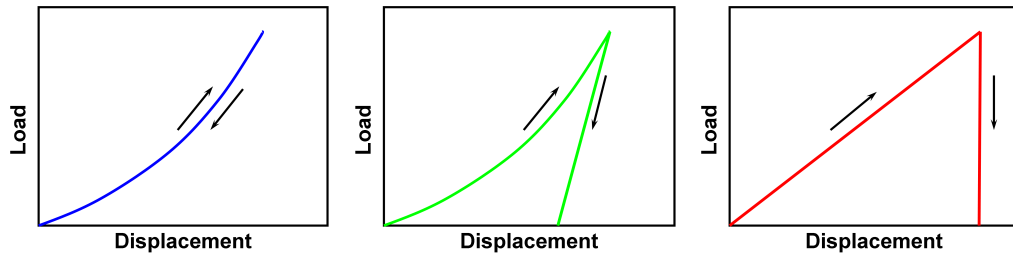


**Figure 3.8:** From left to the right: Load-displacement data demonstration in elasticity of completely elastic material, elastoplastic material, and ideally plastic material [120].

In the nanometer regime, atomic scale heterogeneities can have a large impact on the results. Factors such as location of the indent, surface preparation, surface orientation, the tip radius of the indenter and even the tip material play important role [145, 146].

By using the so called depth-sensing indentation a probe makes indents while recording the applied force and the corresponding displacement using a transducer. These displacement measurements are on the order of nanometers, and the applied force is usually on the order of micro-Newtons. This technique has one significant difference from traditional methods in the scale of resolution. The whole material response is recorded, both the elastic and the plastic deformation.

Nanoindentation utilizes continuous measurement of the displacement as the load is applied and then removed. Fig. 3.8 shows a typical loading profile for three different cases. An elastically deformed material will retrace completely the loading curve by unloading. An elastoplastic material displays a mixture of elastic and plastic behavior. A primarily plastically deformed material will have almost no elastic recovery and keeps the deformations.

As the size of the nanoindents is small compared to the whole sample, after performing calibration methods including tip area function calibration, frame compliance (inverse of the stiffness  $C = S^{-1}$ ) measurement, and tip to optic calibration, the stiffness of the thin film can be isolated by excluding that of the substrate and the measurement frame. It is also assumed that only the normal force is transmitted to the sample. The hardness of the material can then be defined as [120]:

$$H_C = \frac{P_{\max}}{A_C}, \quad (3.27)$$

where  $H_C$  is the hardness,  $P_{\max}$  is the maximum indentation load, and  $A_C$  is the projected area of contact at depth  $h_C$  (Fig. 3.9). The residual deformation is the plastic response, related to the final depth  $h_f$  (see Fig. 3.27). The tip is also assumed to have a very high rigidity; any elastic response is accounted for in the reduced modulus  $E_r$ . From this definition it is obvious that any inaccuracies determining the depth of contact have an influence on the calculated hardness values. Miscalculations in the area of contact influence the calculated applied stress, and can therefore dramatically change the calculated results.

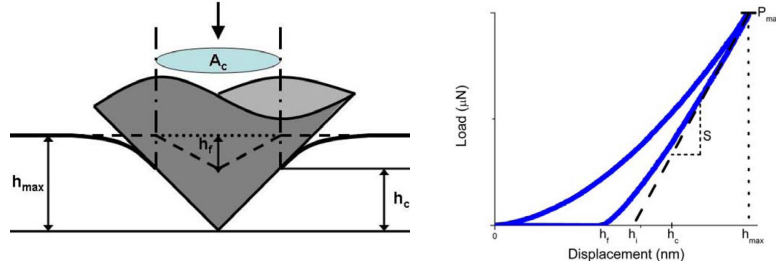


**Figure 3.9:** Schematic of an indenter at maximum load  $P_{\max}$  with an associated total depth of  $h_{\max}$ . The contact between the indenter and the surface at maximum load is defined by depth  $h_c$ , with a corresponding projected area of contact  $A_c$ . The dashed line (left), with a final depth of  $h_f$ , indicates the sample profile after the load has been removed. Corresponding load displacement curve, indicating the final depth  $h_f$ , the intercept depth  $h_i$ , the contact depth  $h_c$ , and the maximum depth [120].

In addition to hardness, the elastic moduli can be obtained from instrumental indentation experiments. The reduced modulus is calculated using the area of contact and the stiffness as follows [144]:

$$E_r = \frac{\sqrt{\pi}}{2\sqrt{A_c}} S. \quad (3.28)$$

The slope of the tangent at maximum load is the dashed line in Fig.3.9b. The stiffness  $S$  is the slope of this line. From here the modulus of the material can be calculated using Eq. 3.29 with values for Young's Modulus and Poisson's ratio of the indenter tip. An efficient method of combining the two moduli is to assume that the two materials behave like springs in series. The reduced modulus can be expressed [120]:

$$\frac{1}{E_r} = \frac{1 - \nu_m^2}{E_m} + \frac{1 - \nu_i^2}{E_i}, \quad (3.29)$$

where  $E_m$  and  $E_i$  are Young's moduli for the sample material and the indenter, respectively and  $\nu_m$  and  $\nu_i$  are the Poisson's ratios, accordingly. The elastic contact is small compared to the overall size of the specimen and the indenter.

The nanoindentation results presented in this work were obtained from a *Hysitron* TI 900 TriboIndenter system equipped with a Performech<sup>TM</sup> controller, Stanford Research System (SRS) 830 DSP lock-in amplifier and National Instruments USB-GPIB adaptor with a sharp Berkovich tip. This system is a powerful quantitative instrument for nanoindentation measurements. It has the ability to image the surface before and after indentation. The system has three main parts: the transducer, the transducer controller and a separate data acquisition system. The scanning probe microscope (SPM) software is used to interpret the voltage signal from the transducer, and the microscope piezos enable displacement control when imaging. The transducer holds the indenter tip which is also functioning as an imaging tip.

The most important part of the TriboIndenter is the patented three-plate capacitive force/displacement transducer, developed by *Hysitron*. For these experiments a nanoDMA III compatible transducer was used, enabling dynamic mechanical analysis, thus making continuous measurements (CMX) of different mechanical properties possible. By dynamic measurement, a sinusoidal loading can be applied in addition to a static loading. With this technique, the load amplitude and frequency (0.1 Hz to 300 Hz) can be defined in addition to the routine controllable parameters for the quasi-static measurement, such as maximum load (displacement), loading (displacement) rate, number of segments, data acquisition rate, etc. [147].

Additionally, the TriboIndenter utilizes an active anti-vibration system, an acoustic enclosure, a stage controller and optic electronics. With the aid of the aforementioned parts, it was possible to control the following items during nanoindentation:

- Atmosphere, humidity and temperature variation.
- Environmental vibrations; vibrations below 200 Hz can be dampened actively with the active anti-vibration system and vibrations above 200 Hz can be dampened passively [147].

The utilized system has a depth resolution of 0.2 nm and can apply indentation loads as high as 10 mN with a resolution of 1 nN [120].

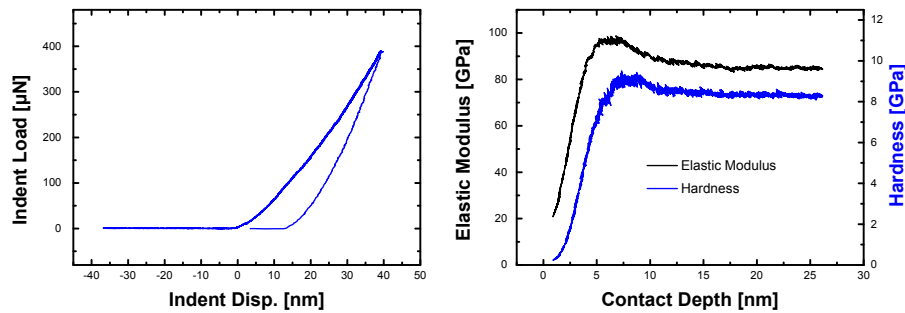


**Figure 3.10:** Left: A diagram of the indent loaded versus indent displacement for an indentation point, right: the from data acquisition system (nanoDM) delivered data; two curves of hardness and elastic modulus of an indentation point on sputtered polycrystalline ITO film.

The continuous hardness measurement was calculated based on the following formula [147]:

$$H = \frac{P + P_{AC}}{A_c}, \quad (3.30)$$

where  $P_{AC}$  is the dynamic actuation force and  $A_c$  is the contact area.

The contact displacement  $h_c$  for the nanoDMA III analysis can be calculated as:

$$h_c = (h + h_{AC}) - \epsilon \times \frac{P + P_{AC}}{k_{storage}}, \quad (3.31)$$

where  $h$  is the maximum displacement,  $h_{AC}$  is the dynamic displacement,  $\epsilon$  is defined as a geometric constant related to the probe,  $P$  is the applied quasistatic force,  $P_{AC}$  is the dynamic actuation force and  $k_{storage}$  is the storage stiffness, which can be calculated by the following equation:

$$K_{storage} = \frac{P_{AC} \times \cos(\theta) + m_T \times \bar{\omega}}{h_{AC}} - k_T, \quad (3.32)$$

where  $\theta$  is the phase shift between dynamic force and displacement fluctuations,  $m_T$  is defined as the mass of the transducer,  $\bar{\omega}$  is the radial frequency and  $k_T$  is defined as the stiffness of the transducer [147].

## 3.3 Device Characterization Methods

The fabricated devices presented in Chapter 4 have been characterized by different techniques for each proper application. In this Section a short introduction to each method is presented.

### 3.3.1 Electrical Measurements

One of the main issues are the electrical properties of ITO material in fabricated NWs. For this purpose a series of I/V measurements were done on the wires in air as well as temperature controlled TCR-measurements in a heatable chamber under defined atmosphere. These measurements were performed by the Laboratory for Measurement Technology at Saarland University with low currents to eliminate the self-heating effect. These measurements delivered the TCR value as well as the resistivity of ITO in form of NWs. The results are presented in Section 4.4.

### Gas Measurement

The fabricated NW-gas sensors with self-heating effect were measured in cooperation with the Laboratory for Measurement Technology (LMT) under coordination of Dr. T. Sauerwald in a gas measurement setup (see Fig. 3.11).

For the measurement a  $\text{NO}_2$  in a dilution of 1000 ppm was used as test gas. The gas pipes are divided into two lines. One pipe carried 100% humidity by passing through a wash bottle and the second one stayed dry. By mixing of these two flows a desired humidity

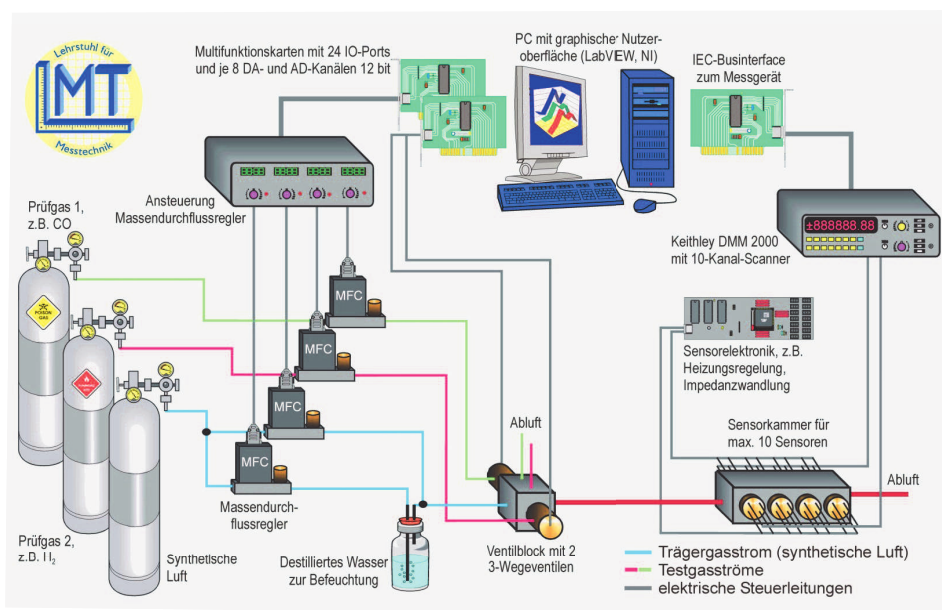


**Figure 3.11:** Schematic design of the gas measurement setup (LMT) [148].

level can be achieved. The gas flow is being adjusted by mass flow controllers which are controlled by a LabVIEW program. The flow goes into an airtight measurement cavity. The gas temperature was kept at room temperature and the flow was adjusted to 200 sccm with different percentages of  $\text{NO}_2$  and a constant relative humidity of 50%. The exact procedure of these measurements is mentioned in Section 3.11.

### 3.3.2 Impedance Spectroscopy

To characterize the fabricated bioelectrodes, a standard method of impedance spectroscopy is applied. In this method an alternating potential is applied to the working and reference electrode and the resulting alternating current is being measured. The ratio between these two measured parameters gives the impedance of the system recorded in phase and amplitude over a wide frequency range of  $10^{-4}$  Hz to  $10^6$  Hz [149].

To reduce nonlinearities in the IV-relation caused by reaction of redox products, it is better to use low voltages of 2 mV to 10 mV. In this range it can be approximated as a linear relation. In such a linear system an applied voltage with a certain frequency induces a current with the same frequency. Otherwise, the induced current would be a superposition of different harmonically generated frequencies [150]. Among other methods, the phase sensitive detection (PSD) with a lock-in technique and a frequency response analyzer (FRA) is the most established method [151].

The PSD method is a proper way to detect weak signals in very noisy environment. The lock-in technique needs a reference modulating signal with a defined frequency. With this technique signals in an up to  $10^5$  times higher noise amplitude environment can be detected. The second method, FRA is based on the correlation of the response impedance signal to

a sine signal with generated sine-shaped and cosine-shaped signals with the same frequency [152].

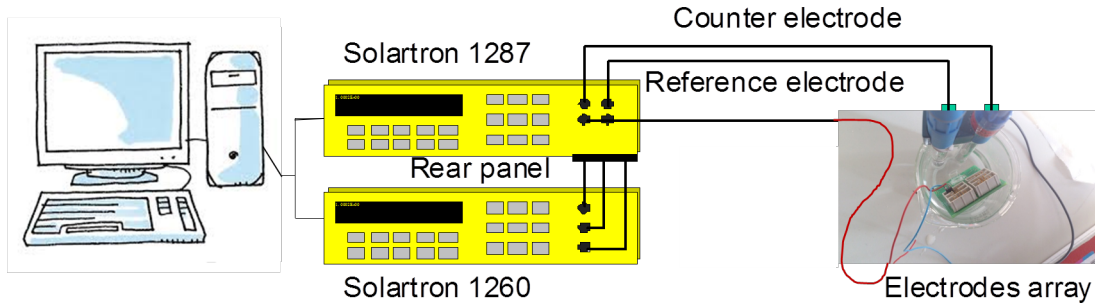


**Figure 3.12:** Schematic design of the impedance spectroscopy measurement setup (IBMT).

The measurements were done in cooperation with Fraunhofer Institute for Biomedical Engineering (IBMT) in the group of Dr. W. Poppendieck. First, an impedance measurement is carried out, then a physically correct equivalent circuit should be fitted to the measurements. Each element in this circuit addresses a certain chemo-physical process. For the calculated parameters of the circuit elements a realistic chemo-physical model must be developed. It can describe and interpret the systemically relevant parameters and processes.

The measuring points are normally being presented in Bode diagrams or Nyquist diagrams. Each method has its advantages and disadvantages and the aimed application defines the employed presenting way. The fitting procedure is based on the complex nonlinear least-squares technique (CNLS) which must be in turn numerically solved by the Marquard-Levenberg method [150, 152]. The clue within this indirect mathematical method is that the equivalent circuit, the initial parameter values and the error value from fits must be controlled carefully to prevent any wrong interpretation.

## **4 From ITO Laser Nanostructuring to Applications**

The following publications are used in Maziar Afshar's PhD thesis. All Co-authors of the below listed peer-reviewed papers and conference proceeding have **confirmed** that these publications may be used. Author contributions are mentioned as follow:

1. **“Efficient nanostructure formation on silicon surfaces and in indium tin oxide thin films by sub-15 fs pulsed near-infrared laser light”**, *Physics Procedia* 12, 16-232 (2011).

This research was designed by Maziar Afshar and Martin Straub. All experiments about ITO as well as etching experiments of silicon were performed by Maziar Afshar. Data were analyzed by Maziar Afshar and Martin Straub. Article was written by Martin Straub and Maziar Afshar and benefits from the feedback made by Dara Feili, Karsten König, and Helmut Seidel. Research was directed by Karsten König and Helmut Seidel.

2. **“Sub-100 nm structuring of indium-tin-oxide thin films by sub-15 femtosecond pulsed near-infrared laser light”**, *Optics Letters* 37 (4), 563-565 (2012).

This research was designed by Maziar Afshar. Experiments were performed by Maziar Afshar. Data were analyzed by Maziar Afshar. High-resolution optical microscopy setup was optimized in collaboration with Martin Straub. Article was written by Maziar Afshar and benefits from the feedback made by Martin Straub, Dara Feili and Helmut Seidel. Research was directed by Karsten König and Helmut Seidel.

3. **“Indium-Tin-Oxide Single-Nanowire Gas Sensor Fabricated Via Laser Writing and Subsequent Etching”**, *Sensors and Actuators B* 215, 525-535 (2015).

This research was designed by Maziar Afshar and Tilman Sauerwald. Experiments were performed by Maziar Afshar, Elisabeth Preiß, Tilman Sauerwald and Marius Rodner. Data were analyzed by Maziar Afshar, Tilman Sauerwald and Elisabeth Preiß. The theoretical backbone was developed by Maziar Afshar and Tilman Sauerwald. Article was written by Maziar Afshar, Tilman Sauerwald and benefits from the feedback made by Elisabeth Preiß, Dara Feili, Martin Straub, Andeas Schütze and Helmut Seidel. Research was directed by Karsten König and Helmut Seidel.

4. **“On-chip nanostructuring and impedance trimming of transparent and flexible ITO electrodes by laser induced coherent sub-20 nm cuts”**, *Applied Surface Science* 360, 494–501 (2016).

This research was designed by Maziar Afshar and Dara Feili. Experiments were performed by Maziar Afshar and Moritz Leber. Impedance measurements were done with Wigand Poppendieck. Data were analyzed by Maziar Afshar and Moritz Leber. Article was written by Maziar Afshar, Moritz Leber and Dara Feili and benefits from the feedback made by Karsten König, and Helmut Seidel. Research was directed by Dara Feili.



## 4.1 Sub-100 nm Structuring of ITO Polycrystalline Thin Films

### 4.1.1 Introduction

The patterning of ITO by laser is a current research topic. The most common method is the direct ablation, in which ITO is removed directly by exposure to the laser beam (see Fig. 4.1 left). For structure definition, the beam can be moved by means of a galvo scanner system or else the sample is moved via stepper motors or piezoelectric scanners [153]. An advantage of this method is the direct writing without the need for further steps like etching or lithography, except for a possible cleaning step. Another benefit is the applicability to non-acid-resistant plastic substrates. No wet chemical etching is necessary, so no chemical changes in the coating and no chemical contamination on underlying layers occurs. However, the processing times are often quite long, because scan rates are limited for many ps and fs lasers. The redeposition of the removed material on the edges of the ablation trench is a further disadvantage, lowering the quality of the structures for some applications.

Using ps- and fs-lasers gives the opportunity to make selective material scribing which is being applied in the fabrication of solar cells and photo diodes by structuring ITO as transparent conductive layer on top of the absorber layer (e.g. Si). Scan speeds of a few ten meters per second have been achieved, in case of structuring processes for CZTSe thin-film solar cells leading to short process times [154, 155, 156].

**Table 4.1:** Parameters used in the literature for ITO laser structuring using nanosecond-lasers (cf. [50]).

Laser	Wavelength [nm]	Pulse Length [ns]	Threshold Fluence [J/cm <sup>2</sup> ]	Trench Width [μm]	Ref.
KrF	248	23	0.3-0.6	-	[157]
F <sub>2</sub>	157	20	0.27	20	[158]
Nd:YLF	1047	15	18	< 20	[159]
Nd:YLF SH	523	15	41	< 50	[159]
Nd:YLF TH	349	15	8	< 30	[159]
Nd:YAG TH	355	35	< 0.1	20	[160]

Many studies for laser structuring of ITO using nanosecond lasers have been done which are summarized in Tab. 4.1<sup>1</sup>. There are also some studies on the removal by femtosecond laser, whose parameters are shown in Tab. 4.2.

It should be noted that the effect of the laser beam on the ITO layer does not only depend on the specified laser parameters, but also on the ITO layer thickness and its optoelectrical properties. Lasers with wavelengths in the ultraviolet range of the spectrum are preferred for ITO structuring because of a high absorbance of ITO in the optical short wavelength

<sup>1</sup>SH and TH stand for second and third harmonic of the initial wavelength of the laser.

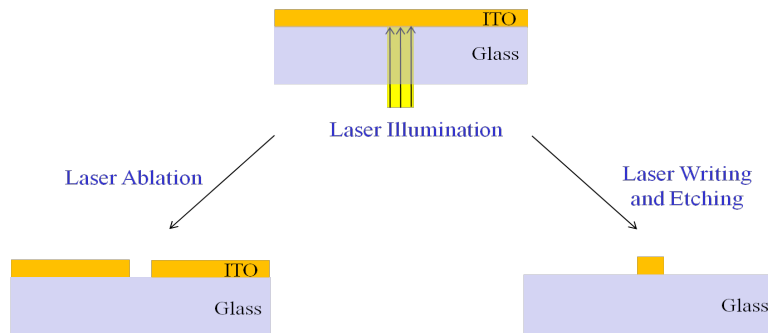
**Table 4.2:** Parameters used in the literature for ITO laser structuring using Ti:sapphire femtosecond lasers (cf. [50]).

Wavelength	Pulse Length	Threshold Fluence	Trench Width	Repetition Rate	Ref.
[nm]	[fs]	[J/cm <sup>2</sup> ]	[ $\mu$ m]	[Hz]	
800	100	0.1	ca. 20	$80 \times 10^6$	[89]
810	150	0.07	< 10	$1 \times 10^3$	[154]
800	60	0.2	3	$1 \times 10^3$	[161]
800	600	0.4	3	$1 \times 10^3$	[161]

range. Thus, lower threshold fluences can be achieved. The optical focusing method is also an essential factor.

A new way of ITO laser structuring is by recrystallization at intensities below the ablation threshold. This approach was primarily investigated in this work and also by one other group [59, 162, 163]. One can also speak of simplified heat treatment or rapid annealing. ITO can be subsequently structured by selective wet chemical etching in halogen acids, since its etching rate depends significantly on the layer properties (Section 2.2.1). The crystallinity of the layer can be significantly improved by the laser annealing process, whereby the etch rate of the processed area drops considerably and only the unprocessed ITO layer is removed [164]. This process behaves like working with a negative resist, as can be seen in the right of Fig. 4.1. In addition to being a clean process with no contamination by removed material, it has the advantage of improved crystallinity, leading to an increase in conductivity and transparency of the film [164].

Fine conductor lines can be produced by direct writing in a short time, whereas in the ablation setup the whole surrounding area needs to be illuminated, requiring much longer process times. In addition, very narrow structures with widths of only a few hundred nanometer even down to sub-100 nm can be realized by using sub-15 fs laser pulses [61].

**Figure 4.1:** Principle of ITO laser structuring through a glass substrate with a near infrared laser beam.

In the literature, examples of laser crystallization with fs laser pulses can be found [162] as well as examples with ns laser pulses [164, 165, 166]. They were carried out with light in the IR and UV range. The ns-laser annealing process was conducted at fluences ranging

from 50–260 mJ/cm<sup>2</sup> (see Tab. 4.3). When structuring large areas with a nanosecond laser, partial cracks can appear, which may be due to thermal shock [166].

In both processing ways, it is important to distinguish between ultra-short pulses (ps and fs) longer pulses (ns), as well as between high (MHz) and low pulse repetition frequencies. Ultra-short pulses generally lead to smaller structures with better boundaries than longer pulses because the laser energy cannot spread by energy dissipation into the layer during the pulse. At low pulse repetition frequencies, the pulse energy can diffuse out of the irradiated focus area before the next pulse arrives. In contrast, the energy at high pulse repetition frequencies accumulates, which leads to a strong rise in temperature [90]. At low pulse repetition frequencies the overlap rate of the laser exposure points have a large impact factor on the outcome [165].

**Table 4.3:** Parameters used in the literature for ITO laser crystallization.

Laser	Wavelength [nm]	Pulse Length [ns]	Threshold fluence [mJ/cm <sup>2</sup> ]	Trench width [μm]	Ref.
Nd:YAG	1064	72	120 - 260	–	[165]
XeCl	308	15	100	–	[166]
XeCl	308	35	50 - 250	–	[164]
Ti:sapphire	800	100 × 10 <sup>-6</sup>	10 - 30	3 - 12	[162]

### 4.1.2 Addendum I

The results of the first characterizations of ITO laser interaction are demonstrated in two journal articles. The first is published 2012 in **Optics Letters** (Impact Factor: 3.292) and presents the effect of oxygen content in reactively sputtered ITO thin films on glass substrates as a result of interaction with sub-15 femtosecond laser pulses in a line scan test. Second publication is published in 2011 in **Physics Procedia** and gives the results of the first investigations.

#### Publication Nr. 1: **Sub-100 nm structuring of indium-tin-oxide thin films by sub-15 femtosecond pulsed near-infrared laser light**

**Authors:** Maziar Afshar, Martin Straub, Henning Völm, Dara Feili, Karsten König, and Helmut Seidel

Accepted in *Optics Letters* (2011), **DOI:** 10.1364/OL.37.000563

**Reprinted** in PhD thesis by permission of the Journal.

**Abstract:** In magnetron sputtered indium-tin-oxide thin films of varying oxygen content, nanostructures were formed using tightly focused high-repetition rate near-infrared sub-15 femtosecond pulsed laser light. At radiant exposure well beyond the ablation threshold, cuts of 280–350 nm in width were generated. Illumination close to the ablation threshold resulted in periodic cuts of typically 20 nm in width at periodicities between 50 nm and 180 nm, as well as single sub – 20 nm cuts. Subthreshold exposure, in combination with hydrochloric acid etching, yielded nanowires of 50 nm minimum lateral dimensions.

# Sub-100 nm structuring of indium-tin-oxide thin films by sub-15 femtosecond pulsed near-infrared laser light

Maziar Afshar,<sup>1,\*</sup> Martin Straub,<sup>2</sup> Henning Voellm,<sup>1</sup> Dara Feili,<sup>1</sup> Karsten Koenig,<sup>2</sup> and Helmut Seidel<sup>1</sup>

<sup>1</sup>Institute of Micromechanics, Microfluidics/Microactuators, Faculty of Physics and Mechatronics, Saarland University, Campus A5.1, D-66123 Saarbruecken, Germany

<sup>2</sup>Institute of Biophotonics and Laser Technology, Faculty of Physics and Mechatronics, Saarland University, Campus Am Markt, Zeile 5, D-66125 Saarbruecken, Germany

\*Corresponding author: m.afshar@imm.uni-saarland.de

Received November 22, 2011; accepted December 9, 2011;  
posted December 22, 2011 (Doc. ID 158636); published February 8, 2012

In magnetron sputtered indium-tin-oxide thin films of varying oxygen content, nanostructures were formed using tightly focused high-repetition rate near-infrared sub-15 femtosecond pulsed laser light. At radiant exposure well beyond the ablation threshold, cuts of 280–350 nm in width were generated. Illumination close to the ablation threshold resulted in periodic cuts of typically 20 nm in width at periodicities between 50 nm and 180 nm, as well as single sub-20 nm cuts. Subthreshold exposure, in combination with hydrochloric acid etching, yielded nanowires of 50 nm minimum lateral dimensions. © 2012 Optical Society of America

OCIS codes: 140.3390, 140.7090, 190.4180, 310.6628, 310.7005, 320.7130.

Indium-tin-oxide (ITO), as one of the established transparent conductive oxides, is used in many devices as electrode material because of its transparency in the visible spectral range and high reflectivity at infrared wavelengths [1]. Vapor deposition of a few hundred nanometers ITO is the standard method to produce ITO films [2,3], and structuring by laser processing has largely replaced wet etching in recent years as the standard industrial method [4,5]. Earlier studies on laser structuring of ITO thin films showed a significant reduction of the threshold fluence using nanosecond pulsed UV lasers [6–8]. Femtosecond pulsed lasers further reduce collateral and substrate damage due to the delayed electron-phonon interaction, thereby providing an increase in ablation efficiency compared to excimer lasers and higher harmonics of Nd:YAG or Nd:YLF lasers [6–10].

In this Letter we report on subwavelength structuring of ITO thin film layers using sub-15 fs pulsed high-repetition rate near-infrared laser light in a wide range of intensities above and below the ablation threshold. Pulse peak intensities in the TW/cm<sup>2</sup> range at wavelengths below the absorption edge of ITO induce multiphoton absorption processes that result in structure dimensions below the optical diffraction limit. A mode-locked Ti:sapphire laser system (*Integral Pro 400, FemtoLasers*, average power 400 mW, central wavelength 800 nm) generated 10 fs pulses at a repetition rate of 85 MHz, which were chirped by a group velocity dispersion precompensation unit in order to facilitate a pulse length of 12 fs at the sample position. The beam was attenuated and passed a pair of motorized wave plates controlling its polarization. It was then deflected by two galvanometric scan mirrors and entered an inverted microscope (*Zeiss AxioObserver.D1*), where it was focused onto the sample by a Zeiss EC Plan Neofluar 40×, NA 1.3 oil immersion objective mounted on a piezoelectric actuator. In our experiments, we used linearly polarized

light at a maximum pulse energy of 300 pJ in the focal spot. Polycrystalline ITO films of a thickness of approximately 150 nm were deposited on glass cover slips (0.17 mm) by magnetron reactive DC-sputtering in a *Von Ardenne machine (type LS 730S)* using an indium-tin (90:10) compound target. The deposition in the Ar/O<sub>2</sub> plasma was optimized with respect to the crystallographic structure and the optoelectrical properties of the films. Three sorts of samples were produced with 2 sccm (ITO-2), 4 sccm (ITO-4), and 6 sccm (ITO-6) oxygen corresponding to 3.3%, 6.6%, and 10% oxygen flow ratio (total flow 60 sccm, chamber pressure 0.003 mbar). The electrical and optical properties of this *n*-type wide band gap semiconductor ( $E_g = 3.5\text{--}4.1$  eV [3,11,12]) strongly depend on the oxygen content. The samples featured a polycrystalline character in grazing incidence X-ray diffractometry (XRD) analysis with a strong peak from (222) crystal planes.

The surface morphology was studied by atomic force microscopy yielding almost identical values of rms-roughness for all three samples (Table 1). The XRD-spectra were largely independent of the oxygen concentration. By transmission and reflection UV-VIS-spectroscopy (*Cary 5000 spectrometer, Varian*), the optical properties of the ITO films were characterized. Variation of the oxygen flow resulted in a minor shift of the absorption edge from 420 nm (ITO-2) to 450 nm

**Table 1. Oxygen Flow ratio, Surface Roughness ( $R_{rms}$ ), and Electrical Resistivity ( $\rho$ ) with Temperature Coefficient ( $\alpha$ ) as Measured for ITO-2, ITO-4, and ITO-6**

O <sub>2</sub> (%)	$R_{rms}$ (nm)	$\rho$ (10 <sup>-4</sup> Ωcm)	$\alpha$ (10 <sup>-3</sup> K <sup>-1</sup> )
3.3	0.516	4.37	1.3
6.6	0.531	14	1
10	0.584	200	5

564 OPTICS LETTERS / Vol. 37, No. 4 / February 15, 2012

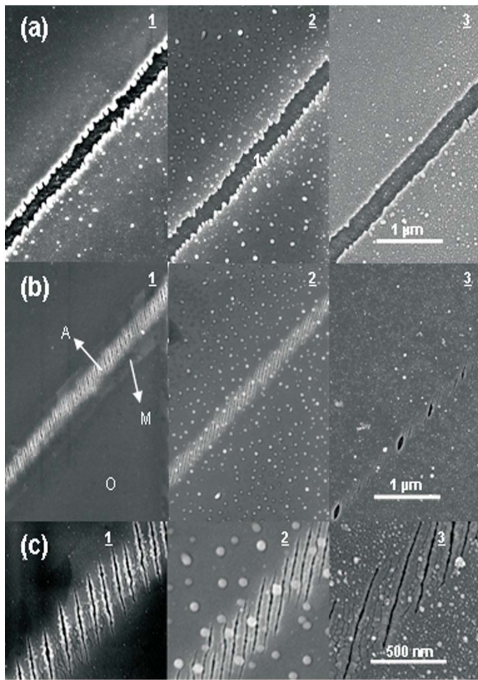


Fig. 1. (a) Grooves in ITO2 (a1), ITO4 (a2), and ITO6 (a3). (b) Periodic cuts in these samples. Three different regions are identified by “O” (original layer), “M” (modified region), and “A” (ablated region). (c) Magnified SEM images of periodic cuts.

(ITO-6), while absorption at the laser wavelengths was negligible. Thus, two- and possibly three-photon absorption dominates over single-photon absorption [13].

The ITO films were illuminated throughout the whole layer with different scan parameters. The average focal power varied between 13.5 and 25.5 mW. At each intensity, the scan speed was varied between 11.5 and 185  $\mu\text{m}/\text{s}$ . Scanning electron microscope (SEM) images revealed three different regimes of structure formation: totally ablated grooves, ablated periodic cuts, and structural modification at exposure levels below the ablation threshold (Fig. 1). In Fig. 1(b)-1, three different morphologies can be identified: region “O” corresponds to the original as-grown surface with fine grains. Region “M” indicates a modified region around the central beam region “A” of periodic or total ablation.

We studied the relationship between structural properties and the conductivity of the films. The film conductivity was examined by four point measurements. As expected [14], the electrical resistivity ( $\rho$ ) increases with oxygen content (Table 1). In tin-doped indium oxide, tin atoms replace the  $\text{In}^{3+}$  ions establishing bonds to the oxygen atoms as  $\text{Sn}^{2+}$  or  $\text{Sn}^{4+}$ . The latter act as electron donors and in combination with oxygen vacancies augment the conductivity [11,12]. Thus, the high electrical conductivity is due to a high carrier density rather than charge mobility, which is relatively low because of scattering processes [5]. In metals, thermal and electrical conductivity are related by the Wiedemann–Franz law [15], as free carriers transport both electric current

and heat. Therefore, we measured the temperature coefficient of the electrical resistance ( $\alpha$ ). All three samples have a positive  $\alpha$  (Table 1) in the range of metals [16]. The slightly higher value of ITO-2 compared to ITO-4 may be due to differences in grain size and film thickness [12]. According to their resistivity and oxygen content, ITO-2 and ITO-4 are highly degenerate with carrier densities above  $10^{20} \text{ cm}^{-3}$  [17]. Thus, thermal conductivity is a combination of free electron and phonon contributions with a decrease of about 30% from ITO-2 to ITO-6 [17]. As the phonon contribution to the thermal conductivity is constant (3.95 W/mK [17]), mainly the electronic contribution varies. Within the total ablation regime, the threshold fluence depended on the conductivity of the layer. In ITO-2, total ablation at a constant scan speed of 11.5  $\mu\text{m}/\text{s}$  required an average power of more than 25.5 mW, whereas 22 mW in ITO-4 and 18 mW in ITO-6 were sufficient. According to Table 1, an increase of the electrical resistivity of about  $0.02 \Omega \text{ cm}$  corresponds to a decrease of  $30 \text{ mJ}/\text{cm}^2$  in the threshold fluence, indicating a drop in the energy required to reach the ablation threshold temperature.

In the total ablation regime, the groove-width depends on the radiant exposure (Fig. 2(a)). In ITO-2, only at lowest scan speeds could grooves be generated at an average width of 270 nm. At intensities below the threshold of total ablation, periodic cuts are observed in each of the

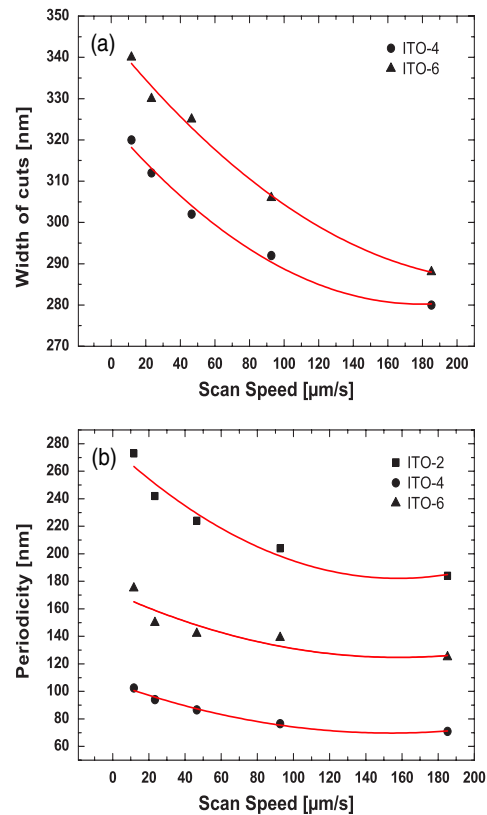


Fig. 2. (Color online) (a) Width of grooves and (b) periodicity of cuts versus scan speed.



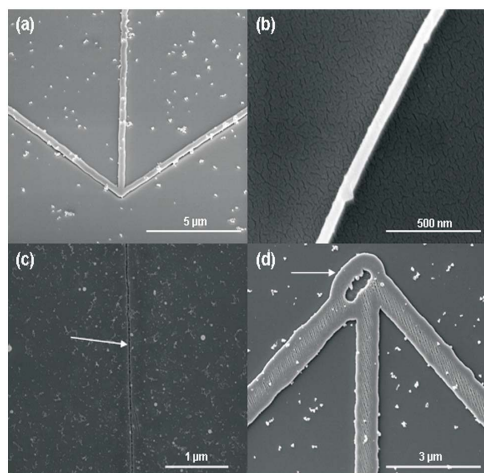


Fig. 3. (a) Modified ITO structure after etching in HCl at room temperature. (b) Nanowire produced at a transverse dimension of 50 nm. (c) Single cut of width 20 nm (length 4  $\mu\text{m}$ ). (d) Etched ITO structure featuring a groove and periodic cuts surrounded by modified regions.

films. In recent years, several theories have been developed to explain the universal phenomenon of laser induced periodic surface structures (LIPSS) on bulk semiconductors in the form of low-spatial frequency as well as high-spatial frequency structures [18–20]. Low-spatial frequency structures are observed in almost any material, but high-spatial frequency structures have been observed exclusively for laser pulse durations in the pico- and femtosecond range at fluences typically below the single-pulse ablation threshold [18–24].

The structures in our ITO films are large cuts through the whole layer at periodicities well below those known from bulk materials. These periodic cuts are perpendicular to the polarization direction of the laser light. The lowest periodicity observed is 50 nm ( $\lambda/15$ ), and the width of cuts is between 10 and 20 nm.

The periodicity depended on the scan speed, but differed between the samples (Fig. 2(b)). However, we did not study the influence of the layer thickness (ITO-2: 150 nm; ITO-4: 120 nm; ITO-6: 130 nm). At a polarization perpendicular to the scan direction, single cuts of width 20 nm were generated using intensities extremely close to the ablation threshold (Fig. 3(c)). However, they were limited in length to a few micrometers, possibly due to local inhomogeneities.

Although modified regions reveal a different texture in SEM images such as Fig. 1(b)-1, transmission electron microscopy combined with energy dispersive X-ray spectroscopy showed a higher degree of crystallinity at almost the same composition. A subsequent etching step in 37% hydrochloric acid (HCl) as a standard etchant of ITO [25] showed that the modified regions are more resistive against HCl and hence remain, whereas the original layer material is removed. This phenomenon

February 15, 2012 / Vol. 37, No. 4 / OPTICS LETTERS 565

was exploited for direct laser writing of ITO structures. Figure 3(a) demonstrates microwires of 250 nm in width, and minimum lateral dimensions down to 50 nm were achieved (Fig. 3(b)). Figure 3(d) shows extended modified regions surrounding an ablated groove after etching. The processed wires may be used as nanowaveguides in electro-optical and as nanoresonators in electromechanical chips.

We acknowledge support by the German Research Foundation (DFG) within Priority Programme 1327, as well as helpful discussions and technical assistance by Prof. K. Jacobs' research group and by Dr. K. Jilavi and G. Marchand.

#### References

1. D. C. Paine, H.-Y. Yeom, and B. Yaglioglu, in *Flexible and Flat Panel Displays* (Wiley, 2005), pp. 79–98.
2. I. Hamberg and C. Granqvist, *J. Appl. Phys.* **60**, R123 (1986).
3. S. Ray, R. Banerjee, N. Basu, A. K. Batabyal, and A. K. Barua, *J. Appl. Phys.* **54**, 3497 (1983).
4. M.-F. Chen, Y.-P. Chen, W.-T. Hsiao, and Z.-P. Gu, *Thin Solid Films* **515**, 8515 (2007).
5. H. Hartnagel, A. Dawar, A. Jain, and C. Jagadish, *Semiconducting Transparent Thin Films* (IOP Publishing, 1995).
6. O. Yavas and M. Takai, *J. Appl. Phys.* **85**, 4207 (1999).
7. J. G. Lunny, R. R. O'Neil, and K. Schulmeister, *Appl. Phys. Lett.* **59**, 647 (1991).
8. M. Y. Xu, J. Li, L. D. Lilge, and P. R. Herman, *Appl. Phys. A* **85**, 7 (2006).
9. R. Tanaka, T. Tokaoka, H. Mizukami, T. Arai, and Y. Iwai, *Proc. SPIE* **5063**, 370 (2003).
10. M. Park, B. H. Chon, H. S. Kim, S. C. Jeoung, D. Kim, J. Lee, H. Y. Chu, and H. R. Kim, *Opt. Lasers Eng.* **44**, 138 (2006).
11. S. Bashar, "Study of indium tin oxide (ITO) for novel optoelectronic devices," Ph.D. thesis (University of London, 1998).
12. J. S. Kim, F. Cacialli, A. Cola, G. Gigli, and R. Cingolani, *Appl. Phys. Lett.* **75**, 19 (1999).
13. K. Koenig, in *Handbook of Biological Nonlinear Optical Microscopy* (Oxford University, 2008), pp. 689–706.
14. H. Kim, A. Pique, J. S. Horwitz, H. Mattoussi, H. Murata, Z. H. Kafafi, and D. B. Chrisey, *Appl. Phys. Lett.* **74**, 23 (1999).
15. G. Wiedemann and R. Franz, *Ann. Phys.* **165**, 497 (1853).
16. R. B. Belser and W. H. Hicklin, *J. Appl. Phys.* **30**, 313 (1959).
17. T. Ashida, A. Miyamura, N. Oka, Y. Sato, T. Yagi, N. Taketoshi, T. Baba, and Y. Shigesato, *J. Appl. Phys.* **105**, 073709 (2009).
18. M. Birnbaum, *J. Appl. Phys.* **36**, 3688 (1965).
19. H. M. Van Driel, J. E. Spie, and J. F. Young, *Phys. Rev. Lett.* **49**, 1955 (1982).
20. A. Borowiec and H. K. Haugen, *Appl. Phys. Lett.* **82**, 4462 (2003).
21. N. Yasumaro, K. Myazaki, and J. Kiuchi, *Appl. Phys. A* **76**, 983 (2003).
22. R. Le Harzic, D. Doerr, D. Sauer, M. Neumeier, M. Apple, H. Zimmermann, and F. Stracke, *Opt. Lett.* **36**, 229 (2011).
23. F. Costache, S. Kouteva-Arguirova, and J. Reif, *Appl. Phys. A* **79**, 1429 (2004).
24. J. Bonse, M. Muz, and H. Sturm, *J. Appl. Phys.* **97**, 013538 (2005).
25. M. Inoue, T. Matsuoka, Y. Fujita, and A. Abe, *Jpn. J. Appl. Phys.* **28**, 274 (1989).

Publication Nr. 2: **Efficient Nanostructure Formation on Silicon Surfaces and in Indium Tin Oxide thin Films by sub-15 fs pulsed near-infrared Laser Light**

**Authors:** Martin Straub, Maziar Afshar, Dara Feili, Helmut Seidel, and Karsten König

Accepted in *Lasers in Manufacturing* (2011), DOI: 10.1016/j.phpro.2011.03.100

**Reprinted** in PhD thesis by permission of the Journal.

**Abstract:** High-repetition rate sub-15 fs pulsed near-infrared laser light facilitates production of self-assembled nanostructures on surfaces of crystalline silicon and in thin indium tin oxide films. Ripples at a periodicity of 130–140 nm as well as random nanopore arrangements were induced on Si(100) surfaces by scanning a high-numerical aperture focal spot in water across a predefined area. In indium tin oxide films periodic parallel cuts as well as single sub-20 nm cuts were generated at pulse energies less than 0.3 nJ. Nanowires of 150–300 nm in diameter were fabricated by laser annealing and subsequent hydrochloric acid etching.



Available online at [www.sciencedirect.com](http://www.sciencedirect.com)

Physics Procedia 12 (2011) 16–23

Physics

**Procedia**

LiM 2011

## Efficient Nanostructure Formation on Silicon Surfaces and in Indium Tin Oxide thin Films by sub-15 fs pulsed near-infrared Laser Light

Martin Straub<sup>a,\*</sup>, Maziar Afshar<sup>b</sup>, Dara Feili<sup>b</sup>, Helmut Seidel<sup>b</sup>, Karsten König<sup>a</sup><sup>a</sup>Department of Biophotonics and Laser Technology, Faculty of Physics and Mechatronics, Saarland University, Campus Am Markt, Zeile 5, D-66125 Saarbrücken, Germany<sup>b</sup>Department of Micromechanics, Microfluidics, and Microactuators, Faculty of Physics and Mechatronics, Saarland University, Campus A5.1, D-66123 Saarbrücken, Germany

---

### Abstract

High-repetition rate sub-15 fs pulsed near-infrared laser light facilitates production of self-assembled nanostructures on surfaces of crystalline silicon and in thin indium tin oxide films. Ripples at a periodicity of 130 - 140 nm as well as random nanopore arrangements were induced on Si(100) surfaces by scanning a high-numerical aperture focal spot in water across a predefined area. In indium tin oxide films periodic parallel cuts as well as single sub-20 nm cuts were generated at pulse energies less than 0.3 nJ. Nanowires of 150 - 300 nm in diameter were fabricated by laser annealing and subsequent hydrochloric acid etching.

*Keywords:* sub-15 fs laser pulses; sub-100 nm structures; crystalline silicon, indium tin oxide; self-organization, surface ripples; nanowires

---

### 1. Patterning of surfaces and thin films by high-repetition rate sub-15 femtosecond pulsed laser light

Laser material processing such as cutting, drilling, welding, soldering, or polishing relies typically on high-power lasers such as continuous wave CO<sub>2</sub> or pulsed Nd:YAG lasers and, hence, on thermal processes which result in large melted zones due to massive heat diffusion [1]. In contrast, ultrashort pulsed lasers can produce extremely fine structures, as electronic excitation faster than the heat transport by lattice vibrations allows for optimum concentration of energy and spatial limitation of ablation. Moreover, nonlinear processes such as multiphoton absorption can be triggered by high focal peak intensities. Thus, structures of controlled shape and size can be manufactured at sub-wavelength resolution by scanning the focal spot of a high-numerical aperture objective along arbitrary pathways. Even finer features of sub-100 nm size can be generated from self-organization processes which require intensities near the threshold of material change. Self-assembly of periodic ripples on silicon surfaces has been under scrutiny since many decades [2-15], but ripple periodicities of 100 nm or below were investigated intensively only in recent years as their generation requires femto- or picosecond pulsed laser light [8-15]. By high-

---

\* Corresponding author. Tel.: +49-681-302-70458; Fax: +49-681-302-70452.  
E-mail address: [m.straub@blt.uni-saarland.de](mailto:m.straub@blt.uni-saarland.de)

resolution laser scanning such self-organized nanostructures can be produced in targeted areas of sub-micron size. Here, we study the formation of rifts and ripples on Si(100) surfaces, which were generated at periodicities of 130 - 140 nm by tightly focusing high-repetition rate 12-fs pulsed Ti:sapphire laser light onto the samples. We also examine random nanoporous surface structures, which were established at fluences well beyond the ablation threshold.

Precise ablation as well as modification of indium tin oxide (ITO) by laser illumination is of high importance, as ITO is a transparent conductor, which is frequently used as electrode material in electronic displays [16-22]. Using sub-15 fs pulsed laser light cuts were generated in thin ITO films ranging in size from a few 100 nm down to less than 20 nm. We also produced self-assembled arrangements of periodic parallel cuts. At lowest exposure levels traces were scanned in the ITO films which were converted into nanowires of 150 - 300 nm in diameter by subsequent etching with hydrochloric acid. Our article demonstrates that sub-15 fs pulsed near-infrared laser light facilitates the efficient manufacture of a large variety of sub-micron and even sub-100 nm structures from materials of high technological relevance.

## 2. Experimental

Figure 1 presents the setup for nanostructure formation by 12-fs pulsed laser light. Pulses from a FemtoLasers Integral Pro 400 mode-locked Ti:Sapphire laser (centre wavelength 800 nm, pulse length 10 fs, repetition rate 85 MHz) are pre-chirped in a pre-compensation unit. The attenuated beam is redirected by a galvanometric scanner and expanded by a telescope (JenLab GmbH, Jena, Germany). In the inverted microscope (Zeiss AxioObserver.D1) it is focused onto the sample by a Zeiss EC Plan Neofluar 40x, NA 1.3 oil immersion objective mounted on a vertical piezoelectric translation stage (piezosystem jena GmbH).

The inset of Figure 1 illustrates the arrangement of samples on the microscope. Si(100) samples were structured with water on the surface in a line scan mode (focal power 24 mW, scan speed 150  $\mu\text{m/s}$ , 20 repetitions/line, scan direction:  $\langle 110 \rangle$ ) or an area scan mode (focal power 7.8 - 14.0 mW, area processing speed 0.67 - 230  $\mu\text{m}^2/\text{s}$ ) using linearly polarized light of varying direction. Before and after removal of silicon dioxide by hydrofluoric acid etching (6% HF in water, duration 3 min) the samples were examined in by scanning electron microscopy (SEM) in an FEI Helios NanoLab DualBeam 600 SEM/FIB workstation which also facilitated energy-dispersive X-ray spectroscopy (EDX). In addition, slices were cut perpendicular to the Si(100) surface by focused ion beam (FIB) milling and analysed by transmission electron microscopy (TEM).

Polycrystalline ITO films at thicknesses of approximately 150 nm were deposited by reactive direct current sputtering (Von Ardenne GmbH, Dresden, type: LS 730 S) at a pressure of 0.003 mbar in an Ar/O<sub>2</sub> plasma and optimized with respect to their crystallographic structure. X-ray diffractometry analysis showed a strong (222)-peak for films sputtered on glass coverslips, which were then mounted onto a special object carrier. Atomic force microscopy analysis yielded a surface rms-roughness of 5 nm. The samples were illuminated from the back side through the coverslips. Single lines were scanned at a focal power of 13.5 - 25.5 mW varying the direction of polarization. Scan times ranged from 12 ms to 3 s. Above-threshold fluences were used for material ablation, whereas films were modified at sub-threshold fluences. ITO nanowires evolved from the annealed regions on etching the films with hydrochloric acid (37% HCl at 25°C).

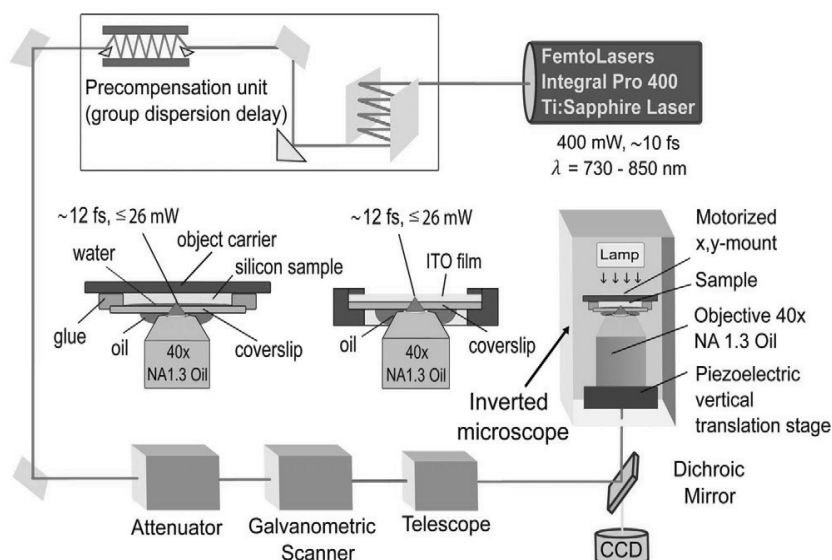


Figure 1. Setup for nanostructure formation by high-repetition rate sub-15 fs pulsed near-infrared laser light. Pulses are pre-chirped in a precompensation unit, pass an attenuator and are scanned across the sample by a galvanometric scanner. Inset: The laser light is focused onto the sample via a high-numerical aperture oil immersion objective. Silicon samples are mounted on an object carrier and exposed with a thin film of water on their surface, whereas ITO films are scanned through the coverslips which they were deposited on.

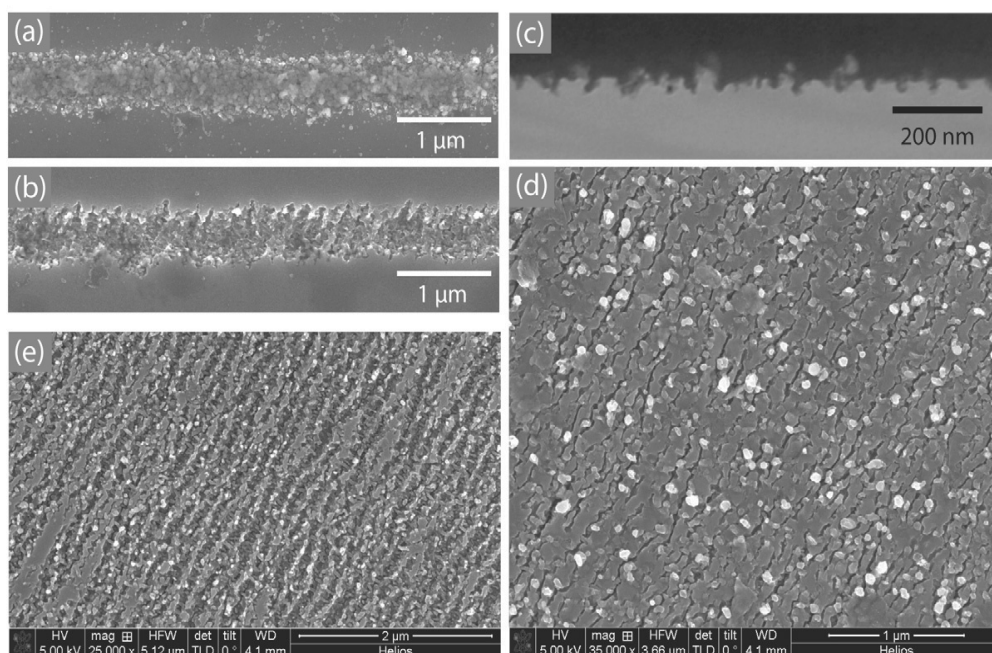


Figure 2. (a) Laser-induced line structure on Si(100) surface before hydrofluoric acid etching. The line trace is covered by oxide particles; (b) The same trace after HF etching reveals rifts at a period of 130 nm. The rifts are perpendicular to the laser polarization; (c) TEM image of a FIB section through periodic rifts generated at near-threshold intensity; (d) SEM image of Si(100) surface rift patterns; (e) At slightly more intense illumination the rifts widen and expand across an increasingly large surface area.

### 3. Results and discussion

Line structures as well as planar structures were produced on Si(100) surfaces. As the structures were generated with water on the silicon surface, a major fraction of the ablated material was oxidized during ejection from the exposed area. Figure 2(a) shows the SEM image of a scanned line trace which is completely covered with small particles. EDX measurements suggest that they are mainly formed from silicon dioxide, as the oxygen  $K_{\alpha}$ -line exceeds the Si- $K_{\alpha}$  emission line in intensity [15]. Figure 2(b) shows the same scanned line trace after removal of the oxidized material by hydrofluoric acid etching. The SEM image reveals parallel rifts in the silicon surface along the edge of the trace at a period of approximately 130 nm. The rifts are oriented perpendicular to the polarization of the infrared laser beam, which was linearly polarized at an angle of  $23^{\circ}$  with respect to the line direction. In the central area of the trace a random nanoporous surface structure is observed (not fully resolved), which is characteristic for surface regions exposed to intensities well beyond the ablation threshold.

The same features result from area scans. At near-threshold intensities Si(100) surfaces are patterned densely with tiny rifts at an average spacing of 130 - 140 nm. While Figure 2(d) presents an SEM top view image, the TEM image in Figure 2(c) of a FIB section through such a surface reveals that the rifts are 20 - 50 nm wide and 50 - 70 nm deep. The bright spots in the SEM image indicate particles which mainly consist of silicon. For slightly higher fluences the rifts widen and consume an increasingly large area of the surface. Figure 2(e) displays such a more

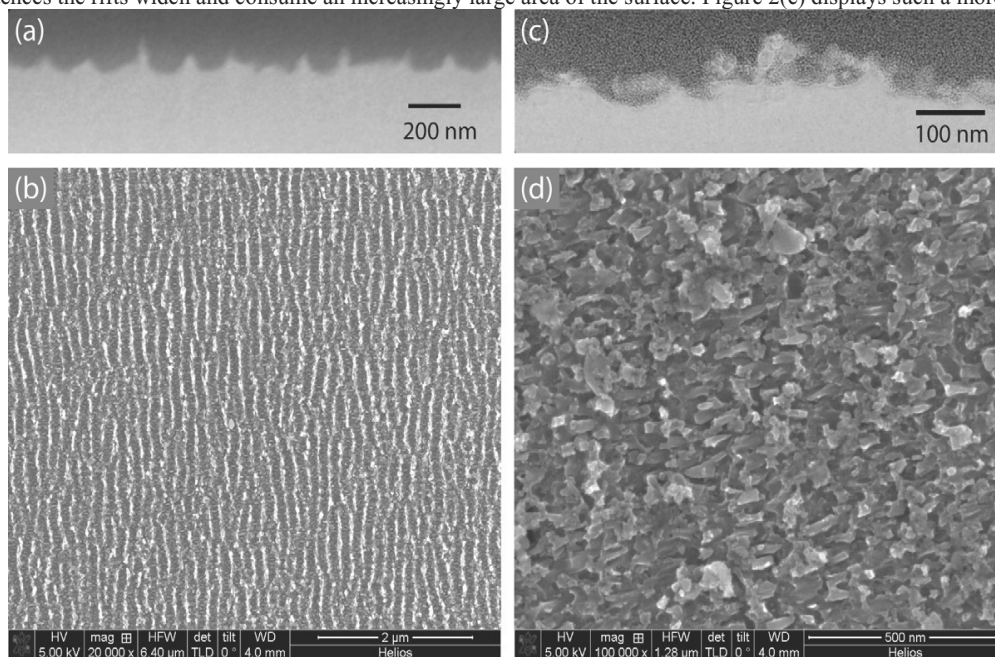


Figure 3. (a) Silicon surface ripples generated at near-threshold intensity (FIB section, TEM transmission image); (b) SEM top view of the periodic ripple arrangement. The ripples are perpendicular to the laser polarization; (c) nanoporous silicon surface generated at a focal intensity well beyond the ablation threshold (FIB section, TEM transmission image); (d) SEM top view of the nanoporous surface structure.

advanced stage in the self-assembly of a periodic surface structure. In some areas rifts are broad and already start to turn into a nanoporous arrangement, whereas other parts of the silicon surface are still unchanged. Figure 3(b) shows periodic ripples on the Si(100) surface, which were generated on further increase of the fluence. Under these conditions rifts widened to an extent that ripple patterns cover the entire surface. The TEM image of a FIB section through this sample [Figure 3(a)] demonstrates that the ripples are 20 - 40 nm in width and approximately 70 nm in height. The average spacing between the ripples is 140 nm. In agreement with the orientation of rifts ripples are oriented perpendicular to the polarization. On increase of the fluence to values well beyond the ablation threshold ripple patterns disappear, and a random nanoporous structural arrangement is established. Figure 3(d) shows an

example of such a surface structure. Structural elements typically have a width of 20 nm or beyond and are elongated in the direction of polarization. We call this structure nanoporous, as structural elements are arranged on the surface in a way that tiny pores of less than 20 nm in diameter are generated between as well as underneath them. The transmission electron image of the FIB section through such a surface is shown in Figure 3(c). The TEM image unambiguously demonstrates the existence of sub-20 nm pores at the surface. However, the exact size, their length, as well as the direction of the pores are largely uncontrolled.

Indium tin oxide films were structured from the back side of the glass substrate throughout the whole layer. At intensities well beyond the ablation threshold straight cuts of a size of 250 - 500 nm were generated dependent on the scan speed. Figure 4(a) shows an SEM image of a cut which was produced in a single-line scan at an average focal power of 24 mW and a scan speed of 200  $\mu\text{m/s}$ . The width of the ablated line trace is modulated at a period of approximately 215 nm. Some debris appears on the surface due to processing under atmospheric pressure, which can be removed in a subsequent cleaning step. Figure 4(b) plots the dependence of the average width of cuts on the scan time required to generate a cut of 35  $\mu\text{m}$  in length with the laser polarization perpendicular to the scan direction (focal power 24 mW). At near-threshold intensities much finer cuts were generated periodically at an orientation close to the polarization direction. Figure 4(c) shows an example of such a self-assembled array of cuts, which was produced by single-line scans in two orthogonal scan directions. The cuts feature an average structural periodicity of 70 nm with their width ranging down to below 20 nm. They overlap perfectly at the crossing of scanned lines.

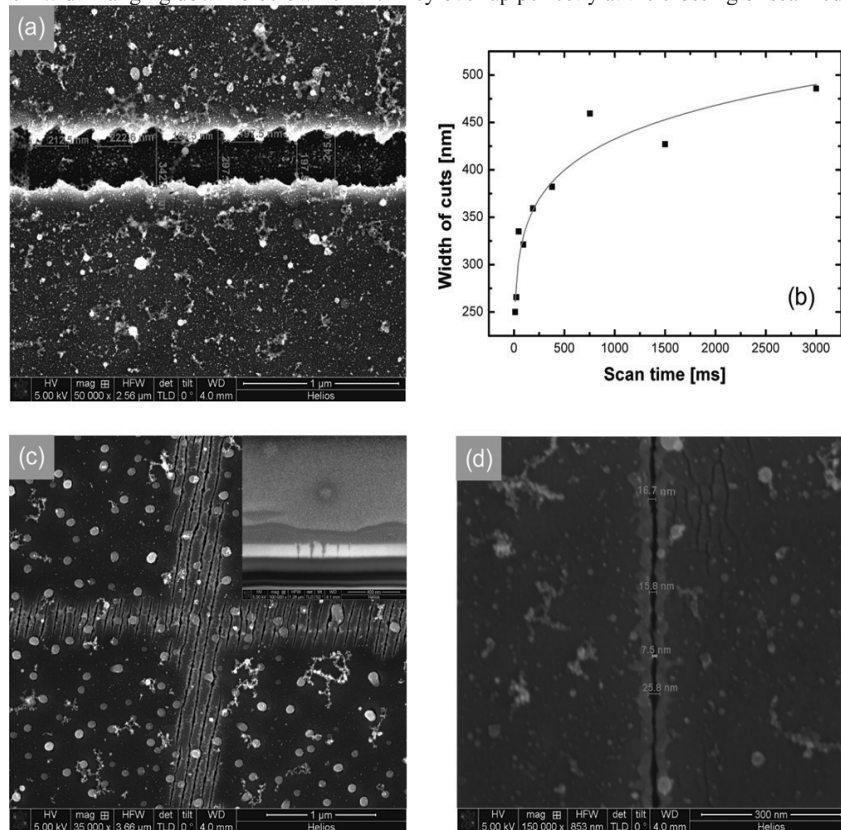


Figure 4. (a) SEM image of a cut in an ITO film on glass. The polarization was perpendicular to the scan direction; (b) Width of cuts generated at an average focal power of 24 mW as a function of the scan time (polarization perpendicular to scan direction). (c) SEM image of periodic cuts obtained by two orthogonal line scans with polarization nearly parallel (vertical line) and perpendicular (horizontal line) to the scan direction, inset: periodic cuts in ITO-film as seen in TEM image of FIB section perpendicular to the scan direction; (d) SEM image of a single cut of sub-20 nm width generated at an intensity of 19.5 mW.

SEM analysis of focused ion beam sections through some cuts revealed vertical walls across the entire layer down to the substrate [inset of Figure 4(c)]. A single-cut regime is observed for slightly less intense illumination. Under these conditions single cuts of an average width of less than 20 nm can be produced. Figure 4(d) shows an example of such a cut, which was generated at an average focal power of 19.5 mW applying a scan speed of 290 mm/s.

On reduction of the intensity below the ablation threshold the exposed areas of the polycrystalline ITO films are transformed into a different phase which is more resistive against etching in hydrochloric acid. This modified region appears in SEM images as a contrast (not shown). The SEM micrograph of Figure 5(a) shows a section of a line trace generated at an intensity of 17 mW and a scan speed of 47  $\mu\text{m/s}$ , which emerges as a 300 nm wide nanowire after etching in hydrochloric acid. The width of the nanowires can be minimized down to the grain size of ITO. Figure 5(b) shows the SEM image of four traces of about 150 nm in width, which were produced at a higher scan speed of 350  $\mu\text{m/s}$  with the polarization close to the scan direction. In Figure 5(c) the magnified section of the third trace demonstrates that the narrowest nanowires consist of a chain of ITO grains. It was verified by energy dispersive X-ray spectroscopy analysis (not shown) that the film composition remains unchanged by the laser illumination. Further studies are required to investigate the electrical and mechanical properties of the ITO nanowires.

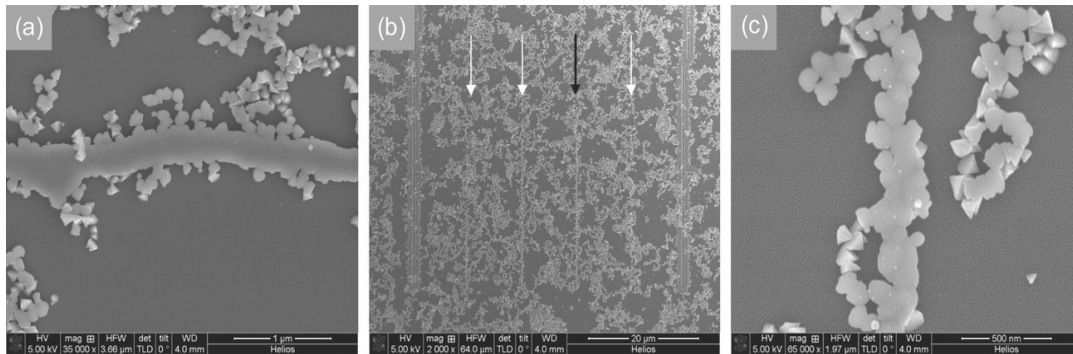


Figure 5. (a) SEM image of a 300 nm wide nanowire generated at 17 mW focal power (scan speed 47  $\mu\text{m/s}$ ) and subsequent etching in HCl; (b) Sequence of traces illuminated at lower fluences followed by a short etch; (c) SEM image of a 150-nm nanowire consisting of a chain of ITO grains recorded at higher magnification [see black arrow in panel (b)]. Nanowires were produced with the polarization close to the scan direction.

Self-assembly of nanostructures by high-intensity laser light is generally described as a process in which laser-induced changes of material properties modify the effective intensity distribution, which then induces further material change. The generation of a laser plasma is a complex process which has been the subject of intense research during the past decades [23]. Laser ablation frequently involves avalanche ionization, as electrons in the conduction bands are accelerated by the electrical field of the laser light and collide with valence band electrons. Thereby, plasma of increasing density is generated which absorbs the laser pulses completely within an extremely small volume, as the plasma frequency approaches the laser frequency. The plasma density and dynamics result in the observed ablation patterns. Charge carriers that seed the avalanche ionization can be generated in silicon by single-photon absorption due to its band gap of 1.1 eV, whereas in ITO the high dopant electron density can be exploited possibly assisted by multiphoton excitation of carriers from the valence band.

Our results demonstrate that sub-15 fs pulses facilitate material ablation from silicon surfaces and ITO films at extremely low average intensities due to optimum confinement of excitation. Sub-100 nm and even sub-20 nm structural features were readily generated. We point out that cuts of a width of the order of 10 nm by far exceed the precision which is currently achieved both in mechanical and conventional laser material processing. The potential to generate extremely fine cuts is also of utmost importance for applications in biology and medicine such as laser transfection of cells and nanosurgery [24–27]. Conducting nanowires may find applications in microelectronics, sensor technology, and microoptics as well as microoptoelectromechanical systems. Periodically nanostructured and nanoporous surfaces with unusual optical, mechanical, and electronic properties may enable biomedical applications such as novel cell substrates as well as technical applications. In conclusion, sub-15 fs pulsed high-repetition rate

near-infrared laser light appears to be a highly useful processing tool, which promises the efficient manufacture of surface features of the order of 100 nm or below in a wide variety of materials.

### Acknowledgements

The authors would like to thank Christoph Pauly (Saarland University, Department of Functional Materials / Material Science) for recording SEM images, Jörg Schmauch (Department of Technical Physics) for recording TEM images, as well as Karin Jacobs (Department of Soft Condensed Matter Physics), Henning Völm (Department of Micromechanics, Microfluidics, and Microactuators) and Günter Marchand (Saarland University, Microtechnology Transfer Centre) for their assistance.

This work was supported by the German Science Foundation (DFG) within the project “Generation of sub-100 nm structures by sub-15 femtosecond laser microscopy”, which is part of the Priority Programme 1327 “Optically induced sub-100 nm structures for biomedical and technical applications”.

### References

- [1] Bäuerle, D.: *Laser Processing and Chemistry*. Springer, Berlin, 2000.
- [2] Birnbaum, M.: Semiconductor surface damage produced by ruby lasers. *J. Appl. Phys.* 36 (1965), 3688 - 3689.
- [3] Fauchet, P. M.; Siegman, A. E.: Surface ripples on silicon and gallium arsenide under picosecond laser illumination. *Appl. Phys. Lett.* 40 (1982), 824 - 826.
- [4] McCulloch, D. J.; Brotherton, S. D.: Surface roughness effects in laser crystallized polycrystalline silicon. *Appl. Phys. Lett.* 66 (1995), 2060 - 2062.
- [5] Singh, A. P.; Kapoor, A.; Tripathi, K. N.; Kumar, G. R.: Laser damage studies of silicon surfaces using ultra-short laser pulses. *Opt. Laser Technol.* 34 (2002), 37 - 43.
- [6] Tan, B.; Venkatakrishnan, K.: A femtosecond laser-induced periodical surface structure on crystalline silicon. *J. Micromech. Microeng.* 16 (2006), 1080 - 1085.
- [7] Guillermin, M.; Garrelie, F.; Sanner, N.; Audouard, E.; Soder, H.: Single- and multi-pulse formation of surface structures under static femtosecond irradiation. *Appl. Surf. Sci.* 253 (2007), 8075 - 8079.
- [8] Jost, D.; Lüthy, W.; Weber, H. P.; Salathé, R. P.: Laser pulse width dependent surface ripples on silicon. *Appl. Phys. Lett.* 49 (1986), 625 - 627.
- [9] Costache, F.; Kouteva-Arguitova, S.; Reif, J.: Sub-damage-threshold laser ablation from crystalline silicon: surface nanostructures and phase transformation. *Appl. Phys. A* 79 (2004), 1429-1432.
- [10] Daminelli, G.; Krüger, J.; Kautek, W.: Femtosecond laser interaction with silicon under water confinement. *Thin Solid Films* 467 (2004), 334 - 341.
- [11] Le Harzic, R.; Schuck, H.; Sauer, D.; Anhut, T.; Riemann, R.; König, K.: Sub-100 nm structuring of silicon by ultrashort laser pulses. *Opt. Express* 13 (2005), 6651 - 6656.
- [12] Wagner, R.; Gottmann, J.; Horn, A.; Kreutz, E. W.: Subwavelength ripple formation induced by tightly focused femtosecond laser irradiation. *Appl. Surf. Sci.* 253 (2006), 8576 - 8579.
- [13] König, K.; Bauerfeld, F.; Sauer, D.; Schuck H.; Uchugonova, A.; Lei, E. et al.: Femtosecond laser nanomachining of silicon wafers and two-photon nanolithography for stem cell research. In: S. Kawata, H. Masuhara and F. Tokunaga (eds.): *Handai Nanophotonics: Nano Biophotonics: Science and Technology*. Volume 3. First edition. Elsevier, 2007, pp. 287-296. ISBN-13: 978-0-444-52878-0
- [14] Schade, M.; Varlamova, O.; Reif, J.; Blumtritt, H.; Erfurth, W.; Leipner, H. S.: High-resolution investigations of ripple structures formed by femtosecond laser irradiation of silicon. *Anal. Bioanal. Chem.* 396 (2010), 1905 - 1911.
- [15] Straub, M.; König, K.: Nanostructure formation on silicon surfaces by high repetition-rate sub-15 femtosecond near-infrared laser pulses. *Proc. SPIE Vol. 7920* (2011), in press.
- [16] Takai, M.; Bollmann, D.; Habberger, K.: Maskless patterning of indium tin oxide layer for flat panel displays by diode-pumped Nd:YLF laser irradiation. *Appl. Phys. Lett.* 64 (1994), 2650 - 2562.
- [17] Yavas, O.; Takai, M.: High-speed maskless laser patterning of indium tin oxide thin films. *Appl. Phys. Lett.* 73 (1998), 2558 - 2560.
- [18] Hosono, H.; Kurita, M.; Kawazoe, H.: Excimer laser crystallization of amorphous indium-tin oxide thin films and application to fabrication of Bragg gratings. *Thin Solid Films* 351 (1999), 137 - 140.
- [19] Tanaka, R.; Takaoka, T.; Mizukami, H.; Arai, T.; Iwai, Y.: Laser etching of indium tin oxide thin films by ultra-short pulsed laser. *Proc. SPIE* 5063 (2003), 370 - 373.
- [20] Park, M.; Chon, B. H.; Kim, H. S.; Jeoung, S. C.; Kim, D.; Lee J.-I.; Chu, H. Y.; Kim, H. R.: Ultrafast ablation of indium tin oxide thin films for organic light-emitting diode application. *Opt. Lasers Eng.* 44 (2006), 138 - 146.
- [21] Chen, M.-F.; Chen, Y.-P.; Hsiao, W.-T.; Gu, Z.-P.: Laser direct write patterning of indium tin oxide films. *Thin Solid Films* 515 (2007), 8515 - 8518.

- [22] Afshar, M.; Saremi, S.; Völlm, H.; Feili, D.; Seidel, H.; Straub, M.; Zhang, H.; König, K.: Multiphoton lithography and ITO structuring by high repetition-rate sub-15 femtosecond laser pulses. *Proc. SPIE Vol. 7920* (2011), in press.
- [23] Mulser, P.; Bauer, D.: *High Power Laser-Matter Interaction*. Springer, Berlin, Heidelberg, 2010, and references therein.
- [24] Tirlapur, U. K.; König, K.: Targeted transfection by femtosecond laser. *Nature* 418 (2002), 290 - 291.
- [25] Uchugonova, A.; König, K.; Bückle, R.; Isemann, A.; Tempea, G.: Targeted transfection of stem cells with sub-20 femtosecond laser pulses. *Opt Express* 16 (2008), 9357 - 9364.
- [26] König, K.: Femtosecond Laser Nanoprocessing. In: P. So and B.R. Masters (eds.): *Handbook of Biological Nonlinear Optical Microscopy*. Oxford University Press, 2008, pp. 689-706. ISBN 987-0-19-516260-8
- [27] König, K.; Riemann, I.; Fischer, P.; Halbhuber, K. J.: Intracellular nanosurgery with near infrared femtosecond laser pulses. *Cell. Mol. Biol.* 45 (1999), 195-201.



## 4.2 Simulation Based Application Design

After the first successful experiments on the interaction of sub-15 fs laser pulses (85 MHz repetition rate) with sputtered ITO layers on glass and after an optimization of structures, several ideas for different applications came up. The periodic nanocuts were applied to ITO bioelectrodes to modify the surface and to change their impedance. ITO crystallization via laser writing was applied to generate nanowire gas sensors with self-heating effect. Such nanowires were also realized as freestanding structures, which can be applied for different applications. These three ideas and the principles of each application are shortly introduced in this Chapter.

The finite element method (FEM) was used to model the functionality of the elements and to optimize the geometrical dimensions of the design with respect to the expected physical behavior. FEM is a numerical method for solving partial differential equations and is commonly used in the development of MEMS and NEMS. It is based on breaking a model into a finite number of domains (meshing), which are interconnected via continuity equations concerning the physical properties under inspection. The differential equations are then solved for the respective meshed elements in a continuous way. Direct solution methods, such as Gaussian elimination, can be used with a relatively small number of elements. However, in general, iterative methods are used, asymptotically approaching the solution of the whole system. The advantage of FEM compared to other numerical methods is its broad applicability and accuracy. The division into elements is done by cross-linking (meshing) of the system. This procedure is usually done by an automated algorithm that is already implemented in the FE-software. However, the user can influence the shape of the network. As can be expected, a finer mesh generally improves the quality of the simulation results at the cost of increasing computation time and performance. Several FEM software packages are available. In this work COMSOL Multiphysics was used.

A model for the FE-simulation is generated gradually. First, the physics needs to be determined, that is, what physical parameters are to be simulated in the model. The geometry can then be set up either directly in COMSOL Multiphysics or it can be imported from a finished CAD model. Next, material properties must be attributed to each component, representing a domain. COMSOL Multiphysics already contains the physical parameters of many materials, but they can also be changed and entered manually, if necessary. The next important step is setting up the boundary conditions, without which the differential equations cannot be solved. The meshing (cross-linking) of the model is possible by different methods. In COMSOL Multiphysics a network in tetrahedral shape is selected by default, based on the physics of the model. It is also possible to generate a sweep mesh, wherein the surface is cross-linked, and the network elements are parallel in the third dimension, which can favorably be used for thin layers. The numerical solver is automatically selected from COMSOL Multiphysics. In general, it is an iterative solver for larger three-dimensional simulations. In this work, FE-simulations were particularly used for determining the following points:

- electrical field simulations on the nanostructured ITO electrodes and their passivation effect using SU8 layer
- relationship between the measured voltage and the resulting Joule heating of the nanowire in gas sensors.
- time dependent thermoelectrical and mechanical simulations for the freestanding ITO nanowires.

## 4.3 On-Chip Nanostructuring and Impedance Trimming of ITO electrodes

### 4.3.1 Introduction

The electrodes play a crucial role in biomedical applications. They act as an interface between the electronic circuitry and the biological medium and connecting the electron conductive system to the ionic conducting system. Bioelectrodes are typically used for stimulation or biosignal sensing. Reducing the impedance of the electrode improves the signal to noise ratio in sensing mode and reduce the required potentials for stimulation mode. Biosignals are in the range of millivolts to microvolts. Therefore, a low impedance electrode is required to achieve a satisfactory signal to noise ratio. Furthermore, to stimulate an organ or a cell, certain current density is needed and if the electrode has high impedance, higher potential is required, which could lead to chemical reaction between electrode and electrolyte and produce toxic compounds. Smaller stimulation voltage enhances the energy coupling at working frequencies and avoids toxic reactions at electrode-electrolyte interface [167].

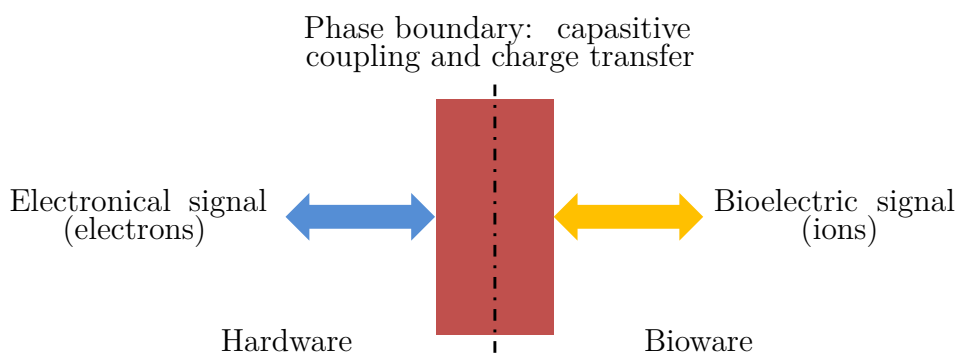


**Figure 4.2:** Schematic diagram of a biomedical electrode.

Nowadays the bioelectrodes are used for *in vivo* and *in vitro* applications. For all these applications the bioelectrodes must satisfy certain requirements. Most importantly, they must be biocompatible and biostable. In the literature, structural biocompatibility is often distinguished from surface biocompatibility. Structural biocompatibility includes the compatibility of the bioelectrode with the biomechanical properties of target organ, tissue or cell. Surface biocompatibility describes the physical, chemical, biological and morphological interactions between the surface of the bioelectrode and the biological material. Non-toxicity is a key requirement of biocompatibility.

Multielectrode arrays (MEA) are a special and common form for electrodes in biomedical engineering. In general, a MEA is considered as an array of electrodes. MEAs are used both for stimulation and for recording electrical activity of biological cells. These electrodes are produced in both planar (2D) and 3D format. Planar electrodes are mostly used for *in vitro* tests. The cells cover the electrode surface completely or only partially. In this way isolated single cells can be examined.

Typical electrode materials are metals (Au, Pt), carbon (graphite), and semiconductors (Si, indium-tin-oxide). Ion-conducting electrolytes are mostly solutions of dissolved  $H^+$ ,  $Na^+$ ,  $Cl^-$  ions in aqueous or non-aqueous solutions.

At the phase boundary a potential difference between the electrode and the electrolyte can be observed. Ions from the electrolyte phase adhere to the electrode surface and form a so-called "Helmholtz" double layer. This double layer can be subdivided into an inner Helmholtz layer formed by partially solvated ions adhering directly to the surface and into an outer Helmholtz layer formed by totally solvated ions. Because of this charge distribution, the double layer is like a capacitor with a large capacity [168]. In Fig. 4.3 the Helmholtz model of the double layer is shown schematically.

The capacitance per unit area (specific capacity) according to the Helmholtz model is calculated for planar electrodes according to [169]:

$$C_{\text{Helmholtz}} = \frac{\epsilon_0 \epsilon_r}{H}, \quad (4.1)$$

with  $\epsilon_0$  and  $\epsilon_r$  the free space and relative permittivity of the electrolyte solution, and  $H$  the thickness of the Helmholtz double layer.  $H$  can be approximated by the radius of the solvated ions.

Gouy and Chapman developed a model that takes the mobility of the ions in the electrolyte into account. Due to diffusion processes and electrostatic forces between the ions, a diffuse double layer (Gouy-Chapman layer) is defined. The equilibrium concentration of the ions is defined by the Boltzmann distribution [169] and can be described by the Poisson-Boltzmann equation [169]:

$$\Delta \cdot (\epsilon_0 \epsilon_r \nabla \psi) = 2zeN_A c_\infty \sinh\left(\frac{ze\psi}{k_B T}\right), \quad (4.2)$$

with  $z$  the valency of the ions,  $e$  the elementary charge,  $N_A$  the Avogadro constant,  $c_\infty$  the molar concentration of ions in the electrolyte solution,  $\lambda_D$  the Debye length,  $\psi$  the local electric potential in the diffuse layer,  $k_B$  the Boltzmann constant, and  $T$  the absolute temperature. A schematic representation of the Gouy-Chapman model and the potentials according to Eq. 4.2 can be seen in Fig. 4.3.

From Eq. 4.2, the specific capacity of the diffuse double layer for a planar electrode is obtained by [169]:

$$C_{\text{Diffus}} = \frac{4zeN_A c_\infty \lambda_D}{\psi_D}, \quad (4.3)$$

for symmetric electrolytes  $\lambda_D = (\epsilon_0 \epsilon_r k_B T) / (\sqrt{2e^2 z^2 N_A c_\infty})$ .

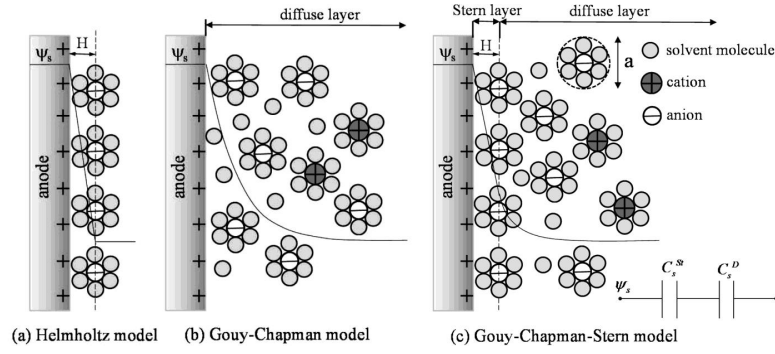


**Figure 4.3:** Schematic representation of the different models for the description of the electrochemical double layer at the phase boundary electrode/electrolyte. In addition, the trend of potentials is shown [169].

Stern made a combination of the Helmholtz model adhering to the surface of the electrode and the diffuse Gouy-Chapman model. Therefore, the potential in the electrochemical double layer can be expressed as [169]:

$$\nabla \cdot (\epsilon_0 \epsilon_r \nabla \psi) = \begin{cases} 0 & \text{in the Stern layer,} \\ 2zeN_A c_\infty \sinh\left(\frac{ze\psi}{k_B T}\right) & \text{in the diffuse layer.} \end{cases} \quad (4.4)$$

Due to a finite size of ions and their arrangement, the Poisson-Boltzmann equation can be modified with "packing parameters"  $\nu = \frac{2c_\infty}{c_{\max}}$ , where  $c_{\max}$  is the maximum ion concentration, which is calculated assuming a cubic arrangement of the ions with a diameter of  $c_{\max} = \frac{1}{N_A a^3}$ . Hence, the specific double layer capacitance can be calculated as follows [169]:

$$C = \frac{2zeN_A c_\infty \lambda_D}{\psi_D} \sqrt{\frac{2}{\nu} \log\left(1 + 2\nu \sinh^2\left(\frac{ze\psi_D}{2K_B T}\right)\right)}. \quad (4.5)$$

The charge transport in and through the phase boundary is limited by various charge transfer mechanisms, which can be divided into three types.

- Non-faradaic current by low voltages and small amount of charge occur through a charge reversal in boundary layer and with a very low charge penetration.
- Faradaic current by redox reactions and tunneling (charge transfer) of the generated electrons through the boundary layer into the electrodes.
- Faradaic current by redox reactions as a discharging of electrons from the adsorbed electrolyte ions on the surface of the electrodes into the electrodes.

The ions in the electrolyte which are involved in the charge transfer at the phase boundary are subject to diffusion processes at the electrode surface. At higher frequencies, these diffusion processes hardly affect the electrode impedance, because the sign of the currents permanently changes [168].

A number of processes takes place at the electrode-electrolyte interfaces. The formation of the electrochemical double layer, the redox reactions, and diffusion influence the electrical properties of the electrode and in particular its impedance. These processes depend on the surface properties of the material and the geometry of the electrodes. Using an equivalent circuit provides a modeling of electrical properties of the electrode to obtain the effect of various electrochemical processes on the impedance. The modeling is an important step to characterize the properties of each electrode and to compare it with other electrodes.

Equivalent circuits are a very important and useful tool for impedance spectroscopy. In the last century various models of equivalent circuits were applied [151]. One well-known model, which is frequently used for a variety of electrodes is given by Randles as shown in Fig. 4.4.

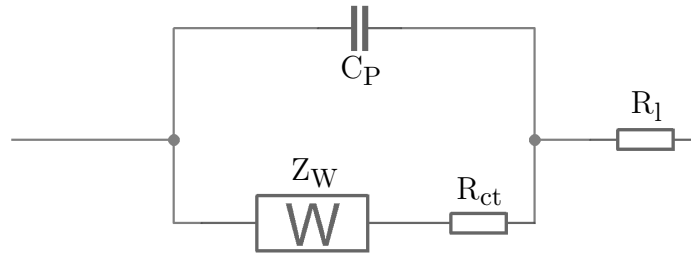


**Figure 4.4:** Randles model as an equivalent circuit for characterization of electrochemical processes at electrodes.

In this model  $R_l$  represents the resistance of the electrolyte solution, which determines the charge transport in the solution between the electrodes. Since the charge transport in electrolyte solutions is ionic, solvated ions have to be transported through the solution to the electrodes. This transport process can be characterized by an ohmic resistance. The phase boundaries capacity  $C_P$  describes both the behavior of the electrochemical double layer and all reversible redox reactions that take place at the electrode electrolyte interface. The charge-transfer resistance  $R_{ct}$  describes the irreversible redox reactions and the associated current through charge exchange.  $Z_W$  represents a Warburg element or Warburg impedance, describing the diffusion processes of the reactants and reaction products to and from the electrodes at low frequencies (typically below 1Hz). The expression for the Warburg impedance results from the solution of the diffusion equations for the semi-infinite space with  $\sigma$  as Warburg-coefficient [149, 150, 151, 168, 170]:

$$Z_W = \sigma \omega^{-\frac{1}{2}}(1 - j), \sigma = \frac{RT}{n^2 F^2 \sqrt{2}} \left\langle \frac{1}{c_{red} \sqrt{D_{red}}} + \frac{1}{c_{ox} \sqrt{D_{ox}}} \right\rangle. \quad (4.6)$$

where  $c_j$  is the molar concentration of each ion in solution. Only at very low frequencies a major influence of the Warburg impedance is expected. The behavior of the Warburg impedance at high frequencies can be explained due to the fact that the diffusion of the reactants is negligible, since the currents permanently change sign and direction [168].

In addition to R, C, and L elements, the equivalent circuits can be extended with the constant phase element (CPE), describing non-linear processes and dispersion effects of the double layer capacitance [170]. They help for describing processes which are affected by the surface roughness and chemical inhomogeneity at the surface. In general, the impedance of such CPEs is defined as follows [170]:

$$Z_{\text{CPE}} = K(j\omega)^{-\beta}, \quad (4.7)$$

with  $j = \sqrt{-1}$ ,  $K$  the impedance value,  $\omega$  the frequency, and  $\beta$  a value between 0 and 1.  $\beta = 0$  makes an ideal resistor behavior with the value  $K$ .  $\beta = 1$  makes an ideal capacitor behavior with a capacity of  $K^{-1}$ .  $\beta$  between 0 and 1 makes the CPE like a "leaking capacitor" [152]. It means that the parameter  $\beta$  is related to the particular surface condition of the electrode [171]. This shows where the name constant-phase element finds its origin. Only its value is frequency dependent, as the phase remains constant and is only  $\beta$ .

### 4.3.2 Addendum II

Nanopatterning of ITO multi-electrode arrays (MEAs) was carried out on thin glass substrates by applying coherent periodic sub-20 nm cuts induced by sub-15 femtosecond laser pulses<sup>2</sup>.

ITO is used as electrode material because of its excellent properties, which allow simultaneous optical (differential interference contrast microscopy) and electrical (impedance spectroscopy) measurements on living cells. In this Section the fabrication technology of ITO multi-electrode arrays (MEAs) is presented. Furthermore a nanopatterning method with high repetition rate Ti:sapphire sub-15 femtosecond laser pulses is used to improve cell sticking and growth and trim the electrode impedance.

The results are published 2015 in **Applied Surface Science** (Impact Factor: 2.735). The laser nanopatterning is the last step after fabrication process of SMD bonded chips.

Publication Nr. 4: **On-chip nanostructuring and impedance trimming of transparent and flexible ITO electrodes by laser induced coherent sub-20nm cuts**

**Authors:** Maziar Afshar, Moritz Leber, Wigand Poppendieck, Karsten König, Helmut Seidel, and Dara Feili

Accepted in *Applied Surface Science* (2015), DOI: 10.1016/j.apsusc.2015.10.119

**Reprinted** in PhD thesis by permission of the Journal.

**Abstract:** In this work, the effect of laser-induced nanostructuring of transparent indium tin oxide (ITO) electrodes on flexible glass is investigated. Multi-electrode arrays (MEA) for electrical and optical characterization of biological cells were fabricated using standard MEMS technologies. Optimal sputter parameters concerning oxygen flow, sputter power and ambient pressure for ITO layers with both good optical and electrical properties were determined. Afterwards, coherent sub – 20 nm wide and 150 nm deep nanocuts of many micrometers in length were generated within the ITO electrodes by a sub-15 femtosecond (fs) pulsed laser. The influence of laser processing on the electrical and optical properties of electrodes was investigated. The electrochemical impedance of the manufactured electrodes was measured before and after laser modification using electrochemical impedance spectroscopy. A small reduction in electrode impedance was observed. These nanostructured electrodes show also polarizing effects by the visible spectrum.

---

<sup>2</sup>The idea and the experimental design originate from the author. The technical implementation was supported by Moritz Leber in his Diplomarbeit under the supervision of the author.

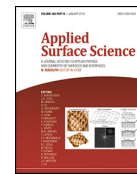


Applied Surface Science 360 (2016) 494–501



Contents lists available at ScienceDirect

Applied Surface Science

journal homepage: [www.elsevier.com/locate/apsusc](http://www.elsevier.com/locate/apsusc)

## On-chip nanostructuring and impedance trimming of transparent and flexible ITO electrodes by laser induced coherent sub-20 nm cuts



Maziar Afshar<sup>a,\*</sup>, Moritz Leber<sup>a</sup>, Wigand Poppendieck<sup>b</sup>, Karsten König<sup>c</sup>, Helmut Seidel<sup>a</sup>, Dara Feili<sup>a</sup>

<sup>a</sup> Lab for Micromechanics, Microfluidics, and Microactuators, Saarland University, Saarbrücken D-66123, Germany

<sup>b</sup> Department of Medical Engineering & Neuroprosthetics, Fraunhofer Institute for Biomedical Engineering, St. Ingbert D-66386, Germany

<sup>c</sup> Lab for Biophotonics and Laser Technology, Saarland University, Saarbrücken D-66123, Germany

### ARTICLE INFO

#### Article history:

Received 13 May 2015

Received in revised form 6 October 2015

Accepted 16 October 2015

Available online 5 November 2015

#### Keywords:

Nanostructuring

Laser trimming

Microelectrodes

Indium tin oxide

Nanocuts

Impedance spectroscopy

### ABSTRACT

In this work, the effect of laser-induced nanostructuring of transparent indium tin oxide (ITO) electrodes on flexible glass is investigated. Multi-electrode arrays (MEA) for electrical and optical characterization of biological cells were fabricated using standard MEMS technologies. Optimal sputter parameters concerning oxygen flow, sputter power and ambient pressure for ITO layers with both good optical and electrical properties were determined. Afterwards, coherent sub-20 nm wide and 150 nm deep nanocuts of many micrometers in length were generated within the ITO electrodes by a sub-15 femtosecond (fs) pulsed laser. The influence of laser processing on the electrical and optical properties of electrodes was investigated. The electrochemical impedance of the manufactured electrodes was measured before and after laser modification using electrochemical impedance spectroscopy. A small reduction in electrode impedance was observed. These nanostructured electrodes show also polarizing effects by the visible spectrum.

© 2015 Elsevier B.V. All rights reserved.

### 1. Introduction

In many medical applications, bio-electrodes are used as the connecting element between a technical system and the biological material. They establish an interface between an ion-conducting biological system and an electronically conducting circuitry, being responsible for the charge transfer from one system to the other. Prominent examples of such electrodes are the pacemaker and the cochlea implant [1]. For a good signal-to-noise ratio (SNR), the electrode impedance must be as small as possible [2]. This applies to electrodes for stimulation and for recording. For the stimulation of neurons or muscle cells, a certain current density is required to induce the depolarization of the cell membrane. In order to obtain this current density, electrodes with larger impedance require higher voltages. This can lead to irreversible electrochemical reactions on the electrode material, which could induce electrode corrosion and cytotoxic reactions. Measurement electrodes, which record bioelectric signals from cells, should also have low impedance. Cardiomyocytes generate signals in the mV range and neurons down in the  $\mu$ V range. A method to reduce the

electrode impedance is to increase the effective surface of an electrode by creating a micro-rough, fractal surface structure and by improving its electrochemical properties. The use of near-infrared (NIR) fs-laser pulses provides the possibility of nanoprocessing inside the bulk without destructive effects at the surface.

Indium tin oxide (ITO) is used as electrode material because of its excellent properties, which allow simultaneous optical (differential interference contrast microscopy) and electrical (impedance spectroscopy) measurements on living cells. ITO in a typical composition is a transparent conducting oxide with a wide optical band gap and a highly degenerate electrical conductivity. It has numerous applications in display technologies, in organic light emitting diodes (OLEDs), in photovoltaics and even in sensors [3–6]. ITO is doped  $\text{In}_2\text{O}_3$ , which can be sputtered from metallic and oxidized targets. In this article, we report on the fabrication technology of ITO multi-electrode arrays (MEAs) and their nanopatterning with a femtosecond laser to trim their impedance.

Multi-electrode arrays (MEAs) of various radii are fabricated on glass substrates with an SU-8 passivation layer. The electrical interconnections are made of gold and the chips are connected to a board with surface mounted device (SMD) technology. With a sealed glass ring, a measurement cell was fabricated. The laser nanopatterning is the last step in the fabrication process of the device. The

\* Corresponding author.

E-mail address: [m.afshar@imm.uni-saarland.de](mailto:m.afshar@imm.uni-saarland.de) (M. Afshar).

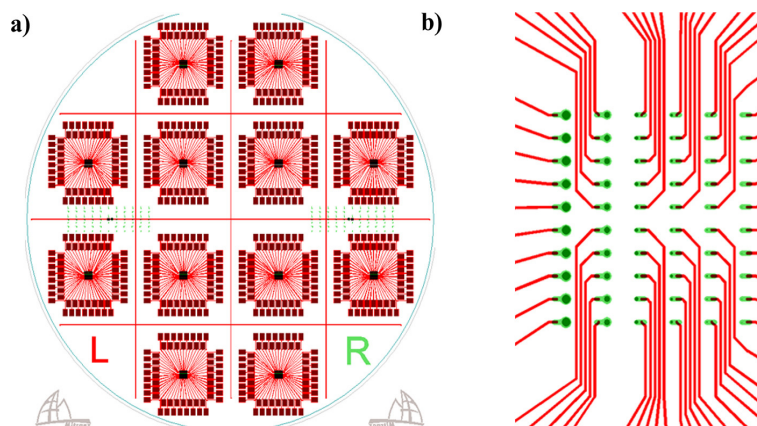


**Fig. 1.** (a) Wafer design of the arrays, (b) Clewin design of a multi-electrode array. Lime green shows ITO structures, dark green shows the holes of the SU-8 passivation layer, and the red lines depict the gold wires. (For interpretation of the references to color in this figure legend, the reader is referred to the web version of this article.)

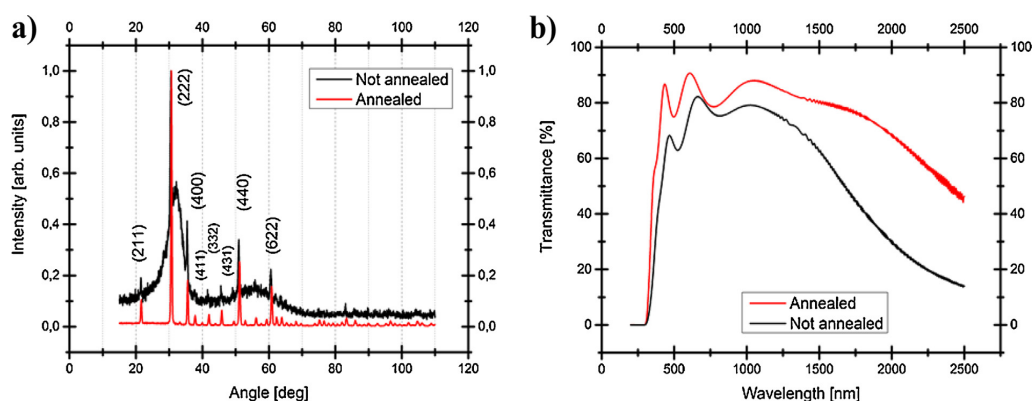


**Fig. 2.** (a) XRD graph of the ITO layer before and after one hour annealing in air at 400 °C, (b) optical transmission spectrum of the layer before and after annealing.

**Table 1**  
Electrical properties of the sputtered ITO layer before and after annealing.

	$R_{\square}$ [ $\Omega/\square$ ]	$\rho$ [ $\Omega\text{cm}$ ]	$N$ [ $\text{cm}^{-3}$ ]	$\mu$ [ $\text{cm}^2/\text{Vs}$ ]
Sputtered ITO	17.74	$2.66 \times 10^{-4}$	$2.56 \times 10^{21}$	9.16
Annealed ITO	26.32	$3.95 \times 10^{-4}$	$2.1 \times 10^{21}$	7.54

nanocuts are optimized with respect to obtaining a homogeneous distribution of cuts over the whole length of the modified region.

## 2. Materials and fabrication

### 2.1. Clewin design and substrate

The fabrication of the chips is based on biocompatible transparent materials. Therefore, we used 4" alkali free thin glass wafers from Schott (AF 32<sup>®</sup> eco) to prevent any contamination of the ITO layer by diffusion. Glass wafers with thicknesses less than 200  $\mu\text{m}$  are flexible. We chose a thickness of 145  $\mu\text{m}$  to use the possibility of substrate flexibility for immersion oil microscopy on cells as well as laser modification through the substrate. Typical MEAs have a radius of 5–15  $\mu\text{m}$  with pitches of 100–500  $\mu\text{m}$  [7–9]. In this article, the laser trimming was studied on thin film ITO electrodes with different radii of 2.5, 5, 10, 15, 25 and 35  $\mu\text{m}$  in a  $10 \times 6$  array with pitches of 194  $\mu\text{m}$  in each row. The surface of the electrodes was defined by the holes in the passivation layer (Fig. 3). The

ITO structures are over-dimensioned by 33% compared to the SU-8 holes to prevent alignment errors during the following lithography steps. Fig. 1 shows the mask design of the whole wafer (a) with 12 chips and a single array without contact pads (b). The tails of the electrodes have a width of 40  $\mu\text{m}$  and the width of the conducting paths is 20  $\mu\text{m}$ .

The study focuses on the relative change of the impedances. This makes an absolute potential measurement irrelevant so that a reference electrode on chip was not included in our design.

### 2.2. Chip fabrication

Polycrystalline ITO films with a thickness of approximately 100 nm were deposited on 145  $\mu\text{m}$  thick glass substrates by reactive magnetron DC-sputtering (Von Ardenne LS 730S) with a compound 6-inch indium–tin (90:10) target. Respecting the crystallographic structure and optoelectrical properties of the films, the deposition was optimized in an Ar/O<sub>2</sub> plasma. Samples were sputtered at a chamber pressure of 0.005 mbar with an oxygen flow rate of 7 sccm corresponding to 11% of the total Ar/O<sub>2</sub> flow rate of 60 sccm. Such conditions yield layers with high electrical conductivity with a sheet resistance  $R_{\square}$  below 100  $\Omega/\square$ , resulting in a metallic contact to the gold pads.

The crystallinity of the films was analyzed by grazing incidence X-ray diffractometry (GIXRD) before and after annealing in an air

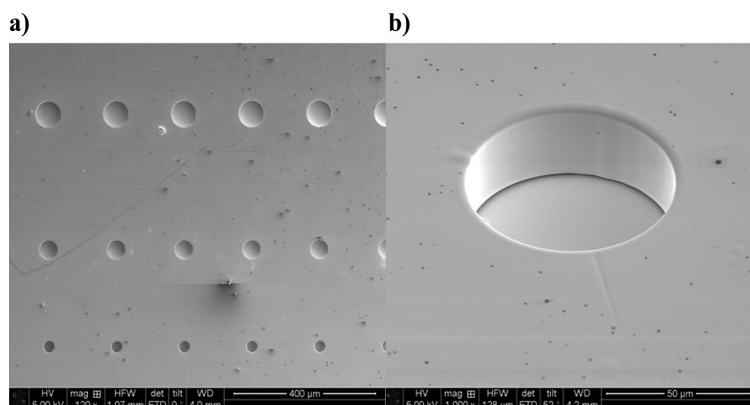


**Fig. 3.** Electron microscope images of the SU-8 passivation layer for different sizes of electrodes (a) and for a 35  $\mu\text{m}$  radius after laser structuring (b).

atmosphere at 400  $^{\circ}\text{C}$  for 1 h. The measurements showed a strong amorphous background, which disappears after annealing (Fig. 2a). Atomic force microscopy (AFM) was used to examine the roughness of the surface (Veeco Image 3100) and rendered a very low  $R_{\text{rms}}$  roughness below 1 nm.

Transmission/reflection UV–vis spectroscopy (Cary 5000 spectrometer, VARIAN) was used for the optical characterization of the ITO films. This measurement showed a high transmission of 80% in the spectral range of the laser and even higher in the visible range of the spectrum (Fig. 2b).

The film conductivity was examined with four-point probe and Hall measurements. ITO films exhibited metal-like electrical conductivities (Table 1). The temperature coefficient of resistivity (TCR)  $\alpha$  in air is positive in the range from 0  $^{\circ}\text{C}$  to 90  $^{\circ}\text{C}$ . The charge carrier density  $N$  in the ITO layers was determined by Hall measurements using a van der Pauw method, yielding a value of  $1.8 \times 10^{21} \text{ cm}^{-3}$  in a 150 nm thick ITO layer with a Hall voltage of about 1.85 mV at a magnetic flux density of 0.5 T.

After ITO sputtering, we used conventional lithography with a positive photoresist (AZ1518 from MicroChemicals GmbH) to pattern the ITO pads in a subsequent wet etching process in 10% hydrochloric acid (HCl). The second lithography step was done with an image reversal photoresist (AZ5214E from MicroChemicals GmbH) to generate gold pads on the ITO films in a lift-off process. After sputter deposition of gold (with 10 nm chromium as adhesion layer), the sample was sonicated in acetone to remove the

photoresist and to lift off the gold layer. The last additional lithography step was for the passivation layer made of SU-8 photoresist. The passivation layer covered the entire surface of the wafer except the openings of the electrodes and contact pads, to passivate the gold connections and define locally the surface of the electrodes for measurements. It also damps the parasitic electrical fields (see Fig. 10b). We chose SU-8 (3025 from MicroChem Corp.) for its good adhesion on glass and optimized the process for a thickness of about 25  $\mu\text{m}$ . The wafers were developed in mr-Dev 600 (micro resist technology GmbH, Berlin) for 4 min. Fig. 3 shows the SEM images of the SU-8 passivation layer after laser processing. The subsequent cross section SEM images of cuts are from the electrode in Fig. 3b.

It was not possible to achieve good results for the smallest electrodes (radii: 2.5 and 5  $\mu\text{m}$ ), so that they are not addressed for the rest of our studies. Fig. 4 shows a schematic view of these fabrication steps.

### 2.3. Integration and chip-packaging

After dicing the MEA-chips, we used a flip chip technology to contact each of the chips to a circuit board with electrical connections. We used a reflow soldering technique with a subsequent heating to connect the pads to the board, avoiding any wire bonding.

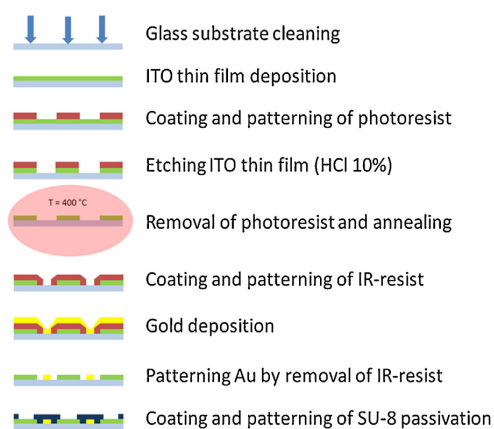


**Fig. 4.** Schematic view of the fabrication steps.

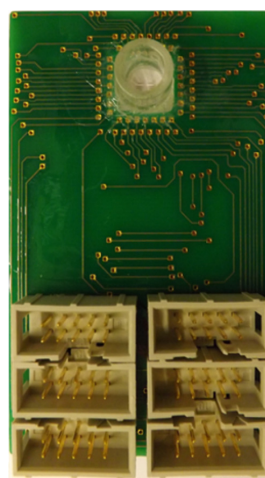


**Fig. 5.** Photograph of the fabricated multi-electrode cell.

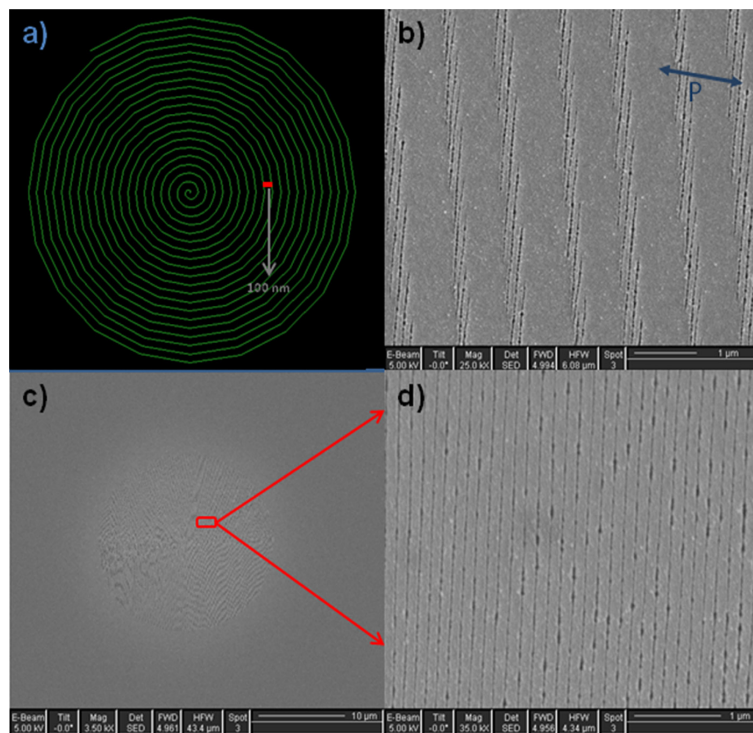


**Fig. 6.** (a) Schematic profile of the scanning spiral line, (b) SEM image of nanocuts of separate lines, (c) SEM image of a circular area with a radius of  $10\ \mu\text{m}$  patterned with parallel nanocuts, (d) magnified SEM image from a section in image c.

Afterwards, a glass ring was mounted and sealed in a predefined window around the chip on the printed circuit board (PCB). This was the electrolyte chamber serving as measurement cell. Fig. 5 shows a photograph of the fabricated module with electrical connections.

### 3. Laser processing

The surface of the ITO electrodes was modified by using a femtosecond laser scanning microscope for nanoprocessing [10]. The laser beam of a broadband mode-locked Ti:sapphire laser (Integral Pro 400, FemtoLasers) propagates through an inverted microscope (Zeiss AxioObserver.D1). It was focused into the sample through an oil immersion objective (Zeiss EC Plan Neofluar  $40\times$ ) with a numerical aperture of 1.3 mounted on a piezo-actuator to adjust the focal plane vertically with nanometer precision. The laser was operated at a central wavelength of 800 nm (bandwidth 120 nm) with a repetition rate of 85 MHz emitting 7 nJ pulses of 10 fs duration. The focal spot featured an effective diameter of  $d \approx 0.61\lambda/NA = 375\ \text{nm}$ . A group dispersion delay precompensation unit chirped the laser pulses and yielded a pulse length of approximately 12 fs at the sample position. The linearly polarized light of the laser could be scanned using galvanometric scan mirrors. A scan controller (GSI Lumonics SC2000) allowed precision manufacturing of complex shapes over a scan range of  $250\ \mu\text{m}$ . The total exposure time of the samples was controlled by a mechanical shutter with a response time of 1 ms. The entire scan procedure was controlled by LabVIEW software.

Laser illumination was performed from the backside of the sample through the substrate. Coordinate points recorded in a text file, including the scan speed data for the controller, defined the scan field. Focusing the beam into the film with a thickness of approximately 100 nm was done manually using the microscope's CCD

**Table 2**  
Electrode areas and modified portions.

Diameter of electrodes [ $\mu\text{m}$ ]	Diameter of modified region [ $\mu\text{m}$ ]	Modified portion
70	60	73.5%
50	40	64%
30	20	44.4%
20	10	25%

camera by adjusting the focal luminescence intensity of the ITO layer under laser illumination at low intensities.

According to the absorption diagram of the ITO layer in Fig. 2b, single-photon excitation at the laser wavelengths remained negligible. Due to a very high transient intensity in the  $\text{TW}/\text{cm}^2$  range, nonlinear absorption processes in the material prevailed. The laser-induced structures in ITO layer were studied in detail previously [10,11]. Here, we address one of the effects at near-ablation threshold exposure, which exhibits the generation of sub-20 nm cuts throughout the entire layer thickness of ITO. These nanocuts are short in length and run perpendicular to the beam polarization (see Fig. 6b).

In this work, we demonstrate a method to generate such nanocuts over a large area and length by carefully optimizing the scan and polarization parameters, leading to a coalescent and coherent cut generation. For this purpose, we wrote  $20\ \mu\text{m} \times 20\ \mu\text{m}$  meander structures, each with a constant intensity and variable scan speeds between 300 and  $2000\ \mu\text{m}/\text{s}$ , to figure out the proper scan parameters.

As a result, an average focal power of 20 mW corresponding to a pulse energy of 0.24 nJ was used for the entire processes. With a scan speed of 1 mm/s and an applied pulse fluence of  $0.21\ \text{J}/\text{cm}^2$  the



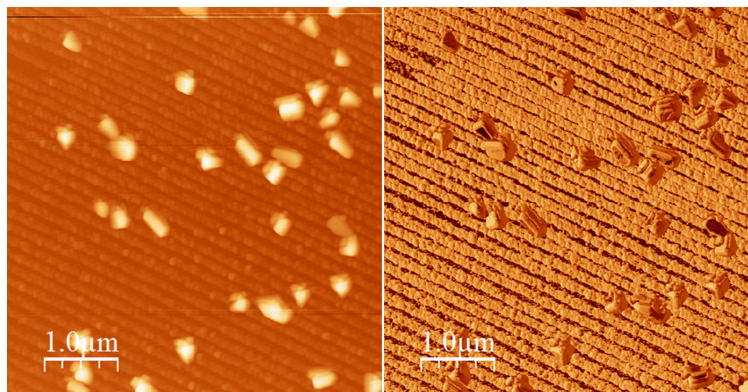


Fig. 7. Amplitude (left) and phase (right) images of the nano-structured surface of the electrode. This shows the periodic nanocuts and also the recontaminations on the surface.

cuts were generated. Fig. 6b shows an SEM image of such meander structures with separated modified regions.

An optimized distribution of cuts in a round area was accomplished with cycled coordination points, arranged in a two-dimensional Archimedean spiral form as shown schematically in Fig. 6a. 100 nm gave the optimum value for the radial increment between points from scan lines in following rounds with the same angle. This gives a dense arrangement of parallel nanocuts with a pitch of approximately 115 nm between cuts. Fig. 6c and d shows an SEM image of a circular modified region with the nanocuts. The focused ion beam (FIB) cross section image in Fig. 10a demonstrates penetration of the nanocuts through the whole layer. Interestingly, the secondary cuts accrete to the prior written cuts. In other words, each single cut can determine the position of the next coming cuts in the next scan line. The reason of this phenomenon is the breaking of lattice-symmetry in cuts, which gives a higher density of crystal defects that contribute to an easier local plasma generation on the surface at these points.

Fig. 6c shows a modified circular electrode with nanocuts perpendicular to the polarization of the laser beam with a homogeneous distribution over the whole area. The length of each cut runs over the entire range of the scanned area from one edge to the counterpart edge.

To protect the passivation layer from any damage, a blank space of 5  $\mu\text{m}$  to the SU-8 edges was left unmodified. The percentage of modified area for each electrode size is listed in Table 2.

The roughness change was characterized by AFM measurements (Fig. 7), although an artifact, caused by the high aspect ratio of the nanocuts, modifies the results. This offers just a shallow penetration of the tip in the cuts, meaning that the absolute values of modified surfaces in reality are even higher but the respective changes are authentic.

The RMS of the roughness of modified electrodes are changed from 0.5 nm for blank ITO (state 1) to 5.7 nm without concerning the recontaminations (state 2). Another raise is according to recontaminations (state 3) to 15.5 nm. As mentioned above, the 100% increase from state 1 to 2 is even more, because of the artifact but the compare between state 2 and 3 with 63% increase is real, because of the same artifact in both cases.

## 4. Results

### 4.1. Impedance spectroscopy

To modify the surface of the SU-8 passivation layer from hydrophobic to hydrophilic in order to increase its wettability, an

oxygen plasma treatment was performed [12]. It attaches polar CO- and COO-groups to the surface of SU-8, thereby rendering it hydrophilic. This treatment was done in a plasma etcher for 1 min at 100 W. This step affects the results of the impedance spectroscopy significantly. This change is a reversible change which is caused by the wettability of SU-8 as mentioned above. The evidence was observed by the measurements before treatment. They revealed a capacitor-like behavior of caused by the air gap in the SU-8 cavity. A possible electrical change of ITO is negligible because of a simultaneous treatment of modified and not modified electrodes on a chip.

The impedance measurements were performed using a frequency response analyzer (FRA) (Solartron 1255) with an electrochemical interface (Solartron 1287). An Ag/AgCl electrode (B2920, Schott) served as reference in the solution, while a platinum electrode (PT 1800, Schott) wire served as counter electrode. The electrolytic solution is an isotonic 0.9% saline solution (NaCl solution).

Fig. 8 shows two Bode plots of 8 electrodes (diameter 70  $\mu\text{m}$ ) before and after the nanopatterning of their surfaces. The two curves look almost alike and cannot be distinguished with certainty due to their overlapping standard deviation ranges. Nevertheless, by comparing the mean value of the characterized electrodes in the relevant range around  $10^3$  Hz, the nanopatterned electrode impedances are lower than the impedances of the unmodified electrodes. Since an unmodified margin of 5  $\mu\text{m}$  (independent of the electrode's surface area) of the patterned area to the SU-8 layer has been left on the ITO layer, smaller electrodes have a much lower fraction of modified surface area than the larger electrodes. Hence, the  $\emptyset$  30  $\mu\text{m}$  electrodes feature a laser patterned surface area of only 45%, whereas the  $\emptyset$  70  $\mu\text{m}$  electrodes exhibit a patterned surface fraction of approximately 75%. Therefore, we did not measure any distinct difference in the impedances for smaller electrodes.

To get a better understanding of the measured curves, the Bode plots were fitted using a modified Randles circuit and the least square method. This was done using the software ZView from Scribner Associates Inc.

Fig. 9 shows the selected equivalent circuit used for the fit. During the fitting process, the impedance values of the saline and the counter electrode were kept constant, resulting in a change of  $R_{f1}$  and  $Z_{CPE1}$  only.  $R_{f1}$  represents the charge transfer resistance, describing the irreversible redox reactions by effective charge transfer through the phase boundary.  $Z_{CPE1}$  represents a constant phase element (CPE), which is a commonly used model to describe the processes at solid state electrode surfaces in electrolytic solutions:  $Z_{CPE} = K(j\omega)^{-\beta}$ . With a coefficient of  $\beta = 0$ , the

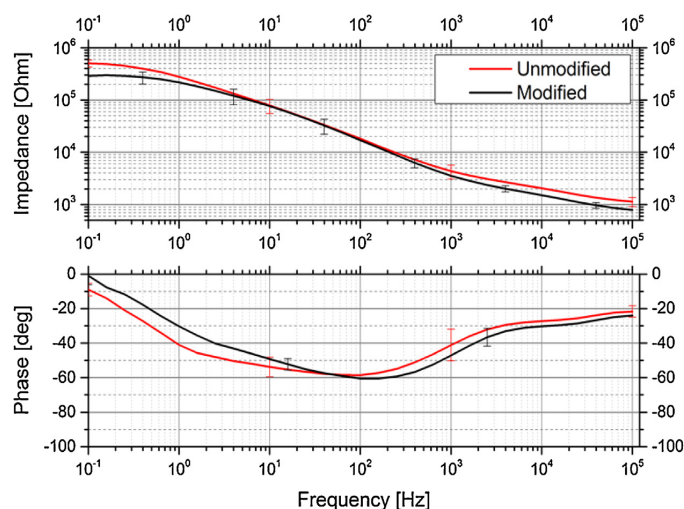


Fig. 8. Bode plots of unmodified and modified ITO electrodes with a diameter of 70  $\mu\text{m}$ . The mean values were calculated from the impedance spectroscopy results of four unmodified and four modified electrodes on the same chip.

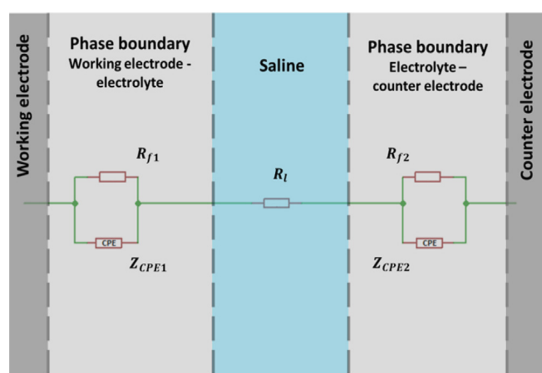


Fig. 9. Equivalent circuit which was used as a model for fitting the impedance results.

CPE has purely Ohmic characteristics, whereas for  $\beta = 1$  it describes an ideal capacitance. Hence, a CPE describes non-ideal leaking capacitor [13,14], where  $K$  quantifies the inverse capacitance  $C^{-1}$  of an ideal capacitor. It was observed that the coefficient  $\beta$  is strongly influenced by the electrodes surface roughness [15]. With the formula of the CPE the values listed in Table 3 were determined for patterned and non-modified electrodes with a diameter of 70  $\mu\text{m}$ .

The CPE can be regarded as a non-ideal capacitance, where  $K^{-1}$  quantifies the capacitance value ( $K^{-1} = C$  for  $\beta = 1$ ). Hence, comparing the fitted values obtained for the nanopatterned electrodes versus the unmodified electrodes, the increasing  $K^{-1}$  value would indicate an increase in the electrodes surface. Furthermore, the decrease of the Faraday resistance  $R_f$  also supports an increasing surface area, since the resistance is inversely proportional to the surface area. However, the relative differences of  $K^{-1}$  and  $R_f$  are not equal, disputing the idea of characterizing the surface area by evaluating both values. The increase of  $\beta$  shows a more capacitance character of the patterned electrode. It can be caused by not wetted cuts containing air gaps.

Table 3

Mean fitting values for nanopatterned and unmodified  $\varnothing$  70  $\mu\text{m}$  ITO electrodes. The relative difference of the values refers to the unmodified electrodes.

	$K^{-1}$ [ $\text{s}^\beta \cdot \Omega^{-1}$ ]	$\beta$	$R_f$ [ $\Omega$ ]
Unmodified	$4.86 \times 10^{-9}$	0.427	$1.03 \times 10^8$
Nanopatterned	$5.34 \times 10^{-9}$	0.464	$3.85 \times 10^7$
Rel. difference	10%	9%	-63%

Nevertheless, the processes at an electro-chemical phase boundary are very complex and the used model is a strongly simplified description of those processes. The possibility of an increase in conductivity of the ITO layer due to a better crystallinity caused by the laser processing can be [16].

#### 4.2. Simulation

Comsol Multiphysics® finite-element (FEM) modeling software was used to study the stray capacitance of the wiring on the chip after passivation, compared to the double-layer capacitance of the electrodes. According to Bard and Faulkner, the double-layer capacitance at the electrode/electrolyte phase boundary is located in the range of 10–40  $\mu\text{F}/\text{cm}^2$ , which is in contrast to a capacitance proportional to the applied voltage [17]. For 0.9% NaCl saline solution with an ion concentration of 154  $\text{mol}/\text{m}^3$  and electrons as major charge carriers in ITO electrodes (n-type) versus  $\text{Na}^+$  cations from electrolyte with an atom radius of 180 pm, the calculated double-layer capacitance is in the range of 100  $\mu\text{F}/\text{cm}^2$ . The model and formula which were used for the calculation can be found in [18].

An FEM simulation of the parasitic capacitance of an electrode with 230 nm gold thickness and 30  $\mu\text{m}$  SU-8 passivation on top renders a value of  $1.7 \times 10^{-4}$   $\mu\text{F}/\text{cm}^2$ , which is five orders of magnitude smaller than the double layer capacitance according to Bard and Faulkner.

A second simulation (presented in Fig. 10) displays the insulation properties of the SU-8 layer by applying a 50 mV voltage in the measurements. Fig. 10b shows the current density in vertical direction, which is only running through the hole in the passivation layer.

500

M. Afshar et al. / Applied Surface Science 360 (2016) 494–501

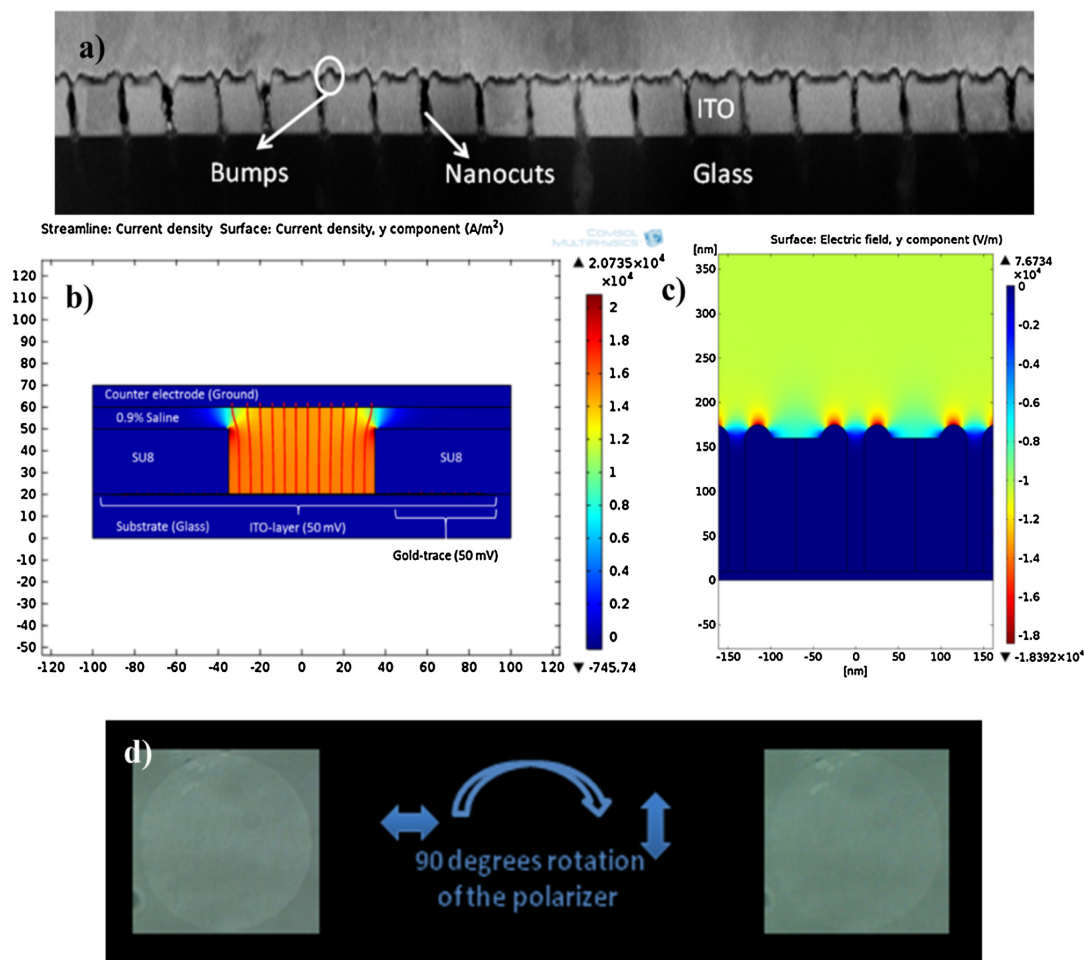


**Fig. 10.** (a) SEM image of the cross section of a modified electrode, (b) simulation of the current density through one electrode, (c) simulation of the electric field distribution in the  $y$ -direction of the nanopatterned ITO layer. The thickness of the ITO layer is 150 nm and the width of one cut is 20 nm, (d) demonstration of the polarization effect of the nanocuts as a change of intensity of the polarized light through the modified circular area.

In order to get a better understanding of the measured impedances, the electric field distribution at the nano-patterned electrode surface was calculated in a COMSOL simulation shown in Fig. 10c. The simulation was done under the assumption of ideal wettability, meaning that the nanocuts and the entire electrode surface are fully covered by the saline solution. As a further simplification an electronic conductivity was assumed instead of an ionic conductivity. The inside of the trenches seems field-free, which can be explained by the high aspect ratio of 15:2. Nevertheless, one observes high electric field densities at the thicker edges of the cuts, which are a side effect of the laser patterning process. Moreover, the ITO layer has a much lower resistivity than the saline solution, leading to almost no electrical current flow in the trenches.

A simple demonstration in Fig. 10d yields polarization effect of the nanocuts on the light. In this experiment, we used the unpolarized light of the microscope with a linear polarizer between the light source and the modified electrode on the microscope. Rotation of the polarizer reveals an obvious change of the intensity on CCD chip for two perpendicular directions of the polarization as shown in Fig. 10d. The ITO lines between the nanocuts serve as wire-grid-polarizer. For the best result, the separation distance

between ITO-wires must be less than the wavelength of the radiation. In our case with an average distance of 20 nm, it should work properly for the visible range of light spectrum. Although, scattering centers on the surface in form of recontaminations and bumps on edges interfere with polarized light inappropriately and reduce the polarizing effect.

## 5. Discussion and conclusions

Nanopatterning of the electrode surfaces increases the real surface area while maintaining the geometrical surface area constant, resulting in a decrease of the electrode impedance. We generated nanometer-size modifications in ITO thin film electrodes using femtosecond laser beams. The change in impedance was characterized by impedance spectroscopy.

To this end, the cell was immersed together with the counter and the reference electrode ( $\varnothing$  70  $\mu\text{m}$ ) in an isotonic saline solution. A decrease in impedance could be observed after nanopatterning with 20 nm wide nanocuts at a density of seven nanocuts per micron. Under the assumption of complete surface wetting, the nanopatterns increased the effective surface area of the electrodes

by more than a factor of four. In contrast, in case of incomplete surface wetting the electrolytic solution does not penetrate into the nanocuts, and the effective surface area decreases by about 14%, resulting in an undesired increase of the electrode impedances. Moreover, even at complete surface wetting, the complicated processes of ion diffusion can take only place in the presence of an electric field within the nanocuts. But due to the high aspect ratio (15:2) of such nanocuts and the high conductivity of ITO, the electric field lines could hardly penetrate the nanocuts. Therefore, the interior of the nanocuts appears to be field-free zones. According to these results, no significant reduction in electrode impedance was achieved by the sole effect of nanocuts. The improvement of impedance is mainly achieved by redeposited ITO micro/nanofractions and 2D bumps on the cut-edges, resulting in a surface roughness increase as shown in the SEM image of the modified layer in Fig. 10a. However, the increase in surface roughness due to nanocuts and redeposited material may play an interesting role in cell adhesion and cell growth. It has been shown that the surface roughness has a significant impact on the cell behavior on surfaces [19].

An experiment with a polarizer provided the proof of principle for a polarizing function of such laser-modified electrodes. Further investigations using different wavelengths and in contact with living cells will reveal a better perspective for applications.

Such nanopatternings could also be covered and filled with solid-state materials in a CVD or PVD process to use the huge surface gain for lower contact resistances and contact impedances for display or thin-film solar cells applications.

#### Acknowledgements

We acknowledge financial support by the German Research Foundation (DFG) within the Priority Program 1327 “Sub-100 nm structures for biomedical and technical applications”. We also thank Prof. F. Mücklich, Dr. M. Straub, and Dr. H. Mousavi for their supports.

#### References

- [1] F. William, E. Agnew, *Neural Prostheses: Fundamental Studies*, 1990.
- [2] W. Franks, I. Schenker, P. Schmutz, A. Hierlemann, Impedance characterization and modeling of electrodes for biomedical applications, *IEEE Trans. Biomed. Eng.* 52 (2005) 1295–1302.
- [3] M.T. Zarin, *Indium Tin Oxide-Polyaniline Biosensor: Fabrication and Performance Analysis*, 2007.
- [4] T. You, *Indium Tin Oxide: High Temperature Ceramic Thin Film Sensors*, Vdm Verlag Dr. Müller, 2008.
- [5] J. Weidner, *Electrodes for Industrial Electrochemistry*, 2009.
- [6] M.A. Scherer, *Prozesstechnologie für GaN-basierende Leuchtdioden*, Cuvillier Verlag, 2004.
- [7] G. Gross, B. Rhoades, D.L. Reust, F. Schwalm, Simulation of monolayer networks in culture through thin-film indium-tin oxide recording electrodes, *J. Neurosci. Methods* 50 (2) (1993) 131–143.
- [8] T. Gabay, M. Ben-David, I. Kalifa, R. Sorkin, Z. Abrams, E. Ben-Jacob, Y. Hanein, Electro-chemical and biological properties of carbon nanotube based multi-electrode arrays, *Nanotechnology* 18 (3) (2007).
- [9] *Microelectrode Array (MEA) Manual: Multi Channel Systems. GmbH*, Reutlingen, Germany, 2013.
- [10] M. Afshar, M. Straub, H. Voellm, D. Feili, K. Koenig, H. Seidel, Sub-100 nm structuring of indium-tin-oxide thin films by sub-15 femtosecond pulsed near-infrared laser light, *Opt. Lett.* 37 (4) (2012) 563–565.
- [11] C. Cheng, I. Lee, J. Chen, Femtosecond laser-induced nanoporous structures and simultaneous crystallization in amorphous indium-tin-oxide thin films, *Appl. Surf. Sci.* (2014) 9–14.
- [12] M. Nordström, R. Marie, M. Calleja, A. Boisen, Rendering Su-8 hydrophilic to facilitate use in micro channel fabrication, *J. Micromech. Microeng.* 14 (12) (2004) 1614–1617.
- [13] A. Lasia, Electrochemical impedance spectroscopy and its applications, *Mod. Asp. Electrochem.* 32 (1999) 143–248.
- [14] E.T. MacAdams, A. Lackermeier, J.A. McLaughlin, D. Macken, The linear and non-linear electrical properties of the electrode-electrolyte interface, *Biosens. Bioelectron.* 10 (1995) 67–74.
- [15] B. Sapoval, J.-N. Chazalviel, J. Peyrière, Electrical response of fractal and porous interfaces, *Phys. Rev. A* 38 (11) (1988) 5867–5887.
- [16] M. Afshar, E.M. Preiß, T. Sauerwald, M. Rodner, D. Feili, M. Straub, K. König, A. Schütze, H. Seidel, Indium-tin-oxide single-nanowire gas sensor fabricated via laserwriting and subsequent etching, *Sens. Actuators B: Chem.* (2015) 525–535.
- [17] A. Bard, L. Faulkner, *Electrochemical Methods: Fundamentals and Applications*, John Wiley & Sons, Inc., 2001.
- [18] H. Wang, L. Pilon, Accurate simulations of electric double layer capacitance of ultramicroelectrodes, *J. Phys. Chem. C* (2011) 16711–16719.
- [19] Y. Fan, F. Cui, S. Hou, Q. Xu, L. Chen, I. Lee, Culture of neural cells on silicon wafers with nano-scale surface topograph, *J. Neurosci. Methods* (2002) 17–23.



## 4.4 Single-Nanowire Polycrystalline ITO Gas Sensors

### 4.4.1 Introduction

There are many different concepts to realize a gas sensor, including optical, electrical and electrochemical methods. Electrical sensors include field-effect transistors with a gas sensitive gate electrode (e.g. for hydrogen-rich gases), measuring a potential change as the sensor signal [172]. It is also possible to make electromechanical gas sensors sensitive to mass changes by the adsorption of gas molecules [172]. Metal oxides, such as zinc oxide or indium tin oxide (ITO), are used for resistive gas sensing [173].

Ozone, methane, carbon monoxide, carbon dioxide and nitrogen oxides are suitable to be detected by ITO as sensor layer. In the literature, ITO thin film based gas sensors for NO and NO<sub>2</sub> [174, 175, 176], CO<sub>2</sub> [177], chlorine [178], isobutane [179], and methane [180] have been presented. A commercial ITO thin film ozone sensor is also available (Sensor SP-16, *FIS Inc*, Japan). A schematic diagram is shown in Fig. 4.5. The power consumption of this sensor is about 600 mW, which is relatively high and prohibitive for battery operation.

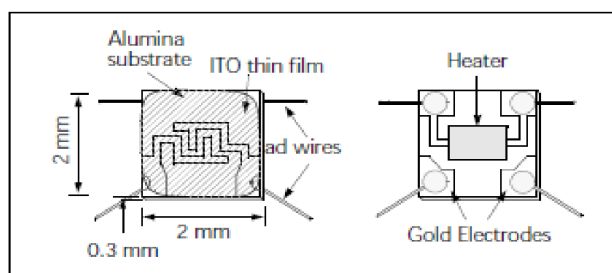


**Figure 4.5:** Commercial ITO thin film sensor (SP-16, *FIS Inc*, Japan). Left: front side of the substrate with ITO sensor layer, right: backside of the substrate with heating element.

A conventional concept for metal oxide (MOX) resistive sensors is as follows [181]: a metal oxide sensing layer is placed on a substrate together with contacting electrodes. In addition, a heating element is placed under the sensing layer, electrically insulated from it.

There are basically two ways in which a resistive gas sensor can be realized; either by macro-structured or by microstructured MOX layers. Gas sensors with macrostructured MOX layers are built on sintered pellets (so called Taguchi sensors [172]) or are structured by screen printing in thick layer technique [182]. Such sensors are still the most commonly available commercial devices. Well known manufacturers are e.g. *Figaro*, *FIS*, *UST*, and *CityTech*. Sensors with compact microstructured MOX layers are realized by using thin film deposition techniques such as CVD, vacuum evaporation or sputtering [173, 172]. Such sensors exhibit shorter response times and lower energy consumption. They can be miniaturized substantially and the use of sensor arrays is possible. Thus, the selectivity of the sensors can be significantly increased by cross-linking multiple sensor signals applied together. The thin film sensors have a much higher reproducibility than sintered powder sensors, but they have lower sensitivity because the gas cannot diffuse much into the compact layer. Thus, the gas-sensor interaction only takes place on the surface of the MOX thin film [183].

The change in resistance is due to a charge carrier exchange between the oxide layer and the adsorbed atoms or ions [181]. Adsorbing oxygen from the air generates a surface layer with new and different electrical properties, which is then additionally modified by the chemical acting of gas molecules on the material. Oxidizing agents such as ozone and nitrogen dioxide take electrons and induce a reduction of the charge carrier density in the n-type sensors and thus in their conductivity. Reducing gases such as  $\text{CH}_4$ ,  $\text{H}_2$ ,  $\text{CO}$ , and  $\text{H}_2\text{S}$  as well as alcohols and isobutane cause an increase in conductivity. The reaction takes place at the surface, and at higher concentrations it may come to saturation effects [184]. Also possible are layered sensors of different oxides in order to increase the selectivity. Some oxides exhibit a particularly high selectivity between different gases, e.g. titaniobat [184]. Even conductive polymers are used as resistive chemical sensors e.g. polythiophenes [185]. The sensitivity and selectivity can be improved by applying a catalyzing layer, whereby low working temperatures can be reached [186].

Resetting of such sensors can be achieved by applying external energy to desorb the molecules attached to the surface. This can be done thermally or by applying electromagnetic energy in the UV range of the spectrum.

The usual operating temperatures of MOX resistors are above  $200\text{ }^\circ\text{C}$  [173, 181]. For heating a separate electrical heater can be used or, alternatively, the sensing resistor can be operated in self-heating mode, combining both functions in one element [179]. The latter mode is used for the nanowire (hot-wire) sensor fabricated in this work. This sensor can be operated in a bridge circuit with a constant temperature configuration, which is more stable than a constant voltage configuration. Should the resistance be reduced, caused by a reducing gas, it causes the increase of current flow through the sensor. It is also possible to sense at room temperature (RT) [104, 187]. The sensor assembly without heating element uses the advantage of the photoreduction using ultra-violet radiation to reset the sensor. Although RT-sensors usually have a lower sensitivity and longer response times than heated sensors, they do have the advantage of a lower power consumption and a simpler structure, since the heater can be omitted.

There are various types of adsorption of the gases on the surface of the oxides. Physisorption already occurs at low temperatures. The resulting effects are very weak because it is based on van der Waals forces [182]. Stronger effects can be achieved by chemisorption, arising from the chemical bonds between the adsorbed gas atoms or molecules. An activation energy must be thermally applied. By chemisorption, a charge carrier exchange takes place between the adsorbed gas molecules and the metal oxide layer, which is decisive for the resistance change and thus for the sensor signal. Chemisorption takes place mainly in the range of  $30\text{ }^\circ\text{C}$  to  $400\text{ }^\circ\text{C}$ ; higher temperatures support the desorption of the gas from the surface. Thus, high temperatures in the range of  $200\text{ }^\circ\text{C}$  to  $400\text{ }^\circ\text{C}$  ensure good sensitivity but also reversibility [182]. The interaction between metal and gas molecules and the resulting change in resistance is still a topic under investigation.

The change in resistance of a compact (non-porous) metal oxide gas sensor as response to oxidizing or reducing gases can be described by a change in the depth of the depletion region on the surface. This depletion layer is formed by the chemisorption of oxygen on the surface

of the MOX and the subsequent charge carrier exchange [182]. The adsorbed surface oxygen atoms act as acceptor [184], leading to a depletion of charge carriers on the surface. The adsorption of oxidizing or reducing gases increases or decreases this depletion region. This in turn implies a change of the total resistance of the oxide layer, since the conductive region is more reduced by a more extended depletion region.

In case of an n-type semiconductor such as tin dioxide, by drawing the electrons from ionized donors via the conduction band, the charge-carrier density at the interface reduces and a potential barrier to charge transport develops. As the surface charge grows, the adsorption of more oxygen is inhibited; the adsorption rate slows down and the coverage saturates at a very low value. Consequently, the number of adsorbed oxygen molecules decreases and it can saturate the sensor [184]. Reducing gases cause a reduction of the adsorbed oxygen, while oxidizing gases can directly interact with the surface and create additional acceptors. The width of the space charge region of MOX ( $z_0$ ) correlates with the band bending  $q \cdot V_s$ , where the Schottky potential  $V_s$  is the potential difference between the bulk and the surface of the MOX [182] (Fig. 4.6). Poisson's equation gives this relation:

$$\nabla^2 V = -\frac{\rho}{\epsilon_0 \cdot \epsilon_r}. \quad (4.8)$$

Assuming that the potential changes only in the  $z$  direction and the charge  $\rho$  in the depletion layer comes only from the donors  $N_D$  ( $q$  is the elementary charge),  $\rho =$  can be written as  $q \cdot N_D$  with a further assumption that the change of electrical potential  $V$  mainly takes place in the  $z$ -direction, it follows that [182]:

$$\frac{dV^2(z)}{dz^2} = -\frac{qN_D}{\epsilon_0 \cdot \epsilon_r}. \quad (4.9)$$

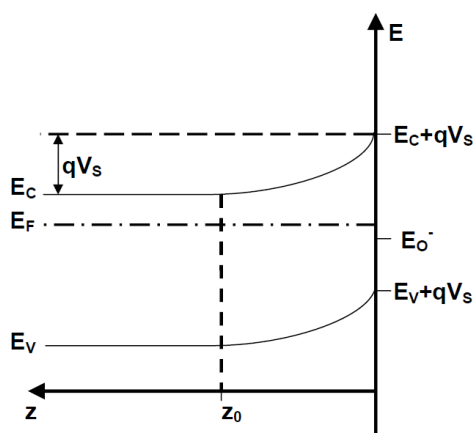


**Figure 4.6:** Band bending caused by the exchange of electrons between MOX and oxygen.  $z_0$  is the width of the depletion layer [182].

With the following boundary conditions, that the potential gradient is perpendicular to the surface ( $z = 0$ ) in  $z$  direction and the potential is supposed to be constant beyond the depletion zone ( $z = z_0$ ) and zero on the surface ( $z = 0$ ) it follows:

$$V_{z=0} = 0, \quad \left. \frac{dV(z)}{dz} \right|_{z=z_0} = 0, \quad (4.10)$$

the following Schottky relation can be achieved:

$$V_s = \frac{q \cdot N_D}{2 \cdot \epsilon_r \cdot \epsilon_0} \cdot z_0^2. \quad (4.11)$$

Therefore, the energy  $qV_s$  must be applied to move a carrier from the highest interior energy level to the surface. Rearranging the equation gives an estimate of the width of the depletion region. The width increases by exposing to oxidizing gases and reduces by reducing gases. It can be seen that the thickness of the sensor layer should be in the range of the depletion region in order to reach a relatively large resistance change due to the exposure to gas and thus a high sensitivity (see. Fig. 4.7 center). This change in resistance, caused by the space charge zone, can be expressed as follow:

$$\Delta R \approx \rho \frac{l}{b d^2} = R_0 \cdot \frac{z_0}{d}, \quad (4.12)$$

where  $\rho$  is the resistivity of the sensor layer,  $l$  is the length,  $b$  is the width and  $d$  is the thickness of the layer or wire. Here,  $R_0$  is the known resistance without considering the depletion region.

These considerations can be applied primarily for thin-layer MOX sensors. In polycrystalline or porous MOX sensors, however, the space charge regions on the surface of the individual grains and the resulting Schottky contacts between the grains dominate the resistance behavior (see Fig. 4.7 left). The oxygen accumulates in particular at the grain boundaries, which represent potential barriers. There are other effects that may contribute to non-ohmic behavior, such as the metal/MOX contacts and the above-discussed surface effects [181]. Due to a high charge carrier density in ITO, an ohmic behavior is expected. In nanowires, a change of the width of the depletion region leads to a strong change in the resistance, if it is completely surrounded by oxygen or oxidized gases, since it greatly reduces the cross-section of the conductor, as also indicated in Fig. 4.7 right. Signals can be obtained from  $\Delta R \approx \frac{z_0^2 - 2z_0 r}{r^2} R_0$ , if  $r$  is the radius of the nanowire.

It is important to also note that the resistance of the MOX strongly depends on the humidity, even at high temperatures up to 600 °C [184]. This is due to the oxygen vacancies which are caused by the interaction with water, according to the following equation, using the example of SnO<sub>2</sub> [188]:

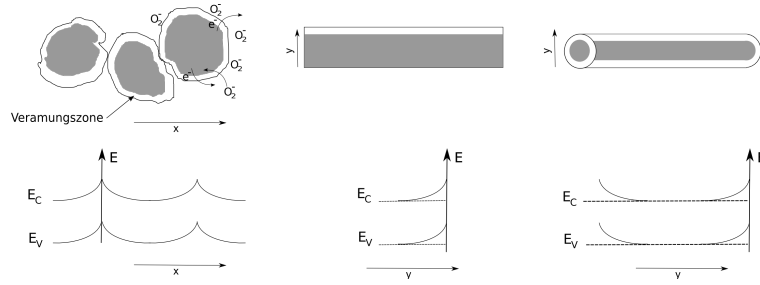
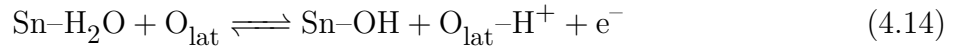


**Figure 4.7:** Schematic demonstration of the band bending caused by the depletion region in porous, thin film and nanowire metal oxide materials. The current is assumed to flow in the x direction [50, 181].



with  $\text{O}_{\text{lat}}$  standing for oxygen lattice atoms. Beyond the chemisorbed oxygen atoms on a tin dioxide surface, oxygen lattice atoms play the main role in the sensing mechanism. The removal of these atoms increases the conductivity because the ratio O:Sn is decreased. More specifically, the oxygen vacancies diffuse to the bulk where they can act as electron donors [188].

Chemical bindings between water and tin generate free electrons and oxygen vacancies. Consequently, the resistance of metal oxides decreases under the influence of moisture. The effect is reversible within the temperature range of 300 °C to 600 °C [184].

In single crystalline nanowires, a regenerating self-heating effect can be obtained with very low energy consumption in the  $\mu\text{W}$  range. That makes such sensors very suitable for portable devices in contrast to their counterparts made of nanocrystalline thin films. But the fabrication is still a challenge on the way to mass-production. The self-heating effect in polycrystalline thin films can decrease the stability of a device.

Use of ITO, as a tin doped  $\text{In}_2\text{O}_3$  with a very broadened usage in gas sensors, does not surprise. The impact of layer properties of indium oxide on gas sensing has been already investigated [104, 189]. Surface roughness and grain size influence the sensitivity of the sensors due to the surface to volume ratio. Surface roughness and grain size increase by increasing thickness and oxygen content in the sputtering chamber.

In compare to indium oxide, the additional tin oxide content in ITO has a significant impact on the sensitivity for example in case of methanol [180]. The sensitivity decreases with increasing ITO layer thickness, which was attributed to larger grains [180]. In summary, the sensitivity of ITO thin films gas sensors mainly dependent on the grain size effects which is controlled by deposition parameters.

Most of realized ITO gas sensors are realized as thin film sensors, with or without heating element. By thin-film sensors, ITO layer is normally deposited on interdigital electrodes.

Thus, an ITO patterning step is not necessary [179]. NO<sub>2</sub> sensors on ITO base showed reasonably good sensitivities. However, there are not enough studies on film properties of respective samples, which also results in different behaviors of sensors. Such sensors were usually operated at high temperatures (over 200 °C [174, 176]).

There are two fundamentally different approaches for fabrication of nanowires: the top-down and the bottom-up method. Most nanowires described so far in the literature are based on the bottom-up concept, where many single crystalline nanowires are generated in an unorganized or self-organizing configuration. This is mostly achieved by chemical vapor deposition (CVD) [190], in some cases also by electrodeposition [191]. In order to obtain a single nanowire for sensor applications, electron beam lithography (EBL) and/or focused ion beam (FIB) techniques are often used to select and contact a single crystalline nanostructure from randomly grown nanowires [190, 191, 192, 193].

Another approach is based on using many nanowires, which are usually dispensed as a dispersion on the contacts or on the substrate and the contacts are directly deposited on them. Gas sensors were realized by such methods with individual (e.g. SnO<sub>2</sub> [194, 195]) and numerous parallel nanowires (e.g. SnO<sub>2</sub> [196]). In the literature there are some examples of ITO nanowire gas sensors, e.g. by electrospinning characterized with NO<sub>2</sub> gas [197] and fabricated by vapor-liquid-solid (VLS) mode and characterized with ethanol gas [198]. In VLS mode, an alloy particle is usually located at the end of the nanowire, and serves as the catalyst between the vapor feed and the solid growth.

These bottom-up approaches yield a high crystal quality but are not applicable for mass production. In contrast to these previous works, a novel technique is presented here by applying a top-down approach to use a single nanowire with well-defined position and geometry which is nanofabricated directly by employing a femtosecond laser beam in combination with a subsequent etch step.

In this way, polycrystalline ITO single nanowires with widths in the range of about 1 μm down to sub-100 nm can be generated. Due to high writing speeds in the range of mm/s this method is applicable for mass production. Further information is given in Chapter 4<sup>3</sup>.

---

<sup>3</sup>The idea and the experimental design originate from the author. The technical implementation was supported by Elisabeth Preiß in her Diplomarbeit under the supervision of the author

### 4.4.2 Addendum III

Polycrystalline ITO single nanowires with widths in the range of about  $1\ \mu\text{m}$  down to sub-100 nm can be generated with the described approach. Due to high writing speeds in the range of mm/s this method is applicable for mass production.

The results of the first application for nanowire of ITO in a self-heating gas sensor are published 2015 in **Sensors and Actuators B** (Impact Factor: 4.286). It presents the fabrication, simulation, and characterization of sensor by measuring  $\text{NO}_2$  as an oxidizing gas with concentrations in lower ppm range <sup>4</sup>.

#### Publication Nr. 3: **Indium-Tin-Oxide Single-Nanowire Gas Sensor Fabricated Via Laser Writing and Subsequent Etching**

**Authors:** Maziar Afshar, Elisabeth Preiss, Tilman Sauerwald, Marius Rodner, Dara Feili, Martin Straub, Karsten König, Andreas Schütze, and Helmut Seidel

Accepted in *Sensors and Actuators B: Chemical* (2015), **DOI:** 10.1016/j.snb.2015.03.067

**Reprinted** in PhD thesis by permission of the Journal.

**Abstract:** We report on the design and nanofabrication of a single nanowire (NW) indium-tin-oxide (ITO) gas sensor and on test results obtained with an oxidizing and a reducing gas. As a novel fabrication approach, direct laser writing and a subsequent etching process on sputtered ITO thin-film layers is applied. For this technique a near-infrared Ti:sapphire laser with sub-15 fs pulses and a repetition rate of 85 MHz is used. NWs for gas sensors are realized in two versions with a thickness of  $125 \pm 25$  nm; one with 350 nm in width and  $90\ \mu\text{m}$  in length the other with 700 nm in width and  $200\ \mu\text{m}$  in length. The sensors are exposed to nitrogen dioxide ( $\text{NO}_2$ ) in synthetic air with concentrations from 1 ppm to 50 ppm showing a significant change in resistance (up to 15.8%), whereas the reaction to 2000 ppm carbon monoxide (CO) turns out to be negligible (0.05%). At ambient temperature, the sensor exhibits integrating dosimeter-like behavior with relaxation times of more than 20 h. By self-heating, the NW can be reset to its initial condition, thus enabling a new dosimeter run at room-temperature. When the sensors are operated in self-heating mode, a conventional behavior is observed, enabling the detection of  $\text{NO}_2$  concentrations down to about 1 ppm at a stationary temperature below  $200\ ^\circ\text{C}$ .

---

<sup>4</sup>The idea and the experimental design originate from the author. The technical implementation was supported by Elisabeth Preiß in her Diplomarbeit under the supervision of the author.



Contents lists available at ScienceDirect

## Sensors and Actuators B: Chemical

journal homepage: [www.elsevier.com/locate/snb](http://www.elsevier.com/locate/snb)

## Indium-tin-oxide single-nanowire gas sensor fabricated via laser writing and subsequent etching



Maziar Afshar<sup>a,\*</sup>, Elisabeth M. Preiß<sup>a</sup>, Tilman Sauerwald<sup>b</sup>, Marius Rodner<sup>b</sup>, Dara Feili<sup>a</sup>, Martin Straub<sup>c</sup>, Karsten König<sup>c</sup>, Andreas Schütze<sup>b</sup>, Helmut Seidel<sup>a</sup>

<sup>a</sup> Lab for Micromechanics, Microfluidics, and Microactuators, Saarland University, Saarbrücken, D-66123 Germany

<sup>b</sup> Lab for Measurement Technology, Saarland University, Saarbrücken, D-66123 Germany

<sup>c</sup> Lab for Biophotonics and Laser Technology, Saarland University, Saarbrücken, D-66123 Germany

### ARTICLE INFO

#### Article history:

Received 11 September 2014

Received in revised form 11 March 2015

Accepted 30 March 2015

Available online 6 April 2015

#### Keywords:

Indium tin oxide  
Femtosecond laser  
Nanowires  
Gas sensor  
Self-heating

### ABSTRACT

We report on the design and nanofabrication of a single nanowire (NW) indium-tin-oxide (ITO) gas sensor and on test results obtained with an oxidizing and a reducing gas. As a novel fabrication approach, direct laser writing and a subsequent etching process on sputtered ITO thin-film layers is applied. For this technique a near-infrared Ti:sapphire laser with sub-15 fs pulses and a repetition rate of 85 MHz is used. NWs for gas sensors are realized in two versions with a thickness of  $125 \pm 25$  nm; one with 350 nm in width and 90  $\mu$ m in length the other with 700 nm in width and 200  $\mu$ m in length. The sensors are exposed to nitrogen dioxide (NO<sub>2</sub>) in synthetic air with concentrations from 1 ppm to 50 ppm showing a significant change in resistance (up to 15.8%), whereas the reaction to 2000 ppm carbon monoxide (CO) turns out to be negligible (0.05%). At ambient temperature, the sensor exhibits integrating dosimeter-like behavior with relaxation times of more than 20 h. By self-heating, the NW can be reset to its initial condition, thus enabling a new dosimeter run at room-temperature. When the sensors are operated in self-heating mode, a conventional behavior is observed, enabling the detection of NO<sub>2</sub> concentrations down to about 1 ppm at a stationary temperature below 200 °C.

© 2015 Elsevier B.V. All rights reserved.

### 1. Introduction

Recently, micro- and nanostructured resistive gas sensors have attracted extensive interest due to their distinctive physical properties, featuring a fast response and reduced power consumption. The behavior of individual or networked single crystalline metal oxide NWs used as gas sensors has been described in previous studies [1–5]. Such sensors show promising results because of their high surface to volume ratio, a deep depletion layer in comparison to the transversal dimensions of the NW, as well as extremely low power consumption. While the sensor response of nanocrystalline thin film sensors is noticeably higher than that of single crystalline NW sensors, the detection efficiency of the latter is significantly higher. In case of SnO<sub>2</sub> a thirtyfold increase was reported by Bruneta et al. [6].

In single crystalline NWs, a regenerating self-heating effect can be obtained with very low energy consumption in the  $\mu$ W range. That makes such sensors very suitable for portable devices

in contrast to their counterparts made of nanocrystalline thin films. But the fabrication is still a challenge on the way to mass-production. The self-heating effect in polycrystalline thin films can decrease the stability of a device because of grain growth [5].

The gas sensitivity is explained by a change of the band bending on the surface of the metal oxides caused by adsorption of gas molecules [7]. This band bending changes the width of the depletion layer and consequently the resistance of the sensor element.

As described by Chen et al. [3], there are two fundamentally different approaches for NW fabrication: the top-down and the bottom-up method. Most NWs described so far in the literature are based on the bottom-up concept, where many single crystalline NWs are generated in an unorganized or self-organizing configuration. This is mostly achieved by chemical vapor deposition (CVD) [3], in some cases also by electrodeposition [8]. In order to obtain a single NW for sensor applications, electron beam lithography (EBL) and/or focused ion beam (FIB) techniques are often used to select and contact a single crystalline nanostructure from randomly grown NWs [1–4,7,8]. These bottom-up approaches yield a high crystal quality but are not applicable for mass production. In contrast to these previous works, we are using a top-down approach, where a single NW with well-defined position and geometry is

\* Corresponding author. Tel.: +49 681 302 4182; fax: +49 681 302 4699.

E-mail address: [m.afshar@imm.uni-saarland.de](mailto:m.afshar@imm.uni-saarland.de) (M. Afshar).



526

M. Afshar et al. / Sensors and Actuators B 215 (2015) 525–535

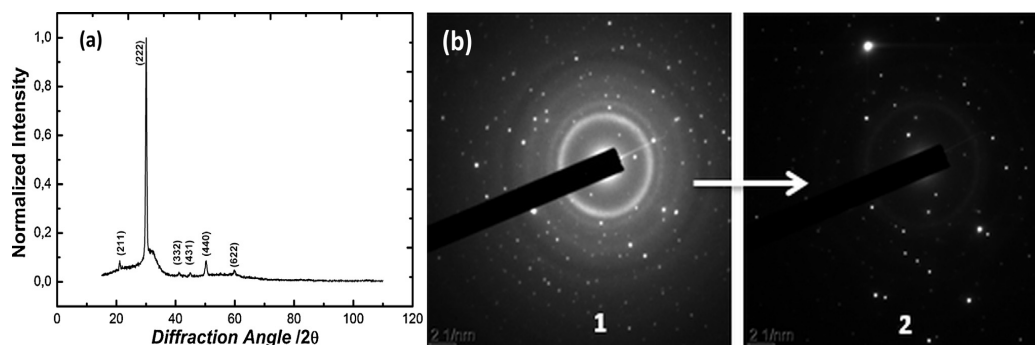


**Fig. 1.** (a) The X-ray diffraction spectrum of the ITO layer exhibits a strong peak from (222) planes with a slight amorphous background. It was reactively sputtered in an  $O_2/Ar$  atmosphere with an oxygen flow ratio of 3.3% out of 60 sccm total flow; (b) SAED pattern of ITO film outside (1) and inside (2) the laser-illuminated area. Laser exposure improves the crystallinity, and the amorphous background disappears.

nanofabricated directly by employing a femtosecond laser beam [9–11] in combination with a subsequent etch step.

In this way, we can generate polycrystalline ITO single NWs with lateral dimensions in the range from 60 nm up to about 1  $\mu m$  [9–11]. Due to high writing speeds in the range of mm/s this method is applicable for mass production.

ITO in a typical composition is a transparent conducting oxide with a wide optical band gap and a highly degenerate electrical conductivity. It has numerous applications in display technologies, in organic light emitting diodes (OLEDs) and in photovoltaics. ITO can be considered as doped  $In_2O_3$ , which is a very common material for gas detection [12]. ITO is being commercially used in thin film sensors for the detection of oxidizing gases such as  $NO_2$  and ozone [13]. In this article, we report on the fabrication technology of ITO polycrystalline NW gas sensors and on their sensor performance with and without self-heating effect.

The gas sensing interactions of metal oxide semiconductors at low temperatures can be more selective than sensing interactions on heated layers due to the presence of adsorbed humidity layers when gas interacts with adsorbed water e.g. in terms of an acid base reaction [14]. Above 200  $^{\circ}C$  some complex chemical reactions determine the sensor behavior; poisoning of the surface and even an oxygen disequilibrium in subsurface regions takes place at temperatures above 400  $^{\circ}C$  [15]. Generally, the measurements shown in this article are performed in the range of low temperatures, up to about 200  $^{\circ}C$ .

## 2. Experimental

### 2.1. ITO film preparation

Polycrystalline ITO films with a thickness of  $125 \pm 25$  nm were deposited on 150  $\mu m$  thick glass substrates by reactive magnetron DC-sputtering (von Ardenne LS 730S). A compound 4-in. indium-tin (90:10) target was used in an  $Ar/O_2$  plasma. The deposition was optimized with respect to crystallographic structure and optoelectrical properties of the films, which strongly depend on the oxygen content and on sputtering conditions. Our studies were performed with samples, which were sputtered at a chamber pressure of 0.003 mbar with an oxygen flow rate of 2 sccm corresponding to 3.3% of the total  $Ar/O_2$  flow rate of 60 sccm. Such conditions yield layers with high electrical conductivity, allowing for a metallic contact to the pads (see Section 5).

### 2.2. ITO film characterization

The crystallinity of the films was analyzed by grazing incidence X-ray diffractometry (GIXRD), which showed a strong peak from

(222) crystal planes (Fig. 1a). Atomic force microscopy (AFM) was used to examine the roughness of the surface (Veeco Image 3100). Scanning electron microscopy (SEM) was used to characterize the fabrication results on the nanometer scale.

The optical characterization of ITO films was performed by using transmission/reflection UV–vis spectroscopy (Cary 5000 spectrometer, VARIAN). Varying the oxygen flow at constant chamber pressure resulted in minor changes of the absorption edge, but single photon absorption at the laser wavelengths remains negligible [9]. Due to a very high intensity of the laser beam with a peak power in the terawatt range, we are dealing with nonlinear absorption processes in the material.

The film conductivity was examined by four-point probe measurements. ITO films sputtered at 100 W exhibited metal-like electrical conductivities (Table 1). The temperature coefficient of resistivity (TCR)  $\alpha$  in air is positive in the measurement range of 0–90  $^{\circ}C$  (Table 1). The charge carrier density in the ITO layers was determined by Hall measurements using a van der Pauw method, yielding a value of  $5.2 \times 10^{20} \text{ cm}^{-3}$  in a 190 nm thick ITO layer with a mobility of  $8.5 \text{ cm}^2 \text{ V}^{-1} \text{ s}^{-1}$ . This macroscopic effective mobility value is an average over charge densities in amorphous boundary layers and single crystal grains and is one order of magnitude below the mobility in single crystal grains. The reduction of the mobility is caused by traps and scattering centers both in the oxygen-rich and tin-rich amorphous grain boundaries [16]. This density value was used to calculate the thickness of the skin effect.

### 2.3. Laser processing

The sputter-deposited film was modified by using a compact optical setup (Fig. 2). The laser beam of a broadband mode-locked Ti:sapphire laser (Integral Pro 400, FemtoLasers) was fed into an inverted microscope (Zeiss AxioObserver.D1) with a galvoscan module (Jenlab GmbH), which focuses the beam into the sample through an oil immersion objective (Zeiss EC Plan Neofluar 40 $\times$ , NA=1.3) mounted on a piezo-actuator to adjust the focal plane vertically with nanometer precision. The laser is operated at a center wavelength of 800 nm (bandwidth 120 nm) with a repetition

**Table 1**  
Properties of the sputtered ITO thin film. The surface roughness  $R_{rms}$  was obtained from AFM measurements. The electrical resistivity ( $\rho$ ) and temperature coefficient ( $\alpha$ ) result from electrical measurements. The film thickness ( $d$ ) was determined by SEM images of focused ion beam sections.

$O_2$ [%]	$R_{rms}$ [nm]	$\rho$ [ $10^{-4} \Omega \text{ cm}$ ]	$\alpha$ [ $10^{-3} \text{ K}^{-1}$ ]	$d$ [nm]
3.3	0.516	4.37	1	100

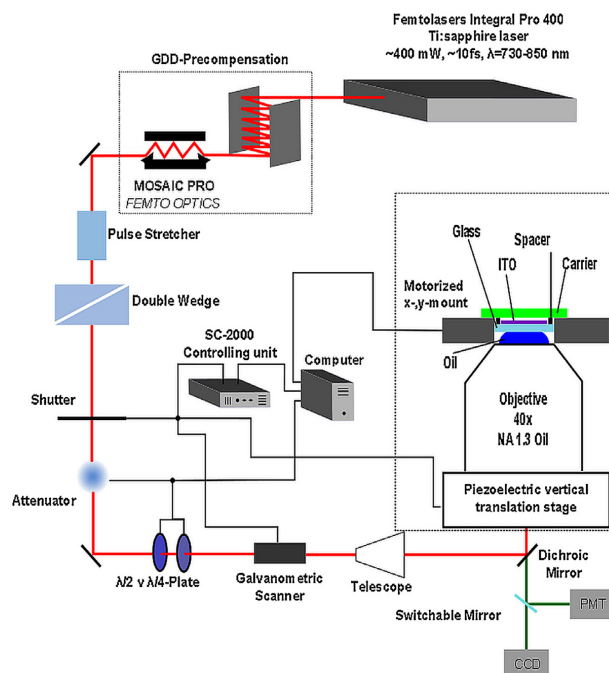


Fig. 2. Nanoprocessing setup based on a 10-fs Ti:sapphire laser combined with an inverted high-resolution optical microscope. The beam is prechirped in a group dispersion delay precompensation unit in order to maintain a pulse length of 12 fs in the focal spot. After passing through an attenuator it is scanned across the ITO-sample via a pair of galvanometric scan mirrors.

rate of 85 MHz emitting 7-nJ pulses of 10 fs duration. A group dispersion delay precompensation unit chirps the laser pulses and, in combination with a double glass wedge, yields a pulse length of approximately 12 fs at the sample position. The ITO films were illuminated through the substrate with linearly polarized light using galvanometric scan mirrors. A scan controller (GSI Lumonics SC2000) allows precision manufacturing of complex shapes over a scan range of 250  $\mu\text{m}$ . The exposure time of the samples was controlled by a mechanical shutter with a response time of 1 ms. The entire scan procedure was controlled by LabVIEW software.

For our ITO layers the applied fluence range is below the single-pulse ablation threshold [9,10]. The absorption in the range of the laser spectrum arises both from the single photon absorption by electrons in and close to the conducting band and from additional multi-photon absorption processes, which are induced by the focal peak intensity in the order of  $10\text{ TW}/\text{cm}^2$ . The modified region can reach extremely small lateral dimensions of less than 100 nm by minimization of the effective absorption volume via the focal fluence. For this purpose, we used an average focal power of 14–17 mW and a scan speed of  $300\ \mu\text{m s}^{-1}$  (corresponding fluence  $0.16\ \text{J cm}^{-2}$ ) to generate structures with lateral dimensions of 700 nm. The wires used in this study exhibit a length of 200  $\mu\text{m}$  or 90  $\mu\text{m}$  with a straight linear shape in order to get a system of low complexity, which simplifies simulation as well as characterization in regard to temperature dissipation and current density distribution.

#### 2.4. Chip fabrication

After ITO sputtering we used conventional lithography with an image reversal photoresist (AZ5214 E from AZ Electronic Materials GmbH) for a lift-off process to generate gold pads on the ITO films. Gold was used as electrode material because of its corrosion

resistance with respect to ITO etchants (hydrochloric acid, HCl) as well as to an  $\text{NO}_2$  atmosphere. After sputter deposition of gold (without adhesion layer) the sample was immersed in an acetone ultrasonic bath to remove the photoresist and to lift off the gold layer. In this way, samples were prepared for laser processing and subsequent wet etching in HCl without necessitating an additional lithography step. Fig. 3 shows a schematic view of these fabrication steps.

Laser illumination was performed from the backside of the sample through the substrate. The length of the wire was numerically controlled by coordinate points in a text file including the scan speed data. Focusing the beam into the film with a thickness of  $125 \pm 25\ \text{nm}$  thick was performed manually using the microscope's CCD camera by adjusting the focal luminescence intensity of the ITO layer under laser illumination at low intensities.

Similar to previous reports we observed that laser processing with the proper set of parameters can change the degree of crystallization in the exposed regions as verified by selected area electron diffraction (SAED) patterns as shown in Fig. 1b. We also verified this transition indirectly, by etching the layer at room temperature in 10% HCl. The laser-modified regions proved to be substantially more resistant against HCl and were not attacked within a few minutes of etching. Non-illuminated film areas, in contrast, were removed completely [9–11,17]. The result is shown in the SEM image in Fig. 4a at two different magnifications for a NW of 200  $\mu\text{m}$  in length and 700 nm in width. The final steps were dicing and wire bonding of the chips. Fig. 4b shows a chip mounted on a TO-8 socket.

#### 2.5. Sensor operation and gas measurements

The electrical characteristics of the mounted sensors were measured at various temperatures and gas atmospheres. Joule heating changes the NW's temperature. A voltage across the NW was

528

M. Afshar et al. / Sensors and Actuators B 215 (2015) 525–535

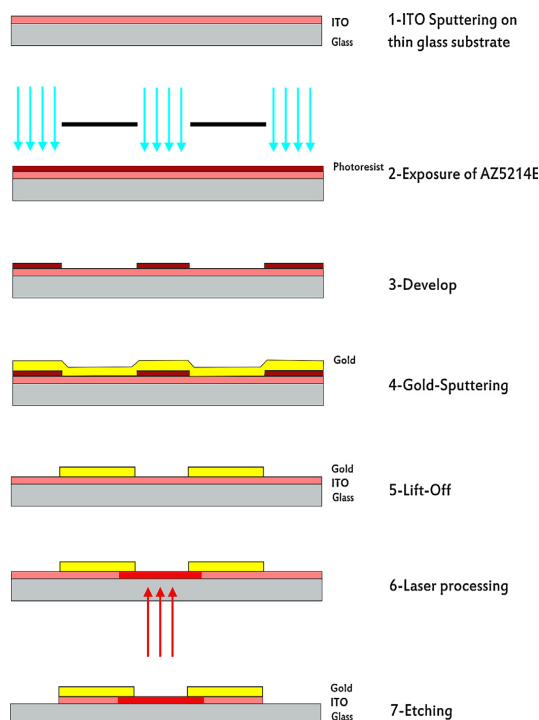


Fig. 3. Schematic diagram of the fabrication process. Main steps include sputtering, lithography, lift-off, laser writing and subsequent etching.

utilized to simultaneously heat the NW and measure its conductance. Two different operation modes were used. First, we used an adaptable constant voltage across the NW. The disadvantage of this mode is that the power dissipation changes with the resistance of the sensor. Therefore, the second set-up uses a constant power to keep the sensor temperature constant at higher temperatures. The constant power source was realized by multiplying the measured current and voltage across the NW, using an analog multiplier (AD633JN). The multiplier's output is used as feedback for an analog control loop. For measurement at ambient temperatures we used small constant voltages. FEM simulations and tests showed that at 0.2 V the energy dissipation of  $20 \mu\text{W}$  only causes negligible self-heating, resulting in nearly ambient temperature measurements (Fig. 5a).

The gas measurements are performed using a gas mixing system. We use a test gas mixture of 1000 ppm  $\text{NO}_2$  in synthetic air, which is diluted with dry and humid synthetic air using mass flow controller (MKS 1179A Mass-Flo). A gas-washing bottle produces the humid air. Throughout the measurements, the flow was kept constant at 200 sccm with 50% relative humidity.

### 3. Results and discussion

We demonstrate a novel and flexible way of fabricating single NW gas sensors. The structures were realized by laser beam writing of ITO thin films in combination with conventional microsystem processes. The NWs fabricated for gas detection possess a width and length of 350 nm/90  $\mu\text{m}$  and 700 nm/200  $\mu\text{m}$ , respectively,

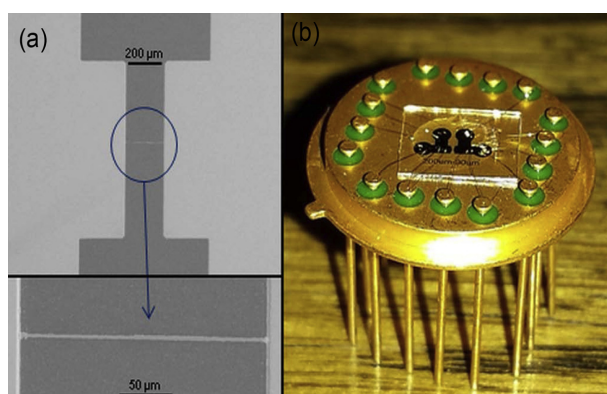
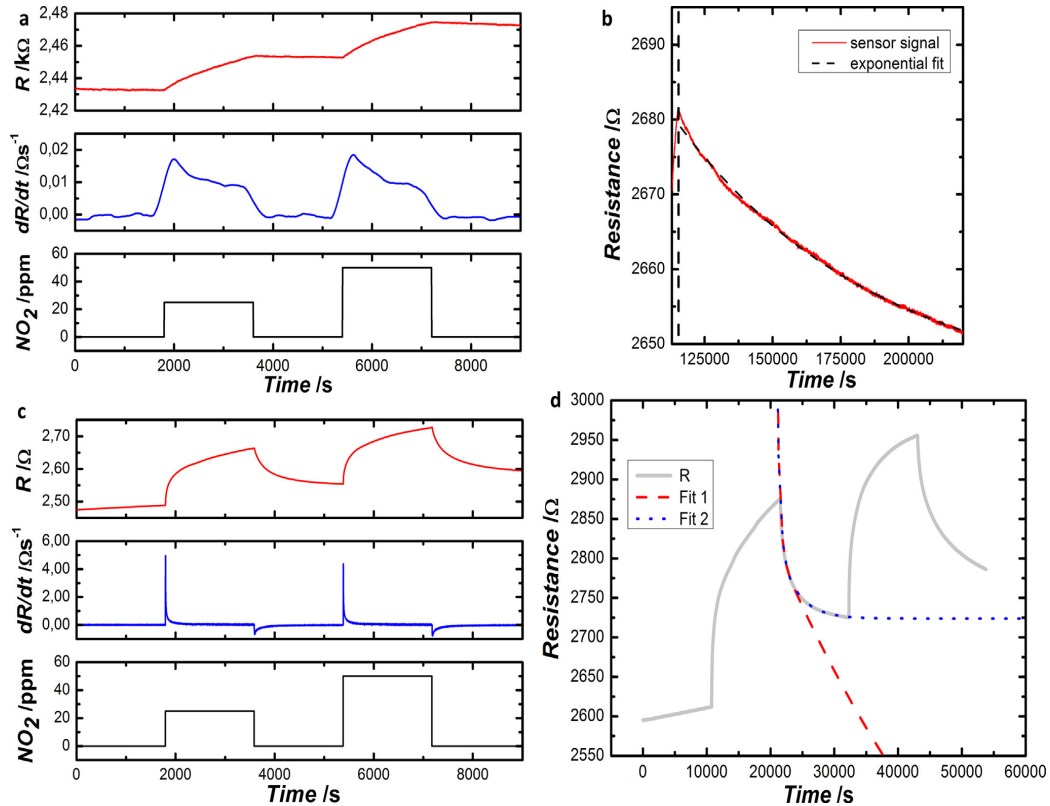


Fig. 4. (a) SEM-graphs of a laser-induced ITO wire with 200  $\mu\text{m}$  length and 700 nm width running between two gold pads; (b) a camera photo of the same chip after dicing and wire bonding on a TO-8 socket.



**Fig. 5.** (a) Response of the two parallel NWs ( $l \approx 200 \mu\text{m}$ ,  $w \approx 700 \text{ nm}$ ,  $t \approx 150 \text{ nm}$ ) at ambient temperature to the exposure of  $\text{NO}_2$  in synthetic air (50% r.h.,  $V \approx 200 \text{ mV}$ ,  $I \approx 100 \mu\text{A}$ ,  $P \approx 20 \mu\text{W}$ ,  $\Delta T \approx 0 \text{ K}$ ); (b) recovery time of a NW-sensor in synthetic air after  $\text{NO}_2$  exposure at ambient temperature; (c) response of the sensor after increasing the voltage ( $V = 4 \text{ V}$ ,  $I \approx 1.6 \text{ mA}$ ,  $P \approx 6.4 \text{ mW}$ ,  $\Delta T \approx 70 \text{ K}$ ); (d) relaxation characteristic of NW-sensor fitted by two double exponential functions corresponding to two different relaxation processes.

corresponding to aspect ratios of more than 250 (Fig. 4). Laser processing and subsequent etching are optimized to an extent that even sub-100 nm widths can be realized [9]. The fabrication is explained in detail in the experimental part (Section 2). Due to the degeneracy of the semiconductor the NWs exhibit a low resistance of a few k $\Omega$ , which makes it possible to use them as self-heating resistive gas sensors with low power consumption (below 5 mW). For a detailed description of the electrical characterization of these sensors see Section 5.

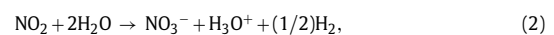
The sensors were exposed to  $\text{NO}_2$  at two different temperatures and at two different gas concentrations in the ppm range. First results are shown in Fig. 5. Low power measurements ( $20 \mu\text{W}$ :  $U = 200 \text{ mV}$ ,  $I \approx 100 \mu\text{A}$ ) at room temperature with negligible self-heating exhibit a long relaxation time, indicating that the desorption process follows a first order exponential function with a time constant  $\tau_1$  of approximately  $7 \times 10^4 \text{ s}$ , which is nearly 20 h (Fig. 5a and b):

$$R = R_0 + A_1 \exp\left(\frac{-\Delta t}{\tau_1}\right), \quad (1)$$

where  $R_0$  and  $R$  are the resistances before and after gas exposure,  $\Delta t = t - t_0$  is the elapsed time between both measurements, and  $A_1$  is a scale factor. Under these conditions, the sensor shows an integrating (accumulating) response when exposed to  $\text{NO}_2$ . Fig. 5 the resistance of the sensor and, in addition, its time derivative ( $dR/dt$ ) as a differentiated sensor output. The differential signal normalized by the gas concentration ( $dR/dt/C$ ,  $C$  is the gas concentration in ppm)

decreases continuously from  $7 \times 10^{-4}$  to  $1.8 \times 10^{-4} \Omega \text{ s}^{-1} \text{ ppm}^{-1}$  during the measurement (Fig. 5a), which indicates that the adsorption is approaching a saturation value. Thus, it exhibits a gas dosimeter like behavior with a non-linear response. In order to reset the NW resistance to its initial value, its temperature needs to be increased through self-heating by increasing the applied electrical power [18].

Many studies show, that the surface of metal oxides and other semiconductors absorb a thin layer ( $\sim 1 \text{ nm}$ ) of condensed humidity from the air, which plays an important role in determining their gas sensing properties [14]. From the literature, it is known that a water monolayer may be present on metal oxides up to temperatures of about  $100^\circ\text{C}$  and that they affect the electrical properties of the sensing films by changing their surface conductivity [14–16,18,19]. While a water monolayer inhibits the response to many reducing gases (e.g. CO), acid gases like  $\text{NO}_2$  (and alkaline gases like ammonia) show a strong response. The assumed mechanism is the dissolution and dissociation of the atmospheric  $\text{NO}_2$  in the surface adsorbate layer:



which leads to a pH change [14]. The pH change in the surface electrolyte layer (SEL), in turn, produces a change in the surface conductivity of the underlying sensing layer. If we take this mechanism as basis for a possible model of explanation, a key prerequisite that such a surface conductivity change does indeed happen is that

530

M. Afshar et al. / Sensors and Actuators B 215 (2015) 525–535

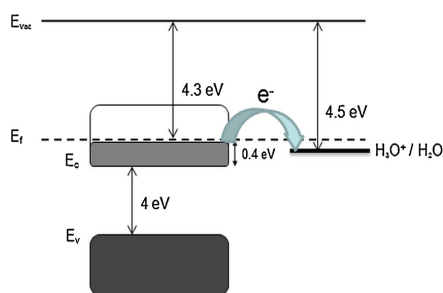


**Fig. 6.** Band diagram model of the interface between ITO and a surface electrolyte layer with dissociated  $\text{NO}_2$  molecules. The energy level of  $\text{H}_3\text{O}^+$  is 0.2 eV below the Fermi-level of ITO, enabling a charge ( $e^-$ ) transfer from ITO into the electrolyte.

there is a reasonable match between the redox level in the SEL and the positions of the conduction or valence bands in the underlying solid. The energy band diagram in Fig. 6 shows that there is indeed an appropriate match between the redox level of the  $\text{H}_3\text{O}^+$  ions in the SEL and the conduction band in the ITO NW. Whereas the first level is situated about 4.5 eV below the vacuum energy ( $E_{\text{vac}} = 0$ ), the ITO conduction band is at  $E_c - 4.3$  eV [20]. A transfer of electrons from the ITO NW to the SEL therefore can take place, which discharges a fraction of the  $\text{H}_3\text{O}^+$  ions in the SEL, leaving a negative excess charge of remaining  $\text{NO}_3^-$  ions there. An equal number of positively charged tin donors in the ITO-NW compensate this negative excess charge. This electrical double-layer, in turn, produces an upward band bending at the surface of the ITO-NW and a concomitantly lower sub-surface conductivity in the ITO, which signifies the presence of the  $\text{NO}_2$  in the ambient air. Our further studies are going to test this model with the help of resetting the process e.g. with gases which make the SEL basic, like ammonia.

A significantly different situation arises, when the operating voltage of the ITO-NW is raised to constant 4V, which corresponds to a power dissipation of  $\approx 6.4$  mW. Under these latter conditions, with elevated temperatures we observed significantly shorter response and drastically reduced recovery time constants. These changes are due to a significant temperature rise of about 70K, induced by self-heating (Fig. 5c). Fig. 5d shows that after the termination of a gas exposure non-exponential decays are observed, which however, can also be modeled by invoking two exponential decays involving different decay time constants  $\tau_{r1}$  and  $\tau_{r2}$ . Similar observations were also made upon gas exposure. Non-exponential decays arise in case the desorption process involves bi-molecular or even higher-order processes. Not being able to argue on such a molecular scale, we prefer an interpretation in terms of two independent mono-molecular processes both in the gas response and in the recovery from a gas exposure. In this way, we were able to extract two time constants  $\tau_{s1}$  and  $\tau_{s2}$  for the response and two more time constants  $\tau_{r1}$  and  $\tau_{r2}$  for the recovery process. In this way, the impact of the sensor operation temperature and of the length of gas exposure time on these parameters could best be illustrated.

Table 2 gives an overview on these time constants for a relatively short time measurement (1800 s) and for a longer time measurement (10,000 s). In the sensing signal there are clearly two time constants ( $\tau_{s1}$ ,  $\tau_{s2}$ ), which directly correlate to two additional time constants ( $\tau_{r1}$ ,  $\tau_{r2}$ ) in the recovery signal. The orders of magnitude of the s1- and r1- as well as s2- and r2-constants stay within the same range for 25 ppm and 50 ppm (see Table 2). Similar correlations of response time and recovery time constants were previously observed in low-temperature studies on  $\text{SnO}_2$  sensors [15].

Shorter time constants are found at 25 ppm. On recovery, time constants of  $\tau_{r1} \approx 100$  s and  $\tau_{r2} \approx 600$  s can be observed, indicating

**Table 2**

Time constants of the double exponential fit for different measurements with 25 and 50 ppm  $\text{NO}_2$  gas flow in short time (1800 s) and a long time (10,000 s) measurement (curves in Fig. 2c).

Measurement	Long time	Short time	Measurement	Long time	Short time
25 ppm $\text{NO}_2$			50 ppm $\text{NO}_2$		
$\tau_{s1}$ [s]	440	60	$\tau_{s1}$ [s]	350	60
$\tau_{s2}$ [s]	3100	1200	$\tau_{s2}$ [s]	4000	1000
$\tau_{r1}$ [s]	300	100	$\tau_{r1}$ [s]	400	100
$\tau_{r2}$ [s]	4000	500	$\tau_{r2}$ [s]	3000	500

at least two distinct desorption processes with differing activation energies. Moreover, we have observed that the sensor reaction is not fully reversible on a time scale of 4 h. This is most likely due to irreversible adsorption at strongly binding surface states and due to volume processes triggered by changes in the gas concentration.

The overall shape of the sensor signals is consistent with many observations on  $\text{SnO}_2$  [19]. With temperature increases of about 140K by self heating a more reversible character is observed as shown in Fig. 7, applying lower concentrations down to 1 ppm. At this elevated temperatures we assume that surface electrolyte layers are no longer present and the sensor can be described by a classical model used for semiconductor gas sensors attributes changes in resistance  $S = (R/R_0) - 1$  to a change of the gas induced depletion layer, caused by trapping of electrons at surface states. In the case of oxidizing gases like  $\text{NO}_2$  additional negative charge at the surface and thence an increased depletion due to the adsorbed  $\text{NO}_2$  is expected. In the case of a single NW, this leads to a reduction of the effective cross section of the wire [4] assuming that the depletion zone is fully depleted. In our case, the depletion layer will be extremely small due to the high carrier concentration of more than  $10^{20} \text{ cm}^{-3}$ , which is estimated from Hall effect measurements (see Section 6). Using the Schottky approximation ( $\epsilon_f \approx 4$ ,  $V_s \approx 2$  V), the depletion layer width is estimated to be approximately 3 nm. The electron density in ITO grains is even higher than this average value of charge density [16] corresponding to an even smaller depletion layer widths. Calculations on the basis of a rectangular cross-section of the NW ( $w \approx 350$  nm,  $t \approx 100$  nm) yield a sensor response of about 4%.

The measured sensor response is extracted from a long time measurement (Fig. 8a) and lies between 8% and 16% resistance change for gas concentrations varying between 2.5 ppm and 50 ppm (see Fig. 8b). These measurements were done with a constant heating power of 4.5 mW ( $U \approx 5$  V,  $I \approx 900 \mu\text{A}$ ) which generates a temperature increase of about 140 K. The sensor response increases over the whole range of concentrations as illustrated by the linear fit in the double logarithmic graph shown in Fig. 8b. At a concentration of 50 ppm  $\text{NO}_2$  we have observed a sensor response of 15.8% which is significantly higher than the one expected from our simple depletion layer model for the surface reaction of a single NW. An obvious reason for this discrepancy lies in the polycrystalline nature of the ITO NWs. As the grain size ( $\approx 50$  nm) is considerably smaller than the length of the NWs ( $\approx 90 \mu\text{m}$ ), charge carriers need to cross many barriers as they move from contact to contact pad. If these internal barriers are accessible to the  $\text{NO}_2$  molecules, a larger gas response is expected than predicted by the model, which is actually observed. Similar effects for porous  $\text{In}_2\text{O}_3$  have been described by Wagner et al. [21].

The expected reducing character of CO on  $\text{SnO}_2$  sensors was not detected. At a concentration of 2000 ppm (18.9% oxygen in flow) a 0.05% reduction of sensor resistance is detected. The oxidation process of CO ( $\text{CO}^{\text{gas}} + \text{O}^{\text{surf}} \rightarrow \text{CO}_2^{\text{gas}} + 0.5\text{O}_2 + e^-$ ) does not affect the electron density of the ITO significantly due to the initially high intrinsic electron density.

The measurements were done repeatedly over several days stretched out over several weeks. The sensor was proved to be



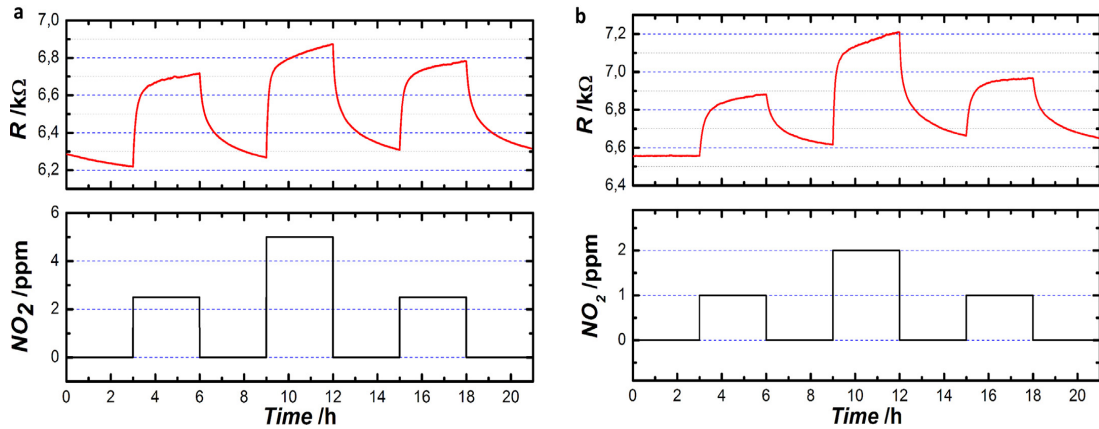


Fig. 7. (a) Response of a self-heated NW-sensor ( $l \approx 90 \mu\text{m}$ ,  $w \approx 350 \text{ nm}$ ,  $t \approx 150 \text{ nm}$ ) to the exposure of 2.5 ppm and 5 ppm  $\text{NO}_2$ , using constant heating power  $P = 3.93 \text{ mW}$  ( $\Delta T \approx 140 \text{ K}$ ,  $U \approx 5 \text{ V}$ ,  $I \approx 800 \mu\text{A}$ ); (b) response of the same sensor to a lower concentration of 1 ppm and 2 ppm  $\text{NO}_2$ .

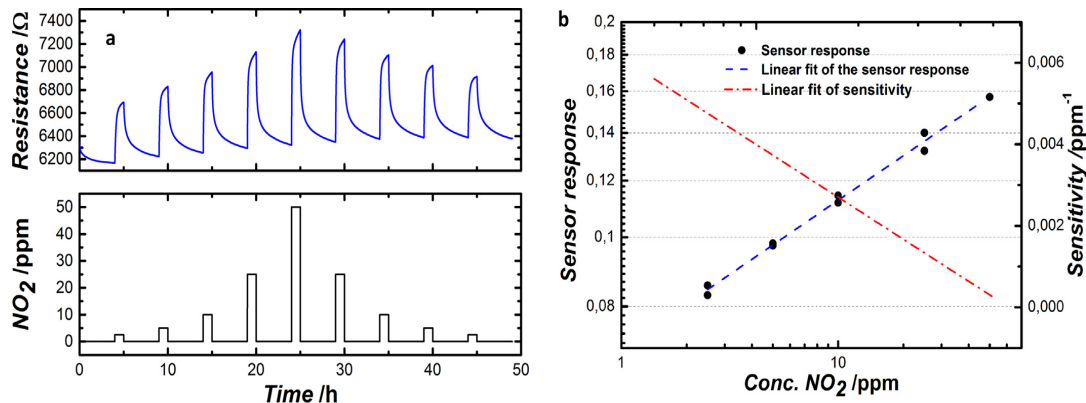


Fig. 8. (a) Long time response of a self heated NW-sensor ( $l \approx 90 \mu\text{m}$ ,  $w \approx 350 \text{ nm}$ ,  $t \approx 150 \text{ nm}$ ) to the exposure of  $\text{NO}_2$  with a constant heating voltage of 5 V ( $I \approx 900 \mu\text{A}$ ,  $P \approx 4.5 \text{ mW}$ ,  $\Delta T \approx 140 \text{ K}$ ); (b) sensor response and sensitivity ( $\Delta R / (R \cdot \Delta \text{Conc}_{\text{gas}})$ ) to different gas concentrations from 2.5 ppm to 50 ppm.

mechanically stable with a small electrical drift which is explained in Section 5. Further investigations concerning the sensor stability are under way and will be published in the future.

#### 4. Finite element method simulation

Because of the small dimensions of the wires, it was impossible to use thermography for the investigation of self-heating. Therefore, FEM simulations with *COMSOL Multiphysics* were used to obtain reliable estimates for the self-heating in wires and the influence of different designs and dimensions. Fig. 9a shows FEM-simulation curves of the self-heating process in air over a voltage range of 0–7 V for a reference NW ( $l \approx 200 \mu\text{m}$ ,  $w \approx 700 \text{ nm}$ ,  $t \approx 150 \text{ nm}$ ) on a glass substrate connected to the gold pads. In one case (dotted line) the backside of the substrate was defined as a surface maintained at a constant room temperature of 293 K (non convective), while in the other cases (solid and dashed lines) heat conduction values from the surfaces to the surrounding atmosphere of  $1 \text{ W m}^{-2} \text{ K}^{-1}$  and  $5 \text{ W m}^{-2} \text{ K}^{-1}$  (as heat transition constant), respectively, were introduced. Accordingly, higher temperatures are achieved when a lower heat conduction towards the surrounding environment is assumed.  $I$ - $V$  measurements were performed in air revealing that the real behavior comes closest to the calculation assuming  $1 \text{ W m}^{-2} \text{ K}^{-1}$ . Up to 3 V the experimental

values showed the same trend as the simulation. For higher voltages the time of measurement ( $\approx 6 \text{ s}$ ) was chosen shorter than the thermal saturation time constant ( $\approx 200 \text{ s}$  cf. Fig. 9c) in order to prevent a permanent change in the resistance or even a destruction of the NW. Therefore, the experimental values are below the simulated curve, which applies to stationary conditions.

Fig. 9b demonstrates how the temperature increases over different wire widths at 5 V for the same two boundary conditions mentioned above. The thermograph in Fig. 9c gives an overview of the temperature distribution on the chip for a change of about 70 K.

The large size of the gold pads has only a negligible impact on the heat distribution along the length of the wire, as shown in Fig. 9d. In the upper diagram, no gold pads at the ends of the wire were involved, whereas in the lower diagram the effect of gold pads was included. The temperature dependency of resistivity is not included in this simulation and the heat transfer to the surrounding air is assumed to be  $5 \text{ W m}^{-2} \text{ K}^{-1}$  at a constant backside temperature.

#### 5. Electrical properties

The temperature coefficient of resistance (TCR) of sputtered ITO was measured by a four point probe operated in air between  $0^\circ \text{C}$  and  $90^\circ \text{C}$ . In tin-doped indium oxide, tin atoms replace the  $\text{In}^{3+}$  ions and establish bonds to the oxygen-atoms as  $\text{Sn}^{4+}$ . They serve

532

M. Afshar et al. / Sensors and Actuators B 215 (2015) 525–535

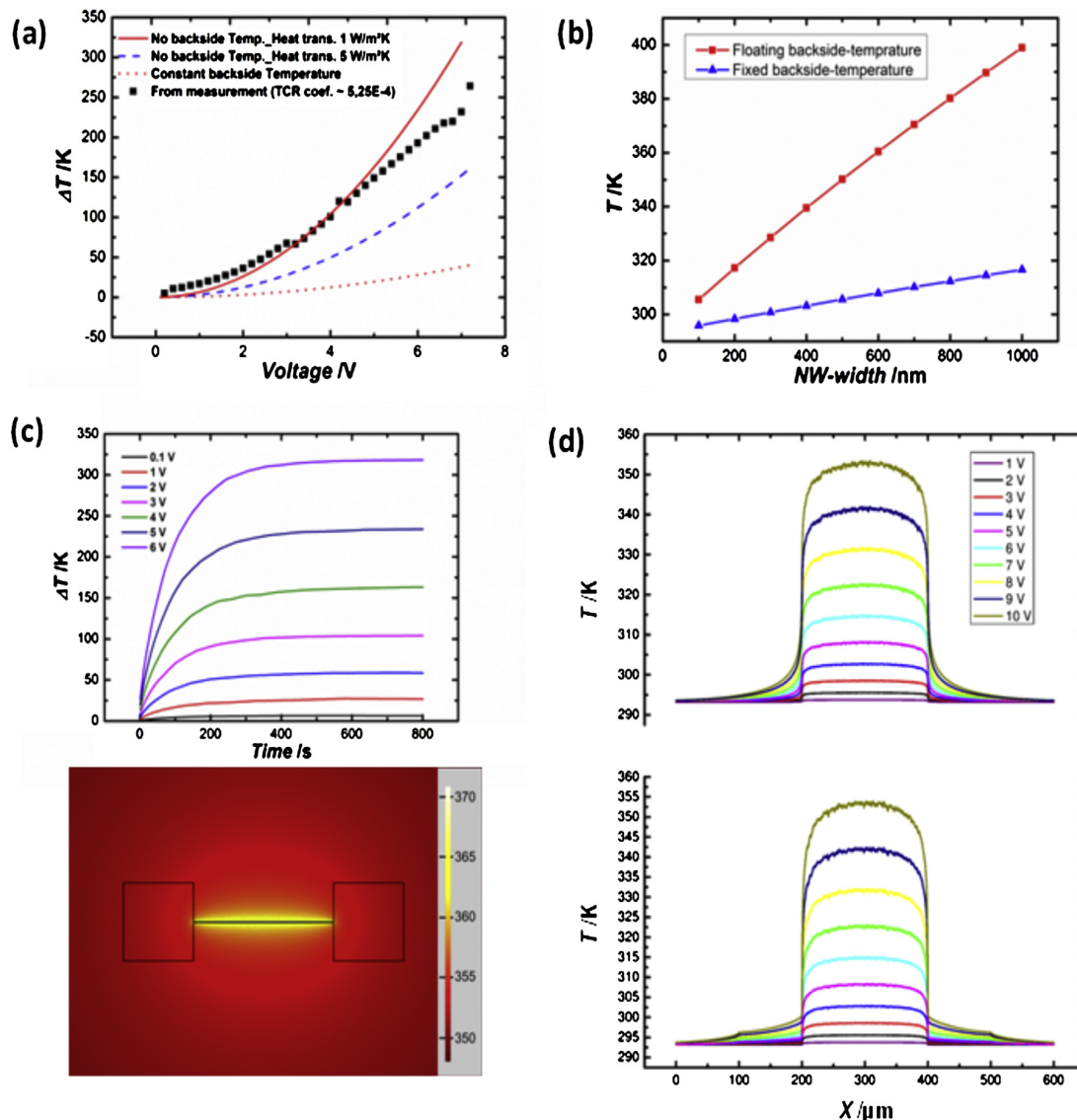


**Fig. 9.** FEM-simulation results for a reference NW ( $w=700$  nm,  $l=200$   $\mu\text{m}$ ,  $t \approx 100$  nm); (a) diagram of self-heating effect in this wire for different voltages with fixed temperature and convective boundary conditions on substrate backside with 1 and 5  $\text{W m}^{-2} \text{K}^{-1}$  heat transition constants compared to calculated values from  $I$ - $V$  measurements with TCR coefficients; (b) simulation of self-heating by 5 V for different widths of NW for a length of 200  $\mu\text{m}$ ; (c) a graphic image of temperature distribution on the substrate and the transient behavior of sensor temperature for different voltages by a heat transition constant of 1  $\text{W m}^{-2} \text{K}^{-1}$  as in vacuum conditions; (d) graph of the temperature in the wire for different voltages with and without gold pads at the periphery. The temperature dependency of resistivity is not considered. Heat transfer to the air is assumed by 5  $\text{W m}^{-2} \text{K}^{-1}$  and a constant backside temperature is used.

as electron donors (as well as the also present oxygen vacancies) and enhance the conductivity [22]. The results of the TCR measurement are shown in Fig. 10a as a linear average over 20 loops. The sheet resistance is drifting toward lower values. This occurs most probably because of Sn diffusion from the grain boundaries into the grains, which transforms passive Sn atoms into active donor sites, thus improving the conductivity [22,23]. The trend is always the same with a positive flank lead which gives a TCR coefficient of  $\alpha = 1.3 \times 10^{-3} \text{ K}^{-1}$  (for the as prepared film) (Table 2). After laser processing we studied  $\alpha$  using a NW with a length of 90  $\mu\text{m}$  and a width of 700 nm in a heatable chamber under an inert atmosphere (Fig. 10). The temperature was varied in the range from 25  $^{\circ}\text{C}$  to

95  $^{\circ}\text{C}$ . This experiment yielded a value of  $\alpha = 5 \times 10^{-4} \text{ K}^{-1}$ , which is smaller by about half an order of magnitude, as compared to the sheet value mentioned above. This empirical value of  $\alpha$  was taken for the simulations of the thermal distribution in the sensor. From the resistance of a wire after laser illumination a new resistivity of  $3.5 \times 10^{-4} \Omega \text{ cm}$  is determined; this shows an improvement of more than 25% compared to the initial value (Table 2) through laser modification.

The electrical properties of this sensor were characterized in vacuum ( $10^{-5}$  mbar) as well. In a first approximation, we observed a nearly linear behavior with current-voltage measurements between  $-5$  and 7 V as shown in Fig. 10b. These measurements

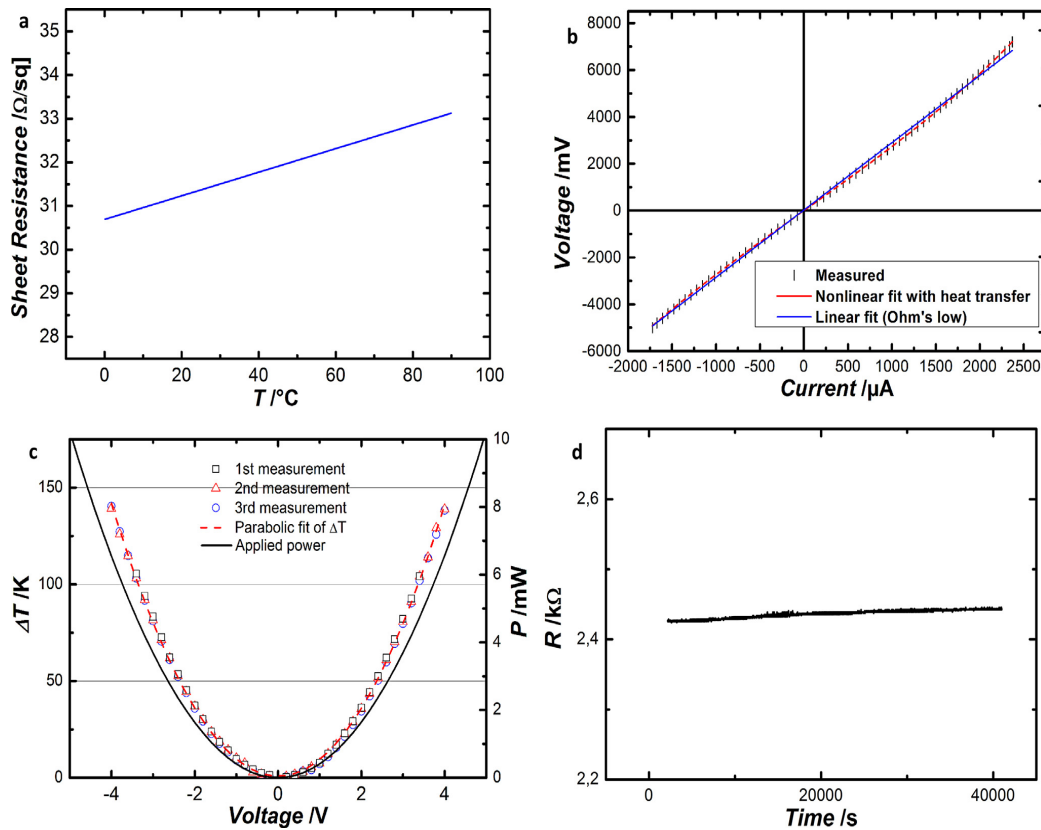


**Fig. 10.** (a) Temperature dependent four point measurement on the sputtered film in air which shows a positive thermal coefficient of resistance; (b) current–voltage diagram of the NW with 2674  $\Omega$  resistance ( $l \approx 90 \mu\text{m}$ ,  $w \approx 700 \text{ nm}$ ,  $t \approx 150 \text{ nm}$ ) in the range of  $-5$  to  $7 \text{ V}$  in vacuum; a linear-fit and a fit with TCR coefficient show an Ohmic character; (c) the calculated temperature increase caused by Joule heating in the measured NW of image (b) for three measurements; (d) a long time measurement with  $3.5 \text{ V}$  on a similar NW in semi-vacuum shows a slight drift over 10 h.

were taken using the four-point technique on the NW with a resistance of  $2674 \Omega$ . The results indicate that the Au/ITO interface exhibits an ohmic behavior. The slight increase of  $R$  at higher voltages (above  $3 \text{ V}$ ) is due to Joule heating. It can be approximated by including a correction term proportional to  $U^2$  (cf. TCR fit). The calculated temperature from the electrical measurement on the wire is shown in Fig. 10c which gives a parabolic fit depending on  $U^2$ .

Measurements taken over a longer period of time on wires with a relatively high current of  $1.4 \text{ mA}$  ( $3.5 \text{ V} - 2425 \Omega$ ) in vacuum ( $10^{-5} \text{ mbar}$ ) yielded an increase of resistance by about  $0.6\%$  over  $10.5 \text{ h}$  with a decreasing gradient (Fig. 10d). This drift was observed both in air and under gas exposure. It is 10 times higher in air as compared to vacuum, yielding a value of almost  $6\%$  over  $10.5 \text{ h}$ . Diffusion processes of oxygen atoms from the air into the ITO-layer, which accelerate the oxidation mentioned above, may be an explanation.

Initial measurements under gas exposure were performed using two parallel NWs with a width of  $700 \text{ nm}$ , a length of  $200 \mu\text{m}$  and a total resistance of  $2430 \Omega$  contacted with an electrically conductive adhesive. The sensor was placed in an airtight chamber with electrical feed-throughs. The change of resistance of the NWs under exposure to nitrogen dioxide ( $\text{NO}_2$ ) was measured, first with a constant current of  $0.97 \mu\text{A}$  corresponding to an energy dissipation of

$2 \text{ nW}$  (Fig. 5a) and later with constant voltage of  $200 \text{ mV}$  corresponding to an energy dissipation of  $20 \mu\text{W}$ . A comparison of the results obtained under constant current and constant voltage conditions indicates that there was no significant self-heating, leaving the sensor response times at an unaltered high value. This is in good agreement with the simulations (Fig. 9a) which predict that no significant self-heating would occur in this range. Next, we measured this sensor in a constant voltage modus using higher power settings ( $4 \text{ V}$ ,  $I \approx 1.6 \text{ mA}$ ) in order to achieve self-heating. This yielded a sensor behavior with a strongly reduced relaxation time as shown in Fig. 5c.

For the third method of measurement we used a single wire sensor with a length of  $90 \mu\text{m}$  operated at a constant power to achieve a more constant temperature. The gas concentration was reduced toward lower concentrations in order to study the sensor response (Fig. 8b). Under these conditions and after a long run-in time of about  $20 \text{ h}$  the tests resulted in an almost perfect sensor behavior of the wire as illustrated in Fig. 8b for gas concentrations of  $1$  and  $2 \text{ ppm}$ .

## 6. Conclusion

The results of our studies indicate that NWs produced by laser processing exhibit very promising behavior for self-heated gas sensors. Only few standard steps (sputtering, lift-off, laser writing and etching) are needed for the fabrication of such sensors. The method



to generate the NWs by laser writing is very flexible, so that a wide range of widths (100 nm to 1  $\mu\text{m}$ ) and lengths (5–200  $\mu\text{m}$ ) can be achieved without any lithography and without masks just by variation of laser parameters [9–11]. In this article we present NWs with 350 and 700 nm width and 90 and 200  $\mu\text{m}$  length from a film with  $125 \pm 25$  nm thickness. The resistors exhibit low noise so that even a moderate change of resistance at low gas concentrations can be detected reliably. The results show that low concentrations of  $\text{NO}_2$  (1 and 2 ppm) can be measured with higher sensitivity ( $\Delta_{\text{sensor response}}/\Delta_{\text{concentration}}$ ) and lower baseline drift (Fig. 8b), as compared to higher concentrations. Future efforts in the development of NWs will also focus on fabricating freely suspended NWs with reduced width and thickness, which would enhance the surface to bulk ratio of the sensor and induce more effective self-heating and lower energy consumption. We expect that these steps will increase the sensitivity down to the ppb range and further reduce response and recovery times. Future research should also clarify the dependence of the self-heating temperature on heating power, especially with respect to the stability of the NWs.

We conclude that our sensor cannot only be operated as a dosimeter at room temperature but also as a direct gas sensor at pulsed elevated temperature cycles. We expect to optimize the sensor and our measurement methods with the aim to obtain response times of less than 100 s at higher temperatures and with much lower power consumption.

#### Acknowledgments

We want to acknowledge the German Research Foundation (DFG) for financial support of this project within the Priority Program 1327 “Sub-100 nm structures for biomedical and technical applications”. We also want to thank Prof. F. Mücklich and his group for SEM and XRD measurements. The XRD equipment is funded by the EU project AME-Lab (European Regional Development Fund C/4-EFRE 13/2009/Br), which we gratefully acknowledge. Our special thanks go to Dr. Gerhard Müller for his valuable discussion and support.

#### References

- [1] M. Law, H. Kind, B. Messer, F. Kim, P. Yang, Photochemical sensing of  $\text{NO}_2$  with  $\text{SnO}_2$  nanoribbon nanosensors at room temperature, *Angew. Chem. Int. Ed.* 41 (2002) 2405–2407.
- [2] F. Hernandez-Ramirez, J. Rodriguez, O. Casals, E. Russinyol, A. Vila, A. Romano-Rodriguez, J. Morante, M. Abid, Characterization of metal-oxide nanosensors fabricated with focused ion beam (FIB), *Sens. Actuators B* 118 (2006) 198–203.
- [3] X. Chen, C.K. Wong, C.A. Yuan, G. Zhang, Nanowire-based gas sensors, *Sens. Actuators B* 177 (2013) 178–195.
- [4] F. Hernandez-Ramirez, J.D. Prades, R. Jimenez-Diaz, T. Fischer, A. Romano-Rodriguez, S. Mathur, J.R. Morante, On the role of individual metal oxide nanowires in the scaling down of chemical sensors, *Phys. Chem. Chem. Phys.* 11 (2009) 7105–7110.
- [5] N. Chinh, N. Toan, V. Quang, N. Duy, N. Hoa, Comparative  $\text{NO}_2$  gas-sensing performance of the self-heated individual, multiple and networked  $\text{SnO}_2$  nanowire sensors fabricated by a simple process, *Sens. Actuators B* 201 (2014) 7–12.
- [6] E. Bruneta, T. Maier, G. Mutinati, S. Steinhauer, A. Köck, C. Gspan, W. Grogger, Comparison of the gas sensing performance of  $\text{SnO}_2$  thin film and  $\text{SnO}_2$  nanowire sensors, *Sens. Actuators B* 165 (2012) 110–118.
- [7] J. Choi, J. Kim, Highly sensitive hydrogen sensor based on suspended, functionalized single tungsten nanowire bridge, *Sens. Actuators B* 136 (2009) 92–98.
- [8] O. Lupan, L. Chow, T. Pauporte, L. Ono, B.R. Cuenya, G. Chai, highly sensitive and selective hydrogen single-nanowire nanosensor, *Sens. Actuators B* 173 (2012) 772–780.
- [9] M. Afshar, M. Straub, H. Völlm, D. Feili, K. König, H. Seidel, Sub-100 nanometer structuring of indium-tin-oxide thin films by sub-15 femtosecond pulsed near-infrared laser light, *Opt. Lett.* 37 (4) (2012) 563–566.
- [10] M. Afshar, M. Straub, H. Völlm, D. Feili, K. König, H. Seidel, Sub-100 nanometer structuring of indium-tin-oxide thin films by sub-15 femtosecond pulsed near-infrared laser light, *Proc. IEEE Int. Conf. Nano/Micro Eng. Mol. Syst. (NEMS)* 6196813 (2012) 441–444.
- [11] K. König, M. Straub, H. Zhang, M. Licht, M. Afshar, D. Feili, H. Seidel, Sub-100 nm material processing with a sub-15 femtosecond laser scanning microscope, *J. Laser Appl.* 24 (2012) 42009-1–42009-9.

- [12] T. Wagner, T. Sauerwald, C.-D. Kohl, T. Waitz, C. Weidmann, M. Tiemann, Gas sensor based on ordered mesoporous  $\text{In}_2\text{O}_3$ , *Thin Solid Films* 517 (2009) 6170–6175.
- [13] “Ozone Sensor Module SP-61,” FIS Inc. 3-36-3 Kitazono, Japan.
- [14] A. Helwig, G. Müller, G. Sberveglieri, M. Eickhoff, On the low-temperature response of semiconductor gas sensors, *J. Sens.* 620720 (2009) 1–17.
- [15] B. Ruhland, T. Becker, G. Müller, Gas-kinetic interactions of nitrous oxides with  $\text{SnO}_2$  surfaces, *Sens. Actuators B* 50 (1998) 85–94.
- [16] D. Mergel, Z. Qiao, Dielectric modelling of optical spectra of thin  $\text{In}_2\text{O}_3$ :Sn films, *J. Appl. Phys. D: Appl. Phys.* 35 (2002) 794–801.
- [17] C.W. Cheng, C.-Y.ing Lin, W.-C. Shen, Y.-J. Lee, J.-S. Chen, “Patterning crystalline indium tin oxide by high repetition rate femtosecond laser-induced crystallization”, *Thin Solid Films* 518 (2010) 7138–7142.
- [18] I. Marr, A. Groß, R. Moos, Overview on conductometric solid-state gas dosimeters, *J. Sens. Sens. Syst.* 3 (2014) 29–46.
- [19] A. Helwig, G. Müller, J. Garrido, M. Eickhoff, Gas sensing properties of hydrogen-terminated diamond, *Sens. Actuators B* 133 (2008) 156–165.
- [20] O.N. Mryasov, A.J. Freeman, Electronic band structure of indium tin oxide and criteria for transparent conducting behavior, *Phys. Rev. B* 64 (2001) 233111–233113.
- [21] T. Wagner, C. Kohl, S. Morandi, C. Malagu, N. Donato, M. Latino, G. Neri, M. Tiemann, Photoreduction of mesoporous  $\text{In}_2\text{O}_3$ : mechanistic model and utility in gas sensing, *Chem. Eur. J.* 18 (2012) 8216–8223.
- [22] J.S. Kim, F. Cacialli, A. Cola, G. Gigli, R. Cingolani, Increase of charge carriers density and reduction of Hall mobilities in oxygen-plasma treated indium-tin-oxide anodes, *Appl. Phys. Lett.* 75 (1999) 19–21.
- [23] D. Mergel, W. Stass, G. Ehl, D. Barthel, Oxygen incorporation in thin films of  $\text{In}_2\text{O}_3$ :Sn prepared by radio frequency sputtering, *J. Appl. Phys.* 88 (2000) 2437–2442.

#### Biographies

**Maziar Afshar** was born in Tehran, Iran in 1979. He received his bachelor's degree in Physics from the University of Tehran in 2002. In 2004, he began to continue his studies in Physics at the Free University, Berlin and in 2008 he completed the research for his thesis which was performed at Helmholtz-Zentrum Berlin für Materialien und Energie (HZB, former HMI) in the field of “Growth and Characterising of Epitaxial Multilayers from  $\text{CuInSe}_2$  and  $\text{CuGaSe}_2$ ”. Since 2009, he has been working on his Ph.D. as research assistant to Labs for Micromechanics, Microfluidics/Microactuators (LMM) at the University of Saarland. His research concerns Laser Lithography, as well as Micro-Structuring and Nano-Structuring with Near-Infrared Femto-Second Laser for engineering applications.

**Elisabeth M. Preiß** studied Micro- and Nanostructures at the Saarland University in Saarbrücken, Germany and completed her studies in 2013 with a thesis on “Femto-Second Laser Induced ITO Nanowires for Gas Sensor Applications” at the Lab for Micromechanics, Microfluidics/Microactuators (LMM). She joined the Robert Bosch GmbH in Gerlingen, Germany in 2013 and is currently working on her Ph.D. in cooperation with the Saarland University. Her research focuses on physical vapor deposition techniques for metal oxides, miniaturized gas sensors and laser processing for microsystem technologies.

**Tilman Sauerwald** has received his Ph.D. at the University of Giessen in 2007 for investigations on the influence of surface reaction to the multi-signal generation of metal oxide sensors. He has worked in the field of nanostructured sensor material and bio-inspired sensor systems. His current focus is the detection of trace gases and the automated monitoring of the sensor function. His general scientific interests are the development of gas sensors and multi-signal operation modes for gas sensors.

**Marius Rodner** received his B. Sc. in Microtechnology and Nanostructures from Saarland University, Germany in 2013 about “Gas detection with Nanowires made of Indiumtin-oxide”. He is going to finish his M. Sc. degree at Saarland University in 2015. Currently he is working at his Master Thesis about gate bias modulation of Tungstenoxide SiC-FETs to enhance selectivity and sensitivity of the sensor.

**Dara Feili** was born in Shiraz, in 1969. He studied electrical engineering at the Technical University of Shiraz, focusing on communications systems. After his B.Sc. he began to work at IEI (Iranian Electrical Industry) on design and development of UHF and wideband omni directional antennas. Afterwards he changed to National Petrochemical Company (NPC) and worked on Kharg Methanol Project. 1999 he began to study electronic on Kassel University focusing on micro optical communication system (MOEMS and MEMS). 2001 he finished his master's degree with a thesis on development novel etch technology for III / V semiconductors, which was supervised by INA Institute (Institute of Nanostructure Technologies and Analytics). Subsequently he started working on his PhD-thesis on advanced technologies for neural stimulation electrodes at Fraunhofer institute for biomedical engineering (IBMT), which he finished in 2005. From then on, he headed the new materials and methods for neural electrode section at IBMT until he changed in 2006 to his current position at the Institute of Micromechanics, Microfluidics/Microactuators (LMM) in Saarland University.

**Martin Straub** received his Ph.D. in Physics from the University of Halle (Germany) in 1997 based on research in nonlinear magneto-optics at the Max-Planck Institute for Microstructure Physics. As a postdoctoral fellow in Prof. Stefan Hell's group at the Max-Planck Institute for Biophysical Chemistry in Göttingen (Germany) he

examined novel applications of multifocal multiphoton microscopy (1998–2000). At Swinburne University in Melbourne (Australia) he investigated photonic crystals and microdevices generated by two-photon photopolymerization (2000–2005). As a Senior Research Fellow at the Fraunhofer Institute for Photonic Microsystems in Dresden (Germany) he established a research group in silicon photonic crystal devices (2007–2009). Since 2010 he studies sub-15 fs laser-induced nanostructures on surfaces and in thin films at the Saarland University in Saarbrücken (Germany).

**Karsten König** is Full Professor and Head of the *Department of Biophotonics and Laser Technologies* at the Saarland University. He is also founder and president of the company JenLab GmbH. He gained the Ph.D. degree in physics and habilitation degree in cell biology from the University Jena. Prof. König published about 500 scientific papers in the field of biophotonics and laser material processing and pioneered fluorescence lifetime imaging, femtosecond laser nanoprocessing and laser transfection, and clinical multiphoton tomography.

**Andreas Schütze** studied Physics and received his doctorate in Applied Physics from Justus-Liebig-Universität in Gießen in 1994 with a thesis on micro gas sensor systems. After some years in industry, he joined the University of Applied Sciences in Krefeld, Germany, as professor for Microsystems Technology from 1998 to 2000. Since 2000 he is a full professor for measurement science and technology in the Department of Mechatronic Engineering at Saarland University, Saarbrücken, Germany. His research interests include microsensors and microsystems, especially

advanced chemical sensor systems, both for gas and liquid phase, for security and control applications.

**Helmut Seidel** studied physics at the Ludwig-Maximilian University in Munich and received his diploma for physics with a work on elementary particle physics at the Max-Planck Society in Munich (Werner-Heisenberg Institute for Physics) in 1980. He began his career as a research associate at the Fraunhofer Institute for Solid State Technology in Munich (until 1985) and at the Fraunhofer Institute for Microstructures in Berlin, where he was the head of the Department of Micromechanics (until 1986). During this period he received his Ph.D. at the Free University of Berlin with a work on electrochemical, anisotropic etching of silicon. Afterwards he joined the corporate research and development departments of several companies in the industry. At the department of micro system technology at MBB and later at DASA (now integrated into the European Aeronautic Defence and Space Company, EADS) he was significantly responsible for the setup of a clean room facility for silicon and microsystems technologies in order to develop micromachined devices for the aerospace industry. When this department later became part of the corporate research department of Daimler-Benz AG in 1993, the main focus switched to automotive applications. He was responsible for a large project to develop accelerometers for the airbag control unit. Starting from 1998 this sensor was produced in large quantities. From 1996 until his professorship at Saarland University he was responsible for the development department of automotive microsensors at TEMIC (a subsidiary of Daimler Chrysler, later belonging to Continental).

## 4.5 Freestanding ITO Nanowires; Fabrication and Simulation (Unpublished Data)

This Section is about a novel technique to make freestanding nanowires by releasing the nanowires presented in the previous Section. The study and results are unpublished data and will be submitted as a manuscript.

### 4.5.1 Introduction

After the fabrication of substrate attached ITO nanowires using sub-15 femtosecond laser pulses and their application as self-heated gas sensors, it becomes obvious, that the performance and energy consumption can be drastically improved by releasing the nanowires from the substrate and making them freestanding. This is caused by the decoupling of thermal energy dissipation to the substrate along the resonator. In addition, such nanowires can be used as electromechanical nanoresonators.

Mechanical resonators can be used to detect small adsorbed masses through shifts in oscillation frequencies [199]. Their size was reduced in recent decades parallel to technical achievements in micro and nanotechnology, specifically in lithography and material synthesis or deposition. Appropriate semiconductor and MEMS fabrication processes are applied by fabricating freestanding structures with geometrical dimensions on the micro- and nanometer scale. The dynamic behavior of such structures is defined through many physical parameters by designing and materials, which exhibit the eigenfrequencies of resonators. By reducing the resonator dimensions the eigenfrequency can reach MHz and even up to GHz [200, 201]. For the fundamental mode response of a simple doubly clamped beam, the following parameters are defined [202, 203]:

$$\text{effective vibatory mass : } M_{\text{eff}} = 0.735ltw\rho, \quad (4.15a)$$

$$\text{dynamic stiffness : } \kappa_{\text{eff}} = \frac{32Et^3w}{l^3}, \quad (4.15b)$$

$$\text{resonance frequency : } f = \frac{\omega_0}{2\pi} = \frac{1.05t}{l^2} \sqrt{E/\rho}, \quad (4.15c)$$

with length  $l$ , thickness  $t$  and width  $w$  of the beam.  $E$  is Young's modulus, and  $\rho$  is the mass density of the beam. These equations are valid for an isotropic material. In anisotropic, single crystalline nanowires the frequency is crystal orientation dependent.

Precise force, position and mass sensors have already been realized. The continuous down scaling of dimensions towards the nanometer range led to remarkable results, including nanoresonators with atomic mass resolution. Such nanoresonators can measure single atoms, molecules or viruses [201, 204, 205, 206, 207, 208, 209, 210, 211]. Such results make this field of

research very interesting with continuously growing application fields. Chemical, biological, gas specific and microfluidic transducers have already been demonstrated [207, 212, 213].

Reducing the dimensions to the nano scale is a technically challenging issue. The surface properties and their controlling, new fabrication and actuating/sensing techniques, reproducibility of nanostructures, and simulation of such NEMS are in focus of many studies [203]. At what size scale does continuum mechanics break down when simulating their mechanical properties and needs corrections from atomistic behavior is answered with molecular dynamics simulations for ideal structures [214, 215]. Studies indicate that continuum mechanics is still valid for structures down to the order of a few tens of lattice constants [203, 214, 215]. Quantum effects only start to become relevant at even smaller dimensions. Hence, for most current works in NEMS, continuum approximations appear to be adequate [203].

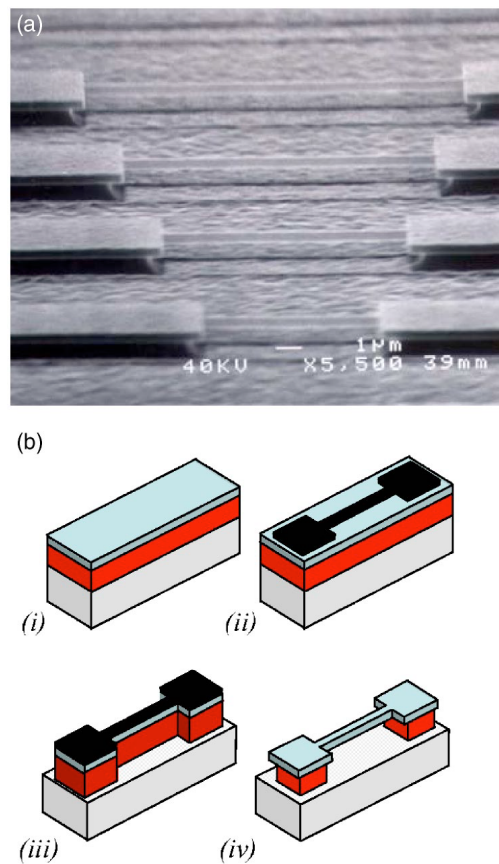


**Figure 4.8:** a) Scanning electron micrograph of SiC nanowires with different lengths and resonant frequencies ranging from 2 MHz to 134 MHz, b) Schematic diagram of process sequence [203].

The small dimensions of nanoresonators ensure low operating power, high responsivity due to high fundamental resonance frequencies [200], and mechanical quality factors ( $Q$ ) in the tens of thousands [202, 216].

In many cases a bottom-up process is used for fabrication where the nanostructures are generated separately and are later connected to the chip. The applied techniques for fabrication of nanoresonators are depending on materials. Nanotubes or monocrystalline nanowire

resonators must be delivered to the chip to be connected separately to electrical contacts in a bottom-up process. In contrast to this, top-down approaches make it possible to fabricate freestanding structures directly on chip with surface micro-/nanomachining techniques and by using a sacrificial layer technique (SL) as shown in Fig.4.8. Beside the growth of the active layers deposited by various methods, etching is another key process.

The functional as well as sacrificial layers are deposited with various methods such as chemical vapor deposition (CVD), molecular beam epitaxy (MBE), and reactive sputter deposition. The functional layers have to be etched in form of a beam and subsequently undercut isotropically to yield free-standing resonators. The etching process requires a mask, which is usually defined by deep-UV or electron beam lithography or in rare cases with other novel methods like electrospinning of PMMA nanofibers, aligned with photolithographically defined auxiliary structures [217].

The former technique has been already applied to silicon on insulator structures [218], gallium arsenide/aluminum arsenide (GaAs/AlGaAs) systems [219], silicon carbide (SiC) on silicon [220], aluminum nitride on silicon [221], nanocrystalline diamond films [222], and amorphous silicon nitride films [223].

Actuation mechanisms of nanomechanical resonators can be divided into local on-chip schemes and schemes relying on external excitation. On chip approaches are based on voltage-induced forces such as internal piezo-electric, capacitive, magnetomotive, electrothermal or static dipole-based dielectric, and dielectric gradient forces (Fig. 4.9). External actuation can be based on photothermal or inertia-based piezo-actuated schemes [224]. In many cases the readout can be a primary challenge in the NEMS field.

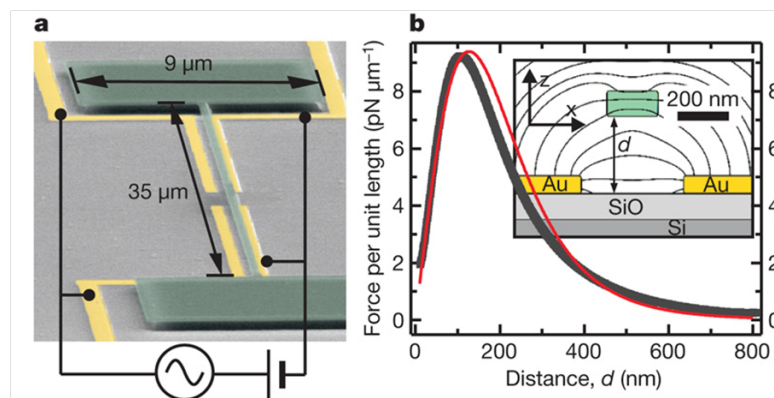


**Figure 4.9:** a) Scanning electron micrograph of a high stress silicon nitride NEMS with a width of 300 nm, b) Electrostatic force in the  $z$  direction in a cross-sectional view, versus distance  $d$  from the electrodes. FEM simulation (black) and approximation by an analytical fit (red) for  $V_{dc} = 2V$  [224].

Finite element simulations with COMSOL Multiphysics were performed to make a proper design. An electrothermal approach can be used for both applications, either as a self-heated chemical gas sensor or as an electromechanical nanoresonator. Both the resonance frequencies and the time dependent thermal behavior of the resonators were simulated.

The resonance detection can be done by an impedance measurement due to the change of resistance in the nanowire and/or by using the change of capacitance between sensing electrodes and the nanowire. Due to their very small dimensions the power consumption is in the  $\mu\text{W}$  and even  $\text{nW}$  range.

The aim of this work is to study the possibility of applying the previously developed 2D structuring method for 3D fabrication of freestanding nanowires of indium tin oxide. The applied approach in this work is a standard top-down approach for surface nanomachining, based on selective etching of a sacrificial layer with respect to ITO. The special feature is the integration of direct laser writing in combination with maskless wet etching steps. The possibility of applying an electrothermal actuating method is theoretically studied. Further information is given in the following Section <sup>5</sup>.

---

<sup>5</sup>The idea and the experimental design originate from the author. The technical implementation and the simulations were supported by Michael Penth and Daniel Gillo in their bachelor's theses under the supervision of the author.

### 4.5.2 Addendum IV (Unpublished Data)

Based on the results achieved for laser scribed substrate-supported ITO nanowires, a new method is developed to fabricate freestanding nanowires, which can also be used for gas sensor applications. In addition to the same approach of laser writing and subsequent wet etching, a sacrificial layer technique was used as a standard surface nanomachining method to release the wires from the substrate. Aluminum nitride (AlN) was introduced as nonconductive transparent sacrificial layer on top of a glass substrate and beneath the structural ITO layer. A tightly focused laser beam (Ti:sapphire near infrared) was used to illuminate the ITO layer from the back through the substrate and through the sacrificial layer.

The mechanical properties of the sputtered ITO layer are a deciding factor for a suspended structure. As mentioned in Chapter 2, nanoindentation was applied to measure Young's modulus (E) and Hardness (H) of the sputtered polycrystalline ITO layer after laser illumination. Average values of about 90 MPa for E and 9 MPa for H were measured (see Section 2.2.1). These values are used in analytical and numerical simulated mechanical models.

The thickness of the functional layer and of the sacrificial layer is controlled by deposition parameters. The thickness of the sacrificial AlN layer was chosen to be 500 nm, defining the gap below the double side clamped nanowire after release. The thickness of the ITO nanowire was set to be around 100 nm by choosing the proper sputter parameters. The typical thickness tolerance obtained on a wafer was  $\pm 10\%$ .

AlN can be sputtered with low stress, low surface roughness and high transparency. It can be etched selectively with respect to ITO in phosphoric acid ( $\text{H}_3\text{PO}_4$ ), thus satisfying all requirements for a sacrificial layer. The substrates are 4 inches alkali-free  $145\ \mu\text{m}$  SCHOTT glass wafers (AF32  $\text{\textcircled{R}}$ eco). After a standard cleaning process with acetone and isopropanol in an ultrasonic bath, AlN was reactively sputtered from a pure aluminum (Al) target in an  $\text{N}_2$  plasma with a chamber pressure of 0.004 mbar and with 1000 W power.

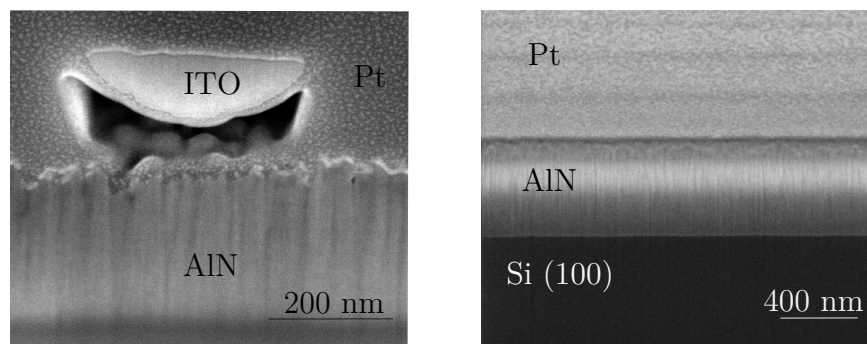


**Figure 4.10:** Electron microscopy micrograph of an AlN cross-section shows c-axis orientation as achieved by A. Ababneh [126].

The initial preconditioning of the pure Al-target is very important. To generate a clean, oxide free surface, the target was sputtered in argon plasma with 0.003 mbar pressure and 1000 W for 600 s. Afterwards a nitrogen conditioning of the target was performed in  $\text{N}_2$



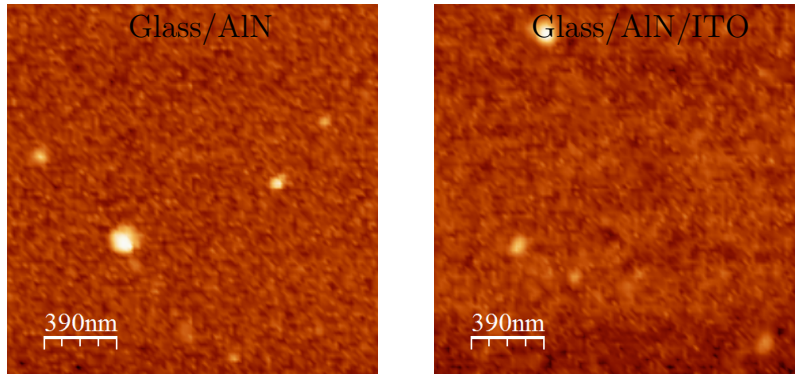


**Figure 4.11:** AFM measurements on sputtered AlN film on glass substrate (left) and the same sample after ITO sputtering on top (right).

plasma for 1800 s to obtain a well defined nitrogen concentration on the target surface using the same parameters as in the main deposition step (see Tab. 4.4).

The sputter deposition parameters optimized by A. Ababneh with respect to obtain a tightly packed growth with *c*-axis orientation on (100) silicon was used. In this case the crystallinity was analyzed by grazing incidence X-ray diffractometry (GIXRD). In this case of a glass substrate, a microscopic inspection (SEM) of the cross-section of the sputtered layer in combination with AFM surface measurements were used leading to the same results. A focused ion beam cut through the layer is shown in Fig. 4.10. A columnar structure is visible, giving a strong indication for *c*-axis orientation.

The next step is the fabrication of a 100 nm thick conductive ITO layer, which was deposited by reactive magnetron DC sputtering (LS 730S from *Von Ardenne*) with a compound metallic 6-inch Indium/Tin (90:10) target. A standard process with an Ar/O<sub>2</sub> plasma (gas flow 53:7 sccm) and a chamber pressure of 0.005 mbar was used. For obtaining reproducible results, the target must be oxidized with the same depth profile, as a critical preconditioning step. The best way to achieve this is by using the same parameters given in Tab. 4.4, aiming for a known voltage difference between target and anode of the machine.

The roughness of each layer was characterized by AFM measurements. It was applied to the glass substrate, to the sputtered AlN on glass substrate, and to the whole stack after sputtering of ITO on top. The topographies of surfaces are shown in Fig. 4.11. Starting by RMS roughnesses below 1 nm for glass substrates, 500 nm AlN on the substrate exhibited a RMS-roughness of 1.55 nm. After sputtering 100 nm ITO on top, this value was increased insignificantly to 1.9 nm.

The laser illumination through the substrate and the sacrificial layer requires a high optical transparency of AlN. Fourier transformed VIS to infrared spectroscopy in the range of 400 nm to 1100 nm was used to make transmission measurements. Fig. 4.12 shows that AlN reduces the transmission of glass by less than 10 percent and shows no absorption line in this range. By adding ITO on top the average transmission reduces again. The band edge of ITO is expected to be at 380 nm, which is reflected by the increasing absorption near this wavelength towards higher photon energies. For the relevant laser spectrum between 700 nm to 800 nm



there is still about 70 percent transmission available. The wavy character of the curves is caused by the interference effect of light in the AlN film.

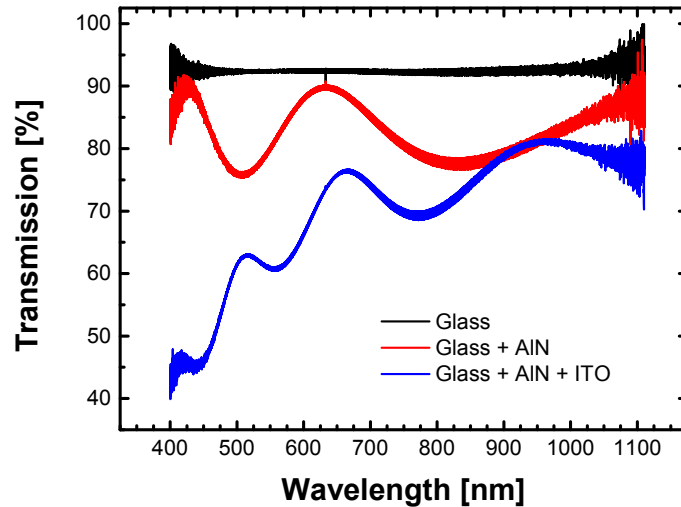


**Figure 4.12:** Change of transmittance of the glass substrate by adding of about 500 nm AlN and 100 nm ITO layers.

The metallic electrical interconnects were generated in a lift-off process. In a photolithography step, using an image reversal photoresist (AZ531B from *MicroChemicals GmbH*) was used for lithography. The exposure was done with the i-line of a mercury vapor lamp of a MA 1006 from *Karl Süss* mask aligner. The image reversal photoresist is applied as a positive photoresist just to benefit from its good thermal resistance in the subsequent sputtering step (see Fig. 4.13).

The used chrome mask was designed in *Clevin* and was written by a laser lithography machine from *Heidelberg Instruments GmbH*, using a positive photoresist on top of the chrome layer.

**Table 4.4:** An overview of sputter parameters used for the fabrication of freestanding ITO nanowires in this work.

Sputtering Parameters	AlN	ITO	Cr	Au	Ti	Pt
Power [W]	1000	100	100	50	1000	100
Ar [sccm]	0	53	80	80	60	80
N <sub>2</sub> [sccm]	50	0	0	0	0	0
O <sub>2</sub> [sccm]	0	7	0	0	0	0
Pressure [mbar]	0.004	0.005	0.003	0.003	0.003	0.003
Deposition Time [s]	1000	400	30	150	10	250
Thickness [nm]	500-600	60-80	5-10	200	5-10	200

Gold (Au) and, alternatively, platinum (Pt) were sputter deposited on the wafers prepared for the lift-off process. The typical thickness was about 150 nm. For adhesion, a very thin sputtered Cr layer is used in the case of gold, whereas Ti is used for Pt. All process parameter

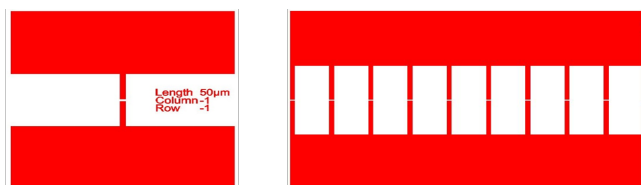
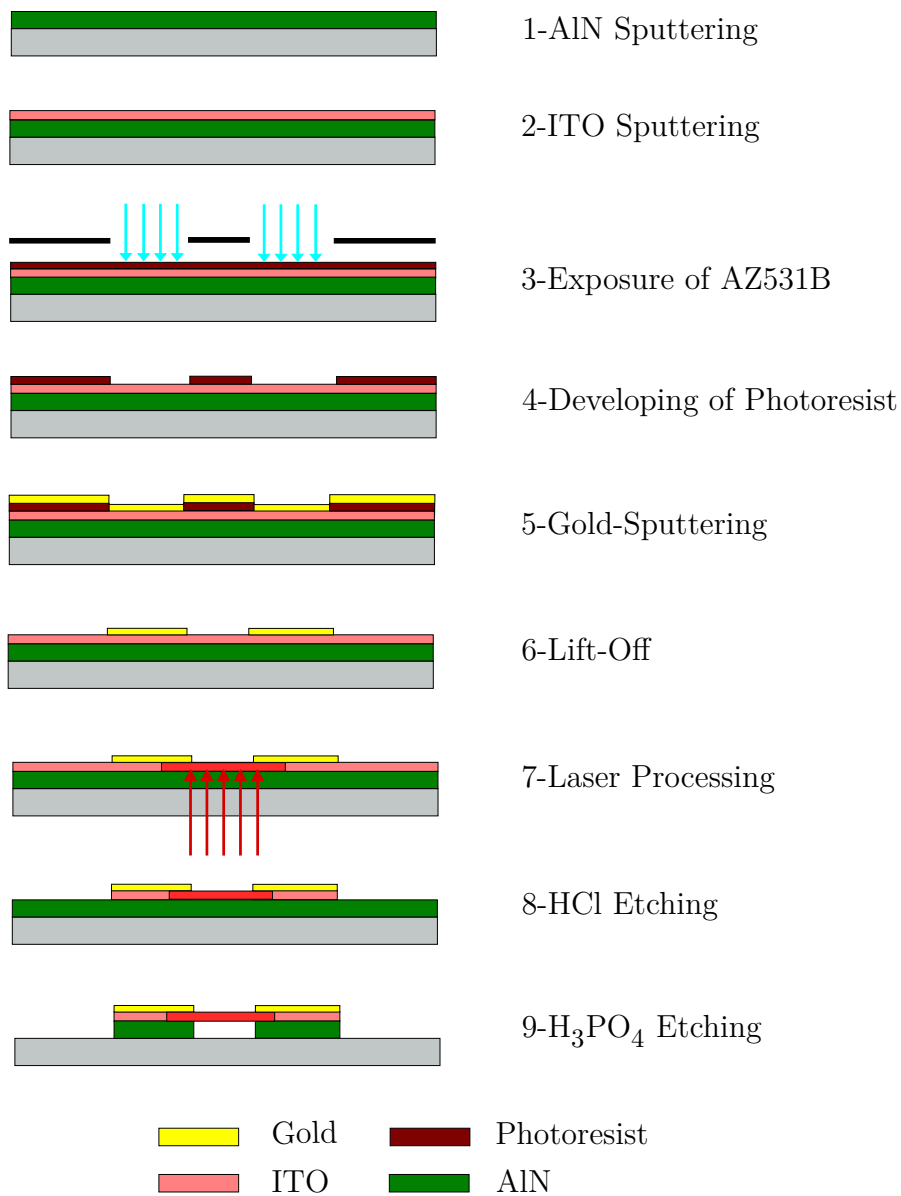


**Figure 4.13:** Schematic view of the fabrication process for freestanding ITO nanowires. The used lithography mask structures are shown for single wires as well as for ten parallel ones.

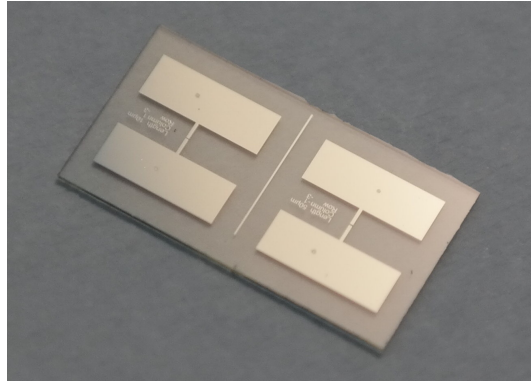


**Figure 4.14:** A photograph of fabricated chips after dicing and with Pt pads.

are listed in Tab 4.4. These metallic contact pads define simultaneously the etching masks for both following wet etching steps.

To prevent an overheating of the photoresist, the sputter processes were divided into several short steps. Pt and Au were sputtered in 15 s steps with 5 min break to let the sample cool down. For Ti, this was 5 s sputtering and 5 min break. This method delivered good results after lift-off as shown in Fig. 4.14 for Pt pads.

The lift-off process was done in an ultrasonic acetone bath. The mask contains contacts with different gap lengths in the range of  $10\ \mu\text{m}$  to  $50\ \mu\text{m}$  as shown in Fig 4.13 for single and multicontact structures. The wafers have to be diced before laser processing, and each single chip can afterwards be mounted on the laser microscope for laser processing (see Fig. 4.14).

Gold and platinum are the established candidates for metallization. However, Pt has turned out to be the favorite metal, due to its positive properties under laser illumination, as mentioned in the following.

Thus, an ITO bridge was generated between two Pt-pads on top of AlN as sacrificial layer on the chips. Its position can easily be found in the laser microscope using a *Zeiss EC Plan Neofluar*  $40\times$ , NA 1.3 oil immersion objective mounted on a vertical piezoelectric stage from *Piezosystem Jena GmbH* to write a nanowire with the desired parameters within this field. The laser intensity defines the lateral dimension of the nanowire after etching.

The laser machining is the same as for the unreleased nanowires. The extra sacrificial layer does not cause any problems for the laser illumination. As a guide for manual focusing, the correct vertical position of the voxel can be found by fluorescent effects occurring in the ITO layer. The material laser interaction is discussed more deeply in Section 2. After focusing and adjusting the laser intensity, scanning can be started. Data for coordinates and scan speed are sent to the scan controlling card of the galvo scanners (*GSI Lumonics SC2000*). For optimizing the illuminating process, samples with different laser power and scan speeds were scanned with a pulse length of about 12 fs.

Because of the reflection and absorption of the laser beam on metallic pads, some deformations in the metallic layer can be seen. These bumps are generated through a temperature

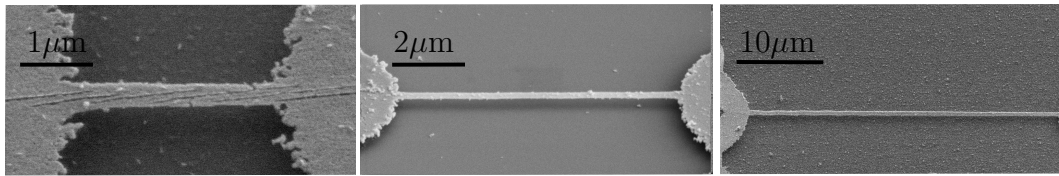


**Figure 4.15:** Fabricated freestanding nanowires. Written by 21.7 mW laser power and a scan speed of 200  $\mu\text{m/s}$ .

and pressure increase at the interface below the pads. This effect is particularly obvious at the start and end points of the line scan and can even end up with the total ablation of the layer in form of a hole. This is due to a delay time between the shutter and the scanner, which holds the spot for a relatively long time on these points. To prevent any side effects on the nanostructures, line scans are written longer than the gap length with about 20  $\mu\text{m}$  extension under the metal pads on each side (see Fig. 4.16).

The interaction of the laser beam with the metal layer does not only lead to the formation of bumps but also to a circular temperature increase in the ITO film near the interface, which anneals the ITO layer and makes it resistant to subsequent etching, as can be seen in Fig. 4.16. The half circle profile reveals a hot spot at the connecting point to the metal pad in the middle. In the case of gold the half circle profiles are only generated on the side where the laser beam leaves the metallic cover, whereas in the case of Pt they can be seen on both sides and even with the same symmetric shape!

Afterwards the lasered chip was etched in 10% HCl at room temperature for about 100 s to etch the ITO nanowires out of the ITO film. An etching rate of 32 nm/min to 48 nm/min was measured. This variation is due to different film qualities on the wafer.

The AlN layer was etched in  $\text{H}_3\text{PO}_4$  at 80  $^\circ\text{C}$  for 210 s with an etching rate of about 75 nm/min. Before and after this step it turned out to be very beneficial to dip the chips in distilled water. The former for an optimum wetting of small gaps and the later even longer step for more than 12 hours to wash off the acid from these small gaps and corners. The last step is a short dip in isopropanol and then letting the chip dry.

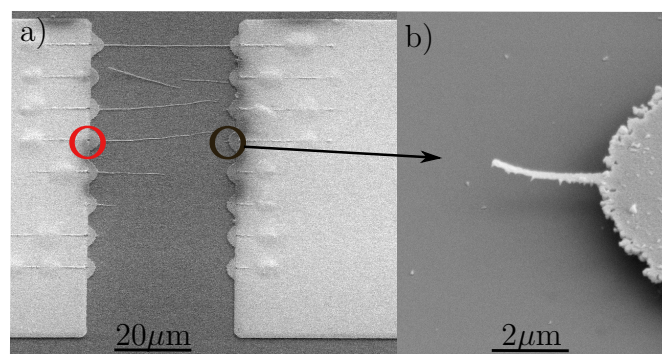


**Figure 4.16:** ITO nanowires with widths of about 100 nm can be generated but they do not survive the whole process including wet etching.

Fabrication of different lengths of such structures exhibits a strong dependency of the yield on the wire length. For standard widths of 200 nm to 300 nm  $10\ \mu\text{m}$  is the proper length as shown in Fig. 4.15. For larger lengths towards  $30\ \mu\text{m}$  the yield reduces dramatically. Nevertheless there are some structures with even  $35\ \mu\text{m}$  length that survive the heavy load of wet etching in a high viscous phosphoric acid and the subsequent surface tensions during the drying process.

The yield turned out to be zero for nanowires with 100 nm width and a length of  $35\ \mu\text{m}$ . This is shown in Fig. 4.16 for about 120 nm width and  $40\ \mu\text{m}$  length. Nevertheless, one side clamped nanowires with a length of a few  $\mu\text{m}$  are still existing as shown in Fig. 4.16b.

The half circle profiles turned out to be essential for the process; they surround the only ablated spot exactly at the interface to the metal pads, caused by a trapped plasma under the bumps as marked with a circle in Fig. 4.15a. This gives the nanowires more stability.

Fig. 4.17 shows different junctions between such nanowires. The laser processing is able to generate monolithic structures in illuminated regions and lines in a top-down approach. The junctions are very homogeneous without any pits or bumps. Even very small negative forms in the range of sub-20 nm can be achieved as shown in Fig. 4.17b. This shows also the flexibility of this method.

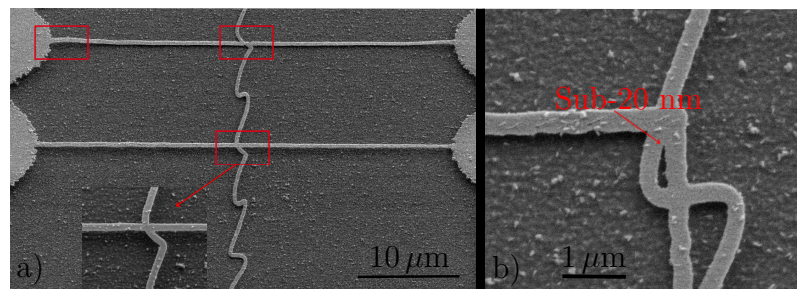


**Figure 4.17:** Fabricated freestanding nanowires with different shapes. The crossing point are very homogeneous and monolithic from ITO without any defects and even in range of sub-20 nm. In Fig. 4.17a there is a bending point in upper structure which is a result of sticking.

This kind of freestanding nanowires can be used for chemical gas sensors as discussed in Section 4.4, with a drastic reduction of heat loss due to their separation from the substrate. Alternatively, they can be used as dynamic double side clamped electromechanical nanoresonators for different physical sensor applications as discussed in Chapter 4.

The mechanical and thermal behavior of the nanowires was studied theoretically. An electrothermal approach can be used for actuating them as resonators.

A simple analytical model for a slender beam with a high ratio between the length and the radius of the cross-section has shown that the Lagrangian mechanics can be reduced to an Euler-Bernoulli model disregarding shear stress and rotation of the beam like in case of the Rayleigh model [225], shear models [226], and Timoshenko model [227]. This model describes a transversal vibration in an out of plane bending mode with very low deflection. It delivers

proper results for the natural frequencies. In this model the bending moment of the whole beam gives the potential energy and the deflection stands for kinetic energy [228, 229].

The analytic model is based on the following assumptions [228]:

- Resonant structures are made of homogeneous and isotropic materials, and are subject to only small deflections. These structures must have a minimum feature size  $> 100$  nm to be able to consider their film mechanical properties.
- Resonators are under concentrated and uniformly distributed loads and bending moments.
- The neutral axis goes along the geometrical center of mass of the beam and the cross-sections of the beam are before and after deformation perpendicular to this line.
- The plane sections of the structures do not deform, i.e., transverse and shear deformations are neglected.
- Structures must have aspect ratios (length/thickness) greater than 10, a necessary condition to employ the Euler-Bernoulli beam theory. For aspect ratios of less than 10, the Timoshenko beam theory must be included.
- Surface and fluid effects, as well as anchor dissipation on the bending response of the resonator are neglected.
- The undercuts of the resonators (caused by isotropic release of the sacrificial layer) are neglected.

Regarding double side clamped boundary conditions, the following equation for the series of eigenfrequencies is obtained [230]:

$$f_n = \frac{((n + \frac{1}{2})\pi)^2}{2\pi l^2} \sqrt{\frac{EI}{A\rho}}, \quad (4.16)$$

here  $l$  is the length,  $A$  the cross-sectional area,  $\rho$  the mass density,  $E$  Young's modulus, and  $I$  the area moment of inertia. For a rectangular cross-section with  $w$  as width and  $t$  as height,  $I$  is  $\frac{1}{12}tw^3$  and the Eq. 4.16 can be rewritten as:

$$f_n = \frac{((n + \frac{1}{2})\pi)^2}{2\pi l^2} \sqrt{\frac{Ew^2}{12\rho}}. \quad (4.17)$$

Calculated values from this equation for different dimensions are in good agreement with FEM simulations, as shown in Tab. 4.5.

For the electrothermal characterization of such nanostructures the analytic studies are based on the thermal conduction equation in a homogeneous material:

$$\rho c \frac{\delta T(\vec{r}, t)}{\delta t} = \lambda \Delta T(\vec{r}, t) + Q, \quad (4.18)$$

**Table 4.5:** Eigenfrequencies of the first mode for different resonator dimensions.

w [nm]	l [ $\mu\text{m}$ ]	Analytical $f_0$ [MHz]	Simulated $f_0$ [MHz]
100	10	3.654	3.657
100	25	0.584	0.584
200	10	7.309	7.308
200	25	1.169	1.170
400	10	14.618	14.534
400	25	2.338	2.339

where  $\rho$  is the mass density,  $c$  the specific heat capacity,  $\lambda$  the thermal conductivity,  $T$  the temperature depending on time and location, and  $Q$  the external thermal energy delivered by time and volume as heat source. When thermal losses through the ambient atmosphere are neglected, this equation can be simplified to a one dimensional heat flow through the wire towards both clamping points. In the simulation this assumption was implemented by assuming a very low heat transfer coefficient of  $0.001 \text{ W/m}^2\text{K}$  for the surrounding ambient.

In reality, the end points are relatively big metallic pads with a huge mass and heat capacity as compared to the nanowire. This justifies the assumption of a fixed room temperature for the contact pads. With an electrical heating source  $Q = P/V = U^2/RV$ ,  $V$  for volume and  $U$  and  $R$  for applied voltage and resistance of the nanowire, Eq. 4.18 can be solved and the temperature at point  $x$  in the nanowire is given by:

$$T(x) = \frac{U^2}{2\lambda VR}(-x^2 + lx) + T_R, \quad (4.19)$$

with  $T_R$  for room temperature. Due to the thermal dependency of electrical resistance in metallic and metallic like materials ( $R = \rho_R(1 + \alpha\Delta T(x))\frac{l}{A}$ ), an average and a maximum temperature can be calculated for the nanowire:

$$\Delta T_m(U) = \frac{U^2}{12\lambda(\frac{\rho_R}{2} + \frac{1}{2}\sqrt{\rho_R^2 + \frac{\alpha\rho_R U^2}{3\lambda}})}, \quad (4.20a)$$

$$\Delta T_M(U) = \frac{U^2}{8\lambda(\frac{\rho_R}{2} + \frac{1}{2}\sqrt{\rho_R^2 + \frac{\alpha\rho_R U^2}{3\lambda}})}, \quad (4.20b)$$

with  $\rho_R$  as specific electric resistivity and  $\alpha$  as temperature coefficient of resistance. This ensures a constant relation between these two temperatures:  $\frac{\Delta T_m}{\Delta T_M} = \frac{2}{3}$ .

The time depending behavior of the nanowire is more interesting for the electrothermal driving concept of the resonators. Eq. 4.18 can be solved one dimensionally for  $Q=0$  to find the parameter for a thermal decay down to room temperature. If an object at one temperature is exposed to a medium of another temperature, the temperature difference

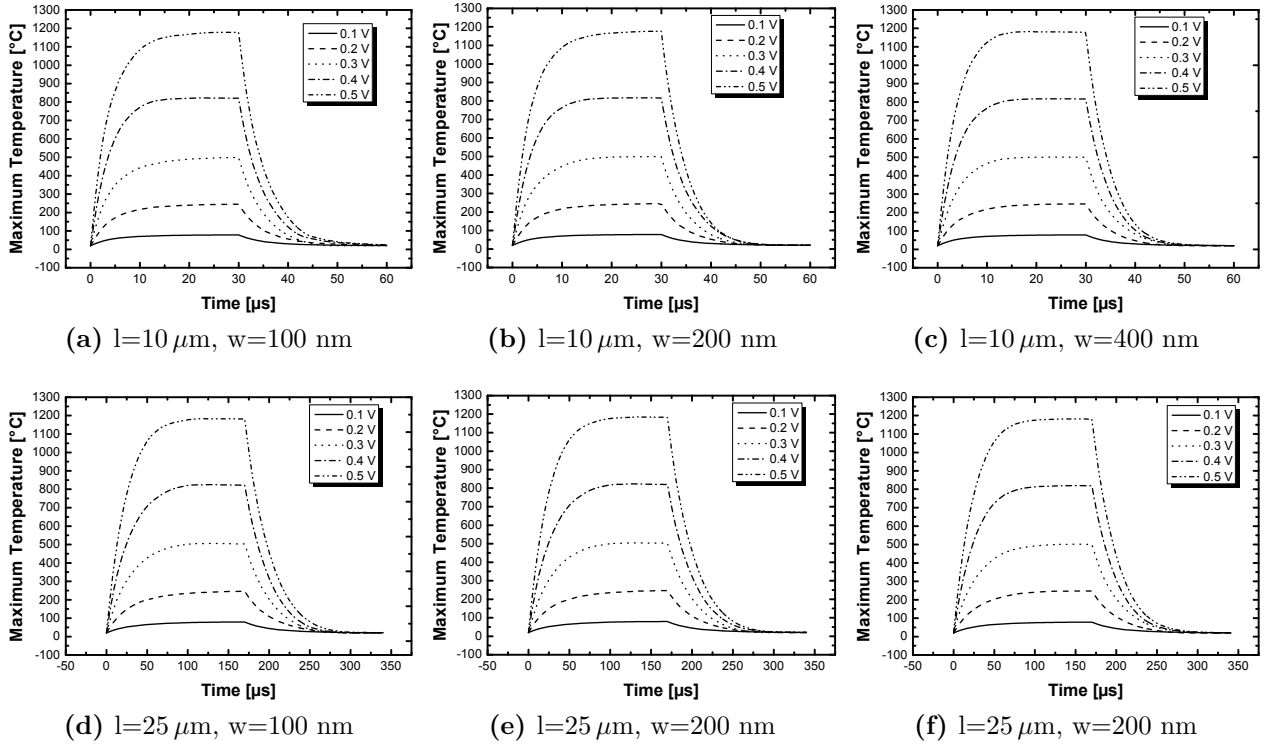


**Figure 4.18:** COMSOL Multiphysics simulations show the electrothermal behavior of nanowires with different dimensions.

between the object and the medium follows an exponential decay with a characteristic time constant  $\tau$  of:

$$\tau(x) = \frac{\rho c(-x^2 + xl)}{2\lambda}, \quad (4.21)$$

for  $T_m$  it yields  $\frac{\rho c l^2}{8\lambda}$ .

FEM simulated results for these properties are for nanowires with different dimensions and in a voltage range of 0.1 V to 0.5 V. The time dependent thermal behavior of  $T_M$  in nanowires with different dimensions has been simulated and the results are shown in Fig. 4.18.

From these curves a thermal decay as in Eq. 4.22 can be fitted with a fall time  $\tau_M$  ( $T_M$  reaches its maximum after about  $20 \mu\text{s}$ ), this is the first fitting point for the thermal decay process.

$$T_M(t) = T_R + (T_M(0) - T_R)e^{-\tau_M t}. \quad (4.22)$$

Values for a nanowires with a cross-section of  $100 \times 100 \text{ nm}$  and with two different lengths of  $10 \mu\text{m}$  and  $25 \mu\text{m}$  are presented in Tab. 4.6:



**Table 4.6:** Fall time of the thermal decay in nanowires. Some of the parameter values are from the literature and some from the measurements.

Length [ $\mu\text{m}$ ]	Analytic $\tau_d$ [ $\mu\text{s}$ ]	Simulated $\tau_d$ [ $\mu\text{s}$ ]
10	5.42	4.9
25	33.88	30.8

For the simulations a collection of physical properties for each material was needed. For gold and glass standard values from the COMSOL Multiphysics material library were used and for ITO a combination of measured values and values from the literature as shown below:

**Table 4.7:** Physical properties of sputtered polycrystalline ITO.

Property	Value	Reference
E-Modulus (E)	90 GPa	Meas.
Mass Density ( $\rho$ )	7120 [ $\text{kg}\cdot\text{m}^{-3}$ ]	[109]
Heat Capacity ( $c_p$ )	362.36 [ $\text{J}\cdot\text{kg}^{-1}\cdot\text{K}^{-1}$ ]	[111]
Heat Conductivity ( $\lambda$ )	5.95 [ $\text{W}\cdot\text{m}^{-1}\cdot\text{K}^{-1}$ ]	[111]
Electrical Resistivity ( $\rho_{\text{el}}$ )	$3.5 \times 10^{-6}$ [ $\Omega\cdot\text{m}$ ]	Meas.
Temperature Coefficient ( $\alpha$ )	$5 \times 10^{-4}$ [ $\text{K}^{-1}$ ]	Meas.

Due to the calculated temperature a voltage of maximum 0.5 V is realistic to keep the ITO nanowires below their melting temperature of about 2000 °C. Maximum deflection by this voltage is 5 nm for 10  $\mu\text{m}$  length and 12.5 nm for 25  $\mu\text{m}$  lengths with a constant cross-section of  $100 \times 100$  nm.

The resonance behavior of a nanoresonator can now be simulated using a sinusoidal alternating driving voltage. This signal shape results in frequency doubling because of heat generation in both the positive and negative half waves.

For a 100 nm wide nanoresonator, the calculated decay times are 20  $\mu\text{s}$  and 120  $\mu\text{s}$  for lengths of 10  $\mu\text{m}$  and 25  $\mu\text{m}$ , respectively. From these values, maximum frequencies of  $f_{10} = 25$  KHz and  $f_{25} = 4.2$  KHz can be calculated. For higher frequencies an excessive accumulation of heat can be expected.

At high temperatures the radiative heat energy loss due to Stefan-Boltzmann radiation law normally becomes relevant for energy loss calculations. However, when one or two dimensions of the radiating object are smaller than the wavelength of the expected radiation, Stefan-Boltzmann's law changes to a two or one dimensional case with a drastic reduction of the heat loss. In this case the two cross-sectional dimensions of the wire are far below 400 nm which is at the lower end of the visual spectrum. This changes the case to a one dimensional version of the radiation law, where the energy losses are only proportional to the square of the temperature instead of the fourth power law in three dimensions. This leads to drastically reduced radiation losses on the order of  $10^{-33}$  J, which is negligible as compared to an applied Joule heating energy in the range of  $10^{-8}$  J.

The heat current density for such nano-dimensional objects strongly depends on the mechanism of the heat carrier scattering. Experimental studies have shown, that the thermal conductivity of nanowires with dimensions below 200 nm is more than twice as big as the value for bulk material [231, 232].

However, there are still no studies on ITO nanowires in the literature but it could be translated from other materials that the heat conductivity of ITO-nanowires is smaller than assumed. This yields to a faster heating and to a slower cooling. Other size effects, e.g. mechanical and electrical properties could not be studied in this work.

# 5 Summary and Outlook

## 5.1 Summary

This thesis is a journey from laser material nanoprocessing toward its integration into microsystem techniques and processes for applications in device fabrication. After a brief general introduction in Chapter 1, Chapter 2 describes the history of laser technology, particularly the technical developments from continuous wave lasers towards pulsed lasers. The underlying physical principles of laser-material interaction are described, with a particular focus on pulsed lasers and on the transition from single pulse regime to pulse trains.

One of the methods to achieve structure definition below the diffraction limit is the application of very high light intensities to trigger nonlinear effects. A powerful tool to do this is the use of ultra-short light pulses as generated e.g. in femtosecond lasers, which offers very high transient intensities in the range of TW. The laser pulse duration is called ultra-short if it is shorter than the time for major relaxation processes in the material. The frequency of pulses, known as repetition rate, has also a strong impact on the way of interaction. Another important parameter is the pulse length, which correlates with the peak power and the fluence of the laser and also directly with the interaction process.

This thesis concentrates on thin film laser processing, being different from bulk material processing. More specifically the focus is on structuring of sputtered indium tin oxide thin films (ITO) as a functional material for further applications. Material structuring experiments yield very interesting results, including the possibility of submicron laser structuring which can be extended into the sub-100 nm range.

The last Section of Chapter 2 describes the materials and their parameters used in this work, particularly indium tin oxide (ITO) Some properties were characterized during this project, some others were just taken from the literature to be used in design-oriented simulations.

Chapter 3 gives an overview of the utilized laser setup as well as characterization methods, which were applied to materials and fabricated chips and devices. Hereby, relevant properties of the used materials were characterized through structural, optical, electrical, topographical, and mechanical analyses. The device characterization was more straightforward and in form of electrical I/V measurements or impedance spectroscopy.

Chapter 4 includes all results achieved in this work. The laser structuring of ITO with a tightly focused sub-15 femtosecond near infrared laser light through the back of a glass substrate and with a high repetition rate of 85 MHz exhibits three different regimes, resulting

in total ablation, periodic nanocuts, and recrystallizations, depending on the laser intensity or rather fluence.

Total ablation occurs in the whole spot sized region and even more up to the micrometer range. Two recent structuring methods can be controlled in such a way to reach sub-100 nm lateral dimensions. Concerning nanocuts the orientation of the cuts can be controlled by the polarization of the laser beam. In case of periodic nanocuts, characteristic dimensions of sub-20 nm for each cut were achieved even as coherent coalescent periodic cuts with an extreme aspect ratio of 1000 (see Addendum I). The modifications in case of recrystallization were released in form of ITO wires with lateral dimensions of 700 nm to sub-60 nm and with aspect ratios of more than 100 (see Addendum I).

The following parts in Chapter 4 are more application oriented. Each application is structured in an introductory part and an addendum describing the results in form of a journal publication or a manuscript. Addendum II presents the first application as nanomodifications on fabricated and SMD bonded micro multielectrode arrays for medical applications. An optimization of the laser structuring method resulted in sub-20 nm wide periodic nanocuts within the ITO electrodes perpendicular to the laser polarization. These sub-20 nm nanocuts were controlled to be as single cuts or to be generated as coherent coalesced nanocuts of many micrometers in length over the whole surface of an electrode. The impact of these modifications on the impedance of bioelectrodes was measured by impedance spectroscopy (see Addendum II). The application in addendum III is based on the top-down fabrication of nanowires through laser modification and subsequent etching, applied for a gas sensor with self heating effect. In the fourth publication, the idea of a self-heated resistive gas sensor for detection of oxidizing gases made of single ITO nanowire was demonstrated by means of NO<sub>2</sub> with a sensitivity in the ppb range and a power consumption in the lower milliwatt range. In Addendum IV such ITO nanowires are released from the substrate and fabricated in form of freestanding nanowires with lengths up to 30  $\mu\text{m}$  and widths down to 150 nm, possessing lateral aspect ratios in excess of 100. For this purpose a standard surface nanomachining technique that includes the use of a sacrificial layer was utilized. Sputter deposited AlN was used as transparent sacrificial layer, which can be etched selectively to ITO.

## 5.2 Outlook

The laser methods presented in this study are a novel and highly interesting way for the fabrication of nanostructures in microchips. They can be used already in small batch sizes in a nearly personalized way.

Presently this process is still mostly manual and rather tricky. It would be highly desirable to go from manual focusing towards auto-focusing by using a closed loop adjustment system between the piezo actuator and the light intensity of the spot measured by the CCD-camera or an extra photodiode.

More material related studies, e.g. on the impact of film thickness and texture on the results would be helpful to achieve a higher reproducibility. Furthermore, a transfer from ITO to other thin films with additional piezoelectric properties such as Al:ZnO is very interesting.

In context with the applications presented in this work, the following further steps are highly interesting:

- In case of modified bioelectrodes, the surface may play an important role for cell adhesion and cell growth. An experiment to detect near field optical or electrical polarizing effects of such laser-modified electrodes can be undertaken at different wavelengths and in contact with living cells. Such nanopatterned trenches could also be covered with solid state semiconductor materials in a CVD or PVD process for solar cell applications. This would increase the surface area and lower the contact resistance, thus improving the performance.
- In case of nanowire gas sensors, future efforts should focus on the fabricating of freely suspended structures with reduced width and thickness, increasing the surface-to-volume ratio of the sensor, thus inducing more effective self-heating and lower energy consumption. More importantly it is expected that these steps will increase the gas-detection sensitivity even more and further reduce response and recovery times. Future research should also clarify the dependence of the self-heating temperature on heating power, especially with respect to the stability of the NWs. It should optimize the sensor and measurement methods with the aim of obtaining short response times at higher temperatures and with much lower power consumption.
- Concerning the laser assisted fabrication of freestanding nanowires, the prove of principle was successfully demonstrated. A logical next step which, in the framework of this work was only omitted for lack of time, is the characterization of their gas responsivity. Furthermore, steps for using them as nanoresonators should be undertaken.
- From the physical point of view it would be very interesting to make extremely small structures in the lower nanometer range, where size effects can be expected.



# List of Figures

2.1	Schematic setup of a passive mode locked femtosecond laser. . . . .	4
2.2	Schematic energy levels and excitation in a two-photon process, e.g. between $S_0$ and $S_1$ states [1]. . . . .	14
2.3	Schematic shape of a focused laser beam profile for thin film ITO processing. A Gaussian focused beam for SPA and a voxel of high intensity for MPA are shown. . . . .	26
2.4	Crystal structure (primitive cell) of indium tin oxide (ITO) [97]. . . . .	28
2.5	Change of band gap for tin doped $\text{In}_2\text{O}_3$ caused by Burstein-Moss-shift $\Delta_{\text{BM}}$ and by band-gap-normalization $\Delta_{\text{RN}}$ , as discussed in [102, 103]. . . . .	29
2.6	Calculated absorption curves from transmission-reflection measurement on sputtered ITO on glass substrate compared with the laser spectrum. . . . .	31
2.7	Thermal conductivity versus electrical conductivity for polycrystalline sputtered ITO films deposited at various $\text{O}_2$ flow rates [111]. . . . .	33
2.8	Standard statistical distribution of the measured elastic modulus from nanoindentation experiments on sputtered polycrystalline ITO thin films on glass substrates. . . . .	35
2.9	Transmittance of the used glass wafers. . . . .	36
2.10	Transmission-reflection measurement on sputtered AlN on glass substrate. . .	37
2.11	Novolac molecular structure. . . . .	39
2.12	SU-8 molecular structure [134]. . . . .	40
3.1	Scheme of the high resolution laser-microscope setup. . . . .	44
3.2	The pulse length of 12 fs is measured with a second-order interferometric scanning autocorrelator on the objective. The laser pulse features an M-shaped broadband spectrum [1]. . . . .	44
3.3	Scheme of the interaction volumes by the various types of scattered electrons and X-rays [136]. . . . .	46
3.4	Schematic view of the Bragg condition by scattering of two beams from two different atoms (atom layers). . . . .	48
3.5	Typical ellipsometry configuration, where linearly polarized light is reflected from the sample surface and the polarization change is measured to determine film thickness and refractive index [137]. . . . .	50
3.6	Flowchart for ellipsometry data analysis [137]. . . . .	51
3.7	ITO thin film in a magnetic field $\vec{B}$ , with $\vec{v}$ the drift velocity of electrons, $\vec{F}$ the Lorentz force, and $\vec{F}_{e1}$ the electric field force [130]. . . . .	56

3.8	From left to the right: Load-displacement data demonstration in elasticity of completely elastic material, elastoplastic material, and ideally plastic material [120]. . . . .	59
3.9	Schematic of an indenter at maximum load $P_{max}$ with an associated total depth of $h_{max}$ . The contact between the indenter and the surface at maximum load is defined by depth $h_c$ , with a corresponding projected area of contact $A_c$ . The dashed line (left), with a final depth of $h_f$ , indicates the sample profile after the load has been removed. Corresponding load displacement curve, indicating the final depth $h_f$ , the intercept depth $h_i$ , the contact depth $h_c$ , and the maximum depth [120]. . . . .	60
3.10	Left: A diagram of the indent loaded versus indent displacement for an indentation point, right: the from data acquisition system (nanoDM) delivered data; two curves of hardness and elastic modulus of an indentation point on sputtered polycrystalline ITO film. . . . .	61
3.11	Schematic design of the gas measurement setup (LMT) [148]. . . . .	63
3.12	Schematic design of the impedance spectroscopy measurement setup (IBMT). . . . .	64
4.1	Principle of ITO laser structuring through a glass substrate with a near infrared laser beam. . . . .	68
4.2	Schematic diagram of a biomedical electrode. . . . .	85
4.3	Schematic representation of the different models for the description of the electrochemical double layer at the phase boundary electrode/electrolyte. In addition, the trend of potentials is shown [169]. . . . .	87
4.4	Randles model as an equivalent circuit for characterization of electrochemical processes at electrodes. . . . .	88
4.5	Commercial ITO thin film sensor (SP-16, <i>FIS Inc</i> , Japan). Left: front side of the substrate with ITO sensor layer, right: backside of the substrate with heating element. . . . .	99
4.6	Band bending caused by the exchange of electrons between MOX and oxygen. $z_0$ is the width of the depletion layer [182]. . . . .	101
4.7	Schematic demonstration of the band bending caused by the depletion region in porous, thin film and nanowire metal oxide materials. The current is assumed to flow in the x direction [50, 181]. . . . .	103
4.8	a) Scanning electron micrograph of SiC nanowires with different lengths and resonant frequencies ranging from 2 MHz to 134 MHz, b) Schematic diagram of process sequence [203]. . . . .	118
4.9	a) Scanning electron micrograph of a high stress silicon nitride NEMS with a width of 300 nm, b) Electrostatic force in the z direction in a cross-sectional view, versus distance d from the electrodes. FEM simulation (black) and approximation by an analytical fit (red) for $V_{dc} = 2V$ [224]. . . . .	119
4.10	Electron microscopy micrograph of an AlN cross-section shows c-axis orientation as achieved by A. Ababneh [126]. . . . .	121
4.11	AFM measurements on sputtered AlN film on glass substrate (left) and the same sample after ITO sputtering on top (right). . . . .	122



---

4.12	Change of transmittance of the glass substrate by adding of about 500 nm AlN and 100 nm ITO layers. . . . .	123
4.13	Schematic view of the fabrication process for freestanding ITO nanowires. The used lithography mask structures are shown for single wires as well as for ten parallel ones. . . . .	124
4.14	A photograph of fabricated chips after dicing and with Pt pads. . . . .	125
4.15	Fabricated freestanding nanowires. Written by 21.7 mW laser power and a scan speed of 200 $\mu\text{m/s}$ . . . . .	126
4.16	ITO nanowires with widths of about 100 nm can be generated but they do not survive the whole process including wet etching. . . . .	126
4.17	Fabricated freestanding nanowires with different shapes. The crossing point are very homogeneous and monolithic from ITO without any defects and even in range of sub-20 nm. In Fig. 4.17a there is a bending point in upper structure which is a result of sticking. . . . .	127
4.18	COMSOL Multiphysics simulations show the electrothermal behavior of nanowires with different dimensions. . . . .	130



# List of Tables

2.1	Fluence per Pixel versus scan speed for an average power of 15 mW; $v$ presents the scan speed and $N_{\text{eff}}$ the pulse number. . . . .	23
3.1	A summary of laser parameters using an oil immersion objective from <i>Zeiss</i> ( $NA = 1.3$ ). . . . .	45
4.1	Parameters used in the literature for ITO laser structuring using nanosecond-lasers (cf. [50]). . . . .	67
4.2	Parameters used in the literature for ITO laser structuring using Ti:sapphire femtosecond lasers (cf. [50]). . . . .	68
4.3	Parameters used in the literature for ITO laser crystallization. . . . .	69
4.4	An overview of sputter parameters used for the fabrication of freestanding ITO nanowires in this work. . . . .	123
4.5	Eigenfrequencies of the first mode for different resonator dimensions. . . . .	129
4.6	Fall time of the thermal decay in nanowires. Some of the parameter values are from the literature and some from the measurements. . . . .	131
4.7	Physical properties of sputtered polycrystalline ITO. . . . .	131



# Bibliography

- [1] A. Ostendorf and K. König, eds., *Optically Induced Nanostructures: Biomedical and Technical Applications*. Berlin/Boston: De Gruyter, 2015.
- [2] K. König, A. Uchugonova, M. Straub, H. Zhang, M. Licht, M. Afshar, D. Feili, and H. Seidel, “Sub-100 nm material processing and imaging with a sub-15 femtosecond laser scanning microscope,” *Journal of Laser Applications*, vol. 24, no. 4, p. 042009, 2012.
- [3] T. H. Meiman, “Stimulated optical radiation in ruby,” *Nature*, vol. 187, no. 4736, pp. 493–494, 1960.
- [4] R. Paschotta, *Encyclopedia of laser physics and technology*. Weinheim: Wiley-VCH, 2008.
- [5] M. Göppert, “Über die Wahrscheinlichkeit des Zusammenwirkens zweier Lichtquanten in einem Elementarakt,” *Naturwissenschaften*, p. 932, 1929.
- [6] M. Birnbaum, “Semiconductor surface damage produced by ruby lasers,” *Journal of Applied Physics*, vol. 36, no. 11, p. 3688, 1965.
- [7] K. Zhao, Q. Zhang, M. Chini, Y. Wu, X. Wang, and Z. Chang, “Tailoring a 67 attosecond pulse through advantageous phase-mismatch,” *Optics Letters*, vol. 37, no. 18, p. 3891, 2012.
- [8] J. Eichler and H. J. Eichler, *Laser: Bauformen, Strahlführung, Anwendungen : mit 57 Tabellen, 164 Aufgaben und vollständigen Lösungswegen*. Berlin: Springer, 6 ed., 2006.
- [9] D. Meschede, *Optik, Licht und Laser*. Wiesbaden: Vieweg + Teubner in GWV Fachverlage, 3 ed., 2008.
- [10] J. C. Diels and W. Rudolph, *Ultrashort laser pulse phenomena: Fundamentals, techniques, and applications on a femtosecond time scale*. Optics and photonics, Amsterdam: Acad. Press/Elsevier, 2 ed., 2006.
- [11] W. T. Silfvast, *Laser fundamentals*. Cambridge and New York: Cambridge University Press, 2 ed., 2004.
- [12] Sven Martin, *Zerstörmechanismen in optischen Materialien bei Anregung mit ultrakurzen Laserpulsen*. PhD thesis, Freie Universität Berlin, Berlin, 2004.
- [13] S. Preuss, M. Späth, Y. Zhang, and M. Stuke, “Time resolved dynamics of subpicosecond laser ablation,” *Applied Physics Letters*, vol. 23, no. 62, pp. 3049–3051, 1993.

- [14] E. G. Gamaly, *Femtosecond Laser-Matter Interaction: Theory, Experiments and Applications*. Hoboken: Pan Stanford, 2011.
- [15] B. Rethfeld, K. Sokolowski-Tinten, D. v. d. Linde, and S. I. Anisimov, “Timescales in the response of materials to femtosecond laser excitation,” *Applied Physics A*, vol. 79, no. 4-6, 2004.
- [16] B. Rethfeld, K. Sokolowski-Tinten, D. v. d. Linde, and S. I. Anisimov, “Ultrafast thermal melting of laser-excited solids by homogeneous nucleation,” *Physical Review B*, vol. 65, no. 9, 2002.
- [17] C. Kittel, *Einführung in die Festkörperphysik*. München: Oldenbourg, 14 ed., 2006.
- [18] B. Chichkov, C. Momma, S. Nolte, F. v. Alvensleben, and A. Tünnermann, “Femtosecond, picosecond and nanosecond laser ablation of solids,” *Applied Physics A Solids and Surfaces*, no. 63, pp. 109–115, 1996.
- [19] Ilja Mingareev, *Ultrafast dynamics of melting and ablation at large laser intensities*. PhD thesis, RWTH Aachen, Aachen, 2009.
- [20] B. Tan, A. Dalili, and K. Venkatakrishnan, “High repetition rate femtosecond laser nano-machining of thin films,” *Applied Physics A*, vol. 95, no. 2, pp. 537–545, 2009.
- [21] P. Rudolph, *Physikalische Chemie der Laser-Material-Wechselwirkung mit BaAl-Borosilikatglas, AlN, SiC-TiC-TiB<sub>2</sub>*. PhD thesis, Freie Universität Berlin, Berlin, 2001.
- [22] B. C. Stuart, M. D. Feit, S. Herman, A. M. Rubenchik, B. W. Shore, and M. D. Perry, “Nanosecond-to-femtosecond laser-induced breakdown in dielectrics,” *Physical Review B*, vol. 53, no. 4, pp. 1749–1761, 1996.
- [23] M. Lenzner, J. Krüger, S. Sartania, Z. Cheng, C. Spielmann, G. Mourou, W. Kautek, and F. Krausz, “Femtosecond optical breakdown in dielectrics,” *Physical Review Letters*, vol. 80, no. 18, pp. 4076–4079, 1998.
- [24] C. B. Schaffer, A. Brodeur, and E. Mazur, “Laser-induced breakdown and damage in bulk transparent materials induced by tightly focused femtosecond laser pulses,” *Measurement Science and Technology*, vol. 12, pp. 1784–1794, 2001.
- [25] N. Bloembergen, “Laser-induced electric breakdown in solids,” *IEEE Journal of Quantum Electronics*, vol. 10, no. 3, pp. 375–386, 1974.
- [26] L. H. Holway, “Temporal behavior of electron distributions in an electric field,” *Physical Review Letters*, vol. 28, no. 5, pp. 280–283, 1972.
- [27] B. C. Stuart, M. D. Feit, S. Herman, A. M. Rubenchik, B. W. Shore, and M. D. Perry, “Optical ablation by high-power short-pulse lasers,” *Journal of the Optical Society of America B*, vol. 13, no. 2, p. 459, 1996.
- [28] B. C. Stuart, M. D. Feit, A. M. Rubenchik, B. W. Shore, and M. D. Perry, “Laser-induced damage in dielectrics with nanosecond to subpicosecond pulses,” *Physical Review Letters*, vol. 74, no. 12, pp. 2248–2251, 1995.

- [29] R. Stoian, *Investigations of the dynamics of material removal in ultrashort pulsed laser ablation of dielectrics*. PhD thesis, Freie Universität Berlin, Berlin, 2000.
- [30] M. Hashida, H. Mishima, S. Tokita, and S. Sakabe, “Non-thermal ablation of expanded polytetrafluoroethylene with an intense femtosecond-pulse laser,” *Optics Express*, vol. 17, no. 15, p. 13116, 2009.
- [31] M. Henyk, D. Wolframm, and J. Reif, “Ultra short laser pulse induced charged particle emission from wide bandgap crystals,” *Applied Surface Science*, vol. 168, no. 1-4, pp. 263–266, 2000.
- [32] A. C. Tien, S. Backus, H. Kapteyn, M. Murnane, and G. Mourou, “Short-pulse laser damage in transparent materials as a function of pulse duration,” *Physical Review Letters*, vol. 82, no. 19, pp. 3883–3886, 1999.
- [33] M. H. Niemz, “Threshold dependence of laser-induced optical breakdown on pulse duration,” *Applied Physics Letters*, vol. 66, no. 10, p. 1181, 1995.
- [34] R. T. Williams, J. N. Bradford, and W. L. Faust, “Short-pulse optical studies of exciton relaxation and F-center formation in NaCl, KCl, and NaBr,” *Physical Review B*, vol. 18, no. 12, pp. 7038–7057, 1978.
- [35] D. K. Ferry, “Energy-gap narrowing and state filling in semiconductors under intense laser irradiation,” *Physical Review B*, vol. 18, no. 12, pp. 7033–7037, 1978.
- [36] M. Schüle, M. Afshar, D. Feili, H. Seidel, K. König, and M. Straub, “Incubation and nanostructure formation on n- and p-type si(100) and si(111) at various doping levels induced by sub-nanojoule femto- and picosecond near-infrared laser pulses,” *Applied Surface Science*, vol. 314, pp. 21–29, 2014.
- [37] S. Baudach, J. Bonse, J. Krüger, and W. Kautek, “Ultrashort pulse laser ablation of polycarbonate and polymethylmethacrylate,” *Applied Surface Science*, vol. 154-155, pp. 555–560, 2000.
- [38] J. Bonse, P. Rudolph, J. Krüger, S. Baudach, and W. Kautek, “Femtosecond pulse laser processing of tin on silicon,” *Applied Surface Science*, vol. 154-155, pp. 659–663, 2000.
- [39] D. Perez and L. J. Lewis, “Ablation of solids under femtosecond laser pulses,” *Physical Review Letters*, vol. 89, no. 25, 2002.
- [40] Y. G. Yingling and B. J. Garrison, “Photochemical ablation of organic solids,” *Nuclear Instruments and Methods in Physics Research Section B: Beam Interactions with Materials and Atoms*, vol. 202, pp. 188–194, 2003.
- [41] N. Bloembergen, “Role of cracks, pores, and absorbing inclusions on laser induced damage threshold at surfaces of transparent dielectrics,” *Applied Optics*, vol. 12, no. 4, p. 661, 1973.

- [42] M. Mosbacher, H. J. Münzer, J. Zimmermann, J. Solis, J. Boneberg, and P. Leiderer, “Optical field enhancement effects in laser-assisted particle removal,” *Applied Physics A Materials Science & Processing*, vol. 72, no. 1, pp. 41–44, 2001.
- [43] P. M. Fahey, P. B. Griffin, and J. D. Plummer, “Point defects and dopant diffusion in silicon,” *Reviews of Modern Physics*, vol. 61, no. 2, pp. 289–384, 1989.
- [44] J. Dickinson, S. Orlando, S. Avanesyan, and S. Langford, “Color center formation in soda lime glass and nacl single crystals with femtosecond laser pulses,” *Applied Physics A*, vol. 79, no. 4-6, 2004.
- [45] J. B. Lonzaga, S. M. Avanesyan, S. C. Langford, and J. T. Dickinson, “Color center formation in soda-lime glass with femtosecond laser pulses,” *Journal of Applied Physics*, vol. 94, no. 7, p. 4332, 2003.
- [46] F. Quéré, S. Guizard, and P. Martin, “Time-resolved study of laser-induced breakdown in dielectrics,” *Europhysics Letters (EPL)*, vol. 56, no. 1, pp. 138–144, 2001.
- [47] B. M. Kim, M. D. Feit, A. M. Rubenchik, E. J. Joslin, J. Eichler, P. C. Stoller, and L. B. Da Silva, “Effects of high repetition rate and beam size on hard tissue damage due to subpicosecond laser pulses,” *Applied Physics Letters*, vol. 76, no. 26, p. 4001, 2000.
- [48] S. Juodkazis, H. Misawa, and I. Maksimov, “Thermal accumulation effect in three-dimensional recording by picosecond pulses,” *Applied Physics Letters*, vol. 85, no. 22, p. 5239, 2004.
- [49] E. M. Preiß, “Herstellung von laserinduzierten Nanostrukturen in ITO (Studienarbeit),” Universität des Saarlandes, 2012.
- [50] E. M. Preiß, “Femtosekundenlaserinduzierte ITO-nanodrähte für gassensoranwendungen (Diplomarbeit),” Master’s thesis, Universität des Saarlandes, Saarbrücken, 2013.
- [51] S. G. Lipson, H. Lipson, and D. S. Tannhauser, *Optical physics*. Cambridge and New York and NY and USA: Cambridge University Press, 3 ed., 1995.
- [52] P. G. Kazansky, H. Inouye, T. Mitsuyu, K. Miura, J. Qiu, K. Hirao, and F. Starrost, “Anomalous anisotropic light scattering in Ge-doped silica glass,” *Physical Review Letters*, vol. 82, no. 10, pp. 2199–2202, 1999.
- [53] M. Huang, F. Zhao, Y. Cheng, N. Xu, and Z. Xu, “Origin of laser-induced near-subwavelength ripples: Interference between surface plasmons and incident laser,” *ACS Nano*, vol. 3, no. 12, pp. 4062–4070, 2009.
- [54] J. Bonse, A. Rosenfeld, and J. Krüger, “On the role of surface plasmon polaritons in the formation of laser-induced periodic surface structures upon irradiation of silicon by femtosecond-laser pulses,” *Journal of Applied Physics*, vol. 106, no. 10, p. 104910, 2009.



- [55] S. Richter, C. Miese, S. Döring, F. Zimmermann, M. J. Withford, A. Tünnermann, and S. Nolte, “Laser induced nanogratings beyond fused silica - periodic nanostructures in borosilicate glasses and ULE<sup>TM</sup>,” *Optical Materials Express*, vol. 3, no. 8, p. 1161, 2013.
- [56] N. Yasumaru, K. Miyazaki, and J. Kiuchi, “Femtosecond-laser-induced nanostructure formed on hard thin films of TiN and DLC,” *Applied Physics A: Materials Science & Processing*, vol. 76, no. 6, pp. 983–985, 2003.
- [57] F. Costache, S. Kouteva-Arguirova, and J. Reif, “Sub-damage-threshold femtosecond laser ablation from crystalline Si: surface nanostructures and phase transformation,” *Applied Physics A*, vol. 79, no. 4-6, 2004.
- [58] R. Le Harzic, D. Dörr, D. Sauer, V. Neumeier, M. Epple, V. Zimmermann, and F. Stracke, “Large-area, uniform, high-spatial-frequency ripples generated on silicon using a nanojoule-femtosecond laser at high repetition rate,” *Optics Letters*, vol. 36, no. 2, pp. 229–231, 2011.
- [59] M. Straub, M. Afshar, D. Feili, H. Seidel, and K. König, “Efficient nanostructure formation on silicon surfaces and in indium tin oxide thin films by sub-15 fs pulsed near-infrared laser light,” *Physics Procedia*, vol. 12, pp. 16–23, 2011.
- [60] M. Straub, M. Afshar, D. Feili, H. Seidel, and K. König, “Periodic nanostructures on si(100) surfaces generated by high-repetition rate sub-15 fs pulsed near-infrared laser light,” *Optics Letters*, vol. 37, no. 2, pp. 190–192, 2012.
- [61] M. Afshar, M. Straub, H. Völlm, D. Feili, K. König, and H. Seidel, “Sub-100 nm structuring of indium-tin-oxide thin films by sub-15 femtosecond pulsed near-infrared laser light,” *Optics Letters*, vol. 37, no. 4, p. 563, 2012.
- [62] M. Straub, M. Afshar, D. Feili, H. Seidel, and K. König, “Surface plasmon polariton model of high-spatial frequency laser-induced periodic surface structure generation in silicon,” *Journal of Applied Physics*, vol. 111, no. 12, p. 124315, 2012.
- [63] S. Höhm, M. Herzlieb, A. Rosenfeld, J. Krüger, and J. Bonse, “Dynamics of the formation of laser-induced periodic surface structures (LIPSS) upon femtosecond two-color double-pulse irradiation of metals, semiconductors, and dielectrics,” *Applied Surface Science*, vol. 374, pp. 331–338, 2015.
- [64] R. Taylor, C. Hnatovsky, and E. Simova, “Applications of femtosecond laser induced self-organized planar nanocracks inside fused silica glass,” *Laser & Photonics Review*, vol. 2, no. 1-2, pp. 26–46, 2008.
- [65] M. Beresna, M. Gecevičius, and P. G. Kazansky, “Polarization sensitive elements fabricated by femtosecond laser nanostructuring of glass [invited],” *Optical Materials Express*, vol. 1, no. 4, p. 783, 2011.

- [66] M. Lenzner, J. Krüger, W. Kautek, and F. Krausz, “Incubation of laser ablation in fused silica with 5-fs pulses,” *Applied Physics A: Materials Science & Processing*, vol. 69, no. 4, pp. 465–466, 1999.
- [67] J. Krüger and W. Kautek, “Femtosecond-pulse visible laser processing of transparent materials,” *Applied Surface Science*, vol. 96-98, pp. 430–438, 1996.
- [68] A. Serafetinides, C. Skordoulis, M. Makropoulou, and A. Kar, “Picosecond and sub-picosecond visible laser ablation of optically transparent polymers,” *Applied Surface Science*, vol. 135, no. 1-4, pp. 276–284, 1998.
- [69] M. Allmen and A. Blatter, *Laser-Beam Interactions with Materials: Physical Principles and Applications*, vol. 2 of *Springer Series in Materials Science*. Berlin and Heidelberg: Springer Berlin Heidelberg, 2 ed., 1995.
- [70] M. Afshar, M. Leber, W. Poppendieck, K. König, H. Seidel, and D. Feili, “On-chip nanostructuring and impedance trimming of transparent and flexible ito electrodes by laser induced coherent sub-20nm cuts,” *Applied Surface Science*, vol. 360, Part B, pp. 494–501, 2015.
- [71] J. Bonse, R. Koter, M. Hartelt, D. Spaltmann, S. Pentzien, S. Höhm, A. Rosenfeld, and J. Krüger, “Femtosecond laser-induced periodic surface structures on steel and titanium alloy for tribological applications,” *Applied Physics A*, vol. 117, no. 1, pp. 103–110, 2014.
- [72] J. Long, P. Fan, M. Zhong, H. Zhang, Y. Xie, and C. Lin, “Superhydrophobic and colorful copper surfaces fabricated by picosecond laser induced periodic nanostructures,” *Applied Surface Science*, vol. 311, pp. 461–467, 2014.
- [73] J. Cheng, C. S. Liu, S. Shang, D. Liu, W. Perrie, G. Dearden, and K. Watkins, “A review of ultrafast laser materials micromachining,” *Optics & Laser Technology*, vol. 46, pp. 88–102, 2013.
- [74] N. Bulgakova, R. Stoian, A. Rosenfeld, I. Hertel, and E. Campbell, “Electronic transport and consequences for material removal in ultrafast pulsed laser ablation of materials,” *Physical Review B*, vol. 69, no. 5, 2004.
- [75] K. Venkatakrisnan, B. Tan, and B. Ngoi, “Femtosecond pulsed laser ablation of thin gold film,” *Optics & Laser Technology*, vol. 34, no. 3, pp. 199–202, 2002.
- [76] A. Vorobyev and C. Guo, “Enhanced absorptance of gold following multipulse femtosecond laser ablation,” *Physical Review B*, vol. 72, no. 19, 2005.
- [77] S. Valette, R. Le Harzic, N. Huot, E. Audouard, and R. Fortunier, “2d calculations of the thermal effects due to femtosecond laser-metal interaction,” *Applied Surface Science*, vol. 247, no. 1-4, pp. 238–242, 2005.
- [78] J. Kim and S. Na, “Metal thin film ablation with femtosecond pulsed laser,” *Optics & Laser Technology*, vol. 39, no. 7, pp. 1443–1448, 2007.

- [79] D. J. Hwang, H. Jeon, C. P. Grigoropoulos, J. Yoo, and R. E. Russo, “Femtosecond laser ablation induced plasma characteristics from submicron craters in thin metal film,” *Applied Physics Letters*, vol. 91, no. 25, p. 251118, 2007.
- [80] A. Y. Vorobyev and C. Guo, “Colorizing metals with femtosecond laser pulses,” *Applied Physics Letters*, vol. 92, no. 4, p. 041914, 2008.
- [81] K. Okamuro, M. Hashida, Y. Miyasaka, Y. Ikuta, S. Tokita, and S. Sakabe, “Laser fluence dependence of periodic grating structures formed on metal surfaces under femtosecond laser pulse irradiation,” *Physical Review B*, vol. 82, no. 16, 2010.
- [82] T. Akane, K. Sugioka, S. Nomura, K. Hammura, N. Aoki, K. Toyoda, Y. Aoyagi, and K. Midorikawa, “F2 laser etching of gan,” *Applied Surface Science*, vol. 168, no. 1-4, pp. 335–339, 2000.
- [83] J. Bonse, S. Baudach, J. Krüger, W. Kautek, and M. Lenzner, “Femtosecond laser ablation of silicon—modification thresholds and morphology,” *Applied Physics A*, vol. 74, no. 1, pp. 19–25, 2002.
- [84] A. Borowiec and H. K. Haugen, “Subwavelength ripple formation on the surfaces of compound semiconductors irradiated with femtosecond laser pulses,” *Applied Physics Letters*, vol. 82, no. 25, p. 4462, 2003.
- [85] R. Tanaka, T. Takaoka, H. Mizukami, T. Arai, and Y. Iwaf, “Laser etching of indium tin oxide thin films by ultra-short pulsed laser,” *Proc. of SPIE*, no. 5063, pp. 370–373, 2003.
- [86] J. Bonse, M. Munz, and H. Sturm, “Structure formation on the surface of indium phosphide irradiated by femtosecond laser pulses,” *Journal of Applied Physics*, vol. 97, no. 5, p. 013538, 2005.
- [87] D. Ruthe, K. Zimmer, and T. Höche, “Etching of  $\text{CuInSe}_2$  thin films-comparison of femtosecond and picosecond laser ablation,” *Applied Surface Science*, vol. 247, no. 1-4, pp. 447–452, 2005.
- [88] J. Bonse, H. Sturm, D. Schmidt, and W. Kautek, “Chemical, morphological and accumulation phenomena in ultrashort-pulse laser ablation of tin in air,” *Applied Physics A Materials Science & Processing*, vol. 71, no. 6, pp. 657–665, 2000.
- [89] D. Ashkenasi, G. Müller, A. Rosenfeld, R. Stoian, I. Hertel, N. Bulgakova, and E. Campbell, “Fundamentals and advantages of ultrafast micro-structuring of transparent materials,” *Applied Physics A*, vol. 77, no. 2, pp. 223–228, 2003.
- [90] R. R. Gattass, L. R. Cerami, and E. Mazur, “Micromachining of bulk glass with bursts of femtosecond laser pulses at variable repetition rates,” *Optics Express*, vol. 14, no. 12, 2006.

- [91] E. Gamaly, B. Luther-Davies, A. Rode, S. Joudkakis, H. Misawa, L. Hallo, P. Nicolai, and V. Tikhonchuk, “Laser-matter interaction in the bulk of transparent dielectrics: Confined micro-explosion,” *Journal of Physics: Conference Series*, vol. 59, pp. 5–10, 2007.
- [92] P. Balling and J. Schou, “Femtosecond-laser ablation dynamics of dielectrics: basics and applications for thin films,” *Reports on Progress in Physics*, vol. 76, no. 3, p. 036502, 2013.
- [93] S. A. Bashar, *Study of Indium Tin Oxide (ITO) for Novel Optoelectronic Devices*. PhD thesis, University of London, London, 1998.
- [94] J. C. C. Fan and J. B. Goodenough, “X-ray photoemission spectroscopy studies of sn-doped indium-oxide films,” *Journal of Applied Physics*, vol. 48, no. 8, p. 3524, 1977.
- [95] H. Kim, C. M. Gilmore, A. Piqué, J. S. Horwitz, H. Mattoussi, H. Murata, Z. H. Kafafi, and D. B. Chrisey, “Electrical, optical, and structural properties of indium–tin–oxide thin films for organic light-emitting devices,” *Journal of Applied Physics*, vol. 86, no. 11, p. 6451, 1999.
- [96] Y. Gassenbauer, *Untersuchung der elektronischen und chemischen Oberflächeneigenschaften von Zinn-dotiertem Indium-Oxid im Hinblick auf die Funktion in organischen Leuchtdioden*. PhD thesis, Technische Universität Darmstadt, Darmstadt, 2007.
- [97] C. Bubel, *Synthese eines neuartigen Precursorsystems und dessen Applikation zu Herstellung von Indium-Zinnoxid-Schichten*. PhD thesis, Universität des Saarlandes, Saarbrücken, 2010.
- [98] M. Hoheisel, A. Mitwalsky, and C. Mrotzek, “Microstructure and etching properties of sputtered indium-tin oxide (ITO),” *Physica Status Solidi (a)*, vol. 123, no. 2, pp. 461–472, 1991.
- [99] O. Mryasov and A. Freeman, “Electronic band structure of indium tin oxide and criteria for transparent conducting behavior,” *Physical Review B*, vol. 64, no. 23, 2001.
- [100] E. Burstein, “Anomalous optical absorption limit in InSb,” *Physical Review*, vol. 93, no. 3, pp. 632–633, 1954.
- [101] H. K. Müller, “Electrical and optical properties of sputtered  $\text{In}_2\text{O}_3$  films. I. electrical properties and intrinsic absorption,” *Physica Status Solidi*, vol. 27, no. 2, pp. 723–731, 1968.
- [102] A. Walsh, J. Da Silva, and S. H. Wei, “Origins of band-gap renormalization in degenerately doped semiconductors,” *Physical Review B*, vol. 78, no. 7, 2008.
- [103] L. Gupta, A. Mansingh, and P. K. Srivastava, “Band gap narrowing and the band structure of tin-doped indium oxide films,” *Thin Solid Films*, vol. 176, no. 1, pp. 33–44, 1989.

- [104] E. Gagaoudakis, M. Bender, E. Douloufakis, N. Katsarakis, E. Natsakou, V. Cimalla, and G. Kiriakidis, "The influence of deposition parameters on room temperature ozone sensing properties of inox films," *Sensors and Actuators B: Chemical*, vol. 80, pp. 155–161, 2001.
- [105] D. Mergel, "Dünne ITO-Schichten als leitfähige, transparente Elektroden," *Vakuum in Forschung und Praxis*, vol. 16, no. 2, pp. 58–61, 2004.
- [106] H. K. Müller, "Electrical and optical properties of sputtered  $\text{In}_2\text{O}_3$  films. II. optical properties in the near infrared," *Physica Status Solidi*, vol. 27, no. 2, pp. 733–740, 1968.
- [107] H. Köstlin, R. Jost, and W. Lems, "Optical and electrical properties of doped  $\text{In}_2\text{O}_3$  films," *Physica Status Solidi (a)*, vol. 29, no. 1, pp. 87–93, 1975.
- [108] Y. Ohhata, F. Shinoki, and S. Yoshida, "Optical properties of r.f. reactive sputtered tin-doped  $\text{In}_2\text{O}_3$  films," *Thin Solid Films*, vol. 59, no. 2, pp. 255–261, 1979.
- [109] I. Hamberg and C. G. Granqvist, "Evaporated Sn-doped  $\text{In}_2\text{O}_3$  films: Basic optical properties and applications to energy-efficient windows," *Journal of Applied Physics*, vol. 60, no. 11, p. R123, 1986.
- [110] R. Franz and G. Wiedemann, "Über die Wärme-Leitungsfähigkeit der Metalle," *Annalen der Physik und Chemie*, vol. 165, no. 8, pp. 497–531, 1853.
- [111] T. Ashida, A. Miyamura, N. Oka, Y. Sato, T. Yagi, N. Taketoshi, T. Baba, and Y. Shigesato, "Thermal transport properties of polycrystalline tin-doped indium oxide films," *Journal of Applied Physics*, vol. 105, no. 7, p. 073709, 2009.
- [112] W. F. Wu and B. S. Chiou, "Mechanical properties of r.f. magnetron sputtered indium tin oxide films," *Thin Solid Films*, vol. 293, no. 1-2, pp. 244–250, 1997.
- [113] G. Kaune, *Röntgenografische Charakterisierung von ITO Dünnschichten*. PhD thesis, TU Chemnitz, Chemnitz, 2005.
- [114] M. Scholten and J. v. d. Meerakker, "On the mechanism of ito etching: The specificity of halogen acids," *J. Electrochem. Soc.*, vol. 2, no. 140, pp. 471–475, 1993.
- [115] P. Monk, "Reductive ion insertion into thin-film indium tin oxide (ITO) in aqueous acidic solutions: the effect of leaching of indium from the ITO," *Journal of Materials Science: Materials in Electronics*, no. 10, pp. 101–107, 1999.
- [116] C. Huang, Y. Su, and S. Wu, "The effect of solvent on the etching of ITO electrode," *Materials Chemistry and Physics*, vol. 84, no. 1, pp. 146–150, 2004.
- [117] J. van den Meerakker, P. Baarslag, W. Walrave, T. Vink, and J. Daams, "On the homogeneity of sputter-deposited ITO films part II. etching behaviour," *Thin Solid Films*, vol. 266, no. 2, pp. 152–156, 1995.
- [118] M. Inoue, "Patterning characteristics of ITO thin films," *Japanese Journal of Applied Physics*, vol. 28, no. 2, pp. 274–278, 1989.

- [119] D. Neerincx and T. Vink, "Depth profiling of thin ITO films by grazing incidence x-ray diffraction," *Thin Solid Films*, vol. 278, no. 1-2, pp. 12–17, 1996.
- [120] Afrooz Barnoush, *Hydrogen embrittlement, revisited by in situ electrochemical nanoindentation*. PhD thesis, Universität des Saarlandes, Saarbrücken, 2007.
- [121] SCHOTT, "Af 32 datenblatt d 0889 1," 2007.
- [122] S. Strite, "GaN, AlN, and InN: A review," *Journal of Vacuum Science & Technology B: Microelectronics and Nanometer Structures*, vol. 10, no. 4, p. 1237, 1992.
- [123] K. Khor, K. Cheng, L. Yu, and F. Boey, "Thermal conductivity and dielectric constant of spark plasma sintered aluminum nitride," *Materials Science and Engineering: A*, vol. 347, no. 1-2, pp. 300–305, 2003.
- [124] N. Kuramoto, H. Taniguchi, and I. Aso, "Translucent AlN ceramic substrate," *IEEE Transactions on Components, Hybrids, and Manufacturing Technology*, vol. 9, no. 4, pp. 386–390, 1986.
- [125] G. A. Slack and T. McNelly, "Growth of high purity AlN crystals," *Journal of Crystal Growth*, vol. 34, no. 2, pp. 263–279, 1976.
- [126] A. Ababneh, *Herstellung und Charakterisierung von dünnen, piezoelektrischen Aluminiumnitrid-Schichten für MEMS Anwendungen*. PhD thesis, Universität des Saarlandes, Saarbrücken, 2009.
- [127] P. Legrand, M. Wautelet, B. Dugnoille, J. Dauchot, and M. Hecq, "Optical properties of sputter-deposited aluminium nitride films on silicon," *Thin Solid Films*, vol. 248, no. 2, pp. 220–223, 1994.
- [128] E. Hering, R. Martin, and M. Stohrer, *Physik für Ingenieure*. Springer-Lehrbuch, Berlin and Heidelberg: Springer Berlin Heidelberg, 11. Aufl. ed., 2012.
- [129] MicroChemicals GmbH, "Product data sheet: AZ1500 series: Standard photoresists."
- [130] M. Leber, "Trimmen der Impedanz transparenter ITO-Elektroden durch Laserinduzierte nanostrukturierung (Diplomarbeit)," Master's thesis, Universität des Saarlandes, Saarbrücken, 2014.
- [131] R. Ayasli, "Femtosekunden-Laser-Nanolithographie (Diplomarbeit)," Master's thesis, Universität des Saarlandes, Saarbrücken, 2015.
- [132] R. Martinez-Duarte and M. Madou, "SU-8 photolithography and its impact on microfluidics," *Microfluidics and Nanofluidics Handbook: Fabrication, Implementation and Applications*, vol. 2011, pp. 231–268, 2011.
- [133] MicroChem, "SU-8 data sheet."
- [134] R. Daunton, A. J. Gallant, and D. Wood, "Manipulation of exposure dose parameters to improve production of high aspect ratio structures using SU-8," *Journal of Micromechanics and Microengineering*, vol. 22, no. 7, p. 075016, 2012.

- [135] MicroChemicals GmbH, “Product data sheet: AZ5214E: Image reversal photoresist.”
- [136] “Electron microscope,” in *Wikipedia, the free encyclopedia Aug. 2016*.
- [137] J. A. WOOLLAM CO. INC., “Ellipsometry: Data analysis,” 2016.
- [138] H. Fujiwara, *Spectroscopic ellipsometry: Principles and applications*. Chichester and England and Hoboken and NJ: John Wiley & Sons, ©2007.
- [139] O. S. Heavens, *Optical properties of thin solid films*. New York: Dover Publ, 1991.
- [140] M. Stockett, *Optical properties of thin transparent conduction oxide films on glass for photovoltaic applications*. 2006.
- [141] H. Topsøe, *Geometric factor in four point resistivity measurement.*, vol. 472-13. 2 ed., 1966.
- [142] D. K. Schroder, *Semiconductor material and device characterization*. [Piscataway and NJ] and Hoboken and N.J: IEEE Press and Wiley, 3 ed., ©2006.
- [143] I. Horcas, R. Fernández, J. M. Gómez-Rodríguez, J. Colchero, J. Gómez-Herrero, and A. M. Baro, “Wsxm: A software for scanning probe microscopy and a tool for nanotechnology,” *Review of Scientific Instruments*, vol. 78, no. 1, p. 013705, 2007.
- [144] K. L. Johnson, *Contact mechanics*. Cambridge [Cambridgeshire] and New York: Cambridge University Press, 1 ed., 1987.
- [145] W. Wang, Y. Zhong, K. Lu, L. Lu, D. L. McDowell, and T. Zhu, “Size effects and strength fluctuation in nanoscale plasticity,” *Acta Materialia*, vol. 60, no. 8, pp. 3302–3309, 2012.
- [146] L. Chen, A. Ahadi, J. Zhou, and J. E. Ståhl, “Numerical and experimental study of the roughness effects on mechanical properties of AISI316L by nanoindentation,” *Modeling and Numerical Simulation of Material Science*, vol. 04, no. 04, pp. 153–162, 2014.
- [147] Hysitron Incorporated, “Triboindenter user manual,” 2011.
- [148] M. Bahner, “Entwurf und Realisierung der Ablaufsteuerung, Datenaufnahme und Visualisierung einer rechnergesteuerten Testanlage für Mikro-Gassensoren mit LabVIEW (Diplomarbeit),” Master’s thesis, Hochschule Niederrhein, Krefeld, 1999.
- [149] A. J. Bard and L. R. Faulkner, *Electrochemical methods: Fundamentals and applications*. New York: Wiley, 2 ed., ©2001.
- [150] D. Ende and K.-M. Mangold, “Impedanzspektroskopie,” *Chemie in unserer Zeit*, vol. 27, no. 3, pp. 134–140, 1993.
- [151] J. R. Macdonald, “Impedance spectroscopy,” *Annals of Biomedical Engineering*, vol. 20, no. 3, pp. 289–305, 1992.
- [152] A. Lasia, ed., *Electrochemical Impedance Spectroscopy and its Applications*. New York and NY: Springer New York, 2014.

- [153] M. F. Chen, W. T. Hsiao, Y. S. Ho, S. F. Tseng, and Y. P. Chen, "Laser patterning with beam shaping on indium tin oxide thin films of glass/plastic substrate," *Thin Solid Films*, vol. 518, no. 4, pp. 1072–1078, 2009.
- [154] M. Park, B. H. Chon, H. S. Kim, S. C. Jeoung, D. Kim, J. I. Lee, H. Y. Chu, and H. R. Kim, "Ultrafast laser ablation of indium tin oxide thin films for organic light-emitting diode application," *Optics and Lasers in Engineering*, vol. 44, no. 2, pp. 138–146, 2006.
- [155] P. Gecys, G. Raciukaitis, A. Wehrmann, K. Zimmer, A. Braun, and S. Ragnow, "Scribing of thin-film solar cells with picosecond and scribing of thin-film solar cells with picosecond and femtosecond lasers," *Journal of Laser Micro/Nanoengineering*, no. 7, p. No. 1, 2012.
- [156] P. Gecys, E. Markauskas, M. Gedvilas, G. Raciukaitis, I. Repins, and C. Beall, "Ultra-short pulsed laser induced material lift-off processing of CZTSe thin-film solar cells," *Solar Energy*, vol. 102, pp. 82–90, 2014.
- [157] T. Szörényi, Z. Kántor, and L. Laude, "Atypical characteristics of KrF excimer laser ablation of indium-tin oxide films," *Applied Surface Science*, vol. 86, no. 1-4, pp. 219–222, 1995.
- [158] M. Xu, J. Li, L. Lilge, and P. Herman, "F<sub>2</sub>-laser patterning of indium tin oxide (ITO) thin film on glass substrate," *Applied Physics A*, vol. 85, no. 1, pp. 7–10, 2006.
- [159] O. Yavas and M. Takai, "Effect of substrate absorption on the efficiency of laser patterning of indium tin oxide thin films," *Journal of Applied Physics*, vol. 85, no. 8, p. 4207, 1999.
- [160] M. F. Chen, Y. P. Chen, W. T. Hsiao, and Z. P. Gu, "Laser direct write patterning technique of indium tin oxide film," *Thin Solid Films*, vol. 515, no. 24, pp. 8515–8518, 2007.
- [161] Q. Bian, X. Yu, B. Zhao, Z. Chang, and S. Lei, "Femtosecond laser ablation of indium tin-oxide narrow grooves for thin film solar cells," *Optics & Laser Technology*, vol. 45, pp. 395–401, 2013.
- [162] C. W. Cheng, C. Y. Lin, W. C. Shen, Y. J. Lee, and J. S. Chen, "Patterning crystalline indium tin oxide by high repetition rate femtosecond laser-induced crystallization," *Thin Solid Films*, vol. 518, no. 23, pp. 7138–7142, 2010.
- [163] M. Afshar, S. Saremi, H. Völm, D. Feili, H. Seidel, M. Straub, and K. König, "Multiphoton lithography and its structuring by high repetition-rate sub-15 femtosecond laser pulses," *SPIE Proceedings*, vol. 7920, no. 15, 2011.
- [164] W. Chung, M. O. Thompson, P. Wickboldt, D. Toet, and P. G. Carey, "Room temperature indium tin oxide by XeCl excimer laser annealing for flexible display," *Thin Solid Films*, vol. 460, no. 1-2, pp. 291–294, 2004.



- [165] M. F. Chen, K. Lin, and Y. S. Ho, "Laser annealing process of ITO thin films using beam shaping technology," *Optics and Lasers in Engineering*, vol. 50, no. 3, pp. 491–495, 2012.
- [166] G. Legeay, X. Castel, R. Benzerga, and J. Pinel, "Excimer laser beam/ITO interaction: from laser processing to surface reaction," *physica status solidi (c)*, vol. 5, no. 10, pp. 3248–3254, 2008.
- [167] W. Franks, I. Schenker, P. Schmutz, and A. Hierlemann, "Impedance characterization and modeling of electrodes for biomedical applications," *IEEE Transactions on Biomedical Engineering*, vol. 52, no. 7, pp. 1295–1302, 2005.
- [168] W. Schmickler and M. Lingner, *Grundlagen der Elektrochemie*. Vieweg Lehrbuch. Physikalische Chemie, Braunschweig/Wiesbaden: Vieweg, 1996.
- [169] H. Wang and L. Pilon, "Accurate simulations of electric double layer capacitance of ultramicroelectrodes," *The Journal of Physical Chemistry C*, vol. 115, no. 33, pp. 16711–16719, 2011.
- [170] E. McAdams, A. Lacknermeier, J. McLaughlin, D. Macken, and J. Jossinet, "The linear and non-linear electrical properties of the electrode-electrolyte interface," *Biosensors and Bioelectronics*, vol. 10, no. 1-2, pp. 67–74, 1995.
- [171] B. Sapoval, J. N. Chazalviel, and J. Peyrière, "Electrical response of fractal and porous interfaces," *Physical Review A*, vol. 38, no. 11, pp. 5867–5887, 1988.
- [172] P. Gründler, *Chemical sensors: An introduction for scientists and engineers*. Berlin and London: Springer, 2007.
- [173] G. Sberveglieri, "Recent developments in semiconducting thin-film gas sensors," *Sensors and Actuators B: Chemical*, vol. 23, no. 2-3, pp. 103–109, 1995.
- [174] G. Sberveglieri, P. Benussi, G. Coccoli, S. Groppelli, and P. Nelli, "Reactively sputtered indium tin oxide polycrystalline thin films as NO and NO<sub>2</sub> gas sensors," *Thin Solid Films*, vol. 186, no. 2, pp. 349–360, 1990.
- [175] G. Sberveglieri, S. Groppelli, and G. Coccoli, "Radio frequency magnetron sputtering growth and characterization of indium-tin oxide (ITO) thin films for NO<sub>2</sub> gas sensors," *Sensors and Actuators*, vol. 15, no. 3, pp. 235–242, 1988.
- [176] T. Sako, A. Ohmi, H. Yumoto, and K. Nishiyama, "ITO-film gas sensor for measuring photodecomposition of NO<sub>2</sub> gas," *Surface and Coatings Technology*, vol. 142-144, pp. 781–785, 2001.
- [177] N. Patel, K. Makhija, and C. Panchal, "Fabrication of carbon dioxide gas sensor and its alarm system using indium tin oxide (ITO) thin films," *Sensors and Actuators B: Chemical*, vol. 21, no. 3, pp. 193–197, 1994.
- [178] A. Galdikas, Z. Martūnas, and A. Šetkus, "Snino-based chlorine gas sensor," *Sensors and Actuators B: Chemical*, vol. 7, no. 1-3, pp. 633–636, 1992.

- [179] S. M. Lee, Y. S. Lee, C. H. Shim, N. J. Choi, B. S. Joo, K. D. Song, J. S. Huh, and D. D. Lee, "Three electrodes gas sensor based on ITO thin film," *Sensors and Actuators B: Chemical*, vol. 93, no. 1-3, pp. 31–35, 2003.
- [180] N. Patel, P. Patel, and V. Vaishnav, "Indium tin oxide (ITO) thin film gas sensor for detection of methanol at room temperature," *Sensors and Actuators B: Chemical*, vol. 96, no. 1-2, pp. 180–189, 2003.
- [181] N. Barsan, D. Koziej, and Weimar. U., "Metal oxide-based gas sensor research: How to?," *Sensors and Actuators B: Chemical*, vol. 121, no. 1, pp. 18–35, 2007.
- [182] G. Wiche, *Metalloxid Gassensor mit Ziliziumcarbid Micro-Hotplate*. PhD thesis, TU Berlin, Berlin, 2007.
- [183] E. Comini, "Metal oxide nano-crystals for gas sensing," *Analytica Chimica Acta*, vol. 568, no. 1-2, pp. 28–40, 2006.
- [184] P. Moseley, "New trends and future prospects of thick- and thin-film gas sensors," *Sensors and Actuators B: Chemical*, vol. 3, no. 3, pp. 167–174, 1991.
- [185] V. Dua, S. P. Surwade, S. Ammu, X. Zhang, S. Jain, and S. K. Manohar, "Chemical vapor detection using parent polythiophene nanofibers," *Macromolecules*, vol. 42, no. 15, pp. 5414–5415, 2009.
- [186] J. F. McAleer, P. T. Moseley, J. O. W. Norris, D. E. Williams, and B. C. Tofield, "Tin dioxide gas sensors. part 2.—the role of surface additives," *Journal of the Chemical Society, Faraday Transactions 1: Physical Chemistry in Condensed Phases*, vol. 84, no. 2, p. 441, 1988.
- [187] M. Sucheá, S. Christoulakis, K. Moschovis, N. Katsarakis, and G. Kiriakidis, "ZnO transparent thin films for gas sensor applications," *Thin Solid Films*, vol. 515, no. 2, pp. 551–554, 2006.
- [188] P. Skafidas, D. Vlachos, and J. Avaritsiotis, "Modelling and simulation of tin oxide based thick-film gas sensors using monte carlo techniques," *Sensors and Actuators B: Chemical*, vol. 19, no. 1-3, pp. 724–728, 1994.
- [189] M. Sucheá, N. Katsarakis, S. Christoulakis, S. Nikolopoulou, and G. Kiriakidis, "Low temperature indium oxide gas sensors," *Sensors and Actuators B: Chemical*, vol. 118, no. 1-2, pp. 135–141, 2006.
- [190] X. Chen, C. K. Wong, C. A. Yuan, and G. Zhang, "Nanowire-based gas sensors," *Sensors and Actuators B: Chemical*, vol. 177, pp. 178–195, 2013.
- [191] O. Lupan, L. Chow, T. Pauporté, L. Ono, B. Roldan Cuenya, and G. Chai, "Highly sensitive and selective hydrogen single-nanowire nanosensor," *Sensors and Actuators B: Chemical*, vol. 173, pp. 772–780, 2012.
- [192] X. J. Huang and Y. K. Choi, "Chemical sensors based on nanostructured materials," *Sensors and Actuators B: Chemical*, vol. 122, no. 2, pp. 659–671, 2007.

- [193] F. Hernandez-Ramirez, J. D. Prades, R. Jimenez-Diaz, T. Fischer, A. Romano-Rodriguez, S. Mathur, and J. R. Morante, "On the role of individual metal oxide nanowires in the scaling down of chemical sensors," *Physical Chemistry Chemical Physics*, vol. 11, no. 33, p. 7105, 2009.
- [194] M. Law, H. Kind, B. Messer, F. Kim, and P. Yang, "Photochemical sensing of NO<sub>2</sub> with SnO<sub>2</sub> nanoribbon nanosensors at room temperature," *Angewandte Chemie*, vol. 114, no. 13, pp. 2511–2514, 2002.
- [195] F. Hernández-Ramírez, J. Rodríguez, O. Casals, E. Russinyol, A. Vilà, A. Romano-Rodríguez, J. Morante, and M. Abid, "Characterization of metal-oxide nanosensors fabricated with focused ion beam (FIB)," *Sensors and Actuators B: Chemical*, vol. 118, no. 1-2, pp. 198–203, 2006.
- [196] I. Castro-Hurtado, J. Herrán, G. Ga Mandayo, and E. Castaño, "SnO<sub>2</sub>-nanowires grown by catalytic oxidation of tin sputtered thin films for formaldehyde detection," *Thin Solid Films*, vol. 520, no. 14, pp. 4792–4796, 2012.
- [197] S. Xu and Y. Shi, "Low temperature high sensor response nano gas sensor using ITO nanofibers," *Sensors and Actuators B: Chemical*, vol. 143, no. 1, pp. 71–75, 2009.
- [198] X. Y. Xue, Y. J. Chen, Y. G. Liu, S. L. Shi, Y. G. Wang, and T. H. Wang, "Synthesis and ethanol sensing properties of indium-doped tin oxide nanowires," *Applied Physics Letters*, vol. 88, no. 20, p. 201907, 2006.
- [199] G. Sauerbrey, "Verwendung von Schwingquarzen zur Wägung dünner Schichten und zur Mikrowägung," *Z. Physik (Zeitschrift für Physik)*, vol. 155, no. 2, pp. 206–222, 1959.
- [200] X. M. Henry Huang, C. A. Zorman, M. Mehregany, and M. L. Roukes, "Nanoelectromechanical systems: Nanodevice motion at microwave frequencies," *Nature*, vol. 421, no. 6922, p. 496, 2003.
- [201] X. L. Feng, R. He, P. Yang, and M. L. Roukes, "Very high frequency silicon nanowire electromechanical resonators," *Nano Letters*, vol. 7, no. 7, pp. 1953–1959, 2007.
- [202] K. L. Ekinici, "Ultimate limits to inertial mass sensing based upon nanoelectromechanical systems," *Journal of Applied Physics*, vol. 95, no. 5, p. 2682, 2004.
- [203] K. L. Ekinici and M. L. Roukes, "Nanoelectromechanical systems," *Review of Scientific Instruments*, vol. 76, no. 6, p. 061101, 2005.
- [204] H. J. Mamin and D. Rugar, "Sub-attoneutron force detection at millikelvin temperatures," *Applied Physics Letters*, vol. 79, no. 20, p. 3358, 2001.
- [205] K. L. Ekinici, X. M. H. Huang, and M. L. Roukes, "Ultrasensitive nanoelectromechanical mass detection," *Applied Physics Letters*, vol. 84, no. 22, p. 4469, 2004.
- [206] M. D. LaHaye, "Approaching the quantum limit of a nanomechanical resonator," *Science*, vol. 304, no. 5667, pp. 74–77, 2004.

- [207] B. Ilic, “Attogram detection using nanoelectromechanical oscillators,” *Journal of Applied Physics*, vol. 95, no. 7, p. 3694, 2004.
- [208] B. Ilic, Y. Yang, K. Aubin, R. Reichenbach, S. Krylov, and H. G. Craighead, “Enumeration of DNA molecules bound to a nanomechanical oscillator,” *Nano Letters*, vol. 5, no. 5, pp. 925–929, 2005.
- [209] Y. T. Yang, C. Callegari, X. L. Feng, K. L. Ekinici, and M. L. Roukes, “Zeptogram-scale nanomechanical mass sensing,” *Nano Letters*, vol. 6, no. 4, pp. 583–586, 2006.
- [210] H. B. Peng, C. W. Chang, S. Aloni, T. D. Yuzvinsky, and A. Zettl, “Ultrahigh frequency nanotube resonators,” *Physical Review Letters*, vol. 97, no. 8, 2006.
- [211] K. Jensen, K. Kim, and A. Zettl, “An atomic-resolution nanomechanical mass sensor,” *Nature Nanotechnology*, vol. 3, no. 9, pp. 533–537, 2008.
- [212] A. K. Gupta, P. R. Nair, D. Akin, M. R. Ladisch, S. Broyles, M. A. Alam, and R. Bashir, “Anomalous resonance in a nanomechanical biosensor,” *Proceedings of the National Academy of Sciences*, vol. 103, no. 36, pp. 13362–13367, 2006.
- [213] T. Adrega, V. Chu, and J. P. Conde, “Electrostatically actuated resonance of amorphous silicon microresonators in water,” *Applied Physics Letters*, vol. 89, no. 14, p. 143109, 2006.
- [214] R. Rudd, “Atomistic simulation of MEMS resonators through the coupling of length scales,” *Journal of Modeling and Simulation of Microsystems*, no. 1, pp. 29–38, 1999.
- [215] R. Phillips, *Crystals, Defects and Microstructures*. Cambridge: Cambridge University Press, 2001.
- [216] K. L. Ekinici, Y. T. Yang, X. M. H. Huang, and M. L. Roukes, “Balanced electronic detection of displacement in nanoelectromechanical systems,” *Applied Physics Letters*, vol. 81, no. 12, p. 2253, 2002.
- [217] S. S. Verbridge, J. M. Parpia, R. B. Reichenbach, L. M. Bellan, and H. G. Craighead, “High quality factor resonance at room temperature with nanostrings under high tensile stress,” *Journal of Applied Physics*, vol. 99, no. 12, p. 124304, 2006.
- [218] D. W. Carr, S. Evoy, L. Sekaric, H. G. Craighead, and J. M. Parpia, “Measurement of mechanical resonance and losses in nanometer scale silicon wires,” *Applied Physics Letters*, vol. 75, no. 7, p. 920, 1999.
- [219] R. Blick, M. Roukes, W. Wegscheider, and M. Bichler, “Freely suspended two-dimensional electron gases,” *Physica B: Condensed Matter*, vol. 249–251, pp. 784–787, 1998.
- [220] Y. T. Yang, K. L. Ekinici, X. M. H. Huang, L. M. Schiavone, M. L. Roukes, C. A. Zorman, and M. Mehregany, “Monocrystalline silicon carbide nanoelectromechanical systems,” *Applied Physics Letters*, vol. 78, no. 2, p. 162, 2001.

- [221] A. N. Cleland, M. Pophristic, and I. Ferguson, “Single-crystal aluminum nitride nanomechanical resonators,” *Applied Physics Letters*, vol. 79, no. 13, p. 2070, 2001.
- [222] L. Sekaric, J. M. Parpia, H. G. Craighead, T. Feygelson, B. H. Houston, and J. E. Butler, “Nanomechanical resonant structures in nanocrystalline diamond,” *Applied Physics Letters*, vol. 81, no. 23, p. 4455, 2002.
- [223] L. Sekaric, D. Carr, S. Evoy, J. Parpia, and H. Craighead, “Nanomechanical resonant structures in silicon nitride: fabrication, operation and dissipation issues,” *Sensors and Actuators A: Physical*, vol. 101, no. 1-2, pp. 215–219, 2002.
- [224] Q. Unterreithmeier, E. Weig, and J. Kotthaus, “Universal transduction scheme for nanomechanical systems based on dielectric forces,” *Nature*, vol. 458, no. 7241, pp. 1001–1004, 2009.
- [225] J. W. Strutt, ed., *Theory of Sound*. London: Macmillan Publications Co., Inc., 1877.
- [226] B. Abbas and J. Thomas, “The second frequency spectrum of timoshenko beams,” *Journal of Sound and Vibration*, vol. 51, no. 1, pp. 123–137, 1977.
- [227] S. P. Timoshenko, “On the correction for shear of the differential equation for transverse vibrations of prismatic bars,” *Philosophical Magazine Series 6*, vol. 41, no. 245, pp. 744–746, 1921.
- [228] S. Han, H. Benaroya, and T. Wei, “Dynamics of transversely vibrating beams using four engineering theories,” *Journal of Sound and Vibration*, vol. 225, no. 5, pp. 935–988, 1999.
- [229] A. L. Herrera-May, P. J. Garcia-Ramirez, L. A. Aguilera-Cortes, H. Plascencia-Mora, L. Garcia-Gonzalez, E. Manjarrez, M. Narducci, and E. Figueras, “Analytical modeling for the bending resonant frequency of sensors based on micro and nanoresonators with complex structural geometry,” *IEEE Sensors Journal*, vol. 11, no. 6, pp. 1361–1374, 2011.
- [230] K. Brueckner, F. Niebelschuetz, K. Tonisch, C. Foerster, V. Cimalla, R. Stephan, J. Pezoldt, T. Stauden, O. Ambacher, and M. A. Hein, “Micro- and nano-electromechanical resonators based on SiC and group III-nitrides for sensor applications,” *Physica Status Solidi (a)*, vol. 208, no. 2, pp. 357–376, 2011.
- [231] D. Li, Y. Wu, P. Kim, L. Shi, P. Yang, and A. Majumdar, “Thermal conductivity of individual silicon nanowires,” *Applied Physics Letters*, vol. 83, no. 14, p. 2934, 2003.
- [232] A. Boukai, K. Xu, and J. R. Heath, “Size-dependent transport and thermoelectric properties of individual polycrystalline bismuth nanowires,” *Advanced Materials*, vol. 18, no. 7, pp. 864–869, 2006.



# Acknowledgements

I would first like to thank my family, especially my Mom and Dad, for the continuous support and love that they have given me throughout my life. I would also like to thank my life companion, my dearest love, Somi for all the comfort and love she has given me. I could not have done this work without you.

Secondly, I would like to express my sincere gratitude to my adviser Prof. Dr. Helmut Seidel for the continuous support over the course of researching, developing, and writing my dissertation. His guidance has been invaluable.

I would also like to kindly thank my second reviewer Prof. Dr. Frank Mücklich for his engagement and support.

I would like to especially thank the rest of my colleagues: Prof. Dr. Dara Feili, Ute Flieger, Dipl.-Ing. Günter Marchand and our whole group, for their valuable insights and encouragement, and also for their constructive teamwork.

I thank the undergraduate students who decided to put their trust in me to advise them in their work. I thank them for their hard work and for the fun we had together. Special thanks go to Elisabeth Preiß, Moritz Leber, Daniel Gillo, Michael Penth, Marius Rodner and also Manuel Bastuck for developing a scan data generating software.

My sincere thanks also go to the external project partners Prof. Dr. Karsten König, Dr. Martin Straub, and Dr. Georg Breunig from Labs of Biophotonics and Laser Technology of Saarland University, with whom I shared the laser lab during this project.

I would also thank those who have supported me through collaboration or by allowing me to use their laboratories and research facilities:

- Prof. Dr. Frank Mücklich, Dr. Flavio Soldera, Sebastian Slawik, and specially Christoph Pauly from Lehrstuhl für Funktionswerkstoffe of Saarland University.
- Prof. Dr. Andreas Schütze and Dr. Tilmann Sauerwald from Labs for Measurement Technology (LMT) at Saarland University.
- Dr. Mohammad Jilavi, Dr. Marcus Koch, Dr. Hadi Mousavi, and Dr. Bruno Schäfer from Leibniz Institut for New Materials (INM).
- Prof. Dr. Karin Jacobs, Dr. Mathias Lessel and Dr. Christian Zeitz from Labs for Condensed Matter Physics at Saarland University.
- Dr. Wigand Poppendick from Fraunhofer Institute for Biomedical Engineering (IBMT).

- Prof. Dr. Herbert Kliem and Dr. Björn Martin from Lehrstuhl für Grundlagen und Materialien der Elektrotechnik of Saarland University.
- Dr. Jörg Schmauch from Labs for Technical Physics at Saarland University.
- Dr. Mohammad Zamanzade from Labs for Materials Science and Methods (MWW) at Saarland University.

Last but not the least, I am deeply grateful to those who helped me in valuable discussions to understand my research area better and sort out the scientific and technical details of my work.

Thank you all, without you and your supports it would not be possible to conduct this research.

Lastly, none of this would have been possible without the Deutsche Forschungsgemeinschaft (DFG) who founded the project as Priority Program 1327.



# Curriculum vitae

Maziar Afshar was born in Tehran, Iran in 1979. He received his bachelor's degree in Physics from the University of Tehran in 2002. In 2004, he began to continue his studies in Physics at the Free University, Berlin and in 2008 he completed the research for his diploma-thesis performed at Helmholtz-Zentrum Berlin für Materialien und Energie (HZB, former HMI) in the topic "*Growth and Characterising of Epitaxial Multilayers from CuInSe<sub>2</sub> and CuGaSe<sub>2</sub>*". Since 2009, he has been working as research assistant to Labs for Micromechanics, Microfluidics/Microactuators (LMM) at Saarland University, where he has also started his Ph.D. thesis in 2010 on *Nanostructuring of Indium Tin Oxide with Sub-15 Femtosecond Laser Pulses for Technical and Biomedical Applications*. His research at the Saarland University concerned laser lithography, as well as micro-/nanostructuring of different materials with a near-infrared femtosecond laser for different applications.

On following pages a list of his publications is presented.

## Persönliche Daten

Vor- und Nachname: Maziar Afshar  
 Anschrift: Paula-Modersohn-Platz 7  
 79100 Freiburg im Breisgau  
 E-Mail: maziar.afshar@gmail.com  
 Tel.: 0176/55516747  
 Geburtsdatum: 12. August 1979  
 Staatsangehörigkeit: Deutsch/Iranisch  
 Familienstand: Verheiratet



## Ausgewählte Veröffentlichungen

### Buchbeitrag:

2015 K. König, H. Seidel, M. Afshar, M. Klötzer, D. Feili, M. Straub, *Optically Induced Nanostructures: Biomedical and Technical Applications*; Kapitel 1, **Walter de Gruyter GmbH & Co KG**.

### Erstautor:

- 2016 M. Afshar, M. Leber, W. Poppendieck, K. König, H. Seidel, and D. Feili, *On-Chip Nanostructuring and Impedance Trimming of Transparent and Flexible ITO Electrodes by Laser Induced Coherent Sub-20 nm cuts*; **Applied Surface Science**, 360, 494-501 (2016).
- 2015 M. Afshar, E. Preiss, T. Sauerwald, M. Rodner, D. Feili, M. Straub, K. König, A. Schütze, and H. Seidel, *Indium-Tin-Oxide Single-Nanowire Gas Sensor Fabricated Via Laser Writing and Subsequent Etching*, **Sensors & Actuators B**, 215, 525-535 (2015).
- 2013 M. Afshar, E. Preiss, T. Sauerwald, D. Feili, H. Seidel, *ITO nanowires for gas-sensor applications*; **Nano/Micro Engineered and Molecular Systems (NEMS)**, 8th IEEE International Conference Japan, 1123-1126 (2013).
- 2012 M. Afshar, M. Straub, H. Voellm, D. Feili, K. Koenig, H. Seidel, *Sub-100 nanometer structuring of indium-tin-oxide thin films by sub-15 femtosecond pulsed near-infrared laser light*; **Optics Letters** 37, Iss. 4, 563-565 (2012).
- 2011 M. Afshar, S. Saremi, H. Völlm, D. Feili, H. Seidel, M. Straub, H. Zhang, K. König; *Multiphoton lithography and ITO structuring by high repetition-rate sub-15 femtosecond laser pulses*; **Proc. SPIE 7920**, Laser Applications in Microelectronic and Optoelectronic Manufacturing (LAMOM) XVI, 792015 (2011).
- M. Afshar, Sascha Sadewasser, Jürgen Albert, Sebastian Lehmann, Daniel Abou-Ras, David Fuertes Marrón, Angus A. Rockett, Esa Räsänen, and Martha Ch. Lux-Steiner; *Chalcopyrite Semiconductors for Quantum Well Solar Cells*; **Adv. Energy Mater.** 1, 1109-1115 (2011).

**Coautor:**

- 2015 M. Klötzer, M. Afshar, D. Feili, H. Seidel, K. König, M. H. Straub; *Generation of laser-induced periodic surface structures in indium-tin-oxide thin films and two-photon lithography of ma-N photoresist by sub-15 femtosecond laser microscopy for liquid crystal cell application*; **Proc. SPIE 9351**, Laser-based Micro- and Nanoprocessing IX, 935110 (2015).
- 2014 M. Straub, M. Schüle, M. Afshar, D. Feili, H. Seidel, K. König, *Sub-15 femtosecond laser-induced nanostructures emerging on Si (100) surfaces immersed in water: analysis of structural phases*; **Applied Physics A** 115 (1), 221-228 (2014).  
M. Schüle, M. Afshar, D. Feili, H. Seidel, K. König, M. Straub, *Incubation and nanostructure formation on n-and p-type Si (100) and Si (111) at various doping levels induced by sub-nanojoule femto-and picosecond near-infrared laser pulses*; **Applied Surface Science** 314, 21-29 (2014).
- 2013 M. Straub, B. Weigand, M. Afshar, D. Feili, H. Seidel, K. König, *Periodic subwavelength ripples on lithium niobate surfaces generated by tightly focused sub-15 femtosecond sub-nanojoule pulsed near-infrared laser light*; **Journal of Optics** 15 (5), 055601 (2013).
- 2012 M. Straub, M. Afshar, D. Feili, H. Seidel, K. Koenig, *Periodic nanostructures on Si(100) surfaces generated by high-repetition rate sub-15 fs pulsed near-infrared laser light*; **Optics Letters** 37, Iss. 2, 190-192 (2012).  
H. Zhang, M. Afshar, D. Feili, H. Seidel, K. König, *Nanometer-size dots-chains at and beneath surfaces of glasses written by picojoule 12-fs laser scanning microscope*; **Appl. Phys. A** 106, Nr. 4 (2012).  
M. Straub, M. Afshar, D. Feili, H. Seidel, K. König, *Surface plasmon polariton model of high-spatial frequency laser-induced periodic surface structure generation in silicon*; **Journal of Appl. Phys.**, 111, 124315 (2012).
- 2011 M. Straub, M. Afshar, D. Feili, H. Seidel, K. König, *Efficient nanostructure formation on silicon surfaces and in indium tin oxide thin films by sub-15 fs pulsed near-infrared laser light*; **Physics Procedia** 12, 16-23 (2011).
- 2010 D. Fuertes Marrón, E. Cínovas, M. Y. Levy, A. Martí, A. Luque, M. Afshar, J. Albert, S. Lehmann, D. Abou-Ras, S. Sadewasser, N. Barreau, *Optoelectronic evaluation of the nanostructuring approach to chalcopyrite-based intermediate band materials*; **Solar Energy Materials and Solar Cells**, 94 (11), 1912-1918 (2010).